CRANFIELD UNIVERSITY

Carlos Soria

Gas Turbine Shaft Over-speed / Failure Modelling

Aero/Thermodynamics Modelling and Overall Engine System Response

School of Engineering

Ph. D. Thesis

SCHOOL OF ENGINEERING
DEPARTMENT OF POWER AND PROPULSION

Full time Ph. D.

Academic Year 2010-2014

Carlos Soria

Gas Turbine Shaft Over-speed / Failure Modelling

Aero/Thermodynamics Modelling and Overall Engine System Response

Academic Supervisor: Dr. V. Pachidis
Industrial Supervisors: A. Rowe, S. Brown

April 2014

This thesis is submitted in partial fulfilment of the requirements for the degree of Doctor of Philosophy

© Cranfield University 2014. All rights reserved. No part of this publication may be reproduced without the written permission of the copyright owner

Executive summary

Gas turbine design needs of high-speed turbomachinery whose layout is organised in compressor-turbine pairs mechanically linked by concentric shafts. The mechanical failure of a shaft leads to compressor-turbine decoupling provoking the acceleration of the free-running turbine. In view of such scenario, it is of paramount importance to guaranty the mechanical integrity of the turbine, in terms of high energy debris release. Certification authorities require proof that any possible failure will be contained; admitting the reliable simulation capability of the event as certification strategy.

The objectives of this research activity have aimed at the development of reliable simulation tools based on analytical and semi-empirical models. The integration of all the different models/modules together in an "all-in-one" tool provides the sponsor company with the capability to simulate and assess various shaft over-speed scenarios during the early stages of an engine's design and development program.

Shaft failure event cannot be understood unless engine components interaction and fast transient effects are taken into account in a global manner. The high vibration level consequence of the breakage, or the thermodynamic mismatch due to the rapid free-running compressor deceleration, trigger the surge of the compression system which affects to the performance of every engine component. Fully-transient simulation capability to model compression system post-stall performance and secondary air system behaviour has been developed. Component map prediction tools have been created for compressor reverse flow performance and turbines affected by inlet distorted flows.

The development of the so-called "all-in-one" simulation tool has been completed and it has been applied to the modelling of a real case of shaft failure. Reliable prediction of thermodynamic properties evolution and over-speeding turbine terminal speed have been shown. The robustness and flexibility of the simulation tool have been demonstrated by its application to different theoretical scenarios.

Acknowledgments

I am grateful to many people who have contributed enormously, not only to make this work possible, but also to make me grow as an engineer and as a person over this three-year period. This work would not have been possible without their trust, technical guidance and support.

Professor Singh and Dr. Pachidis for giving me the opportunity to join the Rolls-Royce UTC and to tackle one of the most beautifully challenging engineering problem that one could imagine. Thanks Vassilios for your guidance in so many ways and your patience, for trusting me even when I would have not trusted myself.

Rolls-Royce plc. for funding this research and the continuous support, providing in-house information, real engine data and expertise. It has been a priceless privilege working close to my industrial supervisors Arthur Rowe and Steve Brown. They are an endless source of knowledge and ideas. Thanks Arthur for sharing a bit of your knowledge with me, the most valuable thing I have learnt from you is that the person who knows more about something is the one who says 'I don't know' more often. Thanks also to Richard Tunstall, he is the perfect manager always able to bring out the best of us. Special mention deserves Dr. Luis Gallar whose invaluable heritage drove something else than my first steps in the shaft over-speed research.

If there is a piece of this thesis worth to be called science or an equation correctly written, I owe it to my professors in the E.T.S.I. Aeronáuticos. In special to: Julio Ramírez, Lola Sondesa, Francisco Higuera, José Salvá, Efrén Moreno and José Luis Montañés. Thanks also to José Ángel González, my math's teacher who encouraged me to do things long time ago.

Luis Sánchez de Leon and Aleixo González have been my family here, in and out the university. More than half of this PhD has been solved in our lunches, coffee breaks or in front of a blackboard with these two geniuses, although they would never admit it. When you work and live with people like them, you only have to

listen and learn. Thanks also to Serena Zoppellari who has been my colleague in fights against common enemies.

To my team, the bright and motivated MSc students I was supposed to supervise and however, I have ended up learning more from them than they could have ever learnt from me: Pablo Sanchis, Alejandro Caro, Luca Gallo, Fernando Andreu, Andrea Garbo, Victor Peña, Jon Sarasola, Guillermo Rodríguez and Alexander Sancho. Some of them crossed the line of friendship even after all I made them suffer.

And because there is life after work even during a PhD, I cannot forget the bunch of people who makes everything else worthy. Javi Gómez, I could always count on you for the 'philosophical non-sense drink'. Gloria García, I would like to be a bit more like you when I grow up. Aida Reig, here, there, nowhere and everywhere; we hold some records together. Mikel Bosque, Edu Piles, Alex Bonillo, Anna Corney, we have made this country almost like home.

The people I left at home and I have missed so much: Vicen, Alex, Fernan, mi primo, Tabordilla, Juan Ángel, Dani Pérez, Hodei, David Fraile and many others.

Last but not least, thanks to my parents and my little sisters, they take care of me from two thousand kilometres away. I could have not done it without their unconditional support.

Carlos Soria

Cranfield, April 2014

Contents

List of Figures

Nomenclature

1D	One-dimensional
2D	Two-dimensional
3D	Three-dimensional
AMC	Acceptable Mean of Compliance
ATSB	Australian Transport Safety Bureau
CFD	Computational Fluid Dynamics
CM	Certification Memorandum
EASA	European Aviation Safety Agency
FADEC	Full Authority Digital Engine Control
FAR	Fuel Air Ratio
FFT	Fast Fourier Transformation
GCI	Grid Convergence Index
HBR	High Bypass Ratio
HP	High Pressure
HPC	High Pressure Compressor
HPS	High Pressure Shaft
HPT	High Pressure Turbine
IGV	Inlet Guide Vane
IP	Intermediate Pressure

IPC	Intermediate Pressure Compressor
IPS	Intermediate Pressure Shaft
IPT	Intermediate Pressure Turbine
IPTOS	Intermediate Pressure Turbine Over-speed Protection System
LPS	Low Pressure Shaft
LPT	Low Pressure Turbine
MGP	Main Gas Path
MIT	Massachusetts Institute of Technology
MRE	Mean Relative Error
NDMF	Non-Dimensional Mass Flow
NGV	Nozzle Guide Vane
PR	Pressure Ratio
SAS	Secondary Air System
SST	Stage-Stacking Technique
SVGV	Split Variable Guide Vane
TET	Turbine Entry Temperature
TR	Temperature Ratio
VCV	Variable Camber Vane
VG	Variable Geometry
VIGV	Variable Inlet Guide Vane
VSV	Variable Stator Vane
A	Area
A_c	Area of the compressor
a	Speed of sound

B	Broyden matrix / Greitzer's B parameter
C	Courant number
C_i	Constants JANAF polynomials
C_p	Heat capacity at constant pressure
C_v	Heat capacity at constant temperature
C_x	Artificial viscosity constant
C_ω	Mass flow coefficient
D	Characteristic length
D_h	Hydraulic diameter
D_i	Inner diameter
D_o	Outer diameter
e	Internal energy
F_x	Axial force
F_{xSS}	Axial force (Steady-state)
$\bar{f_m}$	Body forces vector
Gr	Grashof number
H	Vector increment in Broyden method
H_B	Enthalpy bled
h	specific enthalpy / heat transfer coefficient
I	Intertia
$\vec{i}$	Unit vector axial direction
$\hat{i}$	Incidence angle
L	Length / Lower calorific value
L_c	Length of the compressor

L_{fuel}	Lower calorific value of fuel
M	Molecular mass / Mach number
$\dot{m_{da}}$	Mass flow of dry air
$\dot{m}$	Mass flow
$\dot{m_{sp}}$	Mass flow of stoichiometric products
$\dot{m_{uf}}$	Mass flow of unburt fuel
N	Rotational speed (rpm)
NRT	Corrected rotational speed
Nu	Nusselt number
$\vec{n}$	Surface unit vector
P30	Compressor delivery pressure (HPC outlet)
Pm	Perimeter
Pr	Prandtl number
P_t	Total pressure
p	Static pressure
p_∞	Static pressure far field
Q	Heat addition
q	Heat flux
R	Universal gas constant
Re	Reynolds number
R_g	Specific gas constant
Ro	Rossby number
r	Radius
S	Artificial viscosity term

St	Stanton number
SW	Shaft work
T	Static temperature
Ta	Taylor number
T_b	Blade temperature
T_∞	Static temperature far field
T_s	Wall temperature
T_t	Total temperature
T'_t	Total temperature relative frame
t	Time
U	Blade velocity
U_{o-s}	Blade velocity in over-speed
u	Axial velocity
V	Volume
V_c	Control volume
V_{flight}	Flight velocity
V_p	Volume of the plenum
V_θ	Tangential velocity
$\bar{v}$	Velocity vector
$\bar{v_c}$	Velocity vector of the control surface
v_x	Axial velocity
W	Specific power / Relative velocity (velocity triangle)
W_B	Mass flow bled
w_i	Riemann inveriants

x	Axial coordinate
α	Flow angle absolut frame (velocity triangle)
α'	Flow angle relative frame (velocity triangle)
β	Blade metal angle
γ	Heat capacity ratio
γ_r	Rotor blade stagger angle
γ_s	Stator blade stagger angle
γ^*	Datum stagger angle
Δ	Increment
δ_{ij}	Unit tensor
δ_T	Thermal boundary layer thickness
η_c	Compressor efficiency
η_{comb}	Combustion efficiency
Λ	Darcy friction factor
μ	Viscosity
ρ	Density
Σ	Surface
Σ_c	Control surface
$\vec{\sigma}$	Vector surface
τ	Torque / Total stress tensor / Lag parameter
τ'	Viscous stress tensor
ϕ	Flow coefficient
ψ	Pressure coefficient
ψ_p	Static pressure coefficient

ψ_τ	Torque coefficient
Ω	Volume
ω	Rotational speed / Pressure loss coefficient

A Paula, que se levantaba por las noches y me preguntaba por la infinitud del universo, guarda la curiosidad y no la pierdas nunca.

Chapter 1

Introduction

1.1 Background

The gas turbine layout is based on turbomachinery components which are responsible for the compression and the expansion of the working fluid in the engine. These compressors and turbines are connected together by means of shafts which transmit the power from the turbine end to the compression side. The over-speed term is used to refer to any case when any of these rotating parts accelerates over its design speed. This scenario is carefully considered by engine manufacturers and certification authorities since it can lead to undesired outcomes compromising the safe operation of the engine. This over-speed can be caused by a mal-function of the control system or by a mechanical failure of the parts transmitting the power. A shaft failure scenario is particularly problematic since it provokes the sudden decoupling between turbine and compressor without any instantaneous change on the working fluid leading to the consequent turbine acceleration.

The shaft failure scenario, although highly unlikely, it is considered by the certification agencies. Essentially, there are two ways to certify an aero engine regarding a possible shaft failure event. The manufacturer can show that the consequences do not lead to a hazardous event or, in the case this is not possible, it has to be demonstrated that the probability of failure fulfil the requirements of an extremely remote event.

1.2 The shaft failure scenario

During the normal operation of a gas turbine engine, a certain number of axial turbines extract power from the high-pressure and high-temperature working fluid passing through the engine Main Gas Path. This power is transferred from each turbine to the corresponding compressor by the different shafts which are the mechanical link connecting these turbocomponents. Modern gas turbines, in particular those designed and manufactured by the sponsor, have up to three compressor-turbine groups connected by three concentric spools. These shafts are named following the level of pressure where they operate. Namely, the Low Pressure Shaft (LPS) connects the fan at the front of the engine with the Low Pressure Turbine (LPT), the Intermediate Pressure Shaft (IPS) connects the Intermediate Pressure Compressor (IPC) with the Intermediate Pressure Turbine (IPT) and the High Pressure Shaft (HPS) connects the High Pressure Compressor (HPC) with the High Pressure Turbine (HPT). Figure 1.1 shows the typical layout of a High Bypass Ratio (HBR) turbofan. The figure shows the shafts highlighted in different colours and the position and the kind of the bearings where the shafts are held.

The present work aims to analyse the shaft over-speed scenario, in particular when it is provoked by the mechanical failure of the shaft. The breakage of a shaft leads to the instantaneous decoupling between the turbine and its compressor. This event is also known as "loss of load" for evident reasons. This instantaneous decoupling occurs without any change in the aerodynamic power flow, and therefore, the expected consequences of this unbalance scenario are the rapid deceleration of the compressor which is not powered by the turbine any more, and the rapid acceleration of the turbine which has suddenly lost its load.

When a disc is rotating, centrifugal forces acting on the structure are resisted by the stiffness of the material of the disc. The greater the rotational speed, the greater the stress. When the stress exceeds the yield strength of the material, permanent deformation and disc growth take place. If the stress exceeds the ultimate strength of the material, the disc fails. Therefore, an over-speed scenario may lead to disc burst and the consequent high-energy debris release from the engine since the casing is not designed to contain these high energy fragments. Events involving this kind of high-energy debris release are classified as hazardous by the certification authorities and are unacceptable from the point of view of the engine certification. It is therefore critical that the speed of a turbine disc under any condition does not exceed its burst speed.

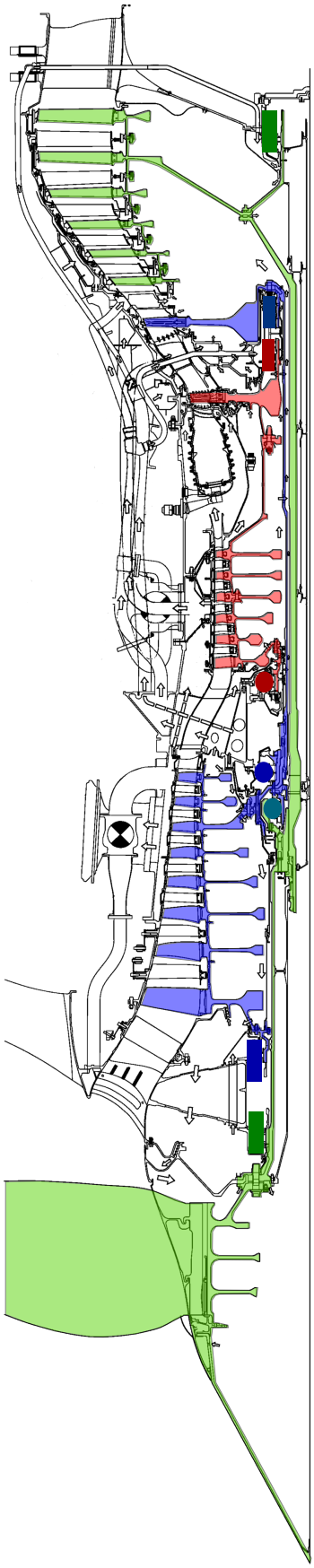

Figure 1.1: Shafts and bearings layout in a 3-spool turbofan

Many aspects must be taken into account to avoid or reduce the probability of a shaft failure. A list of them is advertised by the certification authorities [2]:

- Degradation of a bearing leading to shaft orbiting and subsequent contact between the shaft and other rotating or static part
- Blade failure resulting in imbalance and rubbing of the shaft on other parts
- Corrosion inside the shaft
- Fuel flow instability in the engine control system inducing a resonance in the shaft
- Oil fire around the shaft
- Impingement of hot air on the shaft
- Bearing failure
- Loss of lubrication of a spline
- Failure from stress concentration feature
- Effects of undetected material defects
- Effects of manufacturing tolerance allowed by the design
- Effects of shaft loads which could be transmitted by shock loading resulting from bird strike, blade failure, etc.
- Rubbing between any torque-loaded section of the shaft and adjacent surfaces (other shafts, oil seals, air seals, ...)

Typically, the time needed by a turbine disc to reach 150% over-speed is of several hundredths of a second which is much faster than the reaction of a normal FADEC (Full Authority Digital Engine Control) [89]. It means that the arrest of any over-speed scenario is a problem that must be tackled by specific design features or special protection devices. In general, in case of shaft failure, the objective is to reduce the power available to the turbine as quickly as possible. Typically, mechanisms that can be considered to contribute to limit the terminal speed of the turbine are:

- Disc rubbing

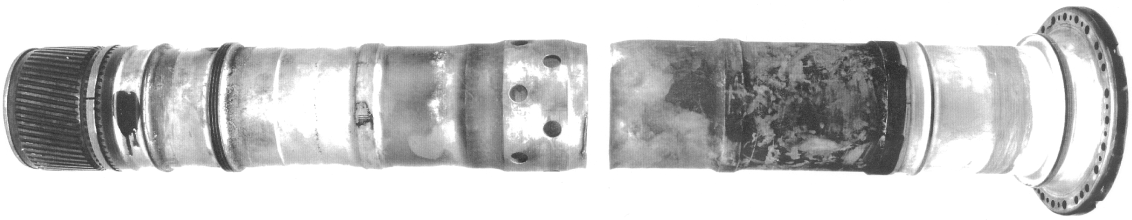

Figure 1.2: IPS after a "clean" break [87]

- Blade interference, spragging or shedding
- Engine surge or stall
- Over-speed protection devices

Experience shows that the occurrence of compressor surge and the later running down in stall is the fastest way to reduce the power available at the turbine for acceleration. Compressor surge is a consequence of the aerodynamic mal-function of the compressor which, under certain circumstances, is not able to maintain the stable pressurization of the working fluid. The consequences of this situation from the point of view of performance are the sudden reduction of air flow through the engine and the rapid compressor delivery pressure (P30) drop. This mechanism of power reduction is considered critical in case of a HPS or IPS failures.

The cause of shaft failure can be classified attending to the level of vibrations induced to the engine in the moments after the failure. Particularly, if the failure is produced by material softening, consequence of an internal fire, a 'clean' break will occur and the resultant failure will produce a low level of remnant vibration. On the other hand, if the failure is provoked by a fatigue crack, the vibrations persisting after the failure will keep a high level for longer. The latter is known as 'dirty' failure. This level of vibration is of paramount importance due to its effect on compressor operation. Vibrations are known to provoke deformation in the compressor casing affecting to the tip clearance. Tip clearance has a direct impact on the position of the surge line in a compressor map. The increment of tip clearance associated with this scenario is known to be more than enough to provoke the HPC surge and, if the remnant vibrations are high enough, compressor recovery is avoided [87].

Another important fact to take into account is the possibility of the free-running turbine to move axially. Depending on the location of the failure and the layout of the bearing systems for each particular shaft (see Figure 1.1), the failure is classified

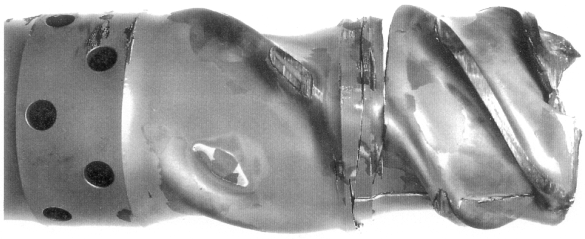

Figure 1.3: IPS after a “dirty” break [87]

as 'located' or 'unlocated'. This feature determines if disc rubbing and blade tangling may take place. The dislocation of the turbine and the necessity to study the contact against downstream static structures introduces a new factor in the event. Since the turbine discs are immersed in the Secondary Air System (SAS) of the engine, the axial force acting on the disc will be the result of the evolution of pressures in the MGP but also in the cavities of the SAS.

1.3 High pressure shaft failure

Modern 3-spool gas turbines operating at design point present choked conditions in the three turbines. Performance analysis shows that, as a consequence of that, the operating point of the HPT remains invariant while the IPT is choked. Since, during an engine deceleration, the unchoking process starts from the rear, the HPT is the one which keeps higher its expansion ratio for longer. In case of HPS failure this is problematic since it means that the HPT is able to extract a high level of power for longer.

In actual designs, the HPS is supported by two bearings, namely, a ball bearing situated at the front end and a roller bearing located at the rear end. This configuration promotes an unbalanced situation in the compressor after the shaft failure which allows radial movement and makes possible the compressor's blade destruction (see Figure 1.4). On the other hand, any failure leaves the HPT unlocated so free to move axially promoting disc rubbing and blade destruction by tangling. Moreover, the HPC unbalance or its rapid deceleration after failure triggers the surge of the compression system.

The evolution of compressor delivery pressure, the possibility of compressor's blade destruction, the inertia split between compressor and turbine, and turbine disc rubbing and blade tangling, are factors to take into account when modelling a HPS failure [88].

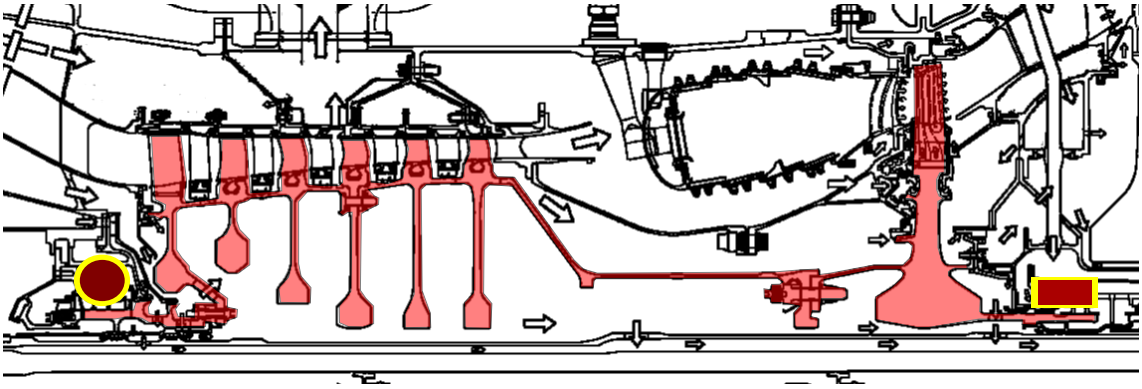

Figure 1.4: HPS bearings arrangement

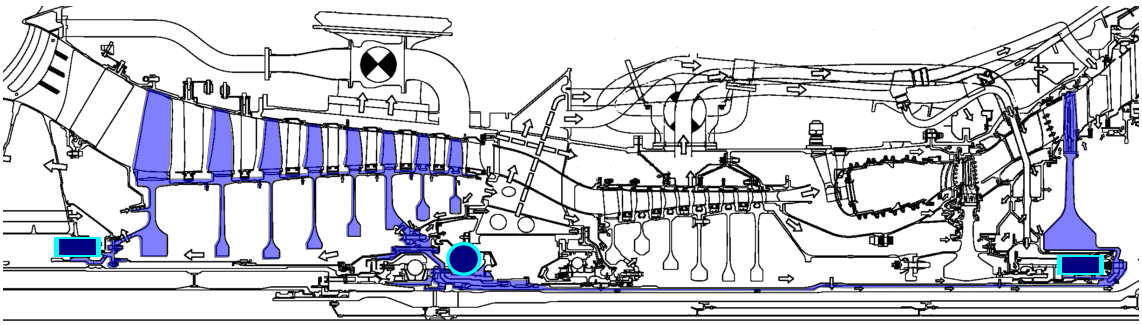

Figure 1.5: IPS bearing arrangement

1.4 Intermediate pressure shaft failure

The IPS failure is considered to be the case most difficult to analyse in 3-spool engines. It was considered to possibly lead to hazardous effects from the beginning of these engines' development. Historically, there have been several examples of this event and a variety of outcomes and factors involved have been observed. In a similar fashion to the HPS failure, the position of the bearings supporting the shaft is important. The IPS is supported by three bearings, namely, a roller bearing at the front of the IPC, a ball bearing at the rear of the IPC, and a roller bearing just before the IPT. For more clarity, this layout can be observed in Figure 1.5. This layout makes unlikely the IPC blade destruction and therefore, in contrary to HPS failure, this cannot be considered an over-speed limiting mechanism.

As in the case of a HPS failure, after an IPS failure the objective is to reduce the power available to the free-running turbine as quickly as possible. The most effective way to achieve that is the occurrence of compressor surge. Apart from that, in case the shaft fails in a position which allows the axial movement of the turbine, contact between the IPT rotor and the static structure downstream contributes to arrest its

over-speed.

Axial compressors in aero engines are designed to promote the recovery in case of surge, nevertheless, recovery is not desired in that case. Compression system operation after the failure depends on several factors:

- **Level of vibration.** It depends on the location and the nature of the shaft breakage. If the failure is provoked by a fatigue crack, the remnant level of vibration is high. In the contrary, if the failure is a consequence of a material softening caused by an internal fire, the remnant level of vibration after the initial peak is low. On the other hand, depending on the position of the failed section regarding bearings and seals, the IPC will result unbalanced at different levels and the vibration level will be a consequence of this.

- **IPC inertia.** The inertia of the compressor determines its deceleration rate after the breakage. It affects to the degree of variable geometry mal-schedule[1] and its timing. If the degree of mal-schedule is large enough, it provokes the IPC surge.

- **Fuel flow injected.** Turbine Entry Temperature (TET) is a consequence of fuel injected and its value determines the throttling of the engine. In general, fuel injection must be cut off to promote the overall engine rundown. Nevertheless, a rapid reduction in fuel flow could help the compressor recovery. This effect must be considered to define any control logic dedicated to arrest shaft over-speed.

- **Variable geometry and bleed valves actuation.** The actuation time of variable geometry is several tenths of a second and bleed valves are even slower. Thermodynamic evolution of the engine cannot be trust to them in the first instants of the shaft failure event but its rapid actuation may have a very important impact on compressor recovery on this time scale.

[1]Modern axial compressors are provided with several variable-geometry vanes whose objective is to improve the efficiency at off-design conditions by helping the flow angles to be as close as possible to its optimum. These devices are moved through hydraulic actuators commanded by the control system of the engine. The combination of a rapid change in compressor speed and the actuation time needed to readjust the schedule of the variable-geometry vanes can provoke variable geometry mal-schedule. In other words, the stagger angle of the vanes are not those which correspond to the compressor speed at a particular instant of time due to the mentioned transient effect. The consequence of this is an aerodynamic mal-funtion which could lead to compressor surge in a extreme case.

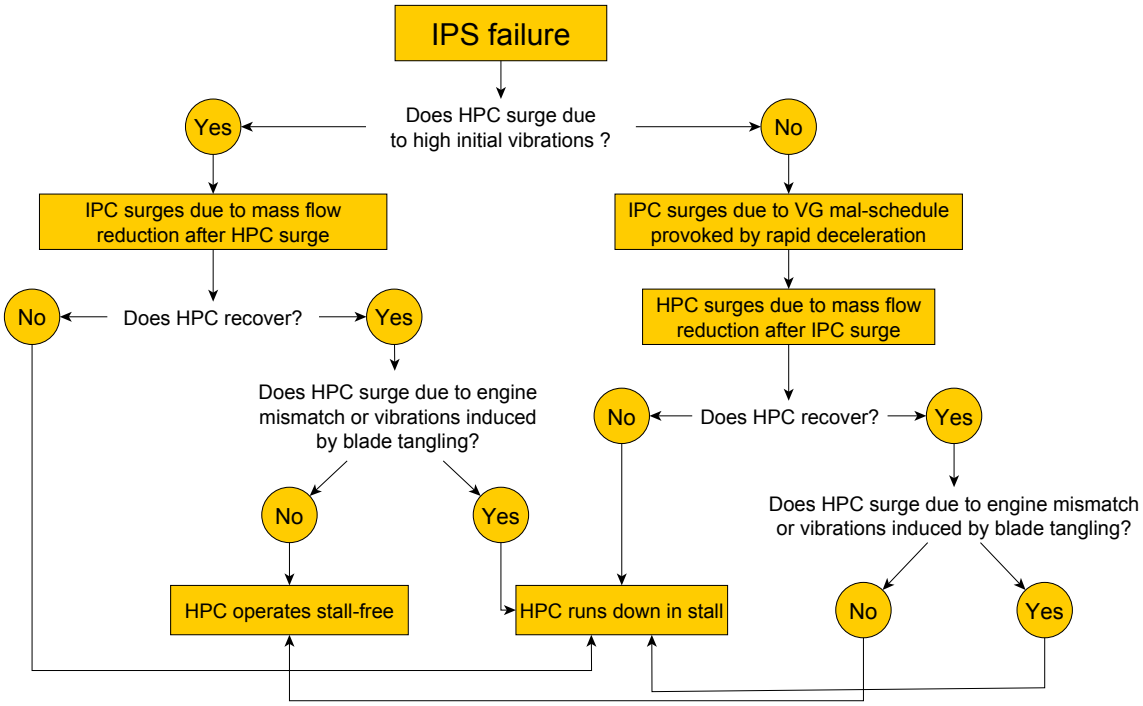

Figure 1.6: Compression system surge sequence - Possibilities after a IPS failure

Depending on the combination of the features listed above and based on observations, there is a variety of possible sequence of events regarding the compression system operation. Figure 1.6 shows a diagram which explains the different possibilities. It has been assumed that the IPC, once has surged, does not recover or, in case of recovery, it does not contribute to P30 due to its rapid deceleration.

During an IPT over-speed, the LPT experiences extremely distorted velocity triangles at the inlet as a consequence of two combined factors, namely, the over-speed of the IPT rotor and the reduction in mass flow provoked by the compressor surge. This extreme off-design situation leads to highly negative incidence angles in front of the first Nozzle Guide Vanes (NGVs) of the LPT (see Figure 1.7). This aerodynamic malfunction provokes the separation of the flow and therefore, a reduction in capacity and an increment in pressure losses across the NGV which reduces the efficiency of this first stage. This reduction in capacity has a positive influence limiting the IPT over-speed.

In case the shaft failure leaves the free-running turbine axially unconstrained (unlocated failure), pressure forces acting on the disc push it rearwards and promote the contact with the downstream static structure. Immediately downstream the IPT rotor there is a major port which connects the SAS with the MGP. As a consequence of this axial displacement, this port is sealed when the free-running disc contacts the

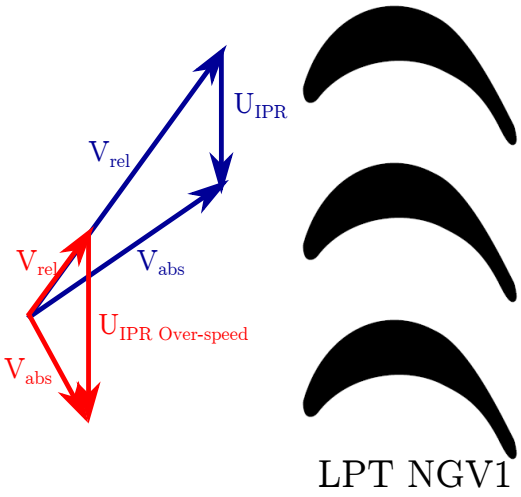

Figure 1.7: Distorted velocity triangles at LPT NGV1

lock plate of the LPT NGV1. The consequence of this phenomenon is the pressure rise in the cavity of the SAS which is discharging through this port. This pressure rise reduces the net axial force acting on the disc towards the downstream static structure and the direct consequence is a reduction of the friction torque that can be derived from this contact. Figure 1.8 can be observed for a better understanding of this event. This phenomenon explains the important role of the SAS dynamics and, in particular, of the evolution of the pressure in its cavities, on the outcome of a shaft failure event. Therefore, the SAS must be included in the simulation of the overall scenario.

Although the compression system dynamics is the most important feature in the outcome of the shaft failure event, a variety of other factors must be taken into account in order to understand the event and to predict its consequences with reliability. These factors are: extreme off-design turbine performance, SAS dynamics and, friction and wear of turbines in contact.

Several models have been developed internally by the sponsor company with the objective to predict the terminal speed of the IPT. These models, in general, are turbine-only models where the compressor dynamics are not calculated but given as an input based on historical data. In a turbine-only model, profiles of P30 and TET are normally provided as an input, a friction torque is calculated based on an empirical friction coefficient and the turbine maps are degraded to take into account the effect of axial movement on tip clearances [87].

Another model was developed recently motivated by the change in the understanding regarding surge inception after a shaft failure [89]. In order to predict the worst

possible scenario, the vibration-triggered HPC surge after failure is not taken for granted any more. Compression system surge is assumed to be triggered by the IPC Variable Geometry (VG) mal-schedule due to its rapid deceleration. In this case, the most important variables influencing the terminal speed of the IPT for different engines are the followings:

- IPS inertia split between compressor and turbine
- Aggressiveness of the VG schedule
- Response of the VG system

It is assumed that the Variable Stator Vanes (VSVs) do not move at all and therefore all the deceleration of the IPC is accounted as mal-schedule. This assumption is perfectly valid during the time scale of the first compressor surge. Apart from that, the strongest assumption in that model is the conservation of the total power (compressor plus turbine) over the event. The model is defined as a 'race' between the IPT acceleration and the IPC deceleration which leads to compressor surge. Therefore, inertia split and VSV schedule law rate of change are the dominant variables. This model allows classifying any engine as a function of these variables and to estimate its IPT terminal speed. Conclusions derived from this study state that modern engines have a better behaviour in case of IPS failure because their turbine radius is higher and the VSV schedule is steeper. Higher radius has been a consequence in new designs which focused on efficiency improvement and loading reduction. VSV schedule has evolved towards steeper functions because modern engines are a greater challenge for compressor matching in part speed.

The approach of these models to the shaft failure analysis is necessarily based on strong assumptions which are a result of a partial approach to a problem which involves most of the engine components interacting in an integrated manner and in fast transient basis. Modelling the shaft failure event is complex and requires a multidisciplinary approach able to assess the interaction between systems through a fully transient methodology.

To end with the description of the IPS failure, the most important design features identified through this historical understanding of the event are listed below:

- **Low compressor-to-turbine inertia ratio.** The inertia ratio has been identified as one of the most influencing parameter since it accounts for the

capability of the turbine to accelerate and the rate of deceleration of the compressor.

- **Rapid bleed opening and VSV closing.** The variable geometry devices of the engine can have a great influence on the outcome of the event but the actuation time must be reduced as much as possible.

- **High fuel flow to avoid recoverability.** The schedule of fuel injection after failure has a determinant impact on compressor recoverability since it determines the throttling of the whole system. The management of the fuel flow schedule is complex because what is desired in case of over-speed is in conflict with the control laws in case of surge and therefore, the use of this feature must be directly related to the implementation of a dedicated detection system for the shaft failure event.

- **Low volume of metal between blades and NGVs for prompt tangling.** The use of blade tangling to arrest the turbine over-speed can be the only way to contain the acceleration in certain cases. The timing of this interaction is given by the amount of material that has to be worn before the tangling is possible. Therefore, limiting this amount of metal to the minimum during the design phase is always beneficial in case of shaft failure.

1.4.1 Qantas incident

Recently, on 4 November 2010, a shaft failure event in service occurred which changed slightly the understanding of this scenario. One of the Rolls-Royce Trent 900 powering the Airbus A380 registered VH-OQA of the airline Qantas suffered an uncontained failure as a consequence of an IPS failure. The flight crew managed the situation and the plane was safely returned to and landed at Changi Airport [3].

The shaft failure was a result of an internal engine fire in the HP/IP bearing support assembly that heated the IPT drive arm softening the material. The fire started when oil was released from a fatigue crack in the pipe that supplied oil to the HP/IP turbine bearing chamber to a region where temperature was high enough for auto-ignition. The Australian Transport Safety Bureau (ATSB) found that the oil pipe cracked because it had a thin wall from a misaligned counter bore that did not conform to the design specification.

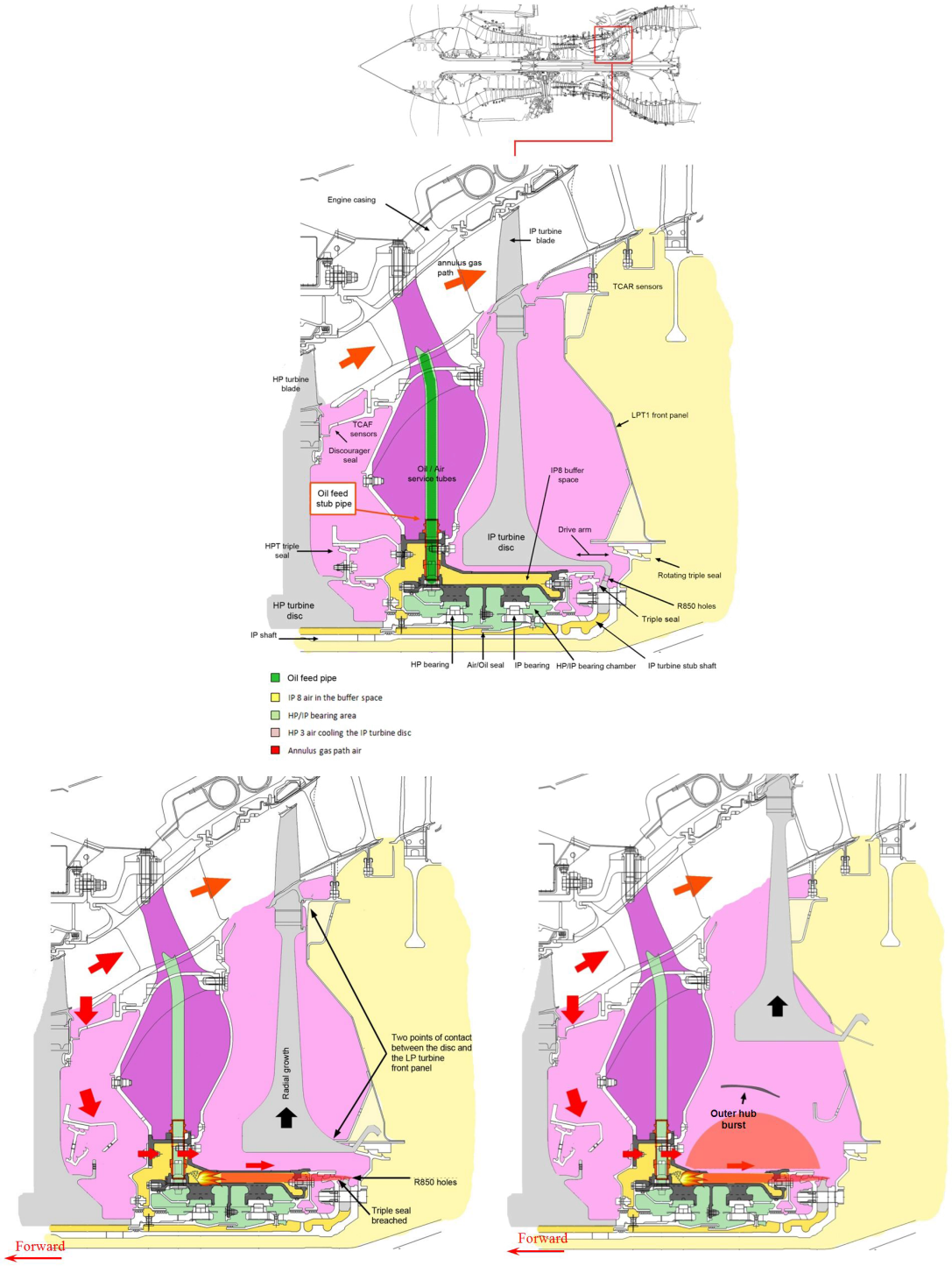

Figure 1.8: Qantas incident - Sequence of events [3]

After the shaft failure, the IPT disc accelerated while moving rearward rubbing against the LPT lock plate and seal segment. This kind of failure, in particular, occurring at the turbine drive arm and provoked by oil fire, may lead to a scenario with low vibration level which could prevent the HPC to surge immediately after failure as expected [38]. The sequence of events regarding the different compressors operation is not perfectly clear since the data was recorded with a frequency of 5 Hz which is much higher than the compressor surge time scale. Previous experience with other shaft failure events allows speculating about the possible sequence of events. It is thought that the compression system surged quickly after the failure. It could have been provoked by two different reasons, namely, HPC surge induced by initial vibration level after failure, or IPC surge due variable geometry mal-schedule provoked by the rapid deceleration of the IPC. Then the HPC managed to recover from surge while the IPC runs down delivering a pressure ratio of 1 [3]. The HPS kept its speed high while the low value of total pressure at the inlet made possible its operating point to stay within the stable region. The stall-free operation of the HPC and the difficulty to blade tangling due to the high amount of metal between the IPT rotor and LPT NGV1 made possible the acceleration of the free-running turbine over its structural capability leading to the final disc burst.

This failure showed that the HPC rundown in stall cannot be considered as certain any more, and therefore, as a consequence, Rolls-Royce has developed an Intermediate Pressure Turbine Over-Speed Protection System (IPTOS) that is designed to shut the engine down before the turbine disc can over-speed, in the unlikely event that a similar failure occurs [3].

1.5 Low pressure shaft failure

LPS failure is the most common because in case of fire it tends to weaken this shaft. In contrary to the cases previously explained, compressor surge is not likely. Following the position of the bearings supporting this shaft, the failure is always unlocated and the tangling is fast. Blade tangling contributes to control the over-speed of the turbine but the blade destruction must occur in a controlled manner to avoid high energy debris. As in any shaft failure scenario, the objective is to reduce the power available at the over-speeding turbine as quickly as possible. Since compressor surge cannot be accounted for contributing to power reduction, the fuel must be shut off as soon as possible. This failure tends to be uncontained if it is not detected on time and the fuel is not shut off. Therefore, in order to certify the

engine against this failure, a special control system is needed. An extra speed probe is used at the turbine side of the shaft. The comparison of measurements of two probes is used to trigger the control logic which carries out the fast shut of the fuel flow.

From the point of view of simulation, which is the interest of this doctoral research, LPS failure does not present a challenge because the absence of surge makes possible the modelling using standard methods and no improvement of capabilities is needed.

1.6 Certification

The European Aviation Safety Agency (EASA) defines as 'Hazardous Engine Effects' those which involve non-containment of high energy debris, uncontrolled fire or complete inability to shut the engine down, among others [2]. Historical experience has shown that shaft failure events leading to the free-running turbine over-speed are a potential cause of uncontained high energy debris if no action is taken, and therefore, its effects might be classified as Hazardous at certain cases following the definition by EASA. Therefore, the objective of the certification process undertaken by the manufacturer is to demonstrate that actions in terms of engine design and/or special protection devices have been taken so the event is controlled and its consequences can be classified as non-hazardous.

EASA's certification normative allows two ways to certify an engine under the shaft failure scenario, namely, the shaft failure itself is shown to be 'extremely remote' or it is demonstrated that the consequences of this failure are non-hazardous. EASA classifies as 'extremely remote' any event unlikely to occur when considering the total operational life, but nevertheless, has to be regarded as being possible. It establishes the probability in the range 10^{-7} – 10^{-9} per engine flight hour. The second case can be claimed by means of demonstrative test or agreeing that the consequences are readily predictable [2]. Experience has shown that the probability of shaft failure cannot be classified as 'extremely remote' and therefore, the analytical or experimental demonstration of its non-hazardous consequences is strictly necessary [2].

Acceptable Means of Compliance (AMC) E 850 established that the claim of non-hazardous engine effects in case of shaft failure can be substantiated by analysis

which should be based upon relevant service or test experience. The control of over-speed can be achieved by means of disc rubbing, blade interference, spragging or shedding, engine surge or stall and/or over-speed protection devices.

Nevertheless, a recent Certification Memorandum (CM) [4]produced by the same agency implies a revision of the previous regulation based on recent experiences on the matter. Essentially, the objective of the memorandum is to establish the necessity for a more reliable validation of the analytical models used to predict the shaft failure event. It recognises as source of inaccuracies the compressor surge prediction and the assumptions in the study of the friction and wear phenomena.

The memorandum clarifies and extents the requirements to claim that the event has non-hazardous consequences. The compliance can still be shown by test and analysis and the features of those are detailed as follows.

> "The test should be performed by initiating the shaft failure at the worst case operating conditions within the flight envelope, in any dispatchable configuration, which will maximise the rotor over-speed and subsequent effects. [...] In addition to initial rotor speed other aspects should also be taken into consideration, such as shaft torque and relevant engine pressures and temperatures."
>
> "If compliance is shown by analysis as allowed by AMC E 850 (2), the following aspects should be considered, whether or not the affected rotor components are designed to be retained substantially in their rotational plane: The analysis should be validated against an actual engine or system or component rig test(s) and/or service events, showing a sufficient degree of similarity with the engine model for which compliance is sought. This similarity should encompass all relevant aspects of the failure mechanism and its consequences such as, but not limited to, aerodynamics, surge characteristics, relevant rotor and stator design features, material, clearances, etc... and should be submitted to the Agency for acceptance." [4]

The most important change introduced by the new CM is the clarification of the terms regarding the analytical demonstration of non-hazardous shaft failure. The previous regulation used the terms 'readily predictable' and 'analysis based upon relevance experience' while the new CM gives a fully detailed definition of model validation for its acceptance.

Besides the shaft failure strictly related certification problem, the prediction capability for shaft failure outcome affects to the design and certification process of the turbine rotors involved. The same regulation dedicates a section to the 'Rotor Integrity' whose certification is directly related to the shaft failure event. To claim the integrity of a rotor, the pertinent analysis or test must be undertaken to guarantee that the rotor will not burst operating 5 minutes at the most critical condition. This critical condition is normally determined by the prediction of the over-speed scenario. The regulation states that the rotor must withstand a 105% of the highest rotor speed that would result from a failure of the most critical component which, in general, will be the shaft [2]. It means that, in order to penalise as less as possible the design of the gas turbine, above all in case of aeronautical application, the actions taken in terms of design and/or protections devices must guaranteed the lowest possible terminal speed in case of shaft failure.

1.7 Summary

So far in this introduction to the shaft failure event, it has been pointed out that there in a variety of aspects and phenomena involved in this scenario. As a consequence, the analysis of shaft failure can be complex and requires a multidisciplinary approach. Compressor surge and rotating stall, distorted turbine aerodynamics, dynamic behaviour of the SAS, mechanical loads, disc rubbing, blade tangling, etc, all play an important role in determining the outcome of the event and the sum of their effects must be considered.

Chapter 2

Project management and thesis structure

2.1 Project management

The present doctoral research has been undertaken in the context of the Rolls-Royce UTC in Performance Engineering at Cranfield University. The research project 'Gas Turbine Shaft Over-speed / Failure Modelling' commenced with Dr. L. Gallar's [38] and Dr. K. Psarra's PhDs [83] in 2007. Their combined work focused on the aerodynamic analysis of over-speeding turbines, the transient modelling of the SAS, the compressor reverse flow performance and the modelling of the turbine mechanical interaction.

In this second phase of the project (period 2010-2014), the research effort has been divided into three PhDs:

- **Compressor surge and rotating stall modelling.** PhD candidate Serena Zoppellari [99]. The aim of this project is to develop a methodology to predict compressor rotating stall characteristics and improve the understanding of the two-dimensional effects involved in these phenomena, in particular, the stall cell growth process and the surge recovery mechanism.
- **Friction and wear modelling of turbines in contact.** PhD candidate Aleixo Gonzalez [44]. This project studies the different phenomena involved in the turbines interaction after a shaft failure. The aim is the development of

models to predict the friction torque and the material wear rate at the different phases of this contact, including, lock plate - seal segment interaction, blade root - platform interaction and blade tangling.

- **Shaft failure modelling - Overall engine response.** PhD candidate Carlos Soria. This project, apart from the dedicated research activities explained in detail in the present manuscript, is meant to be the point of union and integration of the whole research on shaft failure in this context. It is aimed to develop an integrated tool to predict the overall engine response to any shaft failure event.

This doctoral research has been undertaken over a period of 3 years being fully funded by Rolls-Royce. The project has been supervised by Dr. Vassilios Pachidis from Cranfield University and by Mr. Arthur Rowe and Mr. Steve Brown, Rolls-Royce specialists, from the sponsor company. Milestones have been agreed with the sponsor every year to guarantee the progress and the final contribution of the research. The contact with the sponsor company has been arranged by technical meetings normally scheduled in November, February and May. Once a year, the Annual Review scheduled in March or April has been the opportunity to communicate the progress of the Rolls-Royce UTC to a wider audience within the company. Apart from that, special meetings have been arranged when necessary, normally motivated by the achievements of important milestones or the delivery of any outcome of the research. Besides these different forms of formal meetings, regular contact with the specialists has allowed constant technical guidance and data transfer.

The organisation of the Rolls-Royce UTC in the context of the university has allowed the author to be involved in a variety of projects and to collaborate in the task of technical supervision of MSc students. Figure 2.1 shows the different projects and the names of the MSc students which have contributed in each case.

The present manuscript is fully dedicated to the research work undertaken in relation to the shaft failure modelling. Nevertheless, research in other topics has been undertaken by the author over the 3-year period of the PhD as can be seen in Figure 2.1. Brief reviews of these other projects are included in the present section to give an overview of the complete contribution. The exclusion of these works from this manuscript has been decided in order to keep the structural consistency in the present thesis. Detailed record of this work has been kept in dedicated internal reports and other contributions that are referenced appropriately below. The next list summarises the contribution to projects non-related to shaft failure:

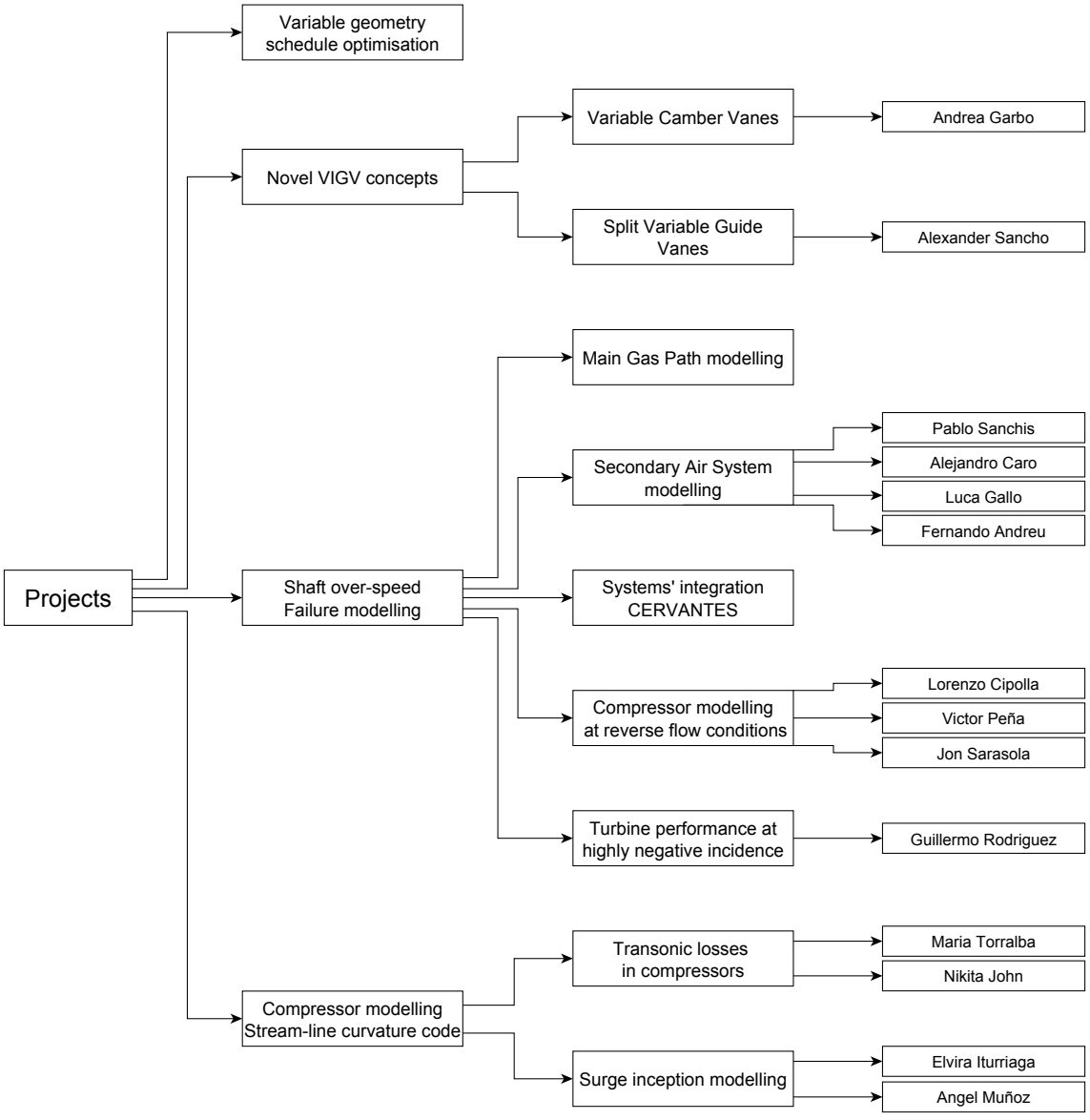

Figure 2.1: Project management and MSc students' contribution

- **Variable geometry schedule optimisation:** Modern axial compressors are provided with several VSVs and a Variable Inlet Guide Vane (VIGV) to improve compressor efficiency and operability at off-design conditions. The stagger angle of these vanes changes following a pre-implemented schedule as a function of the compressor rotational speed. The work undertaken at Cranfield aimed to develop a methodology to find the optimum schedule for each engine. The methodology consisted in the coupling of an optimisation tool based on genetic algorithms with an in-house (Rolls-Royce) compressor performance prediction tool. The methodology was developed initially by L. Gallar and M. Arias [8, 38], the coding of the tool and the first preliminary calculations was carried out by the author in the context of his MSc. thesis [92] and the final calculations and delivery of the code to the sponsor company took place during the first months of this PhD.

- **Novel VIGV designs for performance improvement at off-design conditions:** In modern aero engines, compressor's VSVs need to provoke high flow deflections to guarantee compressor matching and high efficiency at off-design conditions. Actual devices cannot avoid the separation of the flow and the consequent pressure losses derived from this situation. This project aims to suggest and assess new design concepts to improve the VIGV performance.

  - **Variable Camber Vane (VCV):** This first approach aimed to establish the best possible performance that could be expected. VCVs are assume to be made of a flexible material that can be bent by applying a force at the trailing edge. The methodology consists in representing the vane by its camber line and its thickness distribution, being the camber line a 4-point Bezier curve. The last point (trailing edge) of this Bezier curve is movable to make possible the different flow turnings over the operating range. The geometry - 3 fixed points in the Bezier curve - has been optimised by coupling a genetic algorithm with a 2D CFD solver. Once the optimum shape has been found, a 3D CFD model was built and the results showed a reduction of total pressure loss coefficient of 86%. This investigation has been undertaken with the collaboration of Andrea Garbo [42] (MSc. student). The result of this performance assessment were submitted to the sponsor in a internal report.

  - **Split Variable Guide Vane (SVGV):** The promising results shown by VCVs motivated further study on this topic. This project aimed to investigate and assess new possible configurations which could reach a

low pressure loss level, as such appointed by the VCVs, but keeping the manufacturing and actuation process simpler. This investigation came up with a design based on a split vane concept which is provided with a control flow system whose objective is to re-energize the suction surface boundary layer from the separation point by a flow coming from the pressure surface. The results of the 2D CFD analysis showed a high pressure loss reduction. The potentials of this technology was acknowledged by the sponsor and a patent proposal is under consideration. This work has been undertaken with the collaboration of Alexander Sancho [91] (MSc. student).

- **Compressor modelling - Streamline curvature code:** This project aims to enhance the capabilities and reliability of the in-house streamline curvature code for compressor performance. Research has been carried out to improve the prediction of compressor surge inception and to provide the solver with a model of pressure losses in blade rows due to transonic effects. The work has been undertaken with the contribution of four MSc students: Elvira Iturriaga [59] and Angel Muñoz [75] on the surge line prediction, and Maria Torralba [96] and Nikita John [60] on the transonic pressure losses modelling.

2.2 Thesis structure

The present thesis manuscript compiles the research work related to gas turbine shaft failure that has been carried out over the 3-year period of this PhD research. As has been said above in this chapter, the work carried out regarding non-related topics is not included here. This thesis has been built following a general-to-particular philosophy over the different levels of the structure.

The thesis starts presenting the problem and the scope of work. Chapter 1 aims to offer to the reader an overview of the event of shaft failure in aero engines. The generalities of the event are presented, different particular scenarios are described and the importance from the point of view of engine certification is stated. This introduction gives the insight to understand the necessities arising from this problem and therefore the purpose of this doctoral research. This purpose is established in Chapter 3 through the identification of the aims and objectives. The gap in knowledge is identified and therefore, the contribution of the present research is achieved by the fulfilment of the established objectives.

Chapter 4 starts with an introduction to the classic approach to gas turbine performance analysis and continues showing a compilation of the literature review regarding the different approaches to transient engine performance that have been developed over the years and are available in the public domain.

Chapter 5 presents the methodology chosen to tackle the problem of engine simulation during shaft failure events. The methodology implemented here is shown following a general-to-specific approach. Firstly, the overall engine simulation tool and its integration strategy is established. It allows to identify the simulation necessities at a lower level, namely, engine MGP and SAS. Then, the methodology used to simulate the different engine components is included.

Following the general-to-specific philosophy, Chapter 5 allows establishing the next layer of necessities which corresponds to the analysis of the different engine component performances at the extreme off-design conditions which derive from the shaft failure scenario. Therefore, Chapter 6 and 7 are dedicated to compressor and turbine performances respectively. Chapter 6 starts with a general introduction to compressor performance. The first part is dedicated to unstall compressor performance. The second part provides a wide description of the phenomena of compressor surge and rotating stall ending with the simplified model implemented in the overall engine simulation tool. The final part of the chapter compiles the research carried out regarding compressor reverse flow performance in the context of this doctoral research. The chapter ends with a summary of the most important conclusions. Chapter 7 is dedicated to the performance of the turbine which is placed downstream the over-speeding turbine. The chapter includes the description of the methodology developed to derive turbine maps under this circumstances and the results of the application of this tool to a real engine. The chapter ends with a summary of the conclusions of this project.

Chapter 8 is dedicated to the different validation stages of the simulation tool and the final results. The chapter is divided into four parts: numerical scheme validation, post-stall compressor modelling validation, overall engine simulation tool validation by the simulation of a real case of shaft failure, and the results of a case study designed to demonstrate the capabilities of the simulation tool.

Finally, Chapter 9 provides the summary of the thesis. This chapter includes a compilation of the most important conclusions and the statement of the contribution to knowledge. The limitations of the methodologies and suggestions for the way forward are included at the end of the chapter.

Chapter 3

Aims and objectives

Shaft failure event has been recognised to be an important certification issue in aero engines. The details of the certification process have been exposed in Chapter 1. Engine manufacturers need to demonstrate to the certification authorities that the occurrence of shaft failure does not lead to hazardous consequences. Besides this, the prediction of maximum turbine terminal speed has an important impact on the engine design since this is the critical requirement in the structural design of the turbine disc. Therefore, the understanding of this event may potentially lead to future engine designs with a lower terminal speed which would allow lighter turbine discs. Certification agents admit two ways to certify an engine against the shaft failure event in case its classification as extremely remote cannot be guaranteed:

- Full scale engine test showing that a shaft failure occurring at the worst operating conditions does not lead to any hazardous outcome, but to the safe rundown of the engine.
- Overall engine simulation predicting the safe outcome of the event at the same worst conditions. In this case, evidence of accuracy and reliability of the simulation tools based on test or previous real cases must be shown.

The use of full scale test is an expensive procedure since a shaft failure test might imply the destruction of the engine and therefore, their use should be minimised when possible. It makes the second option the most attractive for the manufacturer. However, conventional engine performance models are not applicable to the shaft failure event. As has been explained in Chapter 1, compressor surge is always involved in the shaft failure scenario and it is considered the most effective

mechanism to reduce the power available to the free-running turbine. The major objective of this doctoral research is to assist the sponsor company in the process of certification against the shaft failure event by developing overall engine simulation capability including, in particular, the possibility to predict the post-stall behaviour of the engine.

The three possible shaft failure scenarios that can affect 3-spool gas turbines have been explained in Chapter 1. LPS failure was identified as a particularly easy case from the point of view of simulation. Since compression system surge is not expected to occur in this case, this event can be simulated with the models available in the company. Therefore, in the following, exclusive attention is paid to IPS and HPS failures. In particular, IPS failure is used as the general case of analysis throughout this thesis since this is the most difficult to model and mostly everything which is said for that case can be transferred and applied to the HPS failure.

The main outcome expected from a shaft failure simulation tool is the prediction of the evolution of the rotational speed of the free-running turbine and, in particular, its terminal speed. The acceleration of the turbine is a consequence of the different components of torque acting on it. Two components can be identified here, namely, the gas torque which the turbine continues extracting from the high-pressure and high-temperature gases expanding in the gas path of the engine and a sort of friction torque which is a consequence of the axial displacement of the turbine and the subsequent contact with the static structure of the downstream turbine. The former can be calculated if the evolution of the thermodynamic properties of the fluid are known; the latter is a function of the turbine rotational speed and the axial force acting on the disc. The phenomena involved in the turbines' mechanical interaction are complex and, as was said in Chapter 2, this is the subject of research of a different PhD candidate. From the point of view of this research, friction torque can be considered an existing function of axial force and rotational speed. Regarding the calculation of the axial force acting on the free-running turbine disc, two components have to be accounted, namely, the force derived from the pressure gradient across the blade, and the force provoked by the pressure difference between the tanks of the SAS where the disc is immersed. It means that it is necessary to know the evolution of the flow properties in the SAS too. In summary, the calculation of the turbine rotational speed requires the capability to predict the evolution of the flow properties not only in the MGP of the engine but also in the SAS.

Following the previous rationale and besides the analysis of the turbines' mechanical interaction, the shaft failure simulation has been reduced to a purely fluid dynamic

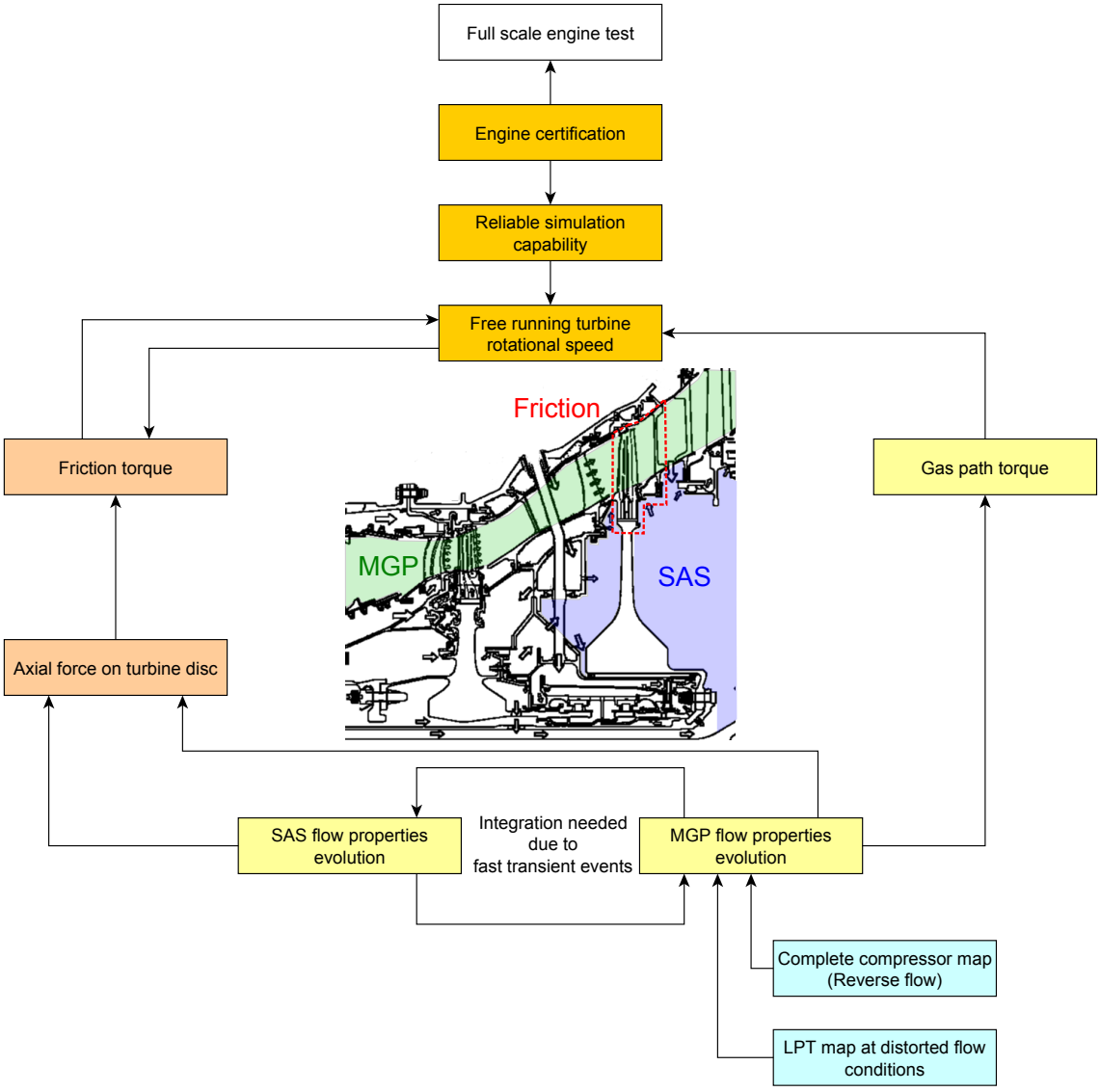

Figure 3.1: Shaft failure simulation problem - Identification of objectives

problem. The performance regarding the MGP is dominated by the compressor instability which is a fast transient event. This fact invites to tackle the problem using a fully transient approach which makes necessary the simulation of the two fluid systems (MGP and SAS) in an integrated manner since they are interconnected. Rapid changes in flow properties over the MGP provoke changes in the boundary conditions of the SAS which are the connection ports where the air is bled or injected from one system to the other. The SAS reacts transiently to this changes, in other words, the time scale of changes in the boundary conditions is comparable to the time needed by the cavities to readapt their pressures.

The necessity to model the MGP of the engine involves other requirements, namely, the necessity to know the response of engine components (compressors, combustor and turbines) at the extremely off-design conditions induced by the shaft failure. Information regarding in-stall compressor performance is needed, including rotating stall and reverse flow characteristics. On the other hand, in case of IPS failure, the LPT will operate with highly distorted inlet flow which will affect its performance. A methodology to predict the LPT map under such circumstances is also necessary. These requirements are understood as objectives of the present doctoral research.

In summary, the aim of this doctoral research is to assist Rolls-Royce in the certification process of aero engines against the shaft failure event, in particular the HPS and IPS failure scenarios. The aim is to achieve that by the development of inexpensive simulation capability. It has been decided to develop everything from scratch and to build a standalone tool dedicated in special to this scenario. Several objectives have been established in order to reach the final goal:

- Develop transient simulation capability to predict the performance of the MGP of the engine including post-stall behaviour.
  - Develop capability to predict compressor reverse flow performance
  - Develop capability to predict turbine maps affected by distorted inlet flow, in particular, highly negative incidence angles
- Develop transient simulation capability to predict the reaction of the SAS to rapid changes in its boundary conditions and variations of its geometry (cavities' volume and ports' area).
- Integrate these simulation tools to build an 'all-in-one' overall engine performance suite able to predict the consequences of the interaction of the different systems during a shaft failure.

The achievements of these goals implies an important impact in both, the sponsor company and the scientific community. The sponsor modelling capability is enhanced and the certification of future engines is facilitated. On the other hand, to the best of the author's knowledge, the integration of these two systems of an aero engine and the final coupling with the friction model to build the 'all-in-one' simulation tool for shaft failure analysis has never being published before and therefore, its achievement would imply a scientific contribution.

Chapter 4

Literature review

Gas turbine performance studies the behaviour of the engine at any possible condition allowed by the control system within the flight envelope of the aircraft [72]. The methodology to calculate the off-design performance of an aero-engine is based on the knowledge of the behaviour of its components. The equations available are those given by the component maps and the compatibility equations which give the information related to the engine layout. In other words, all the components are part of the same system. On one hand, the mass flow compatibility establishes the relationship between the mass flows through the different components. On the other hand, since turbines and compressors are connected in pairs by shafts, mechanical compatibility is established by imposing the relationship between the rotational speeds of the different components. Furthermore, if the analysis is steady state, as it is the case in off-design performance, the compatibility in power must be fulfilled. That is, the power consumed by each compressor must be equal to the power produced by its turbine subtracted the mechanical losses. Several of these assumptions must be relaxed to undertake dynamic analysis as it will be explain later on this chapter.

Over the years, the necessity of improving gas turbine performance has pushed the development of more and more reliable off-design and transient performance simulators. These simulators allow developing reliable control systems to guarantee a specific level of performance and the safe operation of the engine over the flight envelope of the airplane. The availability of these simulators at early design stages can be very useful to assist the design process and to avoid future problems by anticipating the engine response to a wide variety of scenarios [36].

Over this chapter, the evolution of the methodologies to tackle the dynamic simulation of gas turbines is presented. First models were based on the linearization of the problem and were applicable in the operating region near a particular equilibrium point. On the other hand, non-linear models based on the knowledge of the engine layout, the matching of components and the information regarding components characteristics were developed to make possible the analysis over a wider region of the stable operating range. The problem of compressor instability and the necessity to extend simulation capability towards the post-stall region favoured the solvers based on the application of Euler equations of fluid dynamics to the domain defined by the main gas path of the engines. These models evolved to allow a more detailed definition of the phenomena from the 1D analysis towards the 3D approach. The most important contributions available in the public domain are presented in the following sections.

4.1 First works in aero engine transient performance prediction and simulation

Modelling the transient response of a gas turbine were first undertaken in 1950's at NACA. In 1950, E. W. Otto and B. L. Taylor developed a model to study the dynamic response of a single-shaft aero engine [77]. The aim of this study was to come up with a mathematical expression of the engine acceleration as a function of the fuel flow to assist the control system design. The approach was based on the linearization of the engine response around an equilibrium operating point. The shaft speed was expressed as a function of the variables involved being the only independent variable the fuel flow injected. The mathematical problem is linearized by means of a Taylor series and the coefficients of this expression are derived from experimental data or from the analysis of steady-state component maps. This sort of studies showed that the use of steady-state maps to approximate the coefficient of the linear expression was satisfactory and that the modelling of the combustor may be problematic because it was observed that the combustion efficiency suffers transient changes when rapid changes in fuel flow are involved. The linearized model showed to be reliable in representing transient behaviour for cases with shaft speed changes less than 600 rpm/sec.

Other early studies explored an analytical approach based on engine matching and component characteristics. In 1955, J. F. Dugan Jr. presented a research memor-

andum for NACA which attempted the modelling of a 2-spool turbojet [33]. The objectives were to predict transient trajectories to alleviate possible surge problems and to predict any problem of over-speed. The calculation was done in time step basis by evaluating unbalanced torque to calculate the evolution of shaft speeds. The use of steady-state component maps was successfully applied.

An interesting overview of the methods used to predict gas turbine dynamic response was given by A. J. Fawke and H. I. H. Saravanamuttoo in 1971 [36]. Two different approaches are possible, namely, linear systems and component models. The linear system approach tries to model the engine with a simple mathematical expression. They are accurate only for small perturbations around a unique equilibrium point. This is the case of the work of E. W. Otto and B. L. Taylor named above. The component models allow a better insight into engine dynamics. This methodology is based on the knowledge of the engine layout and the characteristics of the different components. This approach is flexible and remains simple even if the number of components or its complexity increases. Models based in linearizations are obviously not applicable to the problem undertaken by this doctoral research and therefore, from now on, only models based on components and other non-linear approaches are considered.

The difference between the analysis of off-design steady performance and transient response is the applicability of two concepts/assumptions: work compatibility and flow compatibility. Both assumptions are right when analysing off-design steady performance and both are false in the analysis of fast transient response. Two ways are presented by Fawke and Saravanamuttoo to deal with that, namely, iterative approach or intercomponent volumes approach. The former assumes flow compatibility over the whole engine even during transient at each time step and relaxes the work compatibility assumption to calculate the evolution of the shaft speed by calculating the unbalanced torque. The latter relaxes both assumptions allowing even flow mismatch. Fawke and Saravanamuttoo implemented engine simulators based on both methods achieving good agreement with experimental results especially with the latter [36].

4.2 Modelling surge and rotating stall in compression systems

Dynamic models presented above did not consider the necessity to simulate engine dynamics beyond the stable region of the compressor map. As it has been explained in previous chapters, shaft failure events are likely to trigger the surge of the compression system of the engine by several reasons. Therefore, it is essential to allow this capability in the developed simulation tool.

Compressor instability is not a fully-understood field yet. Progress on that topic has been done in parallel by experimental test, analytical modelling and numerical simulation over the years. In the present section, the different methods available in the public domain to model analytically and numerically compressor surge and rotating stall are presented. A more detailed description of the compressor instability from a phenomenological point of view is given in Chapter 6. Here, the literature available is examined from the point of view of the simulation of such event.

The benchmarking study in this field that can be considered the initial point and the first try to model compressor surge and rotating stall is the paper of E. M. Greitzer from 1976 [45]. The necessity to model the overall compression system including not only the compressor but also the ducting system and the volume involved was established by the first time. Furthermore, an analytical model was presented based on strong assumptions but applicable to low-speed compressors. The model improved the understanding of the event giving explanation to how different geometrical and operational features of the compression system determines the outcome of the event in terms of three different patterns identified, namely, rotating stall, surge and deep surge.

The evolution of this study is a work published almost ten years later by F. K. Moore and E. M. Greitzer [73, 47]. This model is the continuation of the analytical approach but extended to include circumferential dimension resolution. The objective here is to predict the growth and decay of the stall cell and represent the interaction between the different modal responses associated with each phenomenon. This paper states that the dynamic value of the pressure coefficient during this kind of event is different from the value given by the steady-state characteristics, calculated by time- and circumferential-averaging, due to the dynamic behaviour of stall cell growth and decay. Previous 1D models needed the use of a time lag to account for the 2D effects

related to the stall cell formation. The new model eliminates this necessity since the approach is 2D.

Another interesting approach within the context of the analytical treatment of the problem was published by S. G. Koff and R. F. Davis in 1987 [62]. The objective is always the same, namely, predict surge and rotating stall with resolution in the two dimensions (axial and circumferential). In that case, a control volume approach is applied. The circumferential length is divided into two regions, namely, stall flow and high flow. The method is similar to 'parallel compressors' but the steep boundary between the regions is substituted by a narrow transition region with smooth variations of flow properties to allow capturing the interaction between the two regions and the evolution of the rotating stall cell. The objective of this method is the analytical calculation of the rotating stall characteristic and the stall cell propagation speed.

In 1999, another contribution to the analytical model of Moore and Greitzer is published [70]. This work claims to relax some of the assumptions allowing finite inlet ducts. The method is based on a Fourier series expansion of the periodic dynamic variables along the circumferential length. The problem is solved explicitly by calculating the coefficients of the series. This method allows examining the influence of inlet geometry on the evolution of compressor instabilities.

Analytical methods offer interesting advantages. They permit the pure analysis of the different phenomena separately without being affected by instabilities provoked by a numerical approach [67]. In spite of this, numerical models allow more flexibility and the relaxation of several assumptions which have confined the analytical approach, in general, to low-speed incompressible scenarios. Next, some examples of numerical models published on the public domain are presented.

H. Ishii and Y. Kashimabara published a numerical model of a 17-stage high-speed axial compressor in 1991 [58]. The model solves the 2D, unsteady, inviscid and compressible flow equations. The compressor is modelled row by row by semi-actuator discs whose performance are given by the steady-state laws of pressure loss and deviation as function of the incidence angle. The circumferential direction is solved by a Galerkin method and the axial direction by a finite differences approach. The model is compared against experimental measurements. Different phenomena are captured by the model at different compressor rotational speed, including single-cell rotating stall, multiple-cell rotating stall and incomplete surge cycle followed by single-cell rotating stall. They found the throttle to play an important role affecting the recovery mechanism.

The work of J. F. Escudet and V. Garnier published in 1994 [35] describes the development of two codes. The first one is based on the circumferentially averaged Euler equations and allows the analysis of the axisymmetric flow instability. The second one is a 3D unsteady Euler solver coupled with a multiple through flow solution for the blade rows. The terms representing blade forces are calculated in a similar fashion to the work of Ishii and Kashimabara. A similar work is published in 1995 by Breuer and Servaty [12]. In that case, the solver is a 2D unsteady Euler solver with source terms for blade rows. The performance characteristics of the blade rows are extrapolated by second order polynomial to cover extreme off-design regions including reverse flow. Extrapolation of these performance data is common practise in this kind of methods. However, the blade row or compressor stage behaviour is highly non-linear and these approximations are revised and improved in future works.

In the same context, J. W. Lindau and A. K. Owen published a quasi-3D Euler solver this time in 1997 [65]. The solver allows two velocity components: meridional and circumferential. It relies on tabulated steady-stage loss and deviation data extrapolated to extremely off-design regions. The solver is applied to the Stage 35 whose steady-state performance was well-known after years of studies in NASA.

Special attention deserves the work of J. P. Longley on this field. Longley has developed compressor surge and rotating stall simulation capability over the years [67, 68]. Longley proposes a methodology based on the numerical simulation of the long lengthscales (compressor circumference) and the modelling of short lenghscale phenomena (blade passage effects). The model is applicable to high-speed compressors. Main differences with previous models are: dynamic treatment of body forces by the application of a first order lag to the circulation instead of to deviation; development of a blockage-mixing method and a blockage-transport equation to model blade row performance at extremely off-design conditions such as reverse flow instead of extrapolating characteristics. The model has been validated against two low-speed compressors and it has been applied to a high-speed compression system composed by two compressors (LPC and HPC) for demonstration purposes [68]. The most important advantage of Longley's model is the improvement in modelling blade row performance at far off-design situations.

4.3 Overall engine transient performance

Models and methodologies presented in the previous section seek to improve the understanding of compressor instability in detail. Nevertheless, as it has been stated above in this chapter, the objective of this doctoral research is the development of more general, overall engine simulation tool which makes this kind of approach unattractive. The right strategy in this case is to simulate the compressor dynamics by overall compressor characteristics [67]. This section presents the models available in the public domain which are more suitable for this kind of analysis.

Several publications between 1987 and 1997 describe the development of the simulation software carried out within the Virginia Polytechnic Institute and the Arnold Engineering Development Center (AEDC).

In 1987, the first paper published regarding this work established that the objective was the dynamic analysis of gas turbine performance [26]. The simulation domain was divided axially into control volumes where the governing equations of mass, momentum and energy conservations were solved. This approach removed the assumptions inherent to lumped volume models and treated compressibility explicitly. The presence of engine components such as compressors, ducts and combustor were modelled by external terms of axial force, heat transfer and shaft work. Therefore, in general, this kind of models needs to be provided with quasi-steady component characteristics. In that case, the compressors were modelled stage by stage and a continuous characteristic was used to model the transition from pre-stall to stall. One of the main differences with the models explained in Section 4.2 is that rotating stall was simulated assuming a flow-weighted averaged representation of a fully developed stall cell so the phenomena regarding the dynamic evolution of the stall cell are not captured. This fact makes necessary the use of an auxiliary time lag when the steady-state rotating stall characteristic is used to simulate the growth process of the stall cell. This model was able to capture stall inception, transient drop regarding initial surge-like behaviour and final average in-stall performance [26, 49].

Other difference between this work and those detailed in the previous section is the implementation of a proper combustor. It allowed identifying the important role of the combustor acting as the throttle of the overall compression system. The model was able to predict blowouts and reignitions of the combustor during surge cycle.

In 1995, M. W. Davis, A. A. Hale, K. A. Shahrokhi and G. D. Garrad [25] presented

the 2D extension of this same model via a 'parallel compressors' approach to allow the study of inlet flow distortion. The model was extended even further towards a fully 3D Euler solver using a streamline curvature code to include the radial distribution of blade forces which allows simulating compressors with low hub-to-tip ratio. Apart from the modelling of compressor instability and fuel spikes, this model has been applied to investigate the effect of inlet systems on compressor instability and engine starting transients [43].

The methodology developed within the context of the present doctoral research is based on this approach. The general idea is common, nevertheless, some models have been enhanced and new capabilities have been included to fulfil the particularities of modelling the shaft failure event.

4.4 Previous work on shaft failure modelling

Recently, M. Haake, R. Fiola and S. Staudacher [48] published a work regarding the analysis of the shaft failure event in particular. To the best knowledge of the author, this is the only study available in the public domain which tackles this particular scenario.

The methodology adopted by the authors follows the line of those detailed in the previous section. The simulation of the compression side of the engine, including the compressors and the combustor, is undertaken by means of a 1D solver of the Euler equations with source terms. Compressor performance is represented by experimental maps in the stable region and approximated by scaled characteristics in the stall and reverse flow regions. The turbine model used to calculate the rotational speed evolution of the free-running turbine is standalone. In case of unlocated failure, the friction torque provoked by turbines' contact is approximated by means of different friction coefficients and the wear of the material involved is calculated by a basic energy method. The presence of bleeds, heat soakage, combustor pressure losses and combustor flammability limits are taken into account.

The models of the compression side and turbine acceleration are validated independently. Data regarding fuel spike tests and a known case of shaft failure are used for that purpose. Finally, the model is used to explore the effect of different fuel flow schedules on the outcome of the shaft failure event.

Chapter 5

Methodology

Gas turbine shaft failure is a complex event which involves the different subsystems of the engine operating in extreme off-design conditions. Moreover, these subsystems are operating in an interconnected manner, being of paramount importance the consideration of their interaction to succeed in the simulation purpose. In previous chapters, evidences of the interaction between Main Gas Path (MGP), Secondary Air System (SAS) and the friction and wear process of turbines in contact have been introduced. This interaction invites to tackle this simulation problem from an overall engine point of view. In the present chapter, the simulation strategy followed in this research is presented.

As it was stated in Chapter 3, this doctoral research aims to develop overall engine simulation capability to predict engine behaviour in fast transient events, with especial focus on the shaft failure scenario. In the particular case of shaft failure, the main objective is to predict the evolution of the rotational speed of the free-running turbine after the breakage. The acceleration of this turbine is a consequence of the torque extracted from the MGP and the torque derived from the different contact phenomena in case of unlocated failure. It has been shown how the latter depends on total axial force acting on the turbine disc, involving the SAS in the event, since the disc is affected by the pressure evolution in the cavities where it is immersed. It means that the time-accurate prediction of flow properties over the MGP and also the SAS is needed. Since these two subsystems of the engine operate interconnected through the bleeding and injection ports, the whole engine must be resolved in a fully-integrated manner over the time of the event.

The present chapter presents the methodology followed using a general-to-specific approach. The overall structure of the simulation software is shown first and this is

followed by the explanation of the different models applied to each engine component. This chapter focus on the explanation of the integration process, the development of the MGP simulation tool and the work done regarding the SAS solver.

5.1 CERVANTES - The 'all-in-one' simulation tool

The major objective of this doctoral research aims to develop simulation software to assist the design and certification process of gas turbines by predicting its behaviour after a shaft failure event. This simulation tool has been named CERVANTES following the next acronym: CERtification aim oVer-speed ANalysis Transient Engine Solver. This name will be used along the present thesis to refer to the 'all-in-one' simulation tool.

CERVANTES is able to simulate in a fully integrated manner the different components and phenomena involved in a shaft failure scenario. Furthermore, the simulation tool is applicable to other scenarios. The methodology chosen to build this tool makes it particularly suitable to be applied at any rapid transient events, above all if compressor instability is involved.

In the present section, the overall coupling of the different solvers and the structure of the software developed are explained.

5.1.1 Methodology - A fully integrated simulation tool

Shaft speed integration

The biggest issue regarding the study of gas turbine shaft over-speed from the point of view of certification is to guarantee that the terminal speed of the free-running turbine after a shaft failure is below the limit which does not compromise the integrity of the turbine and therefore, the safe rundown of the engine can be expected. Therefore, as it was explain in Chapter 3, the most important variable whose evolution needs to be predicted is the rotational speed of the free-running turbine.

The second law of Newton for angular acceleration is the differential equation which has to be integrated to calculate the evolution of the rotational speed of the shafts.

$$\frac{d\omega}{dt} = \frac{\tau}{I} \tag{5.1}$$

This is a problem of initial conditions. The equation is an ordinary differential equation and the value of the variable is given at a certain (initial) time (see Equations 5.2 and 5.3). To undertake the integration of this problem in the context of CERVANTES, a second-order explicit numerical scheme has been chosen. In particular, the numerical scheme used is a 2-step Adams-Bashforth. Explicit solvers are those which allow the calculation of the variable at a certain time step as a function of its value in previous time steps so it can be done explicitly avoiding any iterative process in the resolution. The choice of an explicit scheme is convenient because the solver of the flow field chosen is of this same nature.

$$\frac{du}{dt} = F\left(u, t\right) \tag{5.2}$$

$$u\left(t_0\right) = u_0 \tag{5.3}$$

$$u_{n+1} = f\left(u_n, u_{n-1}, \ldots, u_{n-p+1}\right) \tag{5.4}$$

In the formulation, subscripts stand for the time step and (p) is the number of steps of the numerical scheme.

The solver used for the flow field, as it is shown below in this chapter, is a second-order scheme and therefore, in order to be coherent, the same order must be guaranteed at any time. The error in Adams-Bashforth schemes is $(\triangle t)^p$ so the 2-step version of this family has been chosen [51].

The general formulation which allows variable time step is shown in Equation 5.5. The value of $\triangle t$ used in the overall solver is given by the most restricting condition in terms of stability for the different fluid dynamics solvers. This value is calculated following the CFL criterion which is explained in detail below in Section 5.2.1. This value is calculated each time step and depends on the flow field, which is changing.

$$u_{n+1} = u_n + \triangle t_n \left(\left(1 + \frac{\triangle t_n}{2\triangle t_{n-1}} \right) F_n - \left(\frac{\triangle t_n}{2\triangle t_{n-1}} \right) F_{n-1} \right) \tag{5.5}$$

$$\triangle t_n = t_{n+1} - t_n \tag{5.6}$$

$$\triangle t_{n-1} = t_n - t_{n-1} \tag{5.7}$$

When it is applied to integrate Equation 5.1,

$$u = \omega \tag{5.8}$$

$$F = \frac{\tau}{I} = f(t) \tag{5.9}$$

Apart from the data which is explicitly shown in Equation 5.5, the subroutine performing this calculation needs to be provided with information regarding the integrity of each shaft and the nature of the failure (located / unlocated). The logic implemented allows the inertia split from the moment of failure and the rearrangement of the different components of the torque (compressor, turbine and friction).

Torque components and axial force acting on the free-running turbine

In general, in absence of failure, the pair compressor-turbine are part of the same dynamic system so the inertia is the sum of both terms and the total torque acting on the system is also the sum of the torque consumed by the compressor and the torque produced by the turbine. At the time of failure, the shaft is split into two parts and two new initial condition problems are defined. In case the failure is defined as unlocated, the friction torque is calculated and added to the turbine torque.

In summary, capability to calculate three torque components is needed. The torque consumed by each compressor and the torque produced by each turbine can be calculated if the thermodynamic properties over the MGP are known.

On the other hand, the friction torque is a consequence of different mechanical phenomena involved in the contact of the free-running turbine rotor against the rear static structure. This contact occurs in two phases. Initially, the rubbing process of the rotating part against the continuous static platform and seal segment takes place. This process produces the wear of the metallic structures allowing the axial

displacement of the unlocated turbine disc. Eventually, rotor blades penetrate into the region occupied by the NGVs of the downstream turbine and blade tangling occurs. Apart from then, both mechanical interactions, namely, platform rubbing and blade tangling take place in a combined manner. The understanding and modelling of these mechanical interactions is a highly complex problem in its own. This analysis is not tackled by the present doctoral research although the outcome of the model is fundamental for the calculation of the free-running turbine rotational speed. This problem has been undertaken in parallel within the context of the Rolls-Royce UTC at Cranfield University by Aleixo González [44] (PhD candidate). The model has been produced, validated and delivered to this author for its integration into CERVANTES. From the point of view of this thesis, the model is considered a 'black box' and attention is only paid to the input/output variables.

The friction, wear and tangling model is able to calculate the friction torque and the material worn at each time step as a function of the axial force (F_x) pushing the free-running disc rearwards, its rotational speed (ω) and the penetration or axial displacement ($\triangle x$).

$$\tau_{friction} = f\left(\omega, F_x, \triangle x\right) \tag{5.10}$$

Rotational speed is calculated by the process described here, the penetration is calculated by the friction model itself and its progression is stored in one of the variables of the code. Therefore, those can be considered known variables at this point. Finally, the only unknown is the axial force acting on the disc. This is a consequence of the fluid pressure which is surrounding the rotor disc. Rotor blades are part of the MGP of the engine and the force acting on them ($F_{x_{blades}}$) is the consequence of the static pressure drop experienced by the fluid across this turbocomponent. The rest of the disc is immersed in the SAS so the axial force ($F_{x_{disc}}$) is given by the difference in pressure between IPT cavity and the LPT cavity.

$$F_x = F_{x_{blades}} + F_{x_{disc}} \tag{5.11}$$

The axial force acting on the disc is the axial projection of the integral of the static pressure (p) multiplied by the area over the surface of the disc. It can be calculated using the axial projection of the disc area (A_x) independently of the shape of the disc as can be seen in Equation 5.12.

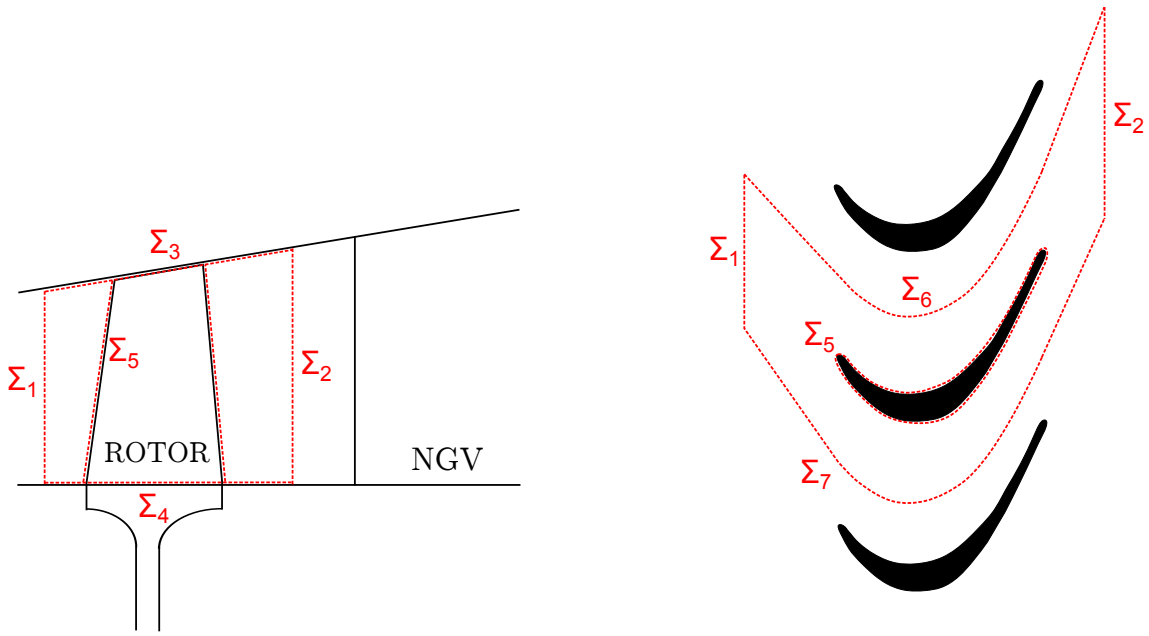

Figure 5.1: Control volume around IPT rotor

$$F_{x_{disc}} = \left(\int_{\Sigma_{disc}} p \cdot d\bar{\sigma} \right) \cdot \vec{i} = \sum_i p_i A_{x_i} - \sum_j p_j A_{x_j} \tag{5.12}$$

In Equation 5.12, index i counts for the cavities in contact with the disc at the left-hand side and index j counts for the cavities at the right-hand side. This is the way to simplify the expression keeping the sign criteria. The engines that are analysed in the present thesis have only one cavity at each side of the disc and therefore, the expression can be simplified as follows.

$$F_{x_{disc}} = A_x \left(p_{IPC} - p_{LPC} \right) \tag{5.13}$$

The calculation of the axial force suffered by the blades can be calculated applying the integral form of the momentum equation to the control volume around the blade as can be seen in Figure 5.1.

$$\frac{d}{dt} \int_{V_c(t)} \rho \bar{v} d\Omega + \int_{\Sigma_c(t)} \rho \bar{v} \left(\bar{v} + \bar{v_c} \right) \cdot \vec{n} d\sigma = \int_{\Sigma_c(t)} \tau \cdot \vec{n} d\sigma + \int_{V_c(t)} \rho \bar{f_m} d\Omega \tag{5.14}$$

Assuming steady state, no effect of body forces and inviscid flow, Equation 5.14 can be simplified as follows,

$$\int_{\Sigma_c(t)} \rho\bar{v}\left(\bar{v}-\bar{v_c}\right)\cdot\vec{n}d\sigma = \int_{\Sigma_c(t)} -p\delta_{i,j}\cdot\vec{n}d\sigma \tag{5.15}$$

taking into account that surfaces Σ_3, Σ_4 and Σ_5 are solid walls, Σ_6 and Σ_7 are periodic, and assuming that flow properties are constant from hub to tip and that the cross sectional area change is negligible, the equation can be simplified as follows (only the axial component is considered).

$$\rho_2 A v_{x_2}^2 - \rho_1 A v_{x_1}^2 = A\left(p_1 - p_2\right) + F_{x_{rotor\rightarrow fluid}} \tag{5.16}$$

At this point, it can be assumed that the axial velocity v_x is approximately constant and therefore, the term regarding axial momentum variation is negligible in comparison with the change in static pressure, the final expression for the axial force acting on the blade is:

$$F_{x_{fluid\rightarrow blade}} \simeq A\left(p_1 - p_2\right) \tag{5.17}$$

MGP and SAS integration

Through the previous analysis, the problem has been reduced to the resolution of the complete aero-thermodynamics of the engine, the necessity to simulate both, MGP and SAS, has been stated.

The study of the MGP comprises the fluid dynamics and performance problem which involves to the mass flow which enters the core of the engine. The major objective of this solver is to capture the dynamics of the engine including compressor in-stall operation. The solver has been divided into two parts, namely, compression side and expansion side. The objective of this division is to simplify the analysis by restricting the fully-transient approach to the compression side. In this project, compression side is the name given to the fluid domain which goes from the engine intake (ambient conditions) to the throat area of the HPT NGVs. Expansion side comprises the region from HPT inlet to the discharge section of the core nozzle.

The main reason to split the domain of the MGP in this manner is the assumption of permanent choking conditions at the HPT NGVs minimum section [86]. From the point of view of the fluid dynamic analysis, a choked section does not allow sound

waves to travel upstream and therefore, no information of any kind is transmitted in that direction. It means that whatever happens downstream of this section cannot affect to the flow field upstream. Furthermore, the combustor is a big volume which acts dumping high-frequency variations in flow properties. The combination of these two effects invites to tackle the problem in a split manner.

In summary, compressor surge is the source of the fast transient phenomena occurring during a shaft failure event; it occurs at the compression side; this part is isolated from the expansion side through the NGVs choked section; and the combustor acts dumping the response in terms of mass flow and pressure at the outlet of the compression side. This scenario invites to tackle the problem with the following approach:

- The compression side solver is a fully-transient 1D solver of the Euler equations of fluid dynamics. The inputs of this solver are the boundary conditions at the inlet, the fuel flow injected at the combustor, the mass flow bled/injected at each section, and the rotational speed of the compressors. The boundary condition at the outlet section is irrelevant, a low pressure value is used just to guarantee the choking conditions at any operating point. The numerical scheme used to solve the system of partial differential equations is explicit. In other words, the resolution of the flow field in the actual time step (t_n) depends only on the flow field in the previous time step (t_{n-1}) which is known. The details about this solver are given below in this chapter (Section 5.2).

- The expansion side solver is a steady-steady turbine matching code whose objective is to calculate the operating points of all the turbines for any set of boundary conditions: inlet flow conditions (taken from the compression side outlet), outlet boundary condition, mass flow bled/injected at each section, and turbine rotational speeds. From the point of view of the integration, it is important to notice that, since this solver is steady-state, the input data needed to calculate the actual time step (t_n) are those corresponding to this very same moment. More details about this solver are given in a dedicated section of this chapter (Section 5.3).

The SAS of a gas turbine, from the point of view of modelling, is a network composed of a certain number of cavities interconnected by pipes and a variety of restrictors such as holes and seals. This network is a fluid system whose dynamics are dictated by its reaction to changes in the boundary conditions. The choice of the limits of the

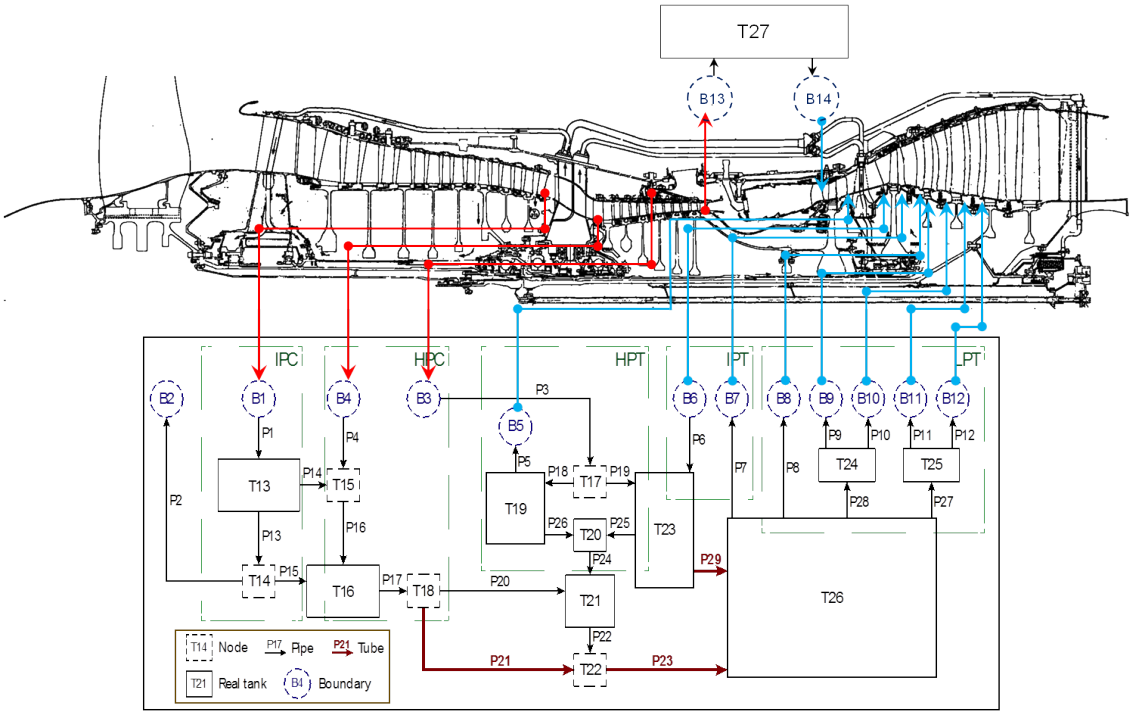

Figure 5.2: MGP and SAS integration scheme

system determines its boundary conditions, in general, the SAS is an open system connected to the MGP at different points over its length. These connection ports act as bleeding or injection points over the MGP depending on the properties of the fluid at both sides of the connection. Figure 5.2 shows a simplified network of the SAS and its connections with the MGP.

The interaction between the SAS and the MGP or vice-versa must be understood happening at two different levels. The analysis of the SAS is a boundary conditions problem. The temporal variation of the fluid properties at the different sections of the MGP determines completely the evolution of the fluid properties over the SAS and therefore, a 'first-order' interaction is established. On the other hand, from the point of view of the MGP, the interaction with the SAS only represents a part of its boundary conditions which would also include the ambient conditions and the fuel flow injected into the combustor. Although accounting the mass flow bled / injected to the MGP through the SAS is important to gain accuracy on engine matching and performance prediction, the quantity is a small fraction of the mass flow managed by the MGP and therefore, the interaction in that sense can be considered of 'second-order'.

Figure 5.3 shows the scheme of the calculation process followed by CERVANTES. At the starting point of a new time step (t_n), the complete solution of the previous

time step (t_{n-1}) is available. The calculation process starts with the compression side which is given boundary conditions: ambient pressure and temperature, fuel flow and the shaft speed of the different compressors. The process starts here because this solver is explicit and only needs information regarding the previous time step which is already known. Once the compressor side solver is executed, the flow field over this domain and the torque consumed by the compressors are known at t_n. The compressor side flow field at t_n is used to give part of the boundary conditions to the SAS solver and to provide the expansion side solver with the inlet conditions at t_n.

Next, the shaft speeds at t_n are calculated, the solver is explicit and therefore only information at t_{n-1} is needed. After that, the information needed to execute the expansion side solver is almost complete with exception of the mass flow bled/injected at the different ports at t_n. Following the previous explanation regarding the order of interaction between MGP and SAS, at that point, it is assumed that the values of mass flow bled/injected at the expansion side ports at t_n can be substituted by the known values of this variables at t_{n-1}. This assumption is supported by two facts, the size of the time step used by CERVANTES is very small (10^{-6}) and the possible error incurred has an impact of second order on the resolution of the expansion side flow field. Once the expansion side has been solved, the complete distribution of thermodynamic properties over the MGP is known.

The next step is the calculation of the flow properties over the SAS at t_n. The inputs needed by this code are two, namely, the value of static properties at the different boundary ports and the geometry of the network, both at t_n. The solver is also explicit so only information regarding the previous time step is needed for the rest of the variables. The geometry of the network has been included here as a variable because capability to modify the geometry of the SAS during the event has been implemented in CERVANTES. The axial displacement suffered by the free-running turbine in case of unlocated failure provokes variation of volume in the cavities and variation of area in the ports at both sides of the disc. Following again the same assumptions explained above, these geometry variations are applied with a lag of one time step since the axial displacement at t_n is not yet available. At that point, the SAS solver is executed so the values of flow properties over the network and the mass flow at the connection points are calculated at t_n. This allows checking the validity of the previous assumption by comparing the new bled/injected mass flows against those used in the expansion side and guarantee that their difference is always below a certain threshold.

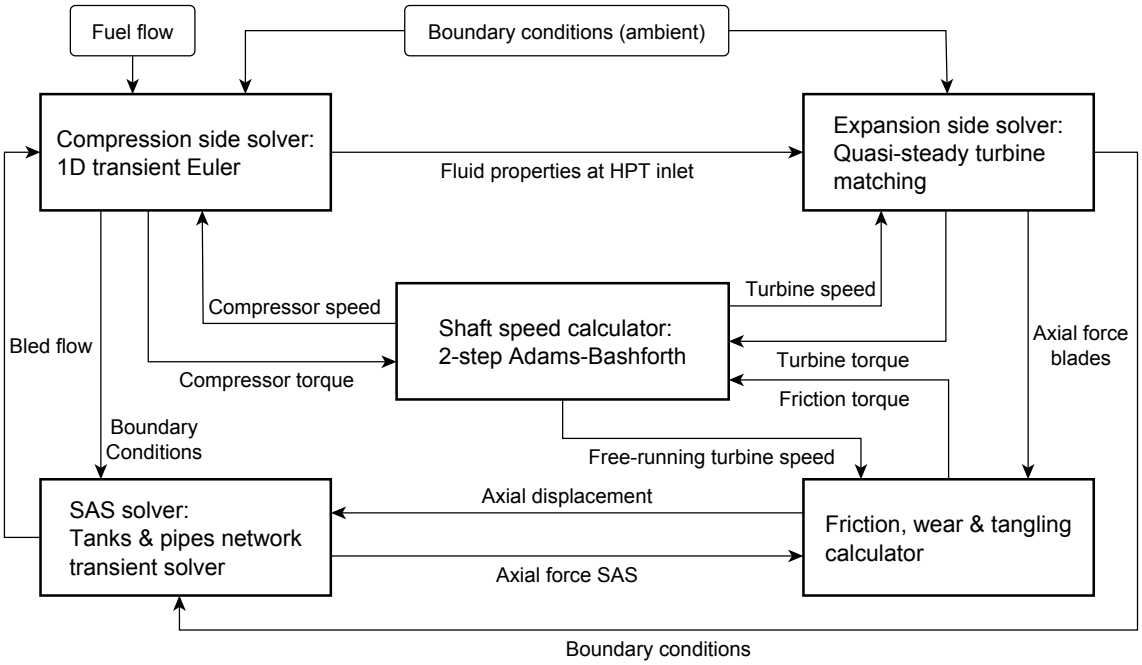

Figure 5.3: CERVANTES integration scheme and calculation process

Finally, once the fluid properties are known completely, the axial force acting on the free-running turbine can be calculated. Since the rotational speed at t_n is also known, the subroutine which calculates the friction torque and the progress in axial dislocation can be executed. At that point, the problem is solved and the time-marching process can continue with the next time step.

CERVANTES is a program implemented from scratch in the context of this doctoral research. Figure 5.4 shows a flow diagram of the software which allows understanding the coding process and its structure. The software needs to be provided with several input files and generates a set of output files. The input files that have to be prepared by the user include the following information: compressor maps, turbine maps, compression side initial conditions, expansion side initial conditions, SAS initial conditions, MGP boundary conditions, MGP geometry and SAS network geometry and connectivity. Regarding the output files, in general, the program generates one file for each flow property which is plotted using two-dimensional carpets: rows are time steps and columns are axial coordinate or element number. Furthermore, an extra file is generated which contains the history of the flow properties over the compression side using the format needed by Tecplot. Tecplot allows the creation of videos which are useful to get a complete visualisation of the transient phenomena.

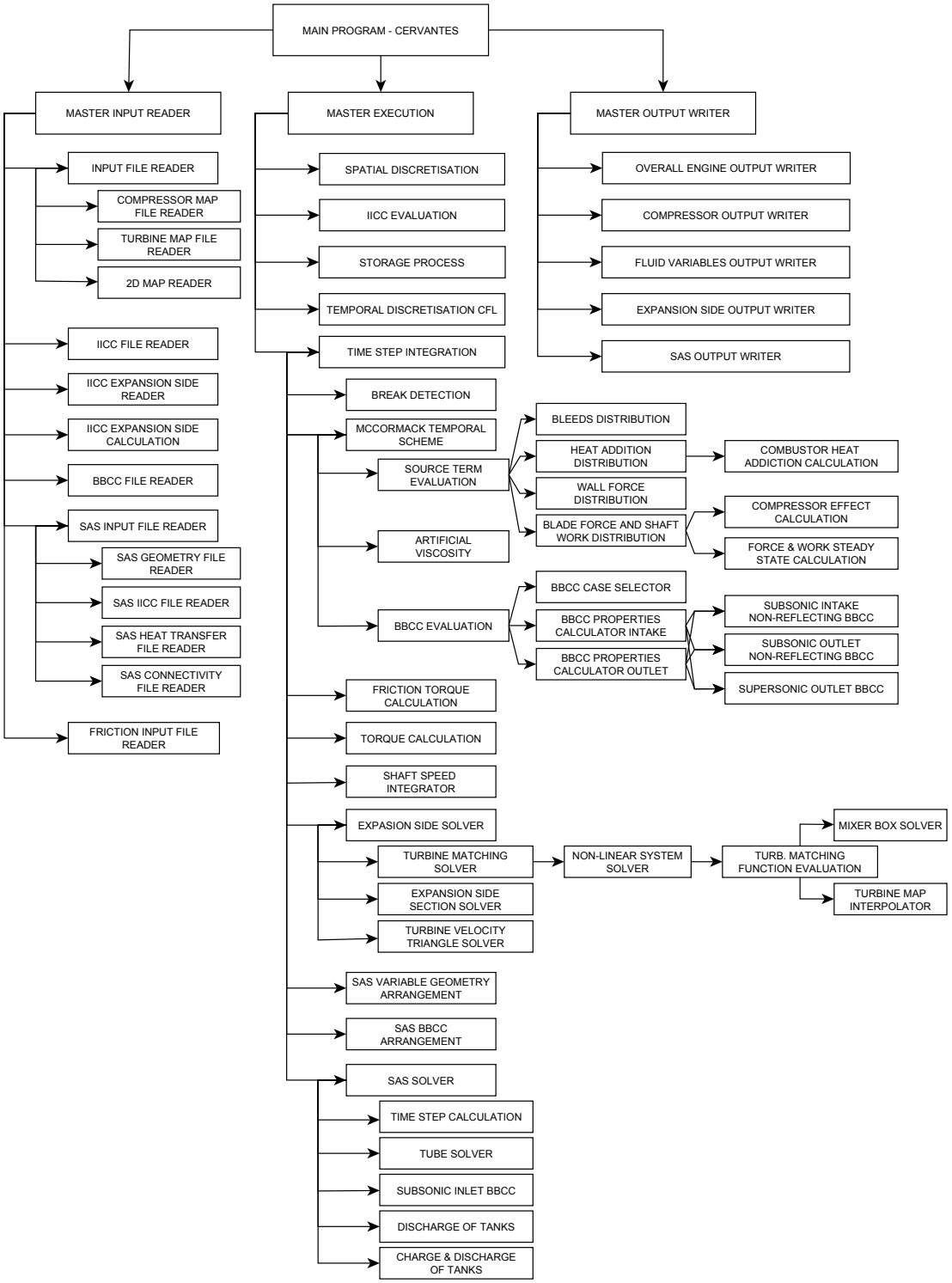

Figure 5.4: CERVANTES flow diagram

5.2 Main gas path simulation - The compression side

The objective of the compression side solver is the simulation of the flow dynamics involving the different axial compressors, the combustor and the ducting system associated in a multi-shaft gas turbine, in particular, modern High Bypass Ratio (HBR) aero engines.

The fluid domain analysed comprises the region of the core gas path of the engine from the intake to the choked area at the HPT NGVs. This choked section isolates this part of the engine from the expansion side as was explained in Section 5.1. Figure 5.5 shows the cutaway of a typical HBR turbofan where the region corresponding with the compression side can be identified.

The compression side domain is the annular duct defined by the inner and outer walls of the MGP. The latter is extrapolated towards the fan inlet to complete the duct. These two walls, from fan inlet to HPC outlet, define a proper variable-area annular duct. The last part of the domain, including the diffuser, the combustor and the duct contraction (nozzle) which ends at the choked throat of the NGVs, is modelled using a simplified abstraction since the equivalent duct is not as well defined as in the other part. Regarding the first part, the shape of the two walls is used to calculate the area distribution. This is a two-dimensional domain which has to be transformed into a one-dimensional one given only by the area as a function of the length parameter. It is assumed that the geometrical mean line is a good representation of the streamline of the flow at mid-span. The length parameter is calculated over this line and its area associated is the area of the intersection of the annular duct with the plane perpendicular to the mean line at that point. Regarding the combustor, the volume, the maximum area, the area at HPC outlet and the choked area at the NGVs are measured and used to calculate the simplest smooth distribution of area using cubic splines which keeps these values.

The bypass flow has not been included in the domain. Core flow and bypass flow are normally studied independently since the working fluid is different. Following a conventional approach, it can be assumed that a streamline exists which splits the fluid into two regions. In that case, a point of this streamline has been calculated at take off conditions in front of the fan, and the outer wall of the core path has been smoothly extrapolated matching that point to define the domain. Figure 5.5 is just an schematic representation.

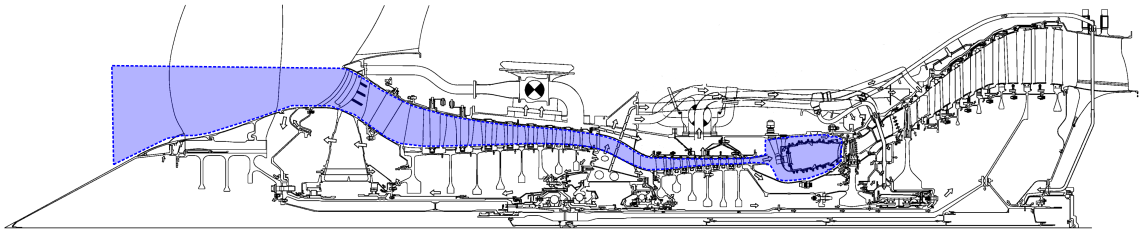

Figure 5.5: Compression side domain

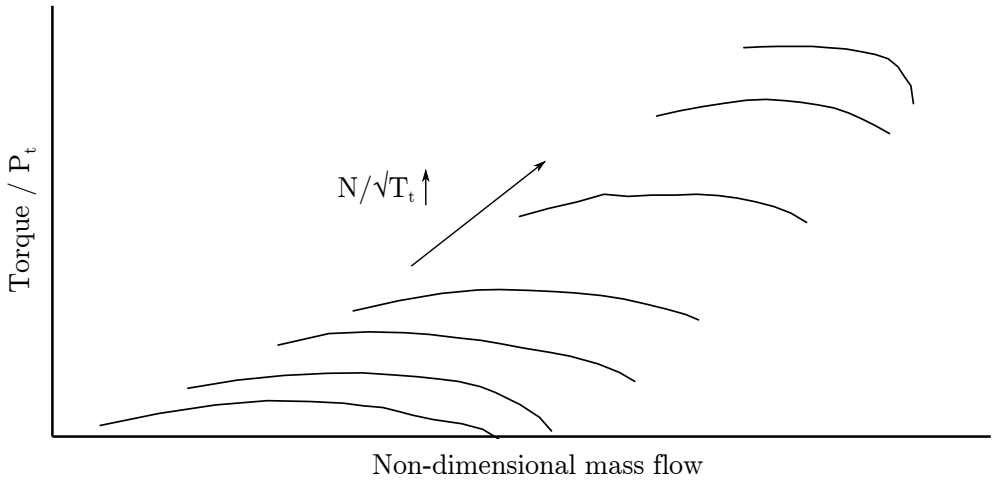

Figure 5.6: Fan torque map

From the point of view of performance, fan map is available to deal with these two regions separately. However, from the point of view of engine matching, the power consumed by the outer part of the fan has to be considered together with the inner part since the whole fan is moved by the LPT. Two assumptions have been applied here to deal with that problem. Firstly, it is assumed that compressor instabilities occurring over the MGP do not develop radially in the fan so the outer part is always working in the stable region of the map. Secondly, the observation of the torque map of the fan shows that the main variable affecting the level of torque is the non-dimensional rotational speed, and that the effect of non-dimensional mass flow can be neglected in a first approximation. The acceptance of these assumptions makes possible to express the torque as a function only of rotational speed which is a known variable. In that way, the resolution of the bypass flow is avoided. Figures 5.6 and Figure 5.7 show the torque map and the correlation derived based on these assumptions.

In conclusion, the compression side domain is given by the area distribution which represents the real annular duct. The different components of the engine are placed over the length of this domain. In the particular case of a 3-spool engine, the domain

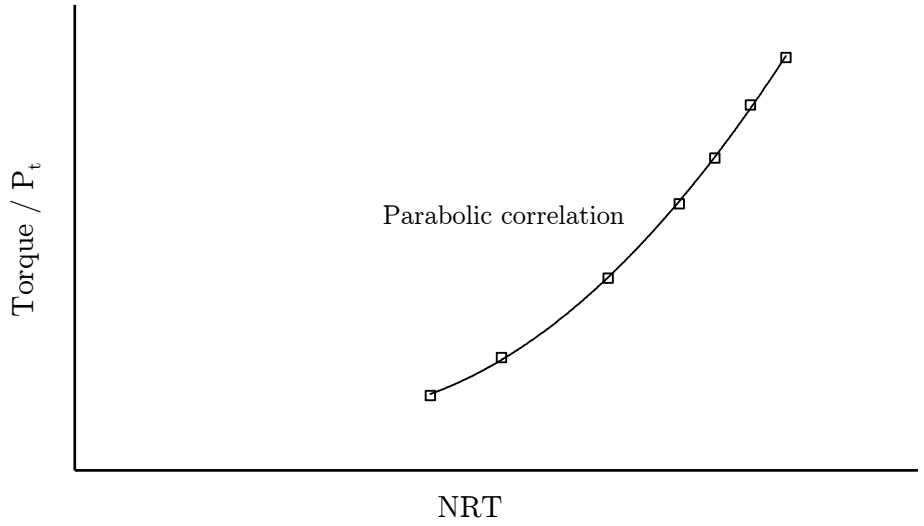

Figure 5.7: Simplified torque correlation

contains the inner part of the fan, the IPC, the HPC, the combustor, portions of duct between components and the different bleed and injection ports over the domain.

5.2.1 Methodology

Equations of motion and gas model

The flow in the compression side of a gas turbine is three-dimensional, unsteady, viscous, and, in certain zones, of variable composition, dominated by chemical reactions and heat transfer. Compressors act on the flow by means of pressure forces communicated to the flow through the blade's surfaces. In the combustor, the temperature and the composition of the flow change by means of a combustion process. Nevertheless, an attempt to model this system including all the complexity of the real physics is unfeasible and it is out of the scope of the present research. Based on previous works presented in the literature review (Chapter 4), the phenomena of compressor surge, stall and recovery needed for the simulation of the shaft failure event can be capture by an approach based on a quasi one-dimensional representation of the flow where the real complexity of compressors and combustor is modelled by external terms.

The flow field in the quasi-1D domain (variable-area duct) which has been used for the mathematical model is 2D, namely, the flow velocity has two non-zero components (axial and radial) due to the area variation. The radial component is not of interest for this analysis and therefore, the objective is to model the flow field

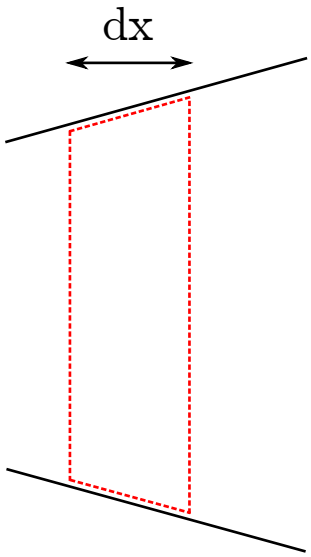

Figure 5.8: Variable area duct control volume

as 1D. This is equivalent to assume that only the axial component of the velocity is non-zero and that the thermodynamic properties are constant at each cross section. This assumption makes necessary to derive a specific set of equations for that particular problem starting from the first principles of continuity, Newton's second law and energy conservation. This system of equations is known as the quasi-1D Euler equations. The classic form of the 1D Euler equations is not applicable to this problem since the radial coordinate needs to be kept to model the effect of area variation. That is the reason why the quasi-1D Euler equations have to be derived by the application of the first principles to the problem defined.

The integral form of the continuity equation is applied to the general control volume that can be seen in Figure 5.8.

$$\frac{\partial}{\partial t}\int_{V_c}\rho d\Omega + \int_{\Sigma_c}\rho\bar{v}d\bar{\sigma} \tag{5.18}$$

$$\frac{\partial}{\partial t}\left(\rho A dx\right) - \rho u A + \left(\rho + d\rho\right)\left(u + du\right)\left(A + dA\right) = 0 \tag{5.19}$$

Neglecting terms of low order in the products and dividing by dx, the conservation form of the continuity equation following the quasi-1D approach is obtained.

$$\frac{\partial\left(\rho A\right)}{\partial t} + \frac{\partial\left(\rho A u\right)}{\partial x} = 0 \tag{5.20}$$

Following the same approach, the integral form of the momentum equation in the axial direction is applied to the same control volume. High order terms are neglected and the pressure derivative is rearranged to obtain the conservation form of the momentum equation (Equation 5.24).

$$\frac{\partial}{\partial t}\int_{V_c}\rho u d\Omega + \int_{\Sigma_c}\rho u\bar{v}\cdot d\bar{\sigma} = \left(-\int_{\Sigma_c} p d\bar{\sigma}\right)\cdot\vec{i} \tag{5.21}$$

$$\frac{\partial}{\partial t}\left(\rho u A dx\right) - \rho u^2 A + \left(\rho + d\rho\right)\left(u + du\right)^2\left(A + dA\right) = \tag{5.22}$$

$$-\left(-pA + \left(p + dp\right)\left(A + dA\right) - 2P\frac{dA}{2}\right)$$

$$\frac{\partial\left(\rho u A\right)}{\partial t} + \frac{\partial\left(\rho u^2 A\right)}{\partial x} = -A\frac{\partial p}{\partial x} \tag{5.23}$$

$$\frac{\partial\left(\rho u A\right)}{\partial t} + \frac{\partial\left(\rho u^2 A + pA\right)}{\partial x} = p\frac{dA}{dx} \tag{5.24}$$

Applying the same process to the integral equation of energy, its conservative quasi-1D version is obtained.

$$\frac{\partial}{\partial t}\int_{V_c}\rho\left(e + \frac{u^2}{2}\right)d\Omega + \int_{\Sigma_c}\rho\left(e + \frac{u^2}{2}\right)\bar{v}\cdot d\bar{\sigma} = -\int_{\Sigma_c} p\bar{v}\cdot d\bar{\sigma} \tag{5.25}$$

$$\frac{\partial}{\partial t}\left(\rho A\left(e + \frac{u^2}{2}\right)\right) + \frac{\partial}{\partial x}\left(\rho u A\left(e + \frac{u^2}{2}\right) + puA\right) = 0 \tag{5.26}$$

The set of equations can be expressed in a condensed way defining the following vectors:

$$U = \left\{\begin{array}{c} \rho A \\ \rho A u \\ \rho A\left(e + \frac{u^2}{2}\right) \end{array}\right\} \tag{5.27}$$

$$F = \left\{ \begin{array}{c} \rho A u \\ \rho A u^2 + pA \\ \rho A u \left(e + \frac{u^2}{2} \right) + pAu \end{array} \right\} \tag{5.28}$$

$$G = \left\{ \begin{array}{c} 0 \\ p\frac{dA}{dx} \\ 0 \end{array} \right\} \tag{5.29}$$

$$\frac{\partial U}{\partial t} + \frac{\partial F}{\partial x} = G \tag{5.30}$$

The system of partial differential equations defined by Equations 5.27, 5.28, 5.29 and 5.30 is the quasi-1D Euler formulation for transient and inviscid flow. The term G is called source term and can be used to include external influences affecting to the flow. As has been said above, these equations have been derived to model the flow evolution over a variable-area duct through a one-dimensional abstraction. Since the physical evolution of a flow within a variable-area pipe involves two dimensions, this approach is unphysical and, to compensate this fact, a non-zero term appears in the component of the vector G which corresponds to the momentum equation. This term is a sort of axial force which modifies the flow properties to adapt it to the area change.

Apart from imposing to the flow the effect of area variation, the source term G is used here to act on the fluid in the different manners which allow simulating the presence of the different components of the engine over the gas path. Regarding the continuity equation, the first component of the source term is used to model bleed ports. Bleed ports are, by definition, a violation of the continuity equation since they change the mass flow contained within the domain which, from the point of view of the equations, is not open at any section except the inlet and the outlet. The way to violate the continuity equations is using a source term (W_B). If part of the flow is remove from the domain, in order to be consistent, the enthalpy of this bled flow has to be removed too. Therefore, an equivalent term accounting for the enthalpy bled (H_B) has to be included in the third component of the source term. The bleeding terms are also used to simulate the injection of fuel in the system. Regarding the momentum equation, the external term is called axial force (F_x) and its use is paramount when modelling gas turbines since it will represent the effect of the compressors. To complete the effect produced by the presence of compressors in

the gas path, the energy transfer which is communicated from the rotor blades to the fluid must be accounted. It is done through the term called shaft work (SW) which is part of the third component of the vector G. The remaining term to complete any possible external interaction is the heat transfer term (Q) which is added to the term corresponding to the energy equation. This term is used to model the presence of the combustion chamber.

In summary, the idea of this methodology is to keep the simplicity of the fluid dynamic model at the minimum (transient and quasi-1D) while the complexity of the component performance is incorporated through the source terms. Following this explanation the final form of the source term is given by Equation 5.31.

$$G = \left\{ \begin{array}{c} -W_B \\ F_x + p\frac{dA}{dx} \\ Q + SW - H_B \end{array} \right\} \tag{5.31}$$

This mathematical problem is given by 3 partial differential equations and 4 unknowns.

$$\rho = \rho\,(x,t) \tag{5.32}$$

$$p = p\,(x,t) \tag{5.33}$$

$$u = u\,(x,t) \tag{5.34}$$

$$e = e\,(x,t) \tag{5.35}$$

To complete the model and to close the problem, a model of gas is needed. CERVANTES has been provided with a model of ideal gas where the value of C_p and C_v are a function of temperature. The calculation of C_p is done using the polynomials of JANAF [17]. The flow is considered a perfect mixture of ideal gases composed by dry air and stoichiometric products. Firstly, the ideal gas equation is given by,

$$p = \rho R_g T \tag{5.36}$$

where the gas constant R_g is a function of the universal gas constant and the molecular mass

$$R_g = \frac{R}{M} \tag{5.37}$$

By definition, the heat capacity at constant pressure (C_p) and the heat capacity at constant volume (C_v) are given by the following expressions:

$$C_p = \frac{dh}{dT} \tag{5.38}$$

$$C_v = \frac{de}{dT} \tag{5.39}$$

They are related to the gas constant by the following expression:

$$C_p - C_v = R_g \tag{5.40}$$

If the gas is considered calorically perfect, C_p and C_v are constant. In this case, the model implemented uses a polynomial expression to calculate C_p and the equivalent integrated expression to calculate the specific enthalpy. Each polynomial is divided into two over the temperature range. The first one applies from 200 K to 1000 K and the second one from 1000 K to 3000 K. Furthermore, two sets of polynomials have been implemented, one for dry air and the other one for stoichiometric products of combustion.

$$C_p = C_0 + C_1 T + C_2 T^2 + C_3 T^3 + C_4 T^4 + C_5 T^5 + C_6 T^6 \tag{5.41}$$

$$h = C_0 T + \frac{1}{2} C_1 T^2 + \frac{1}{3} C_2 T^3 + \frac{1}{4} C_3 T^4 + \frac{1}{5} C_4 T^5 + \frac{1}{6} C_5 T^6 + \frac{1}{7} C_6 T^7 + C_{h0} \tag{5.42}$$

Apart from that, a thermodynamic relationship is needed to close the problem. In this case, the definition of specific enthalpy (h) given by Equation 5.43.

$$h = e + \frac{p}{\rho} \tag{5.43}$$

The air changes its compositions over the length of the engine. This fact is not accounted by the equations of fluid dynamics but a storage process has been implemented to keep in memory the composition of the working fluid after the combustion. The flow is considered to be purely dry air from the engine intake to the combustor inlet. Then, to take into account the change in gas properties due to the composition change provoked by the combustion, the amount of dry air, stoichiometric products and unburnt fuel are stored and they are used at each engine station to calculate the gas properties more accurately. The storage of the gas composition is not only used over the compression side but also over the expansion side. The composition of the flow is assumed to be frozen after the combustion and it is changed just in case of later combustion. Unburnt fuel and its combustion out of the combustion chamber has been observed in engines in some cases of fuel spiking test and compressor surge in general. The capability to burn fuel over the expansion side has been implemented in the code and this is discussed in detail below in Section 5.3.2.

Following the concept of perfect mixture the flow properties are calculated as a pondered average of the properties of each component using the mass fraction.

$$\dot{m} = \dot{m_{da}} + \dot{m_{sp}} + \dot{m_{uf}} \tag{5.44}$$

$$C_{p_{mix}} = \sum_{i=1}^{N} \frac{\dot{m}_i}{\dot{m}} C_{p_i} \tag{5.45}$$

$$h_{mix} = \sum_{i=1}^{N} \frac{\dot{m}_i}{\dot{m}} h_i \tag{5.46}$$

Initial conditions and boundary conditions

The mathematical problem is now completed in terms of number of equations and number of unknowns. Nevertheless, since the problem is an evolution problem in partial differential equations, information regarding initial conditions and boundary

conditions is needed. The initial condition is given by a complete definition of the flow field at $t = 0$.

Initial conditions are given be following expressions:

$$p\left(x,0\right) = p_0\left(x\right) \tag{5.47}$$

$$\rho\left(x,0\right) = \rho_0\left(x\right) \tag{5.48}$$

$$u\left(x,0\right) = u_0\left(x\right) \tag{5.49}$$

The equivalent expression for internal energy (e) can be calculated using the gas model explained above.

Regarding the boundary conditions, it is necessary to take into account that the Euler equations are essentially a wave equation. This sort of equations can be analysed by means of the method of characteristics. The details of the mathematical apparatus which demonstrate this approach is not included here but can be consulted in any introductory book to fluid dynamics [63]. In this kind of problems, certain thermodynamic properties are constant through characteristic lines in the plane (x,t). This fact allows calculating the solution time step by time step based on the information 'travelling' from a previous time step. The boundary conditions are needed when calculating the flow field in the proximity to the boundaries of the domain if the slope of this characteristics indicates that information is entering the domain and therefore, it does not come from the a previous time step solution.

The characteristics are 3 and their slopes are the followings:

$$\left.\frac{dx}{dt}\right|_{C^+} = u + a \tag{5.50}$$

$$\left.\frac{dx}{dt}\right|_{C^-} = u - a \tag{5.51}$$

$$\left.\frac{dx}{dt}\right|_{C^0} = u \tag{5.52}$$

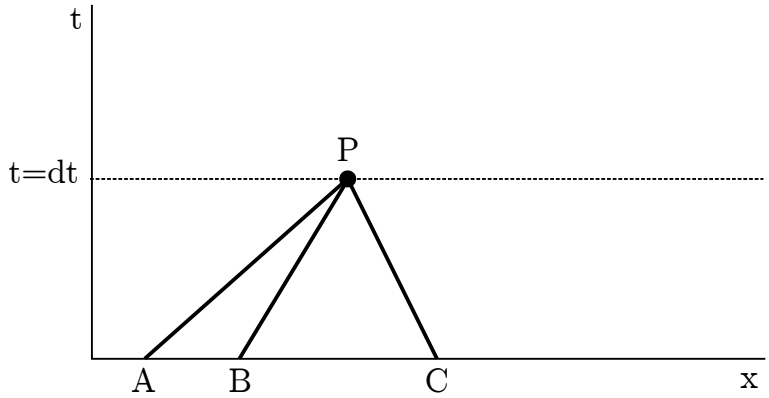

Figure 5.9: Characteristic lines in the plane x-t

Where (u) is the axial velocity of the fluid and (a) is the speed of sound.

Following this explanation it is possible to reason the amount of information needed at each boundary of the domain. As can be deduced from the expressions of the characteristic slopes, the origin of each line depends on the flow being subsonic or supersonic. Let's consider now the possible scenarios.

- Inlet of the domain:
  - Subsonic inlet ($0 < u < a$): C^+ and C^0 are positively sloped so they transport information from outside the domain while C^- is negatively sloped and transport information from inside the domain. In consequence, information regarding two thermodynamic properties is needed as boundary condition in this case.
  - Supersonic inlet ($u > a$): All the characteristics have positive slope and therefore, three thermodynamic properties are needed as boundary conditions in this case. This case is not relevant in the analysis of gas turbines since the inlet mass flow is always subsonic.
  - Subsonic outlet ($-a < u < 0$): C^+ has positive slope and the rest have negative slope. Information regarding one thermodynamic property is needed as boundary conditions in this case. This case is implemented in order to deal with the possible reverse flow associated with the compressor operating at surge conditions.
  - Supersonic outlet ($u < -a$): All the characteristics have negative slope and therefore no information is coming into the domain in that case.
- Outlet of the domain:

- Supersonic outlet ($u > a$): All the characteristics are positively sloped. At the outlet of the domain, it means that all the information is coming from inside and therefore, no information is needed to be imposed by boundary conditions. This case has been the only one implemented. The outlet of the domain has been defined as a convergent-divergent nozzle and a low enough value of the static pressure at the outlet has been imposed to guarantee choking conditions at the throat section leading to supersonic conditions at the outlet section.

The information needed to be provided to the solver at the inlet of the domain to satisfy the necessities for the cases of 'subsonic inlet' and 'subsonic outlet' are the static properties (pressure and temperature) at the far field upstream the domain and the flight speed in case an in-flight case needs to be simulated.

$$p_\infty(t) \qquad T_\infty(t) \qquad V_{flight}(t) \tag{5.53}$$

With this information and assuming that the process followed by the flow from the far field upstream to the domain inlet is isentropic, any needed property can be calculated. More details about that is given in the next subsection where the numerical implementation of the boundary conditions is explained.

Numerical scheme - Euler equations solver and implementation of boundary conditions

The physical problem to be solved has been introduced in the previous subsection. The summary of its governing equations, initial conditions and boundary conditions is shown below. Governing equations are given by Equation 5.54, the gas model is given by Equations 5.55, the needed thermodynamic relation is given by Equation 5.56, the initial condition can be expressed as Equation 5.57 and the needed boundary conditions are given by Equation 5.58.

$$\frac{\partial}{\partial t}\begin{Bmatrix} \rho A \\ \rho A u \\ \rho A\left(e+\frac{u^2}{2}\right) \end{Bmatrix} + \frac{\partial}{\partial x}\begin{Bmatrix} \rho A u \\ \rho A u^2 + pA \\ \rho A u\left(e+\frac{u^2}{2}\right) + pAu \end{Bmatrix} = \begin{Bmatrix} -W_B \\ F_x + p\frac{dA}{dx} \\ Q + SW - H_B \end{Bmatrix} \tag{5.54}$$

$$p = \rho R_g T \qquad C_p = C_p(T) \qquad h = h(T) \tag{5.55}$$

$$h = e + \frac{p}{\rho} \tag{5.56}$$

$$p(x,0) \qquad \rho(x,0) \qquad u(x,0) \tag{5.57}$$

$$p_\infty(t) \qquad T_\infty(t) \qquad V_{flight}(t) \tag{5.58}$$

The numerical scheme chosen to solve this physical problem is the explicit finite-difference technique proposed by MacCormack (1969). This scheme is widely applied in the solution of the Euler equation with source terms [49, 48]. The scheme is second-order accurate in space and time. MacCormack's scheme is a two-step predictor-corrector. It uses forward differences in the predictor and rearwards differences in the corrector. The method is part of the family of Lax-Wendroff schemes but is easier to apply than other methods of equivalent accuracy thanks to the smart use of the predictor-corrector technique which avoids the necessity to calculate second derivatives to build the Jacobian matrix that is needed in the classic second-order Lax-Wendroff scheme [6]. The condensed differential equation and the formulation of the scheme is the following [52].

$$\frac{\partial U}{\partial t} + \frac{\partial F}{\partial t} = G \tag{5.59}$$

$$\bar{U}_i = U_i^n - \frac{\triangle t}{\triangle x}\left(F_{i+1}^n - F_i^n\right) + \triangle t G_i^n \qquad Predictor \tag{5.60}$$

$$\bar{\bar{U}}_i = U_i^n - \frac{\triangle t}{\triangle x}\left(\bar{F}_i - \bar{F}_{i-1}\right) + \triangle t \bar{G}_i \qquad Corrector \tag{5.61}$$

$$U_i^{n+1} = \frac{1}{2}\left(\bar{U}_i + \bar{\bar{U}}_i\right) \tag{5.62}$$

In this formulation the subscript indicate the grid node and the superscript indicates the time step. The objective of the numerical scheme is to calculate the flow field

in the time step $n+1$ as a function of the previous time step. First, the predictor step is calculated ($\bar{U}$). Then, the corrector step ($\bar{\bar{U}}$) is assessed using information from the 'predictor' version of U. Since F and G are function of U (see Equation 5.63), their 'predictor' version ($\bar{F}, \bar{G}$) can be calculated once the prediction of U is available. Finally, the flow field at the next time step is calculated as the average between the 'predictor' and the 'corrector' solutions.

$$\bar{F} = F\left(\bar{U}\right) \qquad \bar{G} = G\left(\bar{U}\right) \tag{5.63}$$

The use of this scheme has shown to provoke high-frequency oscillations generated by discontinuities. To mitigate this errors, it is necessary to introduce some mechanism to damp this phenomenon. This mechanism is based on the addition of dissipative terms proportional to the mesh size and of the same order or higher than the truncation error [52]. This term is known as artificial viscosity.

All the second-order, 3-point central schemes of the Lax-Wendroff family generate oscillations around sharp discontinuities. The method of artificial viscosity was first introduced by Von Newmann and Richtmyer in 1950 to remove the oscillation around discontinuities in second-order schemes. This additional term should simulate the effect of physical viscosity, on the scale of the mesh, locally around the discontinuities and be negligible in smooth regions.

The formulation of the artificial viscosity term is the following [6]:

$$S_i^n = C_x \frac{\left|p_{i+1}^n - 2p_i^n + p_{i-1}^n\right|}{p_{i+1}^n + 2p_i^n + p_{i-1}^n}\left(U_{i+1}^n - 2U_i^n + U_{i-1}^n\right) \tag{5.64}$$

The nature of Equation 5.64 indicates that the artificial viscosity term is a column vector of the same shape than U. The artificial viscosity term has to be added to the numerical scheme. The scheme of MacCormack modified with artificial viscosity results as follows:

$$\bar{U}_i = U_i^n - \frac{\triangle t}{\triangle x}\left(F_{i+1}^n - F_i^n\right) + \triangle t G_i^n + S_i^n \qquad \textit{Predictor} \tag{5.65}$$

$$\bar{\bar{U}}_i = U_i^n - \frac{\triangle t}{\triangle x}\left(\bar{F}_i - \bar{F}_{i-1}\right) + \triangle t \bar{G}_i + \bar{S}_i^n \qquad \textit{Corrector} \tag{5.66}$$

$$U_i^{n+1} = \frac{1}{2}\left(\bar{U}_i + \bar{\bar{U}}_i\right) \tag{5.67}$$

Following the same logic explained in Equation 5.63, the calculation of the 'predictor' version of the artificial viscosity term ($\bar{S}$) can be done once the 'predictor' version of U is available.

The numerical scheme given by Equations 5.65, 5.66 and 5.67 has to be given a value of $\triangle t$ at each time step. The choice of this value is related to the stability of the solution. The governing system of equations is hyperbolic with respect to time. For this kind of problem, the stability criterion introduced by Courant-Friedrichs-Lowry for 1D flows can be used.

$$\triangle t = C\frac{\triangle x}{a+u} \tag{5.68}$$

When the stability analysis is applied to a linear hyperbolic equation being solved with an explicit numerical scheme, the criterion which results is $C \leq 1$, where C is the Courant number. The case that is being solved here is nonlinear and therefore, this criterion can be used only with guidance purposes. In practise, values between 0.8 and 0.9 of Courant number lead to stable behaviour of the solution. The criterion establishes that $\triangle t$ must be less than, or at best equal to, the time it takes a sound wave to move from one grid point to the next. Since the stability criterion depends on the flow properties and the grid size, a different value of $\triangle t$ is obtained for each grid point. The choice is done using the most restrictive value which is the minimum.

$$\triangle t = minimum\left(\triangle t_1^n, \triangle t_2^n, \ldots, \triangle t_i^n, \ldots \triangle t_N^n\right) \tag{5.69}$$

To finalise the implementation of the numerical solver, it is necessary to detail how the boundary conditions are treated numerically. The problem of boundary conditions arises when the numerical scheme established in Equations 5.65, 5.66 and 5.67 is evaluated at the first and the last grid nodes. In the case of the first node, it can be seen that it is necessary to evaluate the vector F in the node -1 during the calculation of the corrector step, this node does not exist in the domain. The equivalent problem arises when evaluating the predictor step at the last node of the grid. It means the the numerical scheme is applicable only from node 1 to n-1 and that the calculation of the properties in first and last grid nodes has to be

carried out by a different method. Besides the necessity from the numerical point of view, the physical meaning of the boundary conditions was stated in the previous subsection. Its implementation must respond to the necessity of information coming from outside into the domain depending on the flow conditions at each boundary.

In general, it is necessary to specify three independent flow variables at the boundaries to define the flow field. There are two ways to give value to these variables, namely, imposing a value based on information from outside the domain (boundary condition) or extrapolating the value from inside the domain. Depending on the number of characteristic lines arriving to the grid node, the number of variables imposed based on outside information would be equal to the number of characteristics coming into the domain while the rest of the variables must be extrapolated from inside. Next, the different cases for boundary condition treatment depending on flow conditions are detailed (only the cases used in this simulation tool are included):

- Subsonic inlet: Two characteristics reach the grid node coming from outside the domain and one characteristic from inside. Therefore, one variable must be extrapolated from the internal flow field and two calculated through the boundary conditions. Several options are possible, J. D. Anderson in his book [6] suggests to extrapolate the axial velocity (u_0). Linear extrapolation is suitable for this purpose. Pressure (p_0) and density (ρ_0) are calculated taken into account that the particle that enters the domain has followed an isentropic evolution from the far field to the inlet and therefore, its total properties remain constant.

- Subsonic outlet: One characteristic reaches the grid node coming from outside, the rest are coming from inside. Therefore, one variable is imposed using information from boundary conditions and two of them are extrapolated. Classically, static pressure (p_N) is imposed to be the static pressure outside since this is the physical discharge condition. Axial velocity (u_N) and density (ρ_N) are extrapolated from inside. The variables are extrapolated using linear extrapolation.

- Supersonic outlet: All three characteristics are coming from inside the domain and therefore, all three independent properties are extrapolated linearly from inside.

The boundary conditions treatment explained above is known as 'physical boundary conditions'. This numerical treatment of boundary conditions allows the perturbation waves to be reflected at the boundaries [52]. This behaviour provokes spurious

solutions since the reflection of perturbation is not a physical phenomenon. In the case of this simulation tool, some dramatic transient phenomena such as the inception of surge in a modern gas turbine provoke perturbation waves which travel over the engine. If the boundary condition treatment allows the reflection of these waves, the solution is characterised by a sort of 'noise' in a range of frequencies similar to the one that would be obtained for something travelling at the speed of sound over the length scale of the engine. This phenomenon has been observed during the development process of this simulation tool. In order to sort this problem out, a second option for the treatment of boundary conditions has been implemented. The software allows the user to choose between 'physical boundary conditions' and 'non-reflective boundary conditions' depending on the nature of the simulation attempted. For example, a simulation run with the purpose of stabilising the steady state operation of the engine at design point will be more accurate if physical boundary conditions are used; nevertheless, a simulation of shaft failure involving compressor surge will need to be run using non-reflective boundary conditions to reduce the spurious noise due to reflection of perturbations.

Non-reflecting boundary conditions express the physical boundary conditions forcing the perturbation generated to disappear. The way to express it mathematically is the following:

$$\frac{\partial w_i}{\partial t} = 0 \tag{5.70}$$

where (w_i) is any of the invariants transported by the characteristic entering the domain. In practise, Equation 5.70 substitutes to the imposition of the properties based on boundary conditions (coming from outside the domain). This technique has been only applied at the inlet of the domain since the choking condition which is always applied at the outlet does not allow any reflection by its nature (all variables are extrapolated from inside). The two options of inlet boundary conditions are subsonic inlet and subsonic outlet (reverse flow). The formulation of non-reflective boundary conditions for these two scenarios is detailed next:

- Subsonic inlet:

$$\triangle w_1 = 0 = \triangle \rho - \frac{\triangle p}{\left(a^n\right)^2} \tag{5.71}$$

$$\triangle w_2 = 0 = \triangle u + \frac{\triangle p}{\rho^n a^n} \tag{5.72}$$

- Subsonic outlet:

$$\triangle w_3 = 0 = \triangle u - \frac{\triangle p}{\rho^n a^n} \tag{5.73}$$

Δ stands for temporal increment and the superscript stand for the time step.

It must be notice that when the information provided by the boundary conditions is substituted by this equations to avoid reflections, the internal flow field has no way to 'see' what is happening outside the domain and therefore, changes in boundary conditions would not be perceived by the system. That is the reason why this boundary conditions treatment should be only used in cases when the fluid problem is dominated by fast transient highly perturbed phenomena and the impact of possible boundary condition changes are negligible from the point of view of the overall solution.

5.2.2 Compressor modelling

This subsection describes the methodology used to model the presence of axial compressors over the MGP. The way to make the fluid feel that the compressor is there is by using the source terms of the Euler equations (Equation 5.54). In particular, the terms used to model the compressor are the axial force (F_x) in the axial momentum equation and the shaft work (SW) in the energy equation.

The calculation of this terms is done following a steady-state approach that is repeated each time step since the forces depends on the state of the fluid. To attempt the calculation of this terms, it has to be taken into account what is the information available for that purpose. The only input used to calculate the action of the compressor is the compressor map. In general, the compressor map gives information of the compressor operation in steady state. For a given operating conditions (non-dimensional mass flow and non-dimensional rotational speed) the map can be read so Pressure Ratio (PR) and Temperature Ratio (TR) can be extracted from them.

Each time step, the state of the flow field is known. With this information the compressor map is read. Known the PR and TR from the compressor map, the inlet conditions are taken from the flow solution as reference, and these values are applied to calculate the fluid properties at the outlet of the compressor which will correspond with this operating point. Then, this mix between real properties (inlet)

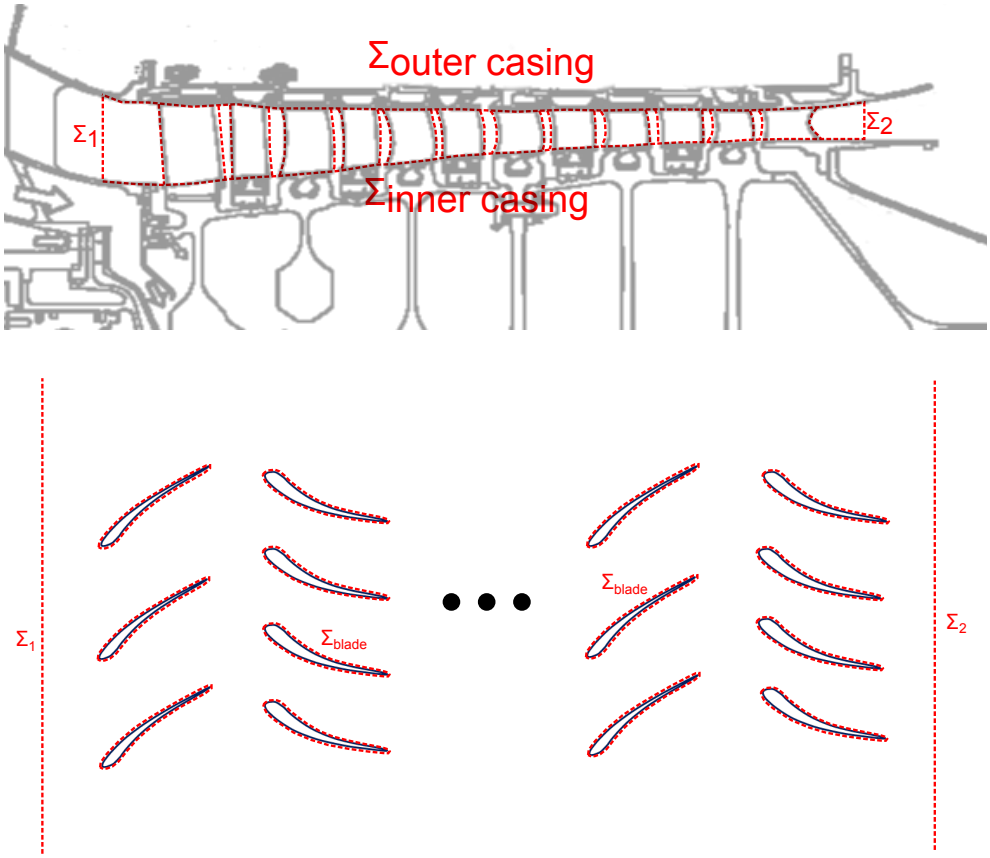

Figure 5.10: Compressor control volume - Calculation of axial force

and theoretical properties (outlet) are used to calculate the axial force and shaft work needed to provoke this change of properties over the length of the compressor. To accomplish this last step of the process the integral forms of the axial momentum equation and the energy equation can be applied to the control volume of the compressor (Figure 5.10). This procedure allows to express the forces applied by the compressor blades as a function of the flow properties at the inlet at the outlet of the domain.

The momentum equation in steady state without body forces applied to the control volume defined by Figure 5.10 takes the following expression:

$$\int_{\Sigma_c(t)} \rho\bar{v}\left(\bar{v}-\bar{v_c}\right)\cdot\vec{n}d\sigma = \int_{\Sigma_c(t)} \left(-p\delta_{ij}+\tau_{ij}^{'}\right)\cdot\vec{n}d\sigma \tag{5.74}$$

Assuming the properties over the inlet (surface Σ_1) and over the outlet (surface Σ_2) are constant over the span and the circumferential direction and knowing that the rest of control surfaces are not penetrated by the fluid, it makes the left-hand side term of Equation 5.74 to be equal to the change in axial momentum. Regarding the

right-hand side of the equation, it is assumed that viscous effect are negligible at inlet and outlet surfaces. The rest of the boundaries of the domain are walls (casing and blades), the integral of the pressure term and the viscous stress term can be accounted as forces.

$$\rho_2 u_2^2 A_2 - \rho_1 u_1^2 A_1 = p_1 A_1 - p_2 A_2 + F_{x_{casing \rightarrow fluid}} + F_{x_{blades \rightarrow fluid}} \tag{5.75}$$

It must be taken into account that the term $F_{x_{casing \rightarrow fluid}}$ is already explicitly accounted in the formulation of the Euler equation and therefore, it must be avoided to account it twice. Therefore, when integrating the Euler equations over a compressor region the source term states as follows:

$$p\frac{dA}{dx} + F_x = \frac{F_{x_{casing \rightarrow fluid}} + F_{x_{blades \rightarrow fluid}}}{x_2 - x_1} = \frac{\rho_2 u_2^2 A_2 - \rho_1 u_1^2 A_1 - p_1 A_1 + p_2 A_2}{x_2 - x_1} \tag{5.76}$$

It is necessary to divide by the compressor length[1] in order to agree with the units of the term in the equations (N/m). Equation 5.76 allows the calculation of the axial force that has to be used to 'force' the system through the source terms in order to get a determined change in flow properties.

Following an equivalent process with the energy equation the expression for the shaft work can be obtained. The work is applied through the rotor blades which are the only surface which is moving. This work is used to increase the enthalpy of the working fluid. The expression to calculate that term is given by Equation 5.77.

$$SW = \frac{\dot{m}\,(h_2 - h_1)}{x_2 - x_1} \tag{5.77}$$

The methodology to calculate compressor blade forces and work presented above is suitable to reproduce most of the cases involving stable and transient operation of the compressor. Nevertheless, this model must be modified to model compressor instability, in particular, the first instants after crossing the surge line. It has been experimentally observed that compressor surge is fundamentally a two-dimensional process. Although previous works have shown that the quasi-1D approach is suitable to predict the overall performance when there is no interest in assessing compressor

[1] x_2 and x_1 are the axial coordinate of the compressor outlet and inlet respectively

instability in detail, it is necessary to add a mathematical apparatus to the force application in order to model the process of stall cell formation at the beginning of the surge event. This process is a two-dimensional phenomenon and therefore, it cannot be modelled by this solver in a 'physical' manner but through a mathematical apparatus which models the 1D effects/consequences of this 2D phenomenon. This stall cell formation process acts by dumping the fall of the compressor operating point into rotating stall. This effect can be simulated by applying a delay in the application of the force. The mathematical apparatus used to impose that is a first order lag given by Equation 5.78.

$$\tau \frac{dF_x}{dt} + F_x = F_{x_{SS}} \tag{5.78}$$

Equation 5.78 is applied only to the force generated by the compressor blades. F_x is the force which is finally applied in the Euler equation, $F_{x_{SS}}$ is the steady-state axial force which is calculated by Equation 5.76 and τ is the time lag constant which following experimental observations [46] takes a value approximately of 3 rotor revolutions. The value of the time constant is variable over the simulation, during normal operation it is given a value of zero which is only changed at the moment of compressor surge.

5.2.3 Combustor modelling

The combustion chamber is modelled by the addition of heat to the working fluid which simulates the fuel combustion process. This is done through the term Q of the energy equation. The fuel injection process increases the mass flow through the engine. This is modelled by means of the bleed terms. The mass flow and the enthalpy added are modelled by the terms W_B and H_B. The pressure losses over the combustor have not been modelled since it is not expected to have an important impact on the terminal speed prediction. Nevertheless, this effect could be added through the term F_x in future versions of CERVANTES.

The evaluation of the heat addition is done following a similar process to the one used in compressor forces. Q is evaluated in steady state by the application of the energy equation to the combustion process as follows:

$$Q = \frac{\eta_{comb} \cdot \dot{m_{f_{burnt}}} \cdot L_{fuel}}{x_2 - x_1} \tag{5.79}$$

The model of combustion efficiency implemented in this first version of CERVANTES is a simple model whose objective is to capture the efficiency reduction due to the extreme off-design values of Fuel Air Ratio (FAR) which are a consequence of the mass flow reduction provoked by the compressor surge. A similar model is applied by the sponsor company to make predictions of TET in case of compressor surge [94]. The model assumes a linear reduction of the combustion efficiency with the FAR. The value of the slop has been adjusted to match the data available for the TET evolution in a real shaft failure event.

Compressor surge, typically present in case of shaft failure, provokes a sudden reduction in the mass flow of air which reaches the combustion chamber. If the fuel flow injected remains constant, it leads to very high values of FAR, far above the stoichiometric value, in the primary zone of the combustor where the combustion reaction takes place. The direct consequence of that is that burning all the fuel injected is not possible. The oxygen contained in the fresh air is the limiting factor for the amount of fuel that can be burnt. A model of fuel burning has been implemented which limits the amount of fuel whose calorific power is released by the combustion. Basically, it assumes that the fuel that can be burnt is the amount which could burn stoichiometrically with the amount of air which enters the primary zone. The model stores the amount of fuel that cannot be burnt in the combustor to allow interturbine burning when more fresh air is injected coming from the SAS. This is a phenomenon which has been observed in other scenarios involving compressor surge [94].

Once the steady-state heat addition has been calculated, the same equation of lag used for the compressor forces in stall has been applied here to dump the reaction of the combustor to fast changes in Q. This method is again used as a mathematical apparatus to simulate some physical principles that have not been implemented in the combustion model, such as changes in the evaporation time.

5.3 Main gas path simulation - The expansion side

In the context of the development of CERVANTES, expansion side is the name used to refer to the part of the MGP which extends from the HPT inlet to the outlet section of the core nozzle. The MGP domain has been split into these two parts in order to simplify the calculation process and make it more efficient in computational terms. The differentiation between compression side and expansion side is possible

thanks to two facts, namely, the HPT NGVs remain choked at any moment, and the volume associated to the combustion chamber is big enough to damp the highest frequencies of the transient behaviour triggered by the compressor surge. As has been explained above in this chapter, the choking conditions in the throat section of the HPT NGVs isolates both sides from the point of view of fluid dynamics, no information can travel upstream a choked section and therefore, no impact on compression side is expected from anything happening in the expansion side. On the other hand, the damping process due to the combustor volume moderates the transient variation of the fluid properties affecting the expansion side and invites to tackle the problem within this region through a quasi-steady approach.

The modelling of the expansion side is based on the calculation of the equilibrium turbine matching each time step. For a given state of the flow at the inlet, a discharge pressure at the outlet of the nozzle and using the information of the turbine maps which are involved in the expansion process, there is a unique distribution of pressure drops at the outlet of each turbine. The methodology takes also into account the change in mass flow over the domain due to the injection of cooling flows into the MGP and the possible heat release due to interturbine burning in cases with FAR over the stoichiometric in the combustor.

5.3.1 Turbine matching solver

Figure 5.11 shows the scheme of the expansion side highlighting the different sections where the flow properties are resolved. The expansion side solver can be understood as an independent program in terms of input/output. This is executed in consonance with the rest of the solvers as it was explained in Section 5.1.

The solver is executed each time step and calculates the equilibrium turbine matching for a given set of input data. The input data are the following:

- Total pressure at HPT inlet (P_{t0}).
- Total temperature at HPT inlet (T_{t0}).
- Mass flow at HPT inlet ($\dot{m}_0$).
- Composition of the flow at HPT inlet: Dry air ($\dot{m_{da}}$), stoichimetric combustion products ($\dot{m_{sp}}$) and unburnt fuel ($\dot{m_{uf}}$).

- Rotational speed of each turbine (N_i).
- Static pressure at the discharge section of the nozzle (p_{out}).
- Mass flow injected in the mixer boxes coming from the SAS ($\dot{m}_{bleeds_j}$).
- Temperature of each flow injected in the mixing boxes coming from the SAS (T_{bleeds_j}).
- Mean line geometry, including blade trailing edge metal angles (β_{TE_k}) and the shape of the mean-line in the meridional plane ($r\,(x)$).
- Incidence angle at the inlet of each turbine ($\hat{i}_i$). In that case, the solution of the flow field in the previous time step is used.
- Turbine maps given by the following expression: $\frac{\dot{m}\sqrt{T_{t_{in}}}}{P_{t_{in}}}, \frac{\tau}{P_{t_{in}}} = f\left(\frac{P_{t_{in}}}{P_{t_{out}}}, \frac{N}{\sqrt{T_{t_{in}}}}, \hat{i}\right)$. In general, the incidence angle is not a variable in the turbine map but, in the case of IPS failure, it is needed to read the LPT map which is affected by distorted inlet flow conditions (see Chapter 7 for more details).

In the nomenclature used above, index i accounts the number of turbine, j accounts the SAS flows connected to the mixing boxes and k accounts for the blade rows.

The objective of this solver is to calculate the complete state of the flow at each section marked with numbers from 0 to 16 in Figure 5.11 including total properties, static properties and velocity triangles. The static properties and the velocity triangles are needed to calculate the axial force acting on the free-running turbine, the incidence angle at the inlet of the LPT whose maps is affected by this variable, and also to be given as boundary conditions to the SAS solver.

The mathematical problem defined here is equivalent to solve a system of non-linear equations. The number of unknowns is equal to the number of turbines. The problem is solved using the Broyden method which is a simplification of the Newton method to find the zero of a function [84]. In order to explain the calculation process, the example of a expansion side consisting of three turbines and a convergent nozzle, as the one represented in Figure 5.11, is going to be used.

The unknowns are the operating points of each turbine which satisfy the equilibrium of the system. These operating points can be given by the value of the total pressure at the outlet of each turbine (P_{t2}, P_{t5}, P_{t14}). To execute the mathematical solver, it is needed to provide it with a first guess of the unknowns. Apart from that, it is

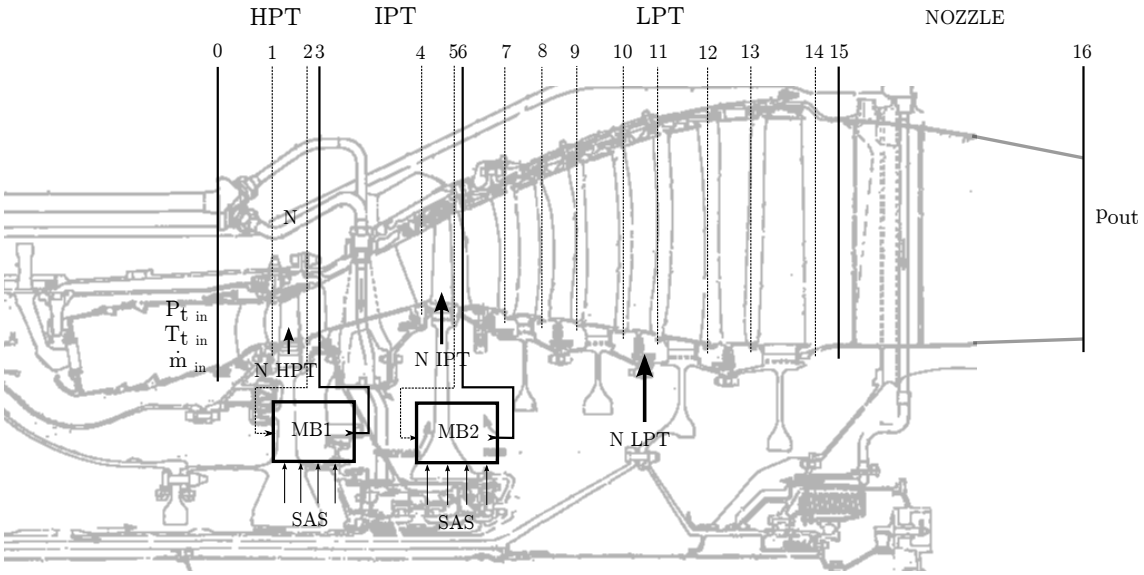

Figure 5.11: Expansion side solver scheme

needed to define the function ($F\{X\}$) which is the vectorial function of error whose zero needs to be found. The calculation process of this function is described next:

- Calculate the PR of the first turbine (HPT): $PR_1 = \frac{P_{t0}}{P_{t2}}$
- Calculate the non-dimensional rotational speed of the first turbine (HPT): $\frac{N_1}{\sqrt{T_{t0}}}$
- Read $\left.\frac{\dot{m}_0\sqrt{T_{t0}}}{P_{t0}}\right|_{map}$ in the turbine map
- Calculate the variable $\left.\frac{\dot{m}_0\sqrt{T_{t0}}}{P_{t0}}\right|_{calculated}$ with the data available
- Calculate the error between these two values: $f_{error_1} = \left.\frac{W_0\sqrt{T_{t0}}}{P_{t0}}\right|_{map} - \left.\frac{W_0\sqrt{T_{t0}}}{P_{t0}}\right|_{calculated}$
- Read the torque map of the turbine to obtain $\frac{\tau}{P_{t0}}$
- Calculate the enthalpy increment ($\triangle h_{0\to 2}$) using the definition of torque: $\tau = \frac{\dot{m}\cdot\triangle h}{\omega}$
- Use the gas model to calculate the total temperature at the outlet of the turbine (T_{t2})
- Assume that the mass flow is constant through the turbine and therefore: $\dot{m}_2 = \dot{m}_0$
- Carry out the mixing box calculation to obtain: $P_{t3}, T_{t3}, \dot{m}_3$ (the calculation process of the mixing box is explained in detail in Section 5.3.2)

At this point, the information needed at the inlet of the next turbine is available and therefore, the process can start again from the first point. The process is repeated as many times as turbines are in the system. At the end of this process, the flow properties at the inlet of the nozzle are available and the values of the error function f_{error_2} and f_{error_3} have been calculated.

The nozzle model assumes that the total properties are constant and therefore the total properties at the discharge section can be calculated. Then, it can be checked if the nozzle is choked or adapted by means of the following equation:

$$if \quad \frac{P_{t16}}{p_{out}} > \left(1 + \frac{\gamma - 1}{2}\right)^{\frac{\gamma}{\gamma - 1}} \quad \rightarrow \quad choked \tag{5.80}$$

In case the nozzle is choked, the value of the Mach number at the discharge section is 1. In case the nozzle is adapted, the value of the static pressure at the discharge section is equal to the discharge static pressure (p_{out}). In any case, the rest of the properties in the section can be calculated applying the definitions of stagnation properties. Taking into account that the area of the nozzle is known, the mass flow ($\dot{m}_{16}$) can be calculated. Since the mass flow at the inlet of the nozzle ($\dot{m}_{15}$) is known and it must be constant, the nozzle is providing the last term of the error equation:

$$f_{error_4} = \dot{m}_{16} - \dot{m}_{15} \tag{5.81}$$

Apparently, the number of components of the error (f_{error}) vector is higher than the number of unknowns which would mean that there is an extra equation. It must be noted that the first value of error calculated for the non-dimensional mass flow of the HPT cannot be used because it conflicts with the assumption of choking conditions at this turbine. This value of error will always be nil due to this assumption and therefore can be eliminated from the vector which now has the same number of values than unknowns.

Finally, the Broyden method used to solve the system of equation can be formulated as follows.

$$F \begin{Bmatrix} P_{t2} \\ P_{t5} \\ P_{t14} \end{Bmatrix} = \begin{Bmatrix} f_{error_2} \\ f_{error_3} \\ f_{error_4} \end{Bmatrix} \tag{5.82}$$

The function F is given by the calculation process described above. The Broyden method allows iterating in $\{X\}$ starting from the initial guess until the zero of the function is found. The algorithm of iteration is the following:

For $k = 0, 1, 2, ...$

$$B^k \cdot H^k = -F\left\{X^k\right\} \tag{5.83}$$

$$X^{k+1} = X^k + H^k \tag{5.84}$$

$$B^{k+1} = B^k + \frac{F\left\{X^{k+1}\right\} \cdot H^{k^T}}{\langle H^k, H^k \rangle} \tag{5.85}$$

At the first iteration, the vector $\{X^0\}$ is given by the first guess and the matrix B^0 is calculated as the Jacobian of the function F around the point $\{X^0\}$. Then, H^k is calculated by solving the linear system of equations given by Equation 5.83. Once H^k is known, the next iteration for $\{X\}$ can be calculated. Finally, the method proposes a formula to calculate the subsequent values of the matrix B which avoid the calculation of the Jacobian at each iteration as it is needed in the Newton method [84].

This method allows calculating the equilibrium solution of the expansion side in few iterations using the previous time step solution as initial guess. Once the matching problem has been converged, some simple assumptions are used to resolve the different section over the turbine. It is assumed that the total properties are constant over the NGVs and the multi-stage turbines are assumed to have equal expansion ratio for all the stages. Finally, the resolution of the velocity triangles allows calculating the velocity components and therefore, the static properties.

5.3.2 Mixing box solver

The objective of the concept 'mixing box' is to simulate the injection of cooling flows into the MGP and to allow the combustion of unburnt fuel when new fresh air is injected. The mixing boxes have been situated at the outlet of each turbine. The main consequence of that is that the flow injected through the turbine does not contribute to the power extraction which is common practise in the industry [86].

The approach used to solve that problem is the application of the first principle of thermodynamics to an open system and the mass conservation equation. The formulation is the following:

$$\dot{m}_{out_{MGP}} = \dot{m}_{in_{MGP}} + \sum_i \dot{m}_i - \sum_j \dot{m}_j \tag{5.86}$$

$$\dot{m}_{out_{MGP}} \cdot h\left(T_{out_{MGP}}\right) = \dot{m}_{in_{MGP}} \cdot h\left(T_{in_{MPG}}\right) + \sum_i \dot{m}_i \cdot h\left(T_i\right) - \sum_j \dot{m}_j \cdot h\left(T_{in_{MGP}}\right) + Q \tag{5.87}$$

Where Q is the heat released by any possible combustion of unburnt fuel.

$$Q = \eta_{comb} \cdot \dot{m}_f \cdot L \tag{5.88}$$

Here, in Equation 5.88, η_{comb} is a low value of combustion efficiency that can be adjusted using experimental values. The amount of fuel that burns at each mixing box ($\dot{m}_f$) is calculated taking into account the available amount of unburnt fuel and fresh air. In Equation 5.87, the right-hand side can be evaluated once the combustion heat is known. Since $\dot{m}_{out_{MGP}}$ can be calculated through Equation 5.86, the enthalpy of the flow leaving the mixing box can be calculated and, finally, the gas model can be used to calculate the total temperature of this gas. Regarding the total pressure, it is assumed that the mixing and possible burning process conserve the total pressure in the MGP. Therefore, all the needed information about the section at the inlet of the next turbine is known.

5.4 Secondary air system

The major part of the working fluid that is breathed by a gas turbine follows completely the main gas path through the engine and, thermodynamically, is involved in all the processes that constitute the Bryton cycle. Nevertheless, there is a non-negligible fraction of this flow that participates only partially in the process of thrust production. Flow is bled at different stations along the engine to be used in a set of complementary purposes which guarantee the integrity and the proper operation of the gas turbine. This bled flow is conducted through a system of cavities and

pipes controlled by restrictors as seals and a variety of holes. This network is known as Secondary Air System (SAS). The SAS plays several roles of importance for the operation of the engine, both for safety and performance reasons. Those functions are the following [19]:

- Deliver air to the turbine for blade cooling purpose
- Internal engine and accessory unit cooling
- Control of axial pressure loading on the bearings
- Prevention of hot gas ingestion into the turbine disc cavities
- Isolation of the oil system
- Control of the turbine blade tip clearances
- Engine anti-icing
- Air supply for the aircraft services

The air that flows through the SAS is bled mainly from different stages along the compression system depending on the purpose. Most of this air is injected back to the main flow at different stages of the turbine after being used for cooling or sealing purposes. The total amount of air bled can reach the 20% of the working fluid, being the most important the bleeding point at the outlet of the HPC to cool the HPT. It gives an idea of the importance of simulating the SAS on the prediction of overall engine performance. For example, the calculation of the TET, which is a consequence of the equilibrium in the energy equation applied to the combustion chamber, is highly dependent of the amount of air that bypasses the combustor to be used in the HPT cooling process.

Beside the necessity of including the SAS as part of any gas turbine simulation tool to achieve the accuracy aimed in performance prediction, the capability to predict the flow properties evolution over the SAS network is of paramount importance in most of the shaft failure events due to a different reason. As was explained in Chapter 1, depending on the breakage point location, a shaft failure can release the turbine rotor from its axial location allowing its rearward movement due to the pressure gradient direction across the turbine. In this case, the free-running turbine disc impacts against the rearward static structure. The direct consequence of this phenomenon is a negative torque component which helps to limit the terminal speed

of the turbine. This toque component is calculated by CERVANTES through the turbine friction and blade tangling models developed by Aleixo Gonzalez [44]. The friction torque depends on the axial force acting on the disc which has two main components, namely, the force provoked by the pressure gradient through the blades and the resultant of the pressure forces acting on the disc because it is immersed in the SAS. Furthermore, the rearward movement of the released disc provokes the closure of the major port of the LPT cavity leading to a pressure increment in this cavity which has negative consequences since it reduces the axial load and consequently the friction torque.

In the previous paragraphs, the necessity to model the dynamics of the flow over the SAS has been established. To accomplish this necessity, a simulation tool has been developed following a fully-transient approach which allows predicting the reaction of the flow within the SAS to high frequency changes in the boundary conditions (flow properties over the MGP). The tool is able to capture any unsteady phenomena involved in the shaft failure event as the time lag associated to the charge and discharge process of big volumes and the flow inertia effects in long pipes.

5.4.1 Methodology

The development of a simulation tool to predict the transient behaviour of the SAS of a gas turbine in the context of the shaft over-speed analysis is a project which starts with the PhD. Thesis of Luis Gallar [38] and which has had a continuation and its end as part of the present doctoral research. The initial objective was the development of a robust and flexible tool to predict the SAS dynamics of any possible network geometry. The baseline of the methodology was developed by Gallar and Calcagni [38, 13]. The methodology assumes that any SAS geometry can be simplified and represented by a network composed of cavities, pipes and convergent nozzles.

The cavities were initially modelled as constant volume chambers with an arbitrary number of orifices through which the flow may enter or exit. These orifices are considered as convergent nozzles characterised by its minimum area. It can be demonstrated [38] that during the combined process of charge / discharge of the cavity the thermodynamic properties are constant in the volume so the continuity and energy equations can be applied in their integral form. The evolution of the flow properties inside the cavities is given by Equations 5.89 and 5.90.

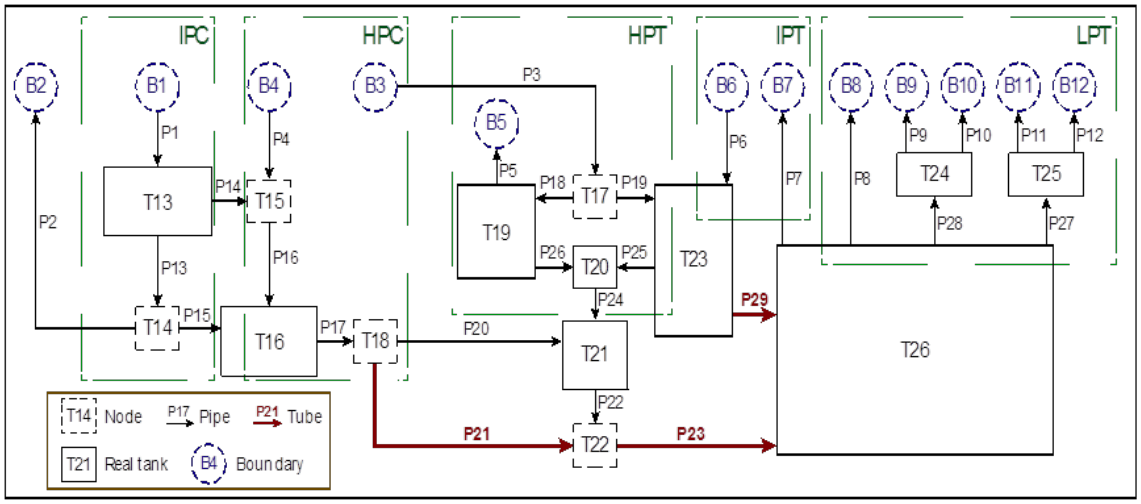

Figure 5.12: Simplified SAS network of the Engine A

$$\rho^{n+1} = \rho^n + \frac{\triangle t}{V}\left(\sum_{l=1}^{M} \dot{m}_{o,l}^n - \sum_{r=1}^{N} \dot{m}_{i,r}^n\right) \tag{5.89}$$

$$p^{n+1} = p^n + \frac{\triangle t}{V}\left((\gamma-1)\sum_{r=1}^{N} \dot{m}_{i,r}^n h_{i,r} - \gamma \sum_{l=1}^{M} \dot{m}_{o,l}^n \frac{p^n}{\rho^n}\right) \tag{5.90}$$

The flow through the pipes is analysed under the following assumptions: one-dimensional, perfect gas, inviscid flow, heat transfer negligible, unsteady flow, buoyancy forces negligible, no chemical reactions and the tube is not moving. As a consequence, the Navier-Stokes equations can be reduced to the Euler equations, the same set of equations that has been used for the simulation of the MGP. The numerical solver applied to integrate these equations is a Roe's approximate upwind Riemann solver [38].

The models developed to simulate the cavities and pipes were validated separately by comparing their results against experimental measurements. Afterwards, the network assembly process was designed. The coupling of the different components is achieved by means of boundary conditions which represent the interaction of a tube with the neighbouring cavities.

The state of the project regarding the SAS gas dynamics modelling at the beginning of the present doctoral research has been established above. The most important weaknesses of this simulation tool were identified to be the lack of a heat transfer model in the cavities and the lack of pressure losses model along the pipes.

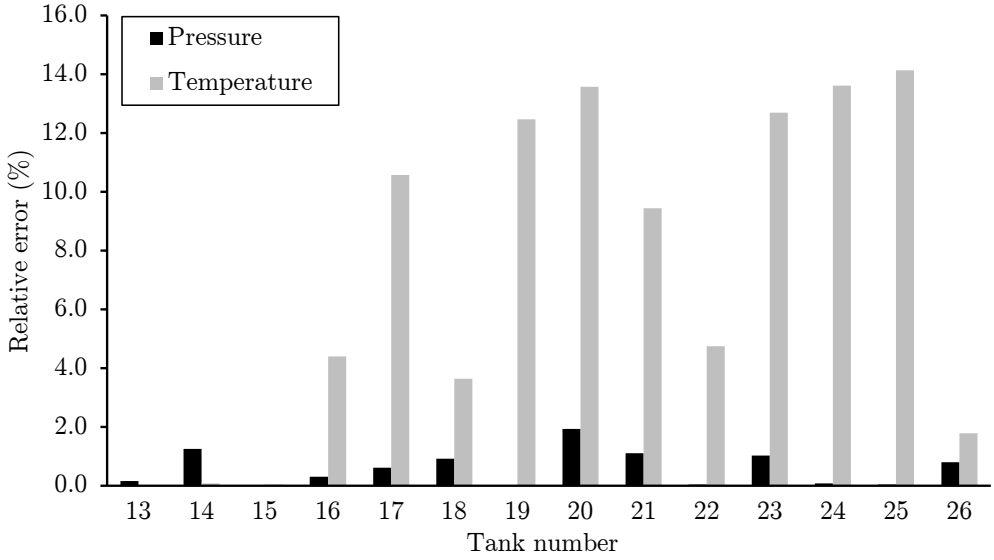

Figure 5.13: Errors in cavity properties before heat transfer model - SAS solver vs SPAN (sponsor's solver)

Heat transfer effects in the cavities had been considered negligible in the past attending to the characteristic time of the shaft over-speed event being much lower than the time needed by any heat transfer phenomena to take place. Although this premise is true, the simulator needs to converge to an initial stable point before the transient simulation starts. The sponsor's proprietary code SPAN has been used to carry out a first try to validate the SAS simulator developed at Cranfield. The results showed an important mismatch in terms of cavity temperature that stated the necessity to add heat transfer capability to the solver in order to match properly the initial stable point inherent to any transient simulation [93].

On the other hand, the flow in pipes was modelled by means of the Euler equations which assume no losses along the tubes. Nevertheless, the first estimation of the losses provoked by turbulence shown that those can reach the 5% and motivated the study which is included in the next section [15, 7].

5.4.2 Pressure losses in pipes

The inter-shaft gap flowfield and pressure losses mechanism

This study focuses on the flow through the most important pipe within the SAS, namely, the intershaft gap. The flow bled in the compression side is conducted through the space between the LPS and the IPS towards the turbines side. The flow

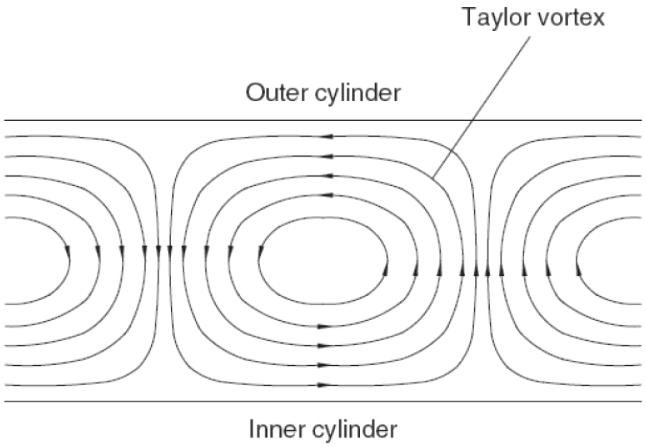

Figure 5.14: Taylor vortices [20]

between rotating cylinders is difficult to study due to the vorticity introduced by the rotational speed of the walls. Viscous and turbulent effects increase the range of situations that can be encountered. The combined action of these factors can cause even the apparition of instabilities within the flow called Taylor instabilities [20].

Taylor studied that phenomenon in 1923 [95]. The onset of these instabilities can be expressed using the Taylor number (Ta). If it is assumed that the annular gap is small in comparison to the mean radius, the critical Taylor number is found to be equal to 41.19 [20]. Many experiments have proven the validity of Taylor's instability criterion, like those carried out by Donnelly and Fultz [32].

$$Ta_m = \frac{\omega R_m^{0.5} \left(R_0 - R_i\right)^{1.5}}{\nu} \tag{5.91}$$

A simplified analysis of the likeliness of Taylor vortices during the post-failure transient has been carried out using data obtained from the previous version of the code [66]. Results yield that Taylor instabilities are very unlikely. It has be observed that the critical Taylor number is many orders of magnitude higher than its counterpart the most of the time, which means that the apparition of Taylor vortices is extremely unlikely [15].

The next step, once the possibility of an unstable flow has been discarded, is the analysis of the different phenomena that can provoke pressure losses. These pressure losses can be provoked by viscosity and turbulence. The high Reynolds number in this kind of flows yields to state that the flow is dominated by turbulence and that the viscosity effect are confined within a boundary layer whose thickness is negligible

in comparison with the diameter of the tube. The critical Reynolds number in a tube lies around 3000 [64].

The Darcy-Weisbach equation is commonly used to predict the pressure losses due to friction in tubes with circular section. This equation is valid either for laminar or turbulent incompressible flow. The equation can be modified to be adapted to tubes of non-circular section by using the hydraulic diameter of the duct in place of the conventional diameter.

$$\triangle p = -\frac{1}{2}\rho u^2 \frac{L}{D_h}\Lambda \tag{5.92}$$

$$D_h = \frac{4A}{Pm} = \frac{4 \cdot 0.25\pi \left(D_0^2 - D_i^2\right)}{\pi \left(D_0 + D_i\right)} = D_0 - D_i \tag{5.93}$$

The Darcy friction factor can be calculated by different expressions depending on the nature of the flow.

The value of the Darcy friction factor in a laminar flow is

$$\Lambda = \frac{64}{Re} \tag{5.94}$$

whereas in a turbulent flow it is given by the following expression:

$$\frac{1}{\Lambda} = 2\lg\left(Re\sqrt{\Lambda}\right) - 0.8 \tag{5.95}$$

An alternative and more useful way of expressing Λ in a turbulent flow was deduced empirically by Nikuradse [64]:

$$\Lambda = 0.0032 + \frac{0.221}{Re^{0.237}} \tag{5.96}$$

The implementation of pressure losses model

The objective of this part of the project was to enhance the tube resolution scheme by adding a pressure loss model. This required the modification of the original system of Euler equations by adding an external force.

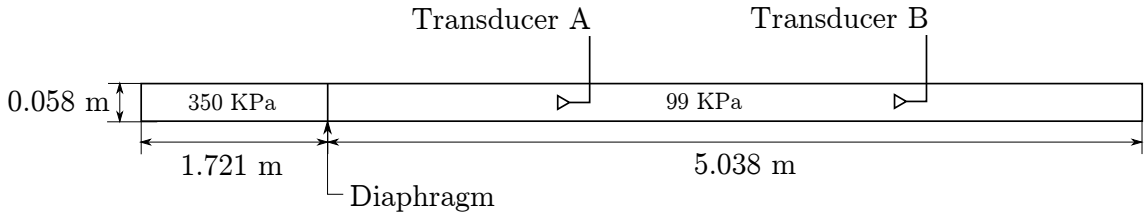

Figure 5.15: Shock tube experiment

The source term can be used to take into account any possible external interaction with the fluid. In that case, only the term of axial force which modifies the momentum equation in the axial direction was added. The model of losses implemented was based on the Darcy-Weisbach equation and the friction factor correlation by Nikuradse given by Equation 5.96. Since the formulation here was given by its differential version, it was necessary to apply the integral form of the momentum equation to a differential of length and impose the pressure loss given by Equation 5.92 to calculate the value of the force per unit of length that has to be applied to provoke such a pressure gradient.

The modification operated in the code implied the necessity of validation, not only to check that the capability to reproduce the physics had not been altered, but to evaluate the improvement in the prediction of experimental results gained by this enhancement of the methodology. In order to make possible the comparison with previous results, the same experimental test used by Gallar [38] in the validation of the first version of the code has been used. This is the shock tube experiment carried out by Felling et al. [37]. Figure 5.15 illustrate the shock tube layout. It essentially consists of a tube of circular cross-section filled with air and closed in both ends. The tube has a diaphragm which splits the tube in two zones. The driver section has a higher static pressure than the driven one. Both sections are in stagnation conditions initially. When the experiment begins, the diaphragm will be suddenly removed and both sections will start to mix by the action of shock and expansion waves. Measurement of static pressure is taken in two sections indicated as section A and section B in Figure 5.15.

The static pressure evolution in station B is shown in Figure 5.16. Although the curve with friction is closer to the experimental one, there is a discrepancy in the first pressure rise. The experimental measurement never reached the level of pressure predicted by the simulator. This is commonly attributed to three-dimensional effects provoked by the diaphragm removal process [31] that cannot be expected to be captured by a 1D model. After the first instants, these effects disappear and the

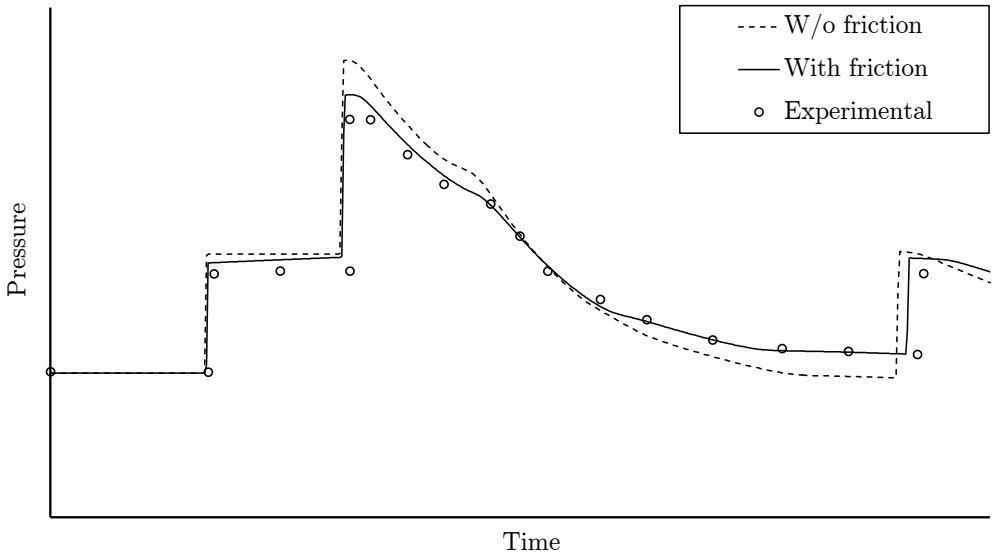

Figure 5.16: Friction model validation

one-dimensional behaviour remains. This would explain why the rest of the static pressure values are being correctly predicted.

In conclusion, the 1D model of the flow in pipes implemented in the SAS simulation tool was enhanced by adding a model of turbulent pressure losses. The validation process showed that the new model allows a more accurate prediction of the reality and therefore, one of the weaknesses of the previous model was superseded. This level of accuracy is considered to be suitable for the final purpose of the SAS simulation tool.

5.4.3 Heat transfer in cavities

The effect of heat transfer on the evolution of the thermodynamic properties inside the cavities of the SAS was neglected during the first stage of the development of this simulation tool. The characteristic time of the shaft failure event is small enough to support this assumption [38]. Nevertheless, the accuracy of the prediction of the SAS dynamics during this fast transient event is compromised when the initial operating point is not captured with the same accuracy. The first try to validate this simulation tool showed a mismatch in tank temperature prediction when a steady operating point is simulated (see Figure 5.13). The simulation tool is based on a fully transient approach and therefore, the stabilisation of a particular operating point requires running a transient simulation with fixed boundary conditions until the solution does not show any sign of transient behaviour. It means that the reason

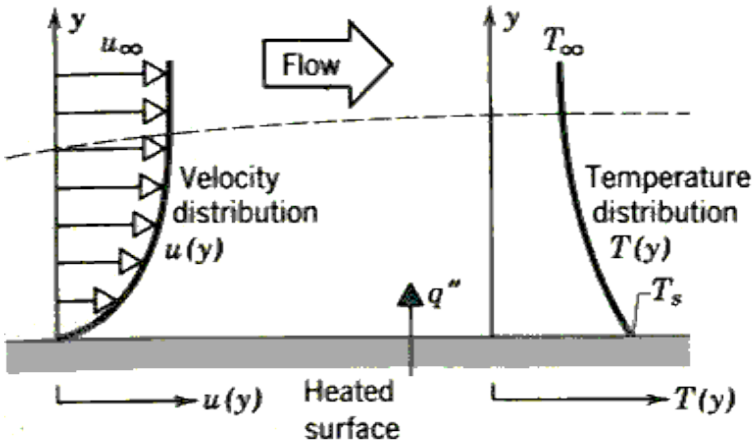

Figure 5.17: Thermal boundary layer [57]

to neglect the heat transfer effect is not valid any more, since the simulation time to stabilise the solution is, by definition, as long as necessary. In conclusion, the enhancement of this simulation software by adding heat transfer effect on the cavity model is necessary to reach the desired accuracy in the prediction of the initial stable point which will influence the later transient simulation.

The cavities of the SAS are characterised by rotating walls so it is going to provoke that the main heat transfer phenomena involved is the convection. The convection heat transfer mode comprises of two mechanisms: the energy transport by the random motion of molecules (diffusion) and bulk motion of the fluid [57]. It is possible to distinguish two types of convection heat transfer, according to the nature of the flow. Forced convection occurs when the fluid motion is generated by some external means while free or natural convection takes place when the flow movement is caused by the density differences due to temperature gradients. In the basic forced convection process, the fluid is moving over an isothermal flat plate at a different temperature. The fluid adjacent to the wall forms a region called thermal boundary layer in which the temperature varies from T_s at y = 0 and T_∞ in the outer of the flow (see Figure 5.17).

The convective heat flux is modelled with a Newtonian law. It is directly proportional to the overall temperature gradient through the heat transfer coefficient (h) (see Equation 5.97). In this coefficient is included everything that affects the convection process. Any study of convection ultimately reduces to a study of the means by which h may be determined [57]. On the other hand, if the Fourier's law of conduction is applied to the region of contact between the fluid and the solid

where there is not relative velocity due to the fluid viscosity (see Equation 5.98), a relation between convective and conductive heat transfer can be established and ultimately, the dimensional analysis of this equation allows defining the Nusselt (Nu) number. In the study of forced convection for particular geometries and flow configuration, the Nusselt number is usually correlated as a function of Reynold and Prandtl numbers. Therefore, the approach followed in the present section consists in the characterisation of each convection heat transfer phenomenon within the SAS by means of its Nusselt number correlation.

$$q = h\left(T_s - T_\infty\right) \tag{5.97}$$

$$q = -k_f \left.\frac{\partial T}{\partial y}\right|_{y=0} \tag{5.98}$$

$$Nu = \frac{h\delta_T}{k_f} \tag{5.99}$$

The analysis of the heat transfer with the SAS network involves two main types of convection, namely, convection within rotating cavities and the internal cooling of the NGVs. Beside these heat transfer mechanism, the temperature in a cavity may also rise due to a phenomena called 'frictional heating' that is also analysed in the present section. The analysis of the rotating cavities is subdivided into three particular cases:

- Convection heat transfer in a rotating cavity with axial throughflow of air
- Convection heat transfer in a rotor-stator system
- Convection heat transfer in a rotating cavity

The present list of heat transfer phenomena is general enough to allow the modelling of a wide range of SAS architectures. Figure 5.18 shows the layout of the SAS of one of the engines of the sponsor. This particular case will be used to illustrate practical examples of the heat transfer phenomena listed above.

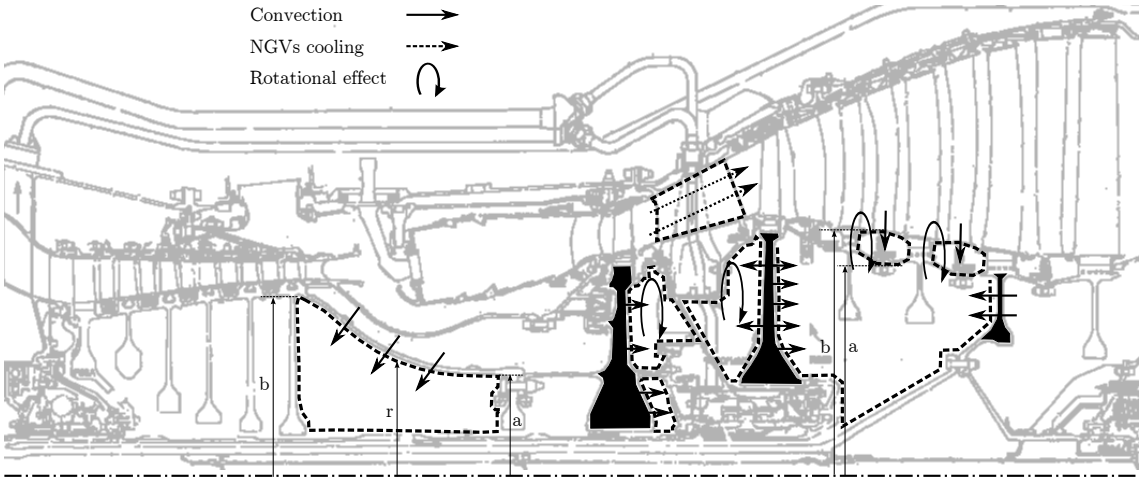

Figure 5.18: Heat transfer effect in the SAS - Scheme

Convection heat transfer in a rotating cavity with axial throughflow - The HPC cavity

The HPC cavity can be seen in Figure 5.18, this may be considered as the combination of six rotating cavities with an axial throughflow of air. An in-depth study of the heat transfer phenomena occurring in the HPC cavity was carried out by Alexiou [5]. The experimental facility used is a scaled reproduction of this particular sort of cavity. Furthermore, the walls had rotation capacity and were heated in the same manner as in the real scenario. The special arrangement of the test guarantees that the Nusselt number correlations derived are suitable to the purpose of this simulation tool.

Experimental findings pointed out that the heat transfer from both the discs and the inner shrouds are governed by the mechanism of free convection. Alexiou [5] estimated the maximum temperature difference between the inlet of HPC cavity (i.e. upstream of the discs) and the disc-cone cavity (i.e. downstream of the discs) to be less than 2 K. Even though in a real engine there are more discs than in the test rig, the disc and shroud heat transfer is still expected to be of secondary importance and therefore, it is going to be neglected in the present study. The most important contribution to heat transfer within this sort of cavity occurs through the conical surface which separates the HPC cavity from the combustor region.

The experimental results indicate that the heat transfer from the inner surface of the cone is affected by two different regimes of flow. The Rossby number is defined to quantify the importance of the axial throughflow ($\bar{u}$) against the effect of rotation:

$$Ro = \frac{\bar{u}}{\omega a} \tag{5.100}$$

The measured local Nusselt number is correlated by equation 5.101 for Ro $<$ 3.5 and by Equation 5.102 for Ro $>$ 3.5.

$$Nu\,(r) = 0.0243 \cdot Re_z^{0.086} \cdot \left(\frac{Re_\phi^2\,(T_s - T_{in})}{T_{in}}\right)^{0.326} \left(\frac{r}{b}\right)^{-1.89} \left(\frac{r}{b} - 1\right)^{-0.022} \tag{5.101}$$

$$Nu\,(r) = 8.936 \cdot 10^{-5} \cdot Re_z^{1.301} \cdot \left(\frac{r}{b}\right)^{-3.523} \tag{5.102}$$

The definitions of the different Reynolds number that appear in the last expressions are the following:

$$Re_\phi = \frac{\omega b^2 \rho_{in}}{\mu_{in} \sin\theta} \qquad and \qquad Re_z = \frac{\dot{m}_{in} D_h \rho_{in}}{\mu_{in}} \tag{5.103}$$

The hydraulic diameter is defined as follows:

$$D_h = 2\,(a - r_{shaft}) \tag{5.104}$$

In order to implement the overall effect of convection heat transfer from the inner surface of the cone, an average Nusselt number is required. For the purpose of the present study and by the shake of simplicity, it has been decided to evaluate the Nusselt number using the area weighted average radius:

$$\bar{r} = \frac{\int_a^b r A dA}{\int_a^b A dA} = \frac{4\,(b^5 - a^5)}{5\,(b^4 - a^4)} \tag{5.105}$$

Convection heat transfer in a rotor-stator system

Poncet and Schiestel [82] modelled the flow structure and the heat transfer phenomena in a high-speed rotor-stator cavity. The study focused on correlating the Nusselt number as a function of the mass flow going through the cavity (C_ω), the rotational

Reynolds number (Re_ϕ) and the Prandtl number (Pr). The numerical predictions were validated against experimental results, and for engineering applications the authors proposed the following empirical correlation:

$$\bar{Nu} = 0.0044 \cdot Re_\phi^{0.8} \left(1000 + C_\omega\right)^{0.11} Pr^{0.5} \tag{5.106}$$

$$C_\omega = \frac{\dot{m}_{in}}{\mu b} \tag{5.107}$$

Valid within the range:

$$5 \cdot 10^{-5} < Re_\phi < 1.44 \cdot 10^{-6} \qquad 0 < C_\omega < 12082 \qquad 1 < Pr < 12$$

Convection heat transfer in a rotating cavity

Owen and Onur [78] correlated experimental results for the Nusselt number on the heated disc for an asymmetrically heated cavity. Four different regimes of heat transfer were identified depending on the Reynolds number associated with rotation (Re_ϕ) and the Grashof (Gr) number defined as follows:

$$Gr = \frac{\rho^2 \left(T_s - T_{in}\right)_{max} \omega^2 b^4}{T_{in} \mu_{in}^2} \tag{5.108}$$

The tangential Reynolds number determines the flow pattern due to the rotation of the walls while the Grashof number determines when the heat transfer by free convection mechanisms provoked by the different temperature of opposite walls is dominant. In gas turbines, the typical rotational speed of the cavities generates a buoyancy-induced chaotic flow pattern but it is not high enough to make the free convection mechanism dominant. The evaluation of these parameters allows selecting the next Nusselt number correlation:

$$\bar{Nu} = 4.11 \cdot Gr^{\frac{1}{9}} C_\omega^{\frac{1}{2}} Re_\phi^{\frac{1}{9}} \tag{5.109}$$

In the LPT cavity of a real engine, both the IPT and LPT discs are heated and rotating at different speeds. In order to quantify the overall rate of heat transfer on

the basis of the experimental correlation shows in Equation 5.109, further approximation are required. First of all, it is assumed that the aforementioned expression for the Nusselt number could be applied to both discs. Since the Nusselt number depends on Re_ϕ, it is required a value for the rotational speed that represents the entire cavity. The area averaged rotational speed is taken. Secondly, the overall rate of heat transfer for a rotating cavity with superimposed flow depends on the temperature difference between the walls and the inlet fluid. The average temperature between the two discs is assumed as surface temperature.

Frictional heating

The typical flow pattern in a shrouded rotating cavity is characterised by the boundary layers on the walls and a central core of rotating fluid that has zero radial velocity. A boundary layer separation from the walls would affect the radial distribution of the rotational velocity of the core. However, at high rotational speeds, for $Re_\phi > 10^{-5}$, the transition point is very close to the peripheral shroud and thus the core velocity would be unaffected. This is the case in real engines.

The flow experiences a temperature rise because of the total windage: the centrifugation of the fluid causes frictional heating, whose effect must be quantified and included in the energy balance of the cavity. Owen and Rogers [79] expressed this effect as a temperature increment following the next expression:

$$T_{ad} = T_{in} + \triangle T_{frict} = T_{in} + R\frac{\omega^2 r^2}{2C_p}(1-\beta)^2 \tag{5.110}$$

The 'recovery factor' (R) and the 'core swirl ratio' (β) are defined as follows:

$$R = Pr^{\frac{1}{3}} \qquad and \qquad \beta = \frac{v_{\phi_{core}}}{\omega r} \tag{5.111}$$

Equation 5.112 is an experimental correlation which can be used to estimate the core swirl ratio for an unsealed cavity (β) as a function of the core swirl ratio for a sealed cavity (β^*) and the turbulent flow parameter (λ_{turb}) which is a function of the non-dimensional mass flow rate and the rotational Reynolds number. The core swirl ratio for a sealed cavity was calculated by Owen and Rogers [79] who obtained a value of 0.431.

$$\beta = \beta^* \left(1 + 12.74 \cdot \frac{\lambda_{turb}}{\left(\frac{r}{b}\right)^{\frac{13}{5}}} \right)^{-1} \tag{5.112}$$

$$\lambda_{turb} = C_\omega Re_\phi^{\frac{-4}{5}} \ , \ where \quad C_\omega = \frac{\dot{m}_{in}}{\mu b} \tag{5.113}$$

Equation 5.112 expresses β as a function of the radius, therefore it is required to consider an average value. Since the relation between β and the radius is linear, the arithmetic mean value can be taken to calculate the average core swirl ratio. On the other hand, the expression for the temperature increment due to frictional heating is also a function of radius. In order to assess the overall temperature rise due to this effect, a radially averaged value is calculated.

$$\overline{\triangle T}_{fricct} = \frac{\int_a^b \triangle T_{fricct} \cdot r dr}{\int_a^b r dr} = R\frac{\omega^2}{4C_p}\left(1-\beta\right)^2\left(b^2+a^2\right) \tag{5.114}$$

Then, it is easy to verify that the radially averaged enthalpy ($\bar{H}$) to be inserted in the energy equation is represented by:

$$\bar{H} = \dot{m}_{in} R\frac{\omega^2}{4}\left(1-\beta\right)^2\left(b^2+a^2\right) \tag{5.115}$$

Heat transfer due to NGVs internal cooling

The layout of the SAS of the sponsor's engines includes the cooling of the IPT NGV using the air that is bled at the HPC. This flow is conducted through the NGV, which is hollow, in its way from the bleeding point to the cavity between the HPT and the IPT.

This cooling process can be understood to be composed of two different heat transfer processes, namely, the heat transfer from the main gas path to the blade metal and the heat transfer from the blade metal to the coolant flow. The later is the one involved in the SAS analysis, being an energy input. The expression to calculate this flux is the following:

$$\bar{q} = St \cdot \rho \cdot U \left(T_b - T_{c_1}\right) A \tag{5.116}$$

Where T_{c_1} is the temperature of the cooling flow at the inlet of the vane, T_b is the metal temperature of the vane, U is the velocity of the cooling flow inside the vane and A is the wet surface.

The Stanton number (St) is the non-dimensional parameter involved in the cooling process and measures the heat that is actually transferred to the coolant mass flow with respect to the thermal capacity of the fluid. Subscript d is used here to refer to the characteristic length of the ducts used by the cooling flows to cross the NGV.

$$St = \frac{\bar{h}_c}{\rho U C_p} = \frac{\overline{Nu}_d}{Re_d Pr} \tag{5.117}$$

The Nusselt number involved here controls the heat transfer process within the internal duct of the NGV and its correlation can be found in [90].

$$\overline{Nu}_d = 0.013 \cdot Re_d^{0.8} \quad where \quad Re_d = \frac{\rho U d}{\mu} \quad and \quad d = 4\frac{A_c}{Pm_c} \tag{5.118}$$

Besides the calculation of the Stanton number, the metal temperature of the blade is also needed to calculate the heat flux. This unknown can be calculated by imposing the energy equation between the heat transferred from the main gas path to the blade and the equivalent from the metal to the coolant flow. The calculation process is straightforward once the Nusselt number correlation for the former is known.

$$\overline{Nu}_g = 0.25 \cdot Re_g^{0.65} \tag{5.119}$$

$$Re_g = \frac{\rho_g U_g C}{\mu} \tag{5.120}$$

$\overline{Nu_g}$ is the Nusselt number of the process of heat transfer between the MGP flow and the vane metal, Re_g is the Reynolds number of the MGP flow based on relative velocity to the vane (U_g) and the chord (C).

Heat transfer model implementation and verification

The heat transfer modelling that has been presented here points out that five different strategies need to be adopted depending on the sort of cavity considered: HPC

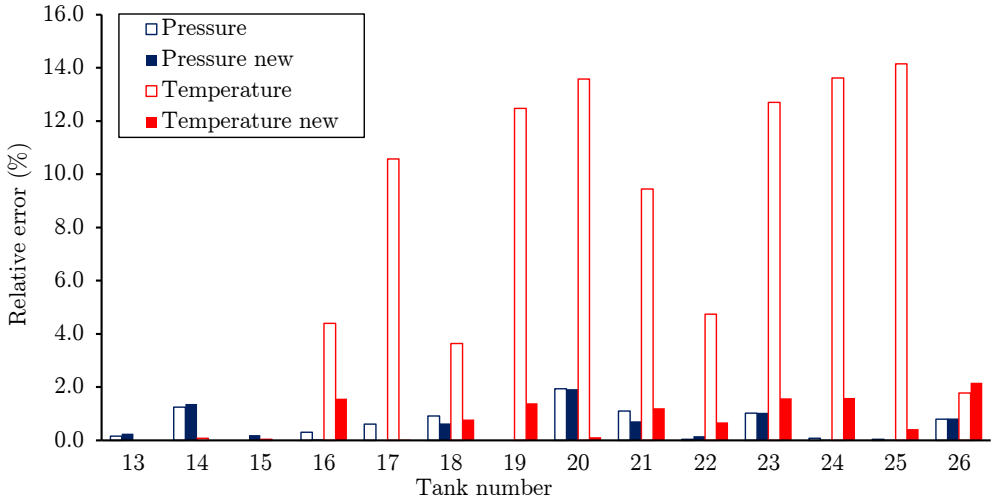

Figure 5.19: Errors in cavity properties - SAS solver vs SPAN (sponsor's solver)

cone, rotor-stator system, rotating cavity, frictional heating phenomenon and IP NGV internal cooling. Following an implementation strategy based on robustness, each heat transfer model was implemented as an independent subroutine. Thus, the process to associate each heat transfer phenomenon with each cavity of the network is a task of the user and this information is provided to the program through the specially designed input file.

From the numerical point of view, the way to include the heat transfer capability into the code is by the modification of the energy equation applied to a cavity. The updated energy equation states as follows:

$$\frac{V}{\gamma-1}\frac{dp}{dt}+\frac{\gamma}{\gamma-1}\frac{p}{\rho}\dot{m}_{out}-\sum_{i=1}^{n_{in}}\dot{m}_{in}h_{in}=\bar{q}=hA\left(T_s-T_\infty\right) \tag{5.121}$$

Once the numerical model was updated, the verification process was undertaken. This verification process had two main objectives: to demonstrate that the simulation capability was not altered; and to demonstrate that the changes did enhance the reliability of the tool by the reduction of the errors in the tank temperature prediction. Thus, the test carried out was the same whose results were shown above in this section (see Figure 5.13).

Figure 5.19 shows the comparison of the cavity pressure relative errors between the updated simulator and those produced by its previous version. The inclusion of heat transfer has led to a general improvement without, however, greatly affecting the general good agreement that was already achieved. On the other hand, the

implementation of heat transfer, as expected, had a major effect on the temperature relative errors. Figure 5.19 shows that the maximum relative error in temperature is around 2%.

In conclusion, through the present analysis, the most important mechanisms of heat transfer taking place over the SAS of a gas turbine were identified. The heat fluxes associated to each case were modelled through Nusselt number correlations mostly derived from experimental test available in the public domain. The simulation tool was enhanced by the implementation of the different scenarios in the most robust manner and finally, the updated version of the SAS dynamics simulation tool was verified and the degree of improvement assessed.

Chapter 6

Compressor performance

6.1 Background

The modelling of the main gas path, and in particular the compression side, relies on the source terms of the Euler equations to simulate the presence of the compressors in the duct. The methodology applied to calculate these source terms has been explained in detail in Chapter 5. The source terms regarding the compressor modelling are the axial force (F_x) and the shaft work (SW). The approach assumes that the dynamics of the fluid in the main gas path is captured by the transient Euler equations with source terms based on the steady-state performance of the components.

The capability to simulate post-stall behaviour is the most important feature of CERVANTES. The stable operation of a compressor is limited by the surge line in the compressor map. Compressor characteristics show that the pressurization capability increases when the mass flow through the compressor decreases. This stable characteristic has an end when the pressure rise reaches a maximum and a further reduction in mass flow leads to an abrupt change in the flow pattern inside the compressor provoked by aerodynamic malfunction [23]. Beyond this point the stable operation of a compression system is not possible any more. Different unstable behaviours have been identified [46]. There are two regions in the map where the unstable operation occurs, namely, the reverse flow region and the rotating stall region. The former extends from the reverse flow transition point (already in the negative part of the mass flow axis) towards higher negative values of mass flow. The latter occupies the region from the reverse flow transition point to the recovery point.

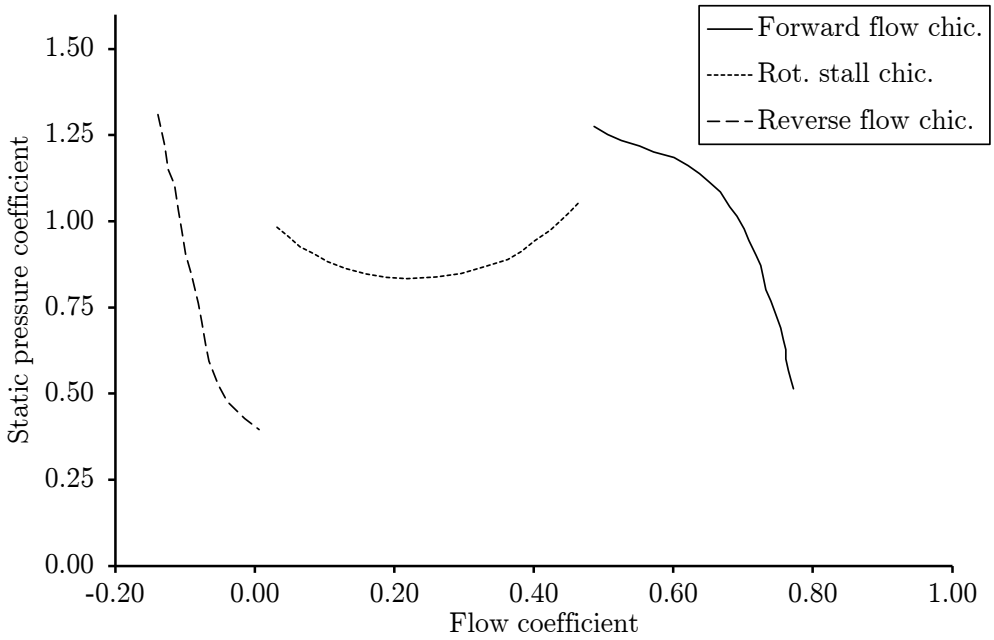

Figure 6.1: Complete compressor map - 3-stage MIT compressor [40]

Figure 6.1 shows these three regions in the 3-stage compressor used by Greitzer at MIT.

CERVANTES needs to be able to read information regarding the compressor performance over the unstable region because the resolution of the dynamics of the flow leads the operating point to explore these regions.

Modern aero-engines, and in particular those produced by the sponsor, are provided with several multi-stage axial compressor in order to reach the maximum pressure of the thermodynamic cycle. There are two possibilities to approach the simulation of a compression system with these characteristics in the context of a quasi-1D solver: dealing with each compressor as a unique machine or splitting the compressor into stages. Advantages and drawbacks can be identified in both approaches. If the former approach is followed, the amount of information needed is lower and the experimental maps provided by the sponsor can be used (unstalled region). On the other hand, phenomena regarding the stage mismatch are missed and the compressor surge is only detected as a punctual event when the operating point goes beyond the surge line. If the stage-by-stage approach is taken, the quasi-1D simulations would allow analysing the overall compressor surge inception attending to the stage mismatching and the progressive stall in the individual stages. Nevertheless, the amount of information needed to educate the model and the lack of experimental maps for each stage makes this approach unattractive. CERVANTES has been programmed to allow both possibilities and therefore, although the simulation work

presented in this thesis has been carried out following the former method, a stage-by-stage model can be built in the future if the stage characteristics are available.

The stable operating region of the compressor map is covered by the experimental maps provided by the sponsor. Regarding rotating stall and reverse flow region some sort of analysis is needed. Previous authors used rescaled experimental characteristics derived for different engines [48] or extrapolation techniques to extend the unstalled characteristic over the stall region [11].

Rotating stall and the prediction of a 'steady-state' characteristic suitable for that region is a challenging topic itself that has not been tackled in the context of this doctoral research. Nevertheless, research has been carried out in parallel at Cranfield in order to provide CERVANTES with rotating stall characteristics specially derived for the geometry of the sponsor engines. This research has been carried out by Serena Zoppellari [99]. Besides the outcome of Zoppellari's work, a simplified methodology has been implemented into CERVANTES whose details are given below in this chapter. Regarding reverse flow performance, extensive work was carried out to develop methodologies and prediction capability to derive compressor maps under these conditions within the context of the present doctoral research.

The objective of the present chapter is to present the different approaches followed to provide CERVANTES with complete information of compressor performance over the three different regions. In Section 6.2, details about the non-dimensional groups used to define a compressor map are given and the process to obtain the unstalled compressor map by means of experimental test is included. In Section 6.3, a description of the unstable operation in compressor is given and the simplified model to represent the rotating stall characteristic in CERVANTES is explained. Finally, in Section 6.4, the methodology developed to predict compressor performance at reverse flow conditions is presented.

6.2 Unstalled compressor performance

Multi-stage axial-flow compressors are a critical part in any modern aero engine. A certain number of stages consisting in a rotor-stator layout are placed along a convergent duct to communicate energy to a certain mass flow of working fluid in a way that this energy is used to increase the pressure of the fluid. Essentially, rotor and stator are composed by blades whose function is to change the circumferential

component of the flow velocity in order to transform kinetic energy into pressure increment. The desired pressure rise is achieved applying this same process stage by stage. Blades are fundamentally aerodynamic devices whose performance are limited by concepts such as separation of the flow and stall in a similar fashion as occurs in the wings of a plane. In general, axial compressors pressure rise capability increases when mass flow through the compressor decreases. However, the stable operation of the axial compressor is limited by aerodynamic reasons to a relatively narrow mass flow range. At a given rotational speed, maximum mass flow through the compressor is limited by the choke point when sonic conditions are reached at a certain point within the blades layout. On the other hand, a minimum mass flow exists that provokes the stall of a number of blade rows so higher values of pressure rise are not achievable, the stable operation of the compressor is not possible for a mass flow lower than surge point. Compressor operation between choke point and surge point is known as unstalled operation.

The representation of the compressor performance is summarised in the compressor map. These maps show the region where the stable operation of the compressor is possible for different rotational speeds. The knowledge of compressor performance is complete when Pressure Ratio (PR) and efficiency (η_c) are given as a function of Non-Dimensional Mass Flow (NDMF) and corrected speed (NRT).

Different processes can be followed to obtain a compressor map. If the compressor has already been designed and built, the more accurate method to obtain its map is the measurement of its performance by experimental methods. In case the compressor has not been manufactured yet, different approaches can be adopted to predict its performance depending on the geometrical information available at a certain point in the development process.

During the first stages of the design process a method based on overall performance correlations can be used to estimate the performance of the future compressor. This method relies on correlations of overall performance of existing designs expressed in terms of a number of fundamental parameters which, given the design geometry of a new compressor, allow the overall performance to be predicted [71]

Other sort of methods can be grouped under the stage stacking technique approach. These methods assume that the performance of a stage is known or can be predicted and the overall map can be derived by repeating the single-stage characteristics assuming that the inlet of the next stage is the outlet of the previous one. If the stage performance is unknown, this has to be predicted. Depending on the geometrical

features known at a certain point in the design process and the level of accuracy pretended, the analysis can be carried out attending exclusively to the mean-line geometry or extending it to take into account the variation of the flow field along the span-wise direction. What these methods have in common is that all of them rely on correlations for the pressure losses and deviation across a blade row. More details about these methods are given in the Section 6.2.3.

6.2.1 Non-dimensional variables in compressor performance analysis

The objective of a compressor map is to characterise this machine reducing to the minimum the number of experimental measurements needed to describe its performance. In order to get that, the non-dimensional analysis of the compressor operation is necessary. Let's consider a compressor operating between the inlet section (1) and the outlet section (2). Complete compressor performance can be defined through the pressure ratio and the adiabatic efficiency, in other words, knowing the stagnation pressure (P_{t2}) and the stagnation temperature (T_{t2}) at the outlet. In general, these variables are a function of the following variables:

- Intake conditions: P_{t1}, T_{t1}
- Operation conditions: Mass flow ($\dot{m}$) and rotational speed (N)
- Gas characteristics: R_g, C_p, μ, k
- Design: It is given by a characteristic length (D)

$$P_{t2}, T_{t2} = f\left(P_{t1}, T_{t1}, W, N, R, C_p, \mu, k, D\right) \tag{6.1}$$

In order to reduce the number of variables and so the number of test needed to get a complete definition of the compressor performance, the Π-Buckinham theorem is applied [72]. The fundamental magnitudes involved in this problem are four so using P_{t1}, T_{t1}, R_g and D to non-dimensionalise, the following functional relation is obtained:

$$\frac{P_{t2}}{P_{t1}}, \frac{T_{t2}}{T_{t1}} = f\left(\frac{\dot{m}\sqrt{RT_{t1}}}{P_{t1}D^2}, \frac{ND}{\sqrt{RT_{t1}}}, \gamma, \frac{\mu\sqrt{RT_{t1}}}{P_{t1}D}, \frac{k\sqrt{RT_{t1}}}{P_{t1}RD}\right) \tag{6.2}$$

Since the Prandtl number of the air is approximately one, it can be noticed that the last two non-dimensional groups are of the same order of magnitude and in most cases negligible. These terms are inversely proportional to the Reynolds number and it is commonly admitted [53] that its effect is negligible apart from a critical value.

$$Pr = \frac{\mu C_p}{k} \tag{6.3}$$

$$\mu \approx \frac{k}{C_p} \approx \frac{k}{R} \tag{6.4}$$

Following this reasoning, the functional relation which defines the compressor performance results as follows:

$$\frac{P_{t2}}{P_{t1}}, \frac{T_{t2}}{T_{t1}} = f\left(\frac{\dot{m}\sqrt{RT_{t1}}}{P_{t1}D^2}, \frac{ND}{\sqrt{RT_{t1}}}\right) \tag{6.5}$$

Furthermore, it can be assumed that the working fluid is always air so the heat capacity ratio and the gas constant do not appear in the functions. Finally, if it is considered that the compressor is a particular given machine, the factor D is a constant that can be eliminated from the functions.

$$\frac{P_{t2}}{P_{t1}}, \frac{T_{t2}}{T_{t1}} = f\left(\frac{\dot{m}\sqrt{T_{t1}}}{P_{t1}}, \frac{N}{\sqrt{T_{t1}}}\right) \tag{6.6}$$

Although these variables are not strictly non-dimensional any more due to the final simplification assuming a given machine operating with air, they are universally known as the non-dimensional groups in the study of compressor performance. The parameter $(\frac{N}{\sqrt{T_{t1}}})$ is proportional to the ratio of the blade speed to the speed of sound so it is a form of 'blade Mach number' and the non-dimensional mass flow $(\frac{\dot{m}\sqrt{T_{t1}}}{P_{t1}})$ is a function of the Mach number of the flow at entry [53].

Figure 6.2 shows the map of a HPC provided by the sponsor. Several concepts discussed above can be identified, namely, the use of the non-dimensional groups, the stable region delimited by the surge line and the narrow stable operation of the compressor for a given rotational speed.

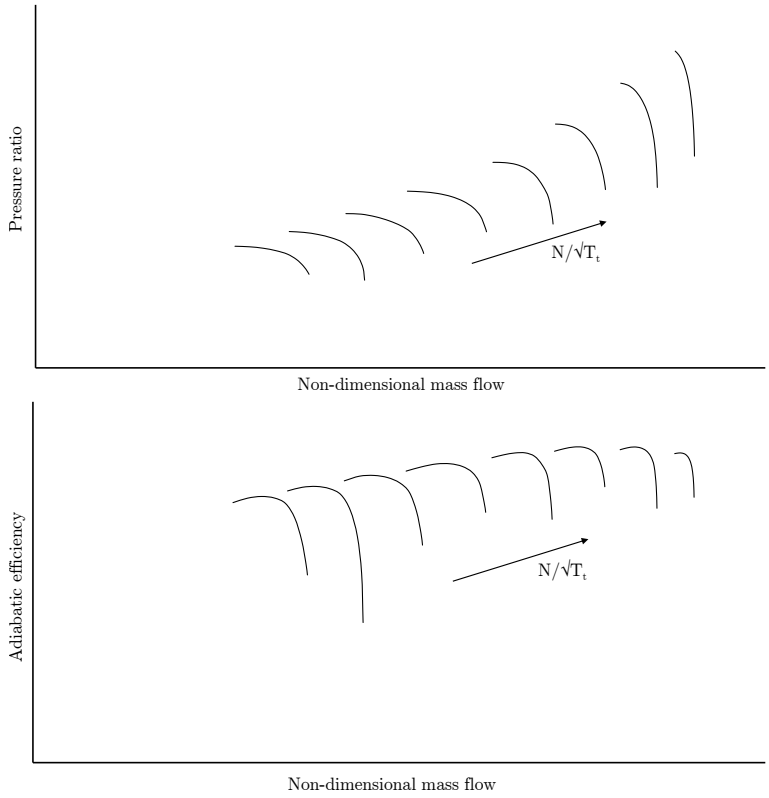

Figure 6.2: Compressor map

The non-dimensional groups used in Equation 6.6 are the most commonly used but different combinations of them can be used without losing their properties. In this particular application, the use the non-dimensional mass flow at the outlet has been proven to be more suitable. The shape of the compressor characteristics given by Equation 6.6 makes impossible the extrapolation in the region around the choke point since they become vertical. The phenomenon of choking can only be explained if the two-dimensional blade-to-blade analysis is considered. Since CERVANTES is a quasi-1D solver, this phenomenon is not captured and the simulations may produce values of mass flow above the choke point due to the abrupt transient evolutions occurring during compressor unstable operation. This situation causes problems in the interpolation-extrapolation process of maps. The strategy adopted to avoid this problem consists in a variable change in the compressor maps which changes the shape of the characteristic avoiding the vertical region [86]. The variable change is carried out as follows:

$$\frac{\dot{m}\sqrt{T_{t1}}}{P_{t1}} \cdot \frac{P_{t1}}{P_{t2}} \cdot \sqrt{\frac{T_{t2}}{T_{t1}}} = \frac{\dot{m}\sqrt{T_{t2}}}{P_{t2}} \tag{6.7}$$

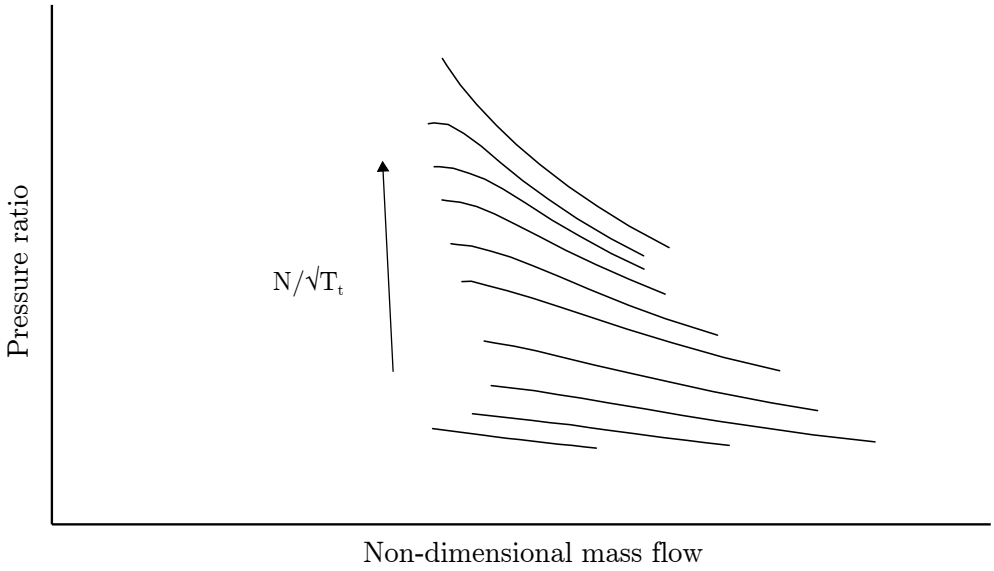

Figure 6.3: Compressor map using non-dimensional mass flow at the outlet

$$\frac{P_{t2}}{P_{t1}} = g_1\left(\frac{\dot{m}\sqrt{T_{t2}}}{P_{t2}}, \frac{P_{t2}}{P_{t1}}, \sqrt{\frac{T_{t1}}{T_{t2}}}, \frac{N}{\sqrt{T_{t1}}}\right) \tag{6.8}$$

$$\frac{T_{t2}}{T_{t1}} = g_2\left(\frac{\dot{m}\sqrt{T_{t2}}}{P_{t2}}, \frac{P_{t2}}{P_{t1}}, \sqrt{\frac{T_{t1}}{T_{t2}}}, \frac{N}{\sqrt{T_{t1}}}\right) \tag{6.9}$$

$$\frac{P_{t2}}{P_{t1}}, \frac{T_{t2}}{T_{t1}} = g_3\left(\frac{\dot{m}\sqrt{T_{t2}}}{P_{t2}}, \frac{N}{\sqrt{T_{t1}}}\right) \tag{6.10}$$

As it has been demonstrated, the variable change does not alter the nature of the non-dimensional groups so the maps represented following the relations given by Equation 6.10 are still valid. Figure 6.3 shows the same compressor map shown in Figure 6.2 after the variable change. It can be observed how the change in characteristic shape makes possible the momentary extrapolation that is sometimes needed during the simulation of unstable performance.

6.2.2 Experimentally derived compressor maps

The most accurate way to characterise a compressor is by deriving compressor maps through experimental test. In practice, an operating point on the compressor map is obtained for known values of entry properties (P_{t1} and T_{t1}). The mass flow, the total pressure at the outlet and the total temperature at the outlet are measured at

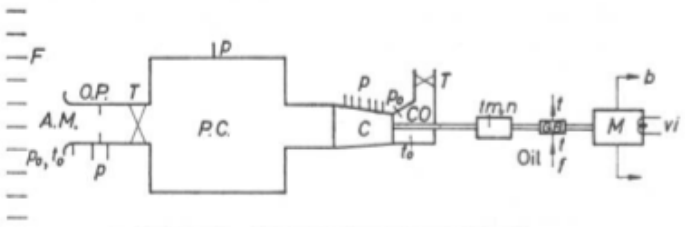

Figure 8.1. Diagram of compressor test cell

F	Filters	*C*	Compressor
A.M.	Air meter	*T*	Throttles
O.P.	Orifice plate	*M*	Drive motor
P.C.	Plenum chamber	*G.B.*	Gear box
CO	Collector		

Instrumentation

p	Pressure	f	Flow meter
p_0	Total pressure	b	Torque balance
t	Temperature	tm	Torque meter
t_0	Total temperature	n	Tachometer
vi	Power input		

Figure 6.4: Typical compressor test facility [53]

a certain rotational speed. Therefore, pressure ratio and the temperature ratio can be calculated directly and efficiency can be estimated from the relation

$$\eta_c = \frac{\frac{P_{t2}}{P_{t1}}^{\frac{\gamma-1}{\gamma}} - 1}{\frac{T_{t2}}{T_{t1}} - 1} \tag{6.11}$$

Keeping fixed the rotational speed and ambient temperature (i.e. fixed $\frac{N}{\sqrt{T_t}}$), the mass flow may be varied by throttling of the test system, either upstream or downstream of the compressor. P_{t1}, P_{t2}, T_{t2} and $\dot{m}$ may be measured at each throttle setting so the characteristics $PR = f\left(\frac{\dot{m}\sqrt{T_{t1}}}{P_{t1}}\right)$ and $TR = f\left(\frac{\dot{m}\sqrt{T_{t1}}}{P_{t1}}\right)$ can be obtained at a constant speed parameter.

If the throttling process is done downstream of the compressor, the process is simple because the total properties at the inlet are not modified. However, system throttling upstream the compressor may be useful when testing large compressors in case of limited power available. If the entry flow is throttled, P_{t1} is reduced below the ambient stagnation pressure while T_{t1} remains the same as the ambient temperature. It allows to obtain large values of non-dimensional mass flow with lower values of mass flow which help to reduce the maximum power needed to carry out the test [53].

Figure 6.4 shows the scheme of a typical layout for a compressor test. Mass flow is obtained by measuring the pressure drop across the entry airmeter. Total entry

temperature is obtained by measuring the ambient temperature since adiabatic flow in the entry duct can be assumed. Entry total pressure is obtained by measuring the static pressure in a plenum chamber between the entry throttle and the compressor. Total properties at the outlet can be measured at the exit diffuser. It is recommended to measure the total pressure using several Pitot tubes placed around the annulus. It is also interesting to obtain a measurement of the power input that can be used as an alternative indirect estimate of the temperature rise.

6.2.3 Predicted compressor maps

Although the experimentally derived compressor map is more appropriate to assist the calculation of overall engine performance, there are some situations where maps predicted by semi-analytical methods can be useful. During the design process the compressor has not been built yet so the experimental map is not available, in case a performance analysis is needed at that stage, it is essential to have the most accurate prediction capability to produce an approximate version of the future compressor map. Even if the experimental map is available the use of prediction methods is valuable when it is necessary to carry out parametric analyses. Some modern compressors are provided with variable geometry, the setting of these variable vanes is given by the nominal schedule which is a relation between the vane position and the rotational speed of the compressor. During the process to derive a compressor map, only the nominal schedule is tested and therefore, no information regarding mal-schedule of variable geometry is available through the experimental compressor map. In this situation, the use of an accurate prediction method may allow the analysis of variable geometry mal-schedule performance.

Many methods have been proposed and are available in the public domain to predict compressor stage performance. Most of them follow a two-dimensional approach evaluating the flow field in the blade-to-blade plane. Some methods solve the flow field in the hub-casing surface applying the radial equilibrium equation. These are known as throughflow methods. All these methods are based on two sets of correlations, namely, deviation angle and pressure losses. Deviation angle is correlated as a function of incidence and allows deriving the work characteristics. Pressure losses across the blade rows are correlated as a function of incidence and allow deriving the pressure rise characteristic [53]. In case of high speed flows where compressibility effects are non-negligible, this correlations are also function of Mach number.

VU59 is the mean-line compressor performance prediction tool developed by the

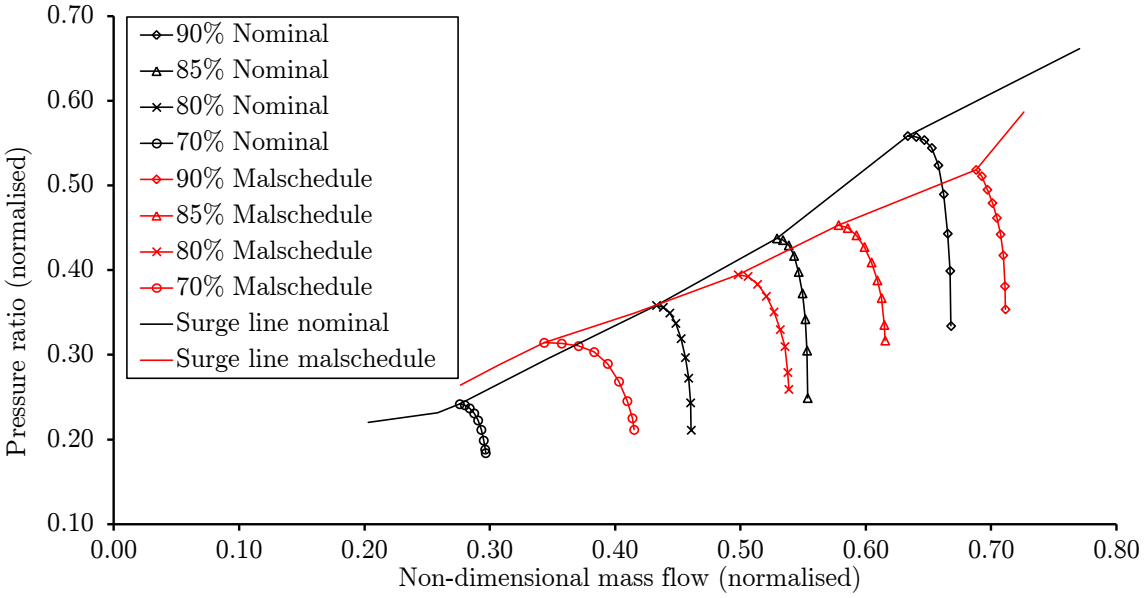

Figure 6.5: Effect of VG mal-schedule on the compressor map

sponsor. This code uses blade row stacking techniques to predict overall performance in multi-stage compressors. Inputs to the model are the blade geometry at mid-span and the annulus geometry. The model can be given any variable geometry setting and therefore, predictions of compressor map affected by variable geometry mal-schedule can be performed. This model was provided with an empirical deviation model and a pressure loss model taking into account end wall losses, shock losses and Reynolds number effect. The empirical coefficients were calibrated with single stage test data at design and part speed. The capability of VU59 to predict compressor maps under variable geometry mal-schedule circumstances is interesting from the point of view of the shaft failure analysis.

The time scale of the transient phenomena involved during a shaft failure scenario is low enough to provoke compressor variable geometry mal-schedule. After the breakage, the free-running compressor suffers a rapid deceleration while the control system is not able to actuate the variable geometry following the change in rotational speed. This scenario provokes the variable vanes to be more 'open' than expected during the compressor deceleration.

VU59 is a powerful tool that allows carrying out parametric analysis by producing compressor maps with a different blade geometry or variable geometry malfunction. These maps can be provided to CERVANTES to assess the qualitative effect on the outcome of a shaft failure scenario. This sort of analysis lacks the accuracy provided by experimental compressor maps but may provide a qualitative insight into how

the shaft failure scenario is affected by small changes in compressor geometry or variable geometry mal-schedule.

6.3 Surge and rotating stall performance

Throttling a compressor beyond its stability limit triggers the unstable behaviour of the compressor which is in general characterised by a drop in the compressor delivery pressure and strong fluctuations in pressure and mass flow able to provoke high level of damage in blading and casing. Compressor surge in the context of a gas turbine must be avoided at all cost. It is necessary to establish a surge margin between the operating line of the engine and the surge line of the compressors. That margin of operation provokes a sacrifice in performance in order to guarantee the stable operation and the life of the components. In normal operation of aero engines, the established surge margin and the actuation of variable geometry and bleed valves guarantee that the surge line is not crossed at any moment. On the other hand, in the context of the shaft over-speed event, compressor surge can be triggered by the compressor blades tip clearances fluctuation provoked by the vibration level after the shaft breakage or, it can be trigger by the mismatch of the variable geometry during the rapid compressor deceleration after the failure [87, 89]. In that case, unrecovered compressor surge is desirable since it leads to a rapid reduction of the power available at the over-speeding turbine.

Throttling the compressor reduces the mass flow through it provoking stall cells to appear. Stall cells are the reaction of the compressor trying to shut down part of the annulus by blocking it with the stall cells so that the rest of the annulus can operate at a more comfortable flow rate [28]. This stall cells rotate in the same direction as the rotor due to an effect that can be explain attending to changes in incidence angle at the boundaries of the cell provoked by the presence of the stall cell itself [34]. The stall cell tends to grow and decelerate and, apart from that moment, two possible outcomes are possible, namely, the size of the stall cell stabilises and the compressor operates at a stable point on the 'steady-state' stall characteristic or, if the energy contained in the plenum of the system is too high, the operation in rotating stall is not stable and the flow reverses destroying the rotating stall cell and leading to surge. Rotating stall is a phenomenon characterised by a high-frequency oscillation of low amplitude while surge is dominated by a low-frequency but more abrupt change in properties dominated by the process of charge and discharge of the plenum. Rotating stall shows a marked hysteresis which makes difficult the

engine recoverability while surge allows the recovery if the reason which triggered it is removed. This is possible because part of the surge cycle itself drives the operating point through the stable characteristic.

In the present section, an overview of the surge and stall phenomena is given through the most important contributions published in the public domain on this field. The simple model to predict the quasi-steady stall characteristic based on experience and first-principles developed by Day, Greitzer and Cumpsty [30] is presented. Finally, the simple approach implemented in CERVANTES to allow post-stall modelling is shown.

6.3.1 Compressor surge and stall phenomena

First studies and publications regarding the compressor instabilities appear on the 50s'. Papers by H. W. Emmon, C. E. Pearson, M. C. Hupper and W. A. Benser [34, 81, 56, 55] offered a qualitative understanding of the surge and stall phenomena. By the first time, surge was identified with high-speed operation and rotating stall with low-speed operation in the compressor. The effect of plenum volume was also encountered. The first modelling approaches were based on a linear analysis of the problem. However, this was not suitable in that scenario due to the large amplitude pulsations which characterises these phenomena.

In 1976, E. M. Greitzer [45, 46] carried out a complete study following a double approach to the problem. A simple analytical model was developed at the same time that experimental tests were carried out to support the model. Greitzer realised that it was necessary to analyse the whole fluid dynamic system, including ducts, compressor, plenum and throttle to understand the phenomena. This approach allows distinguishing between the kinetic energy associated with compressor, ducts and throttle and the potential energy of the pressurised flow stored in the plenum. The model is an application of the one-dimensional transient momentum equation to the compressor duct and throttle, and the continuity equation to the plenum. The compressor is modelled as an actuator disc and a polytropic process is assumed in the plenum. Incompressible flow is assumed in the duct and throttle. The model needed to be provided with compressor performance characteristics which relate the pressure ratio with the mass flow across the compressor. These characteristics were extracted from the experimental test for unstalled and in-stall regions. Furthermore, a first order lag was applied to model the time needed by the stall cell to develop in the transition from unstalled to in-stall operation.

The non-dimensional analysis of the equations derived by Greitzer allowed to find the B parameter which establishes a relation between the geometry of the overall system and the compressor operation. This parameter can be used to predict which situations tend to provoke surge or rotating stall during post-stall operation.

$$B = \frac{U}{2a}\sqrt{\frac{V_p}{A_c L_c}} \tag{6.12}$$

The numerical solution of the analytical problem allowed the identification of three different phenomena that were classified by Greitzer as rotating stall, classic surge and deep surge. Low values of B parameter lead to rotating stall. In this case, the compressor operating point follows a transient trajectory from the stable point to a new operating point where throttle line crosses the stall characteristic. The compressor stays there operating with a low delivery pressure and very low efficiency. The operating point looks stable from the point of view of the compressor map. Classic surge occurs for higher values of B parameter (above critical value). This phenomenon is characterised by oscillations in pressure and mass flow within the low flow coefficient region of the map. This oscillation takes place around the point where the throttle line crosses the stall characteristic. The compressor can be seen to pass in and out of rotating stall as the mass flow changes during the cycle. Finally, the third phenomenon was identified for higher values of B and smaller throttle areas. Deep surge was understood as a different phenomenon which involves the whole compression system. In that case, the plenum contains enough energy to provoke the reverse flow through the compressor. The oscillation here is related to the discharge and charge process of the plenum and is compared with the dynamic of a mass-spring-dump system with energy addition. No coherent rotating stall is observed.

The second part of this work summarises the experimental test carried out with a 3-stage low-speed compressor. The experimental test offered a successful qualitative comparison with the analytical model. A relatively sharp boundary between surge and rotating stall was found. Rotating stall was characterised by a unique stall cell rotating at 25-30% of the rotor speed. Important effects of the throttle area on the post-stall behaviour were identified.

The study of surge and rotating stall has been found difficult to tackle from an analytical point of view. The analysis of experimental results is paramount to improve the understanding of this event. Several authors have reported experimental

results for axial compressor rotating stall and surge. D. K. Das and H. K. Jiang tested a 3-stage axial-flow compressor in 1984 [24]. The main objective was to assess the impact of different inter blade row spacing on unstable compressor operation. Fast response transducers were used here to study the flow at eight axial planes and five radial positions. Most important parameters to understand the flow field were monitored, namely, axial velocity, tangential velocity, total pressure and static pressure. A unique full-span rotating stall cell was identified and the flow field inside it was observed to be highly three-dimensional and dominated by tangential velocity. Reverse flow was measured ahead of rotors and radial motion was identified in both rotor and stator. It was seen that the stall cell extends axially through the compressor and that the unstalled flow does not pass through the stall cell. No important influence of the blade row spacing was found.

Less common is to find experimental data about high-speed axial compressors in the public domain. In 1993, W. W. Copenhaver carried out an experimental study of rotating stall in a 10-stage high-speed compressor [21]. The main objectives of this work were the followings: to identify parameters affecting the recoverability, to obtain the quasi-steady in-stall characteristics stage by stage and for the overall compressor, and to obtain time-resolved performance in rotating stall. This research found that the axial extent of the stall cell through the whole compressor cannot be taken for granted in multi-stage high-speed compressors. Furthermore, Copenhaver showed the importance of stage matching in the surge inception and recoverability. It was seen that the three first stages operate unstalled even when the overall compressor is in stall. This is provoked by the matching of the stages during the design process. In that case, the first stages are low loaded in order to make them able to deal with inlet flow distortion. Therefore, the reduction in mass flow associated with the stall operation of the whole compressor is not enough to push the first stages beyond their stall point. This phenomenon was seen to provoke a poor recoverability. On the other hand, choking process of the last stage which is also a consequence of stage matching decided at design point was also identified as a potential limit to recovery. In conclusion, the work of Copenhaver showed the importance of stage matching and stage-by-stage analysis to understand rotating stall in multi-stage high-speed compressors.

The understanding of compressor surge reaches an important level of consistency with the work of I. J. Day in the Whittle Lab of the University of Cambridge [27, 29, 28]. Day carried out its experimental study in a 4-stage low-speed compressor but he states that compressibility effects do not add big differences. This work

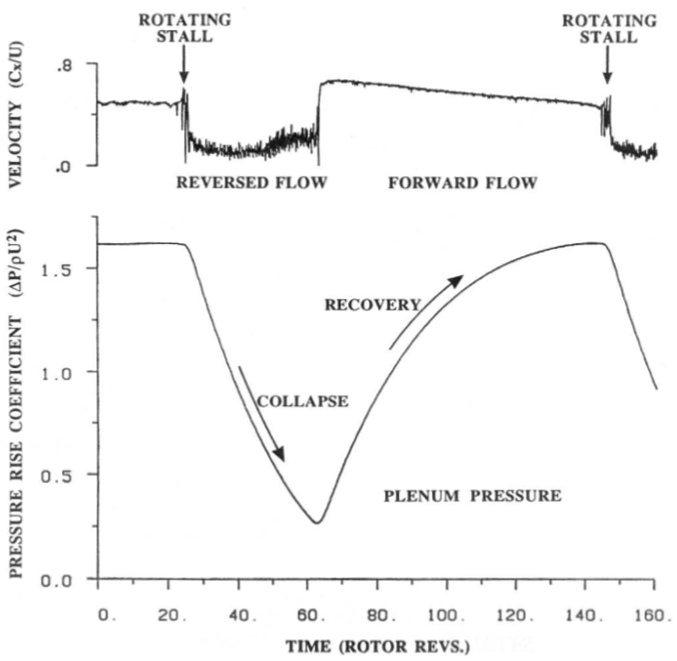

Figure 6.6: Deep surge and recovery process [28]

showed that rotating stall and surge are part of the same process, in fact, rotating stall is always present in the inception of surge, a sequence of cause and effect was identified. Rotating stall is defined as a circumferential disturbance of the flow in the region of the blades which does not affect the flow downstream neither upstream while surge is a disturbance which affects flow conditions throughout the whole compressor system. Day states that, in the process of throttling the compressor, a small stall cell appears, it rotates and grows and finally, when it has reached a certain size, after 4-5 revolutions, it collapses and the flow reverses in the compressor if the energy of the system is enough; in case energy is not enough to reverse the flow the phenomenon observed is classic surge or rotating stall. The recovery process is equivalent to the stall one, a cell of unstalled flow grows until it occupies the whole annulus. It is observed that this phenomenon requires only half time than the stall process.

Differences between Greitzer's compressor and the compressor used by Day (C106) were found. The influence of the B parameter was confirmed in terms of the existence of a sharp border between surge and rotating stall, however, the critical value obtained was very different in both compressors. Day proposed a redefinition of the B parameter scaling it with the values of pressure coefficient and flow coefficient at the peak point of the unstalled characteristic in order to universalise this criterion [27].

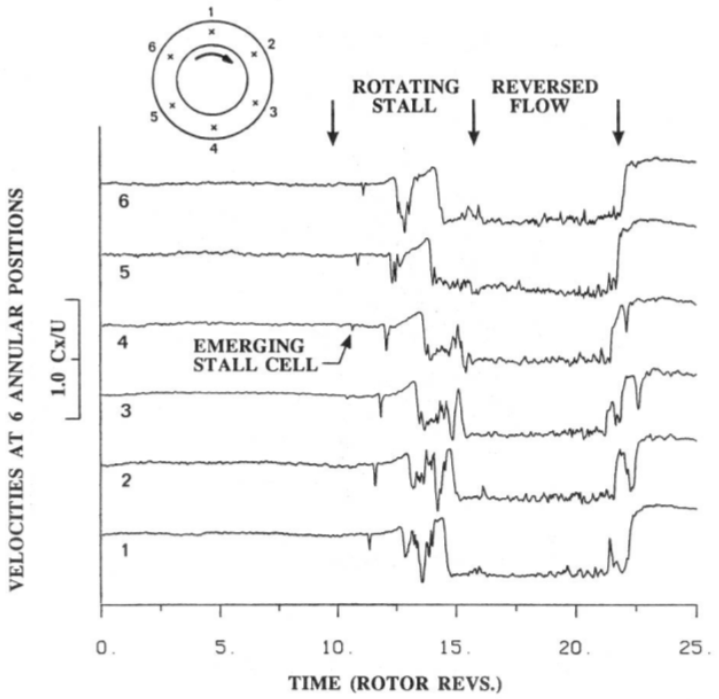

Figure 6.7: Compressor surge induced by rotating stall [28]

Apart from the work carried out with the compressor C106, Day extended the study of surge and rotating stall to high-speed compressors by analysing experimental data obtained with the VIPER (Rolls-Royce engine). This data allow confirming that stalling, surging and their inception processes are fundamentally the same in low and in high-speed compressors [29]. VIPER was seen to suffer rotating stall when the surge line is crosses between 65-85 % of the design rotational speed and that the energy stored in the combustor was enough to provoke surge for rotational speeds above 85 % of the design value. Surge at maximum power was seen to provoke such a dramatic mass flow fluctuation that leaded to combustor flame out followed by a rapid drop in rotational speed and therefore, only the first part of the surge cycle is observed in those tests.

Day confirmed the importance of stage matching in high-speed compressors through the analysis of the VIPER data. In that case, all stages were matched properly within the range of 75 to 83 % of rotational speed. The rotating stall affected to the whole axial length of the compressor and to the whole span of the blades. In that case the time needed by the disturbance to fully develop was five revolutions.

In conclusion, compressor instabilities have been intensely studied since 50's, reaching a consistent understanding of the event throughout the works of Greitzer, Cumpsty and Day since 1976 to early 90's. Experimental test in low-speed and high-speed

compressors have been carried out by different authors allowing the progress in the understanding of the event. The flow field within the stall cell has been measured repeatedly and it is considered as highly three-dimensional but dominated by tangential velocity. The whole phenomenon has been understood as a cause-effect process where rotating stall is always present in the inception of the event leading to surge or rotating stall depending mainly on the energy available in the overall system. In modern aero engines, it has been seen that the volume of the combustor is enough to provoke deep surge when the surge line is crossed at high power levels.

6.3.2 The rotating stall characteristic

One-dimensional models of the compression system requires to be provided with 'steady-state' in-stall characteristics of the compressors involved in the analysis. This necessity has motivated research on in-stall performance prediction capability. One of the first studies on that topic was published by I. J. Day, E. M. Greitzer and N. A. Cumpsty in 1978 [30].

The objective of this work was to come up with a systematic understanding of the influence of physical parameters on the overall features of operating during rotating stall. Data derived from the analysis of 13 compressors were used to check the validity of the methodology. These compressors covered a certain range of geometrical parameters such as: number of stages, design flow coefficient, design reaction and rotor and stator stagger and camber angle. Hub to tip ratio varies from 0.6 to 0.8. All the compressors tested were low-speed machines and the model was developed under the assumption of incompressibility. The main assumptions of the model can be summarised as follows:

- The stall cell occupies the whole compressor length (experimentally supported).
- Static pressure is assumed constant at compressor outlet.
- Constant inlet total pressure.
- Total inlet to static outlet pressure coefficient per stage is constant in stall and independent of compressor geometry. The value taken is 0.11.
- During rotating stall the compressor behaves like two compressors in parallel: one operating at zero flow coefficient ($\phi = 0$) and the other operating unstalled at the same level of total to static pressure coefficient.

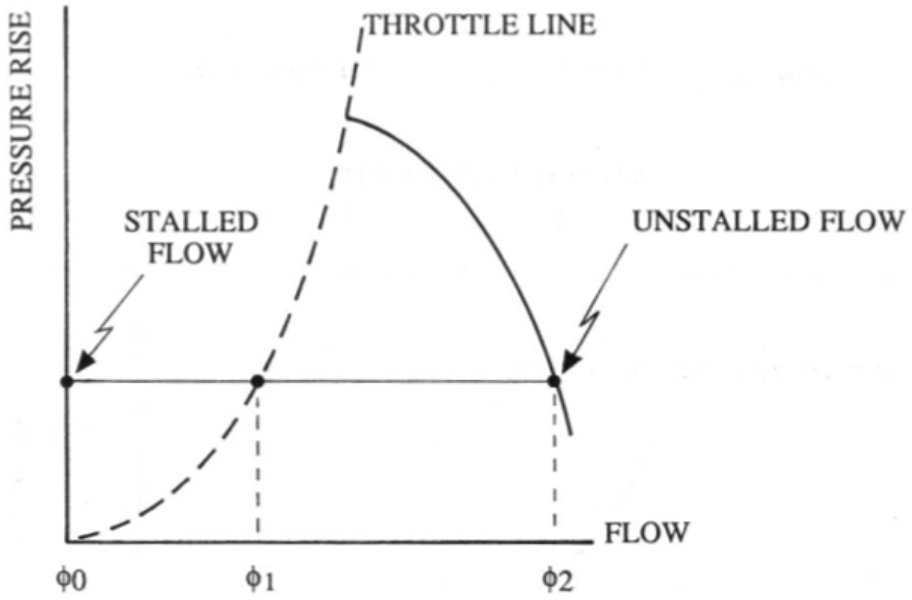

Figure 6.8: Rotating stall characteristic based on simple parallel compressor approach [28]

The method allows predicting a horizontal stall characteristic in the map given by total-to-static pressure coefficient and flow coefficient. The value of total-to-static pressure coefficient for a given compressor is calculated multiplying the single-stage value times the number of stages.

$$\psi_{ts}\,(Nstages) = N \cdot \psi_{ts}\,(1stage) \tag{6.13}$$

The operating point is assumed to be in the intersection of the throttle line with this horizontal characteristic. Based on observations, the authors choose the recovery point when the size of the stall cell goes below 30% of the annulus. This is the point where transition from full-span to part-span stall is observed.

The methodology was applied to an important number of different low-speed compressors and the level of agreement observed was satisfactory taking into account the simplicity of the method.

6.3.3 Simplified stall modelling in CERVANTES

The prediction of in-stall compressor characteristics is not part of the objectives of the present doctoral research. As it was explained in Chapter 3, the shaft failure

research within the context of the Rolls-Royce UTC at Cranfield University involves another two PhD. candidates apart from the author. The research regarding the development of methodologies to predict compressor characteristics in stall operation has been undertaken in parallel to the present project by Serena Zoppellari [99] and therefore, the present project has been organised assuming that the information regarding this part of the compressor map is provided as an input. Nevertheless, the necessity to carry out simulations with validation purpose and provide demonstration capability along the development process of CERVANTES has motivated the implementation of a provisional model of rotating stall. In the present section, the approach chosen is explained. This model is based on simple assumptions following first principles as those used in the model presented in section 6.3.2 and the analysis of experimental data provided by the sponsor, which allows to adapt this methodology to the reality of high-speed compressors commonly used in the modern high-bypass ratio turbofans which are the aim in the analysis of the shaft failure scenario.

The data provided by the sponsor include 22 full-scale engine tests where compressor surge has been provoked by fuel spike. The engine is a 3-shaft HBR turbofan and therefore, the conclusions derived from these data are considered representative and directly applicable to the present research. The information extracted from here is used with a double purpose, namely, to allow the alignment of the models of in-stall characteristic and to validate overall engine simulations of a fast transient event involving compressor instability.

Fuel spike tests are commonly used to provoke compressor surge in an overall engine environment. The engine is stabilised at a particular operating point which is a consequence of the amount of fuel injected and the equilibrium reached by the 3-shaft engine layout for a given variable geometry schedule and bleed valves opening. Next, a sudden increment in the fuel flow is delivered. In that case, the fuel flow is increased around three times its value in a characteristic time of a hundredth of a second. This provokes a fast increment of the TET due to the fast reaction of the combustion process. The throttle of the compression system within this overall engine layout is given by the choked section of the HPT NGVs which imposes the next constrain:

$$\left.\frac{\dot{m}\sqrt{T_t}}{P_t}\right|_{HPT_{inlet}} = Constant \tag{6.14}$$

Therefore, the temperature increment provokes the pressure increment at the com-

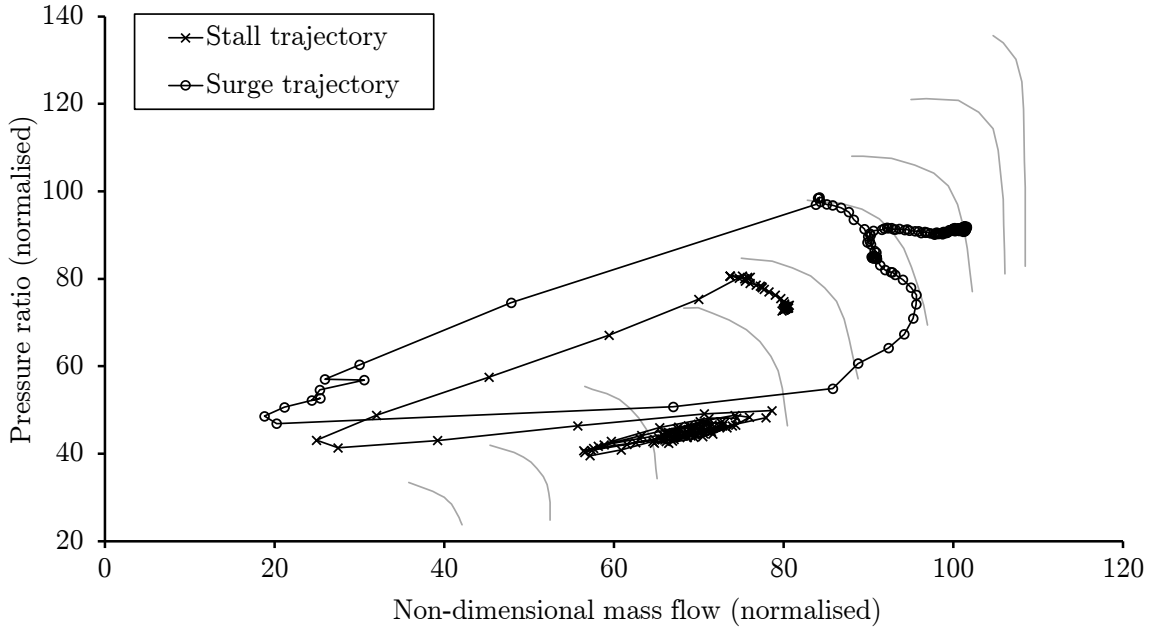

Figure 6.9: Operating point trajectory during a fuel spike test

bustor and the reduction of the mass flow. The engine tries to readapt to the new situation by increasing the shaft speed since there is an excess of power available at the turbine, nevertheless, the inertia of the shaft makes the acceleration phenomenon much slower than the change in fluid properties being reasonable to assume that the variation in rotational speed is negligible. The consequence of that is that the operating point of the engine follows a trajectory that goes directly towards the surge line when it is visualised on top of the compressor map. It makes a fuel spike very effective when trying to provoke compressor surge. Once the surge has been triggered, the fuel flow is reduced in the same fashion to the initial value. This kind of test allows observing two different scenarios, namely, the engine runs down into rotating stall or it surges and recovers since the cause that provoked the surge has been quickly removed.

Each test explored a different initial operating point from 66.7% to 86.7%. Presumably, the test was not extended to maximum power due to the destructive consequences of high power surge. Although very valuable information is extracted from these tests, the instrumentation used was not suitable for the study of compressor instability so limitations are found when extracting conclusions from these results. Pressure probes are the most reliable while measurements of temperature are thought to be 'laggy' [86]. Furthermore, no circumferential resolution is available but a unique measure per section.

The analysis of these data allows the identification of a sharp boundary between

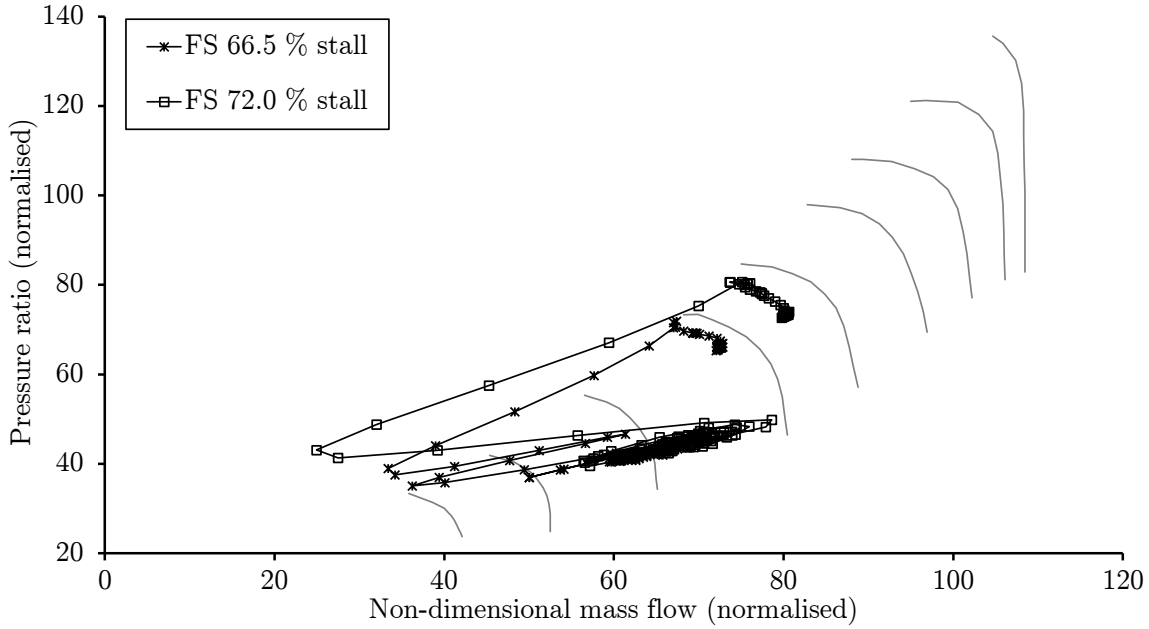

Figure 6.10: Fuel spike test - Stall

rotating stall and surge for this engine. If the engine power level is defined as the ratio of HP shaft speed over its speed at maximum take off conditions, this boundary is observed at 72%. Fuel spike tests provoked at a HP shaft speed below 72% lead to rotating stall while for higher power levels the compressor tend to surge and recover after only one surge cycle.

Figure 6.10 shows two low power trajectories, one for the lowest power level tested and the other one for the highest power level which leads to rotating stall. The rest of the tests in between these two initial operating points show exactly the same behaviour. The next operating point tested was 72.2%, being that case the first one which shows recovery so it is identified as the first case of surge. Figure 6.14 shows two representative cases of surge and recovery. The rest of the cases in between these two (72.2% and 86.7%) show a very similar behaviour. Rotating stall trajectories shown in Figure 6.10 and Figure 6.12 have been filtered using a low-pass filter at 15Hz. This allows to show the transient trajectory on the compressor map as clean as possible while more detail about the signal recorded is shown below.

Next, the evolution of the most important measurements with time is shown. Figure 6.12 presents a comparison of the same two representative cases of rotating stall. First plot shows the fuel flow so the timing of the fuel spike can be compared with the reaction of the engine. Second graph shows the evolution of the mass flow through the compressor measured at the inlet. This signal is the most suitable to observe the different frequencies involved in the event. It can be observed the abrupt reaction

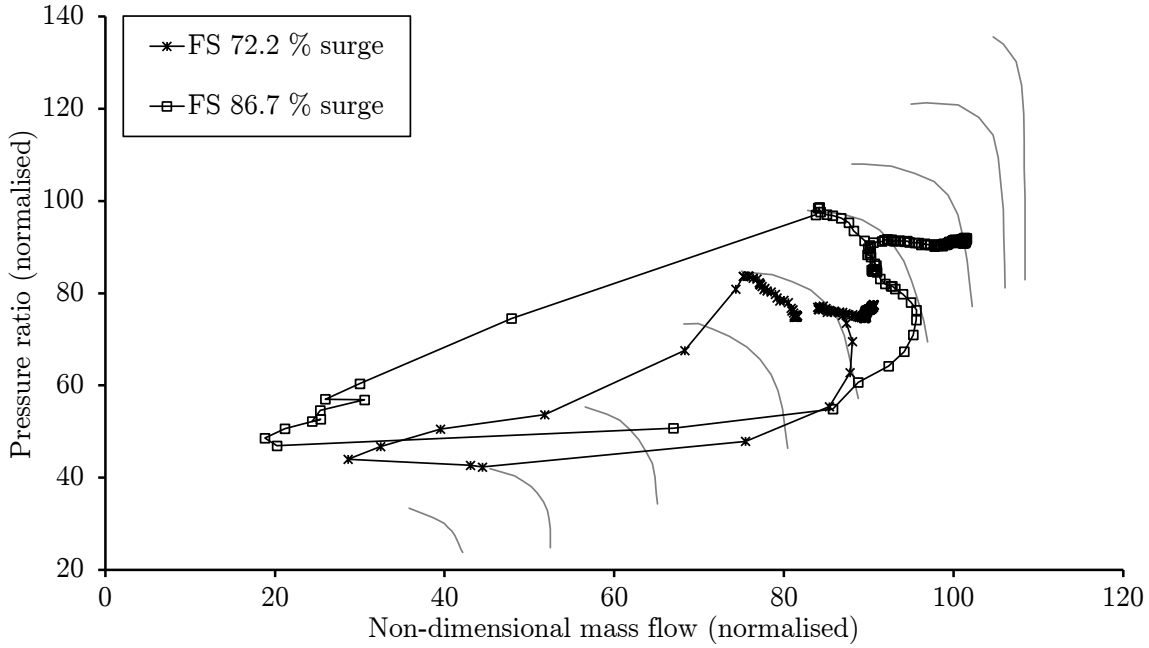

Figure 6.11: Fuel spike test - Surge

of the engine through a sharp reduction of mass flow just after the operating point crosses the surge line. After that, there is a low-frequency fluctuation of different duration in both cases. In the case at 66.7%, the initial low-frequency oscillation ends after 0.3 seconds when the signal clearly changes to a higher frequency and lower amplitude pattern. In the case at 72%, the pattern changes after 0.5 seconds. The same oscillation pattern can be observed in the rest of plots. The next two graphs show the evolution of the total pressure at compressor outlet and the pressure ratio. The most interesting conclusion that can be derived from these results is that the rotating stall pressure ratio can be considered a constant independent of the initial power level of the engine. This feature will be used to derive the simple provisional model of in-stall characteristic implemented in CERVANTES.

The measurements of mass flow rate have been used to carry out the Fourier analysis of the signal. Fast Fourier Transformation (FFT) technique has been applied to this signal to explore its characteristics in terms of frequencies. The sample rate of the signal recorded is 10^{-2} seconds. This sample, in theory, allows to capture phenomena below 50 Hz. Figure 6.13 confirms clearly the presence of the two frequencies commented above. The low frequency oscillation is found to be around 11 Hz and agrees with the values observed in the literature regarding surge phenomena. The high frequency oscillations are captured around 48Hz. Although it is close to the limit imposed by the signal sample, the value agrees with the frequency associated with rotating stall.

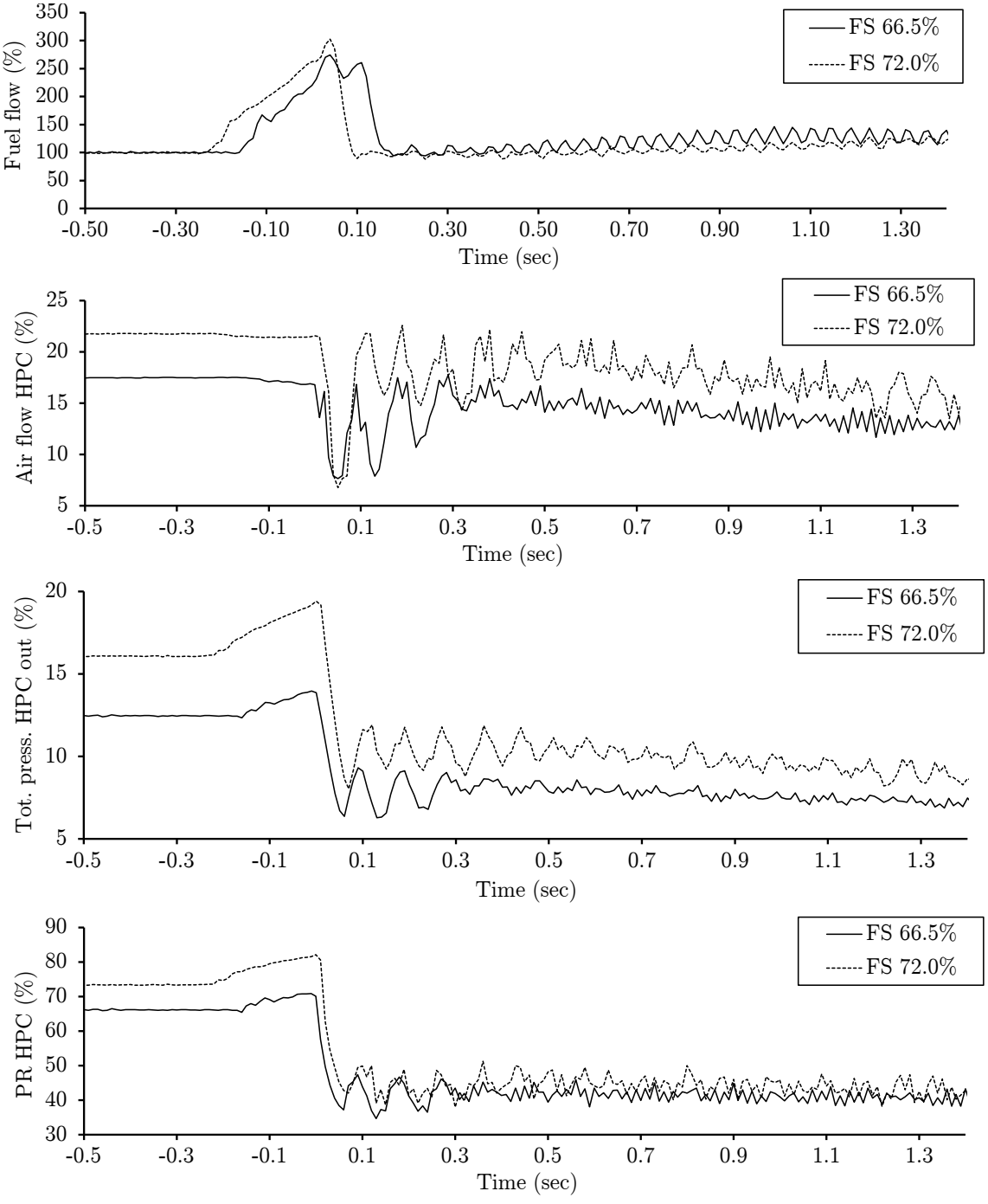

Figure 6.12: Fuel spike test - Properties evolution in stall

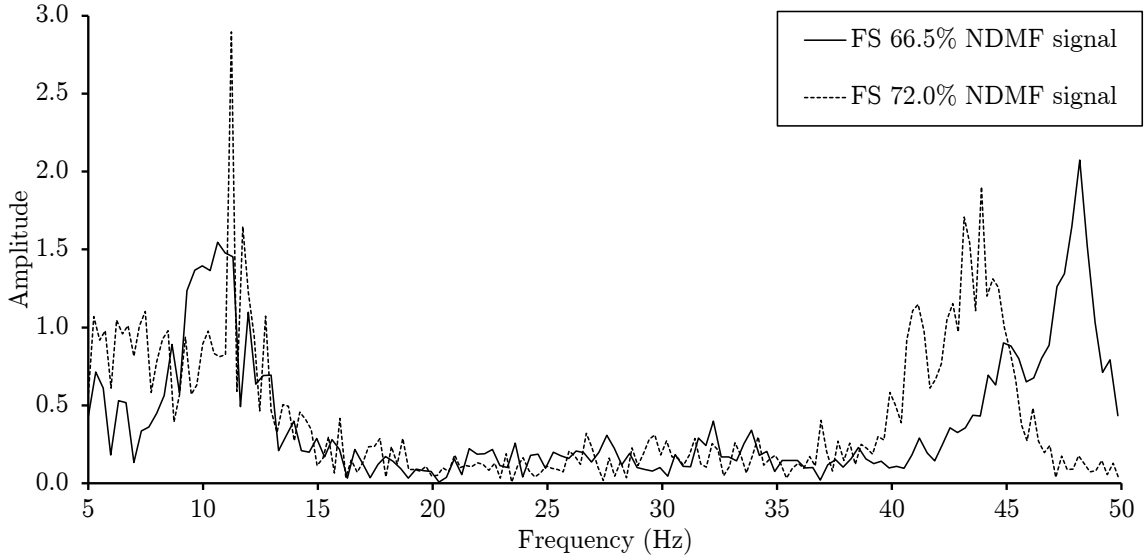

Figure 6.13: Fuel spike test - Frequency analysis

Figure 6.14 shows the same properties plotted for the two chosen cases of surge and recovery. In that case, only the first cycle can be seen. The phenomenon is dominated by the abrupt drop in mass flow and pressure at the moment of surge inception and the engine recovery after the minimum in pressure is reached. This cycle extends approximately over 0.1 seconds so its frequency is around 10 Hz. Reverse flow has not been detected in any case so it can be deduced that the power available at the combustor at 86.7% of engine power level is not enough to provoke the axisymmetric reverse flow in the compressor. At that point, nothing else can be said since experimental results at maximum power are not available.

Regarding the prediction of an approximation for the in-stall compressor characteristic, this data set has been compared against the prediction of the incompressible model of Day, Greitzer and Cumpsty [30]. The results show that the total-to-static pressure coefficient associated with the in-stall operation of this compressor is independent of the rotational speed for the range available in the data set (67-72%). Nevertheless, when this pressure coefficient is divided by the number of stages the value obtained (0.41) is far from the value suggested by the authors of the work described above (0.11). It suggests that the major assumption supporting this methodology is not extrapolative to high-speed compressors.

The definition of the pressure coefficient stage by stage in a high-speed compressor is problematic since the density varies over the compressor and its variation is not negligible. Following the analysis of the results detailed above, the most convenient is the use of the pressure ratio. It has been observed that the value of pressure ratio

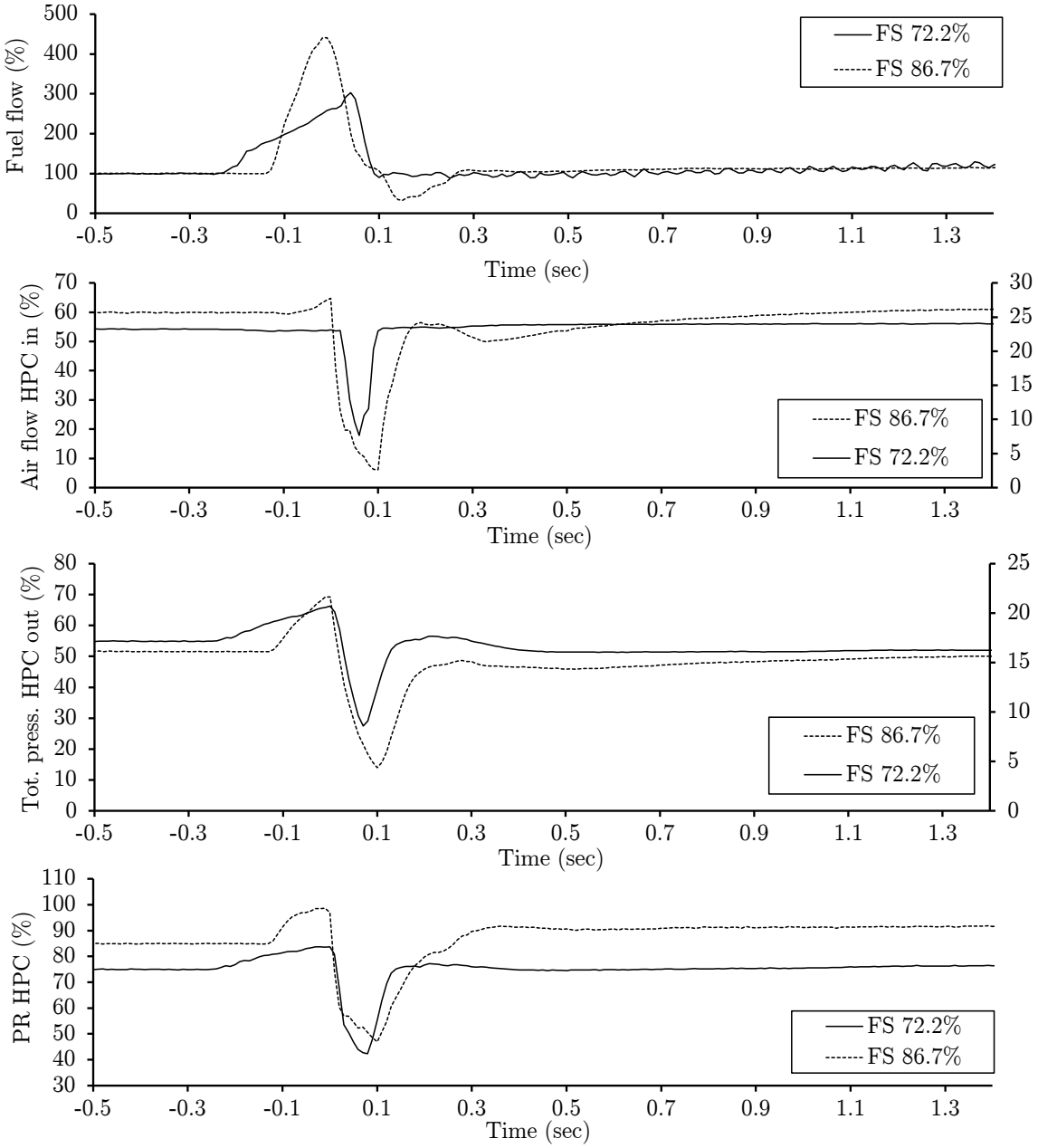

Figure 6.14: Fuel spike test - Properties evolution surge and recovery

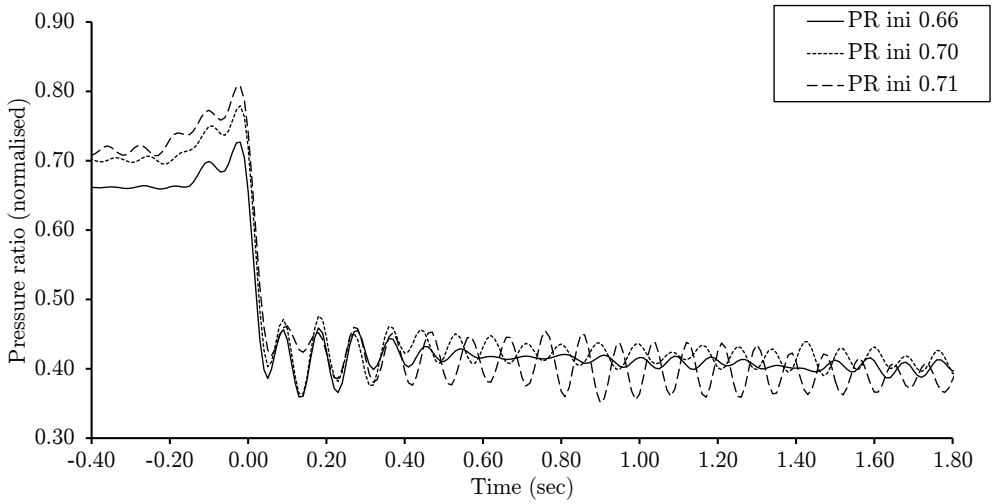

Figure 6.15: Pressure ratio evolution in stall

reached when the compressor locks in rotating stall is fairly constant independently of the initial power setting. Therefore, the simplified stall model implemented in CERVANTES follows the same assumptions of the methodology presented in Section 6.3.2 but it is corrected by changing from pressure coefficient to pressure ratio and using a single-stage in-stall pressure ratio value derived from the observation of this set of experimental data.

Figure 6.15 shows the low-pass filtered signal for three representative cases in the region of rotating stall. The in-stall average value of pressure ratio for all the eight rotating stall test have been plotted in Figure 6.16 as a function of the initial value of pressure ratio (operating point). The average value is 40.6% of the reference value and the deviation is 2.5%. If it is assumed that every stage contribute in the same manner to the compression in rotating stall, the single-stage pressure ratio obtained is 30.6% of the reference value. This methodology leads to use an horizontal line as in-stall characteristic in the compressor map which only depends on the number of stages of the compressor.

In conclusion, data of a high-bypass ratio turbofan engine surge test have been analysed to extract the minimum information needed to establish a provisional model of in-stall compressor characteristic. The model is based on qualitative assumptions derived from observations of low-speed compressor surges [30] and modified to adapt the quantitative parameters to the reality of a high-speed modern axial compressor. The model is implemented within the simulation tool CERVANTES to allow validation and demonstration capability but it is considered a preliminary model until more reliable information about in-stall characteristic is available.

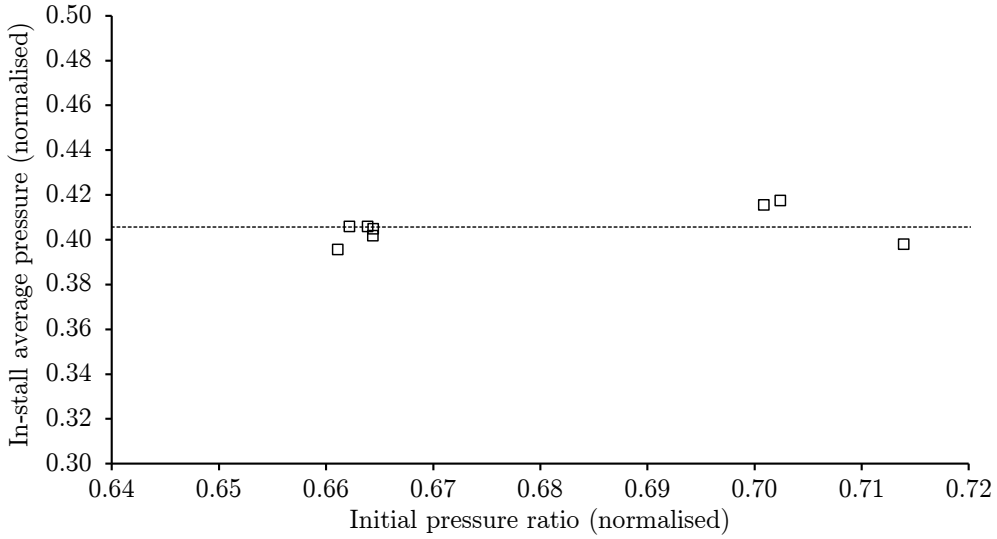

Figure 6.16: Average pressure ratio in stall

6.4 Reverse flow performance

Reverse flow operation in axial flow compressors occurs when the working fluid is going through the compressor in the opposite direction. This phenomenon may happen when the compressor is affected by a deep surge scenario. Therefore, reverse flow needs to be studied in order to improve the understanding of compressor performance during unstable operation. Reverse flow characteristics curves 'widen' the compressor map by providing information within the negative part of the non-dimensional mass flow axis. This information is necessary, particularly in the context of 1D methodologies for the simulation of the gas turbine engine's main gas path which need to be provided with complete compressor maps, including all 3 operating regions.

The main objective of this part of the research is to develop capability to predict axial compressor reverse flow characteristics. The methodology has been thought to be generic enough to allow its application to any multi-stage axial compressor. It is conceived to be robust and non-expensive from the point of view of time and computational cost.

In the present section, the reverse flow phenomenon is described through the analysis of the previous work published in the public domain. The understanding of the event allows the establishment of the methodology followed in this research. Then, the methodology is explained in detail, the assumptions are stated and the process to build the standalone prediction tool developed is described. Furthermore, the

validation of the tool against the available experimental data is included. Finally, the tool is applied to several modern axial compressors to show its capability and the results are analysed.

6.4.1 Compressor reverse flow phenomenon

During reverse flow, the compressor is assumed to operate with an axi-symmetric and steady negative mass flow. This simplification can be done from the point of view of the analysis of this particular event, although the reverse flow in compressors is just a part of the transient unstable operation known as deep surge. The term axy-symmetric in turbomachinery should not be understood as strictly axy-symmetric but as periodic in the circumferential coordinate of the compressor.

Dynamics of reverse flow are not fully understood by the wider research community yet. The difficult and the cost involved in carrying out experimental studies probably explain the little progress done in this area. Therefore, the information available in the public domain is limited. This information could be classified in the following manner: experimental research, modelling attempts and CFD analysis. The experimental test could be divided into complete compressor experiments and cascade tests. The former includes the work of Gamache [40], Gamache and Greitzer [41], Koff and Greitzer [62], and Day [27]. The latter includes the work of Corneal [14], O'Brian [76] and Chenaux, Schönenborg and Ott [18]. Regarding the analytical modelling, Koff [61] proposed a model based on a 2D potential flow analysis of stalled flow in blade cascades published by Cornell [22]; and Gallar [39] published a model based on the same principles and the studies of Mosses and Thomason [74] about stall flow in blade cascades including adjustable coefficients that allow the alignment against experimental measurements. Regarding CFD analysis, a successful comparison between CFD predictions and experimental measurements can be found in the paper of Chenaux, Schönenborg and Ott [18].

A good understanding of the flow field features during compressor reverse flow can be reached through the published works mentioned above.

Based on the work of Gamache [40] and Gamache and Greitzer [41], the problem of reverse flow could be tackle using a full-annulus-stalled approach where the radial effects are going to play an important role. Particularly important is to understand the flow pattern in the blade-to-blade plane. Figure 6.17 and 6.18 show the flow pattern (rotating frame) in the blade-to-blade plane at mid-span for the last stage

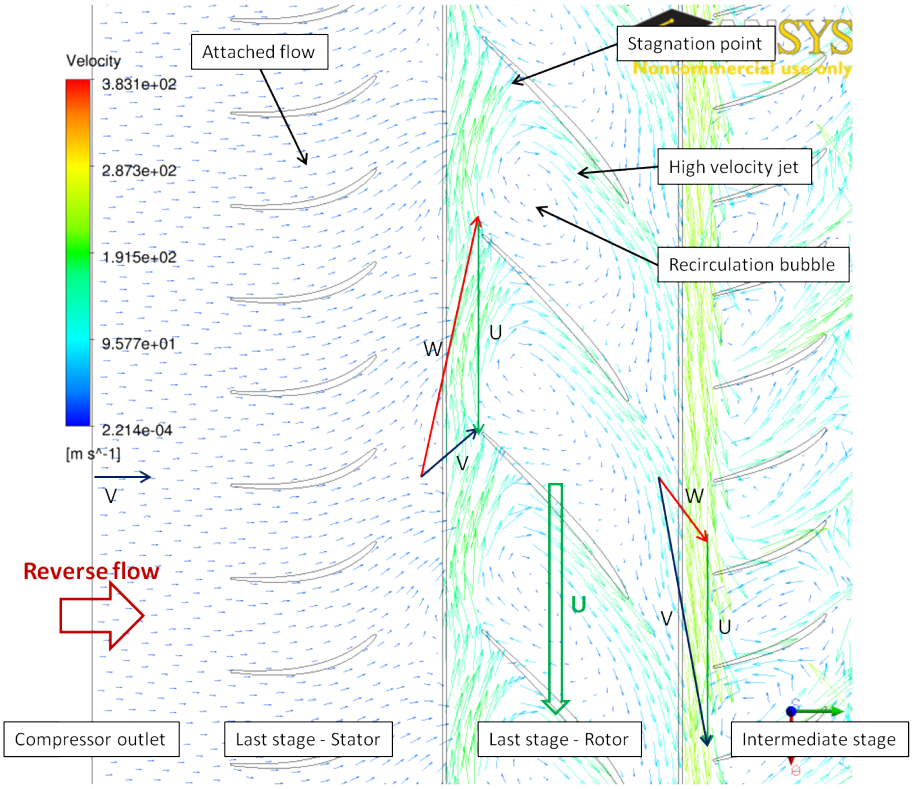

Figure 6.17: Flow pattern at reverse flow conditions - Last stage

and the penultimate stage respectively. It can be observed how the flow remains attached across the first stator since it is aligned with the flow. Further downstream, the extremely high incidence angle at the rotor trailing edge provokes the separation of the flow resulting in a flow pattern which consists of a dominant recirculation bubble and a high velocity jet. The velocity triangle downstream the rotor blade row shows the magnitude and the direction of the absolute velocity which provokes a similar flow pattern in the next stator. Downstream this blade row, the flow pattern can be considered repeating in the successive blade rows.

High level of torque (compressor power consumption) was observed by Gamache [40]. The very large flow direction change that can be observed in the analysis of the blade-to-blade flow pattern and the qualitative application of the Euler equation for turbomachinery (see Equation 5.54) explain this feature. Although the mass flow that can cross the compressor in reverse flow is almost an order of magnitude lower than the mass flow in forward flow, the compressor power consumption is of the same level or even higher.

$$W = \omega \cdot |V_{\theta 1} r_1 - V_{\theta 2} r_2| \tag{6.15}$$

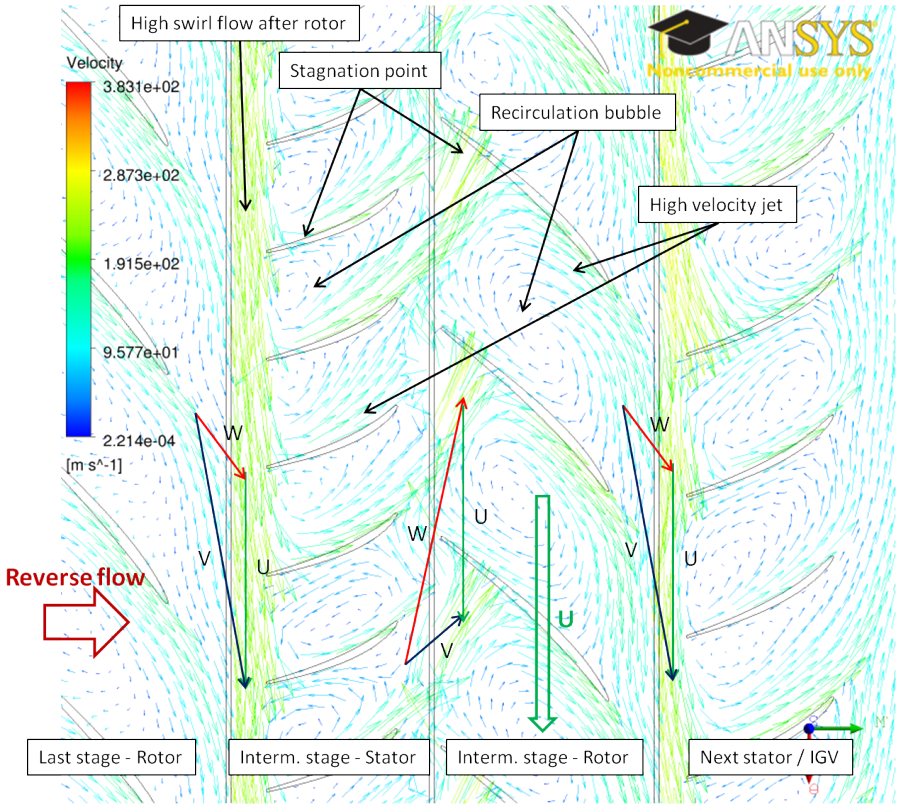

Figure 6.18: Flow pattern at reverse flow conditions - Intermediate stage

It is worth to pay attention to the deviation angle at the outlet of each blade row [41]. At mid-span, the deviation at rotor leading edge in the rotating frame is not important, so the assumption of zero deviation imposing that the flow angle is the same than the metal angle can be applied. Nevertheless, deviation at stator leading edge cannot be neglected since it reaches values about 40 deg.

Evidences of the highly three-dimensional flow field at compressor reverse flow conditions are stated in the work of Gamache and Greizter [41]. High radial velocities in the rotor blades are observed. The overall picture in the meridional plane shows that the flow is ejected from the tip portion of the rotor blades pressure surface while the opposite is happening in the stator blade rows. These evidences are here used to defend the features of the methodology applied in the present research which is presented in the next section.

Regarding the effect of blade geometrical features on reverse flow performance, some evidences are given by the work of Gamache [40]. Two different compressor builds were tested to explore the effect of variations of 5 deg in rotor stagger angle and 10 deg in stator stagger angle. The results showed that reverse flow performance are almost insensible to blade shape variations due to the highly separated flows. Since

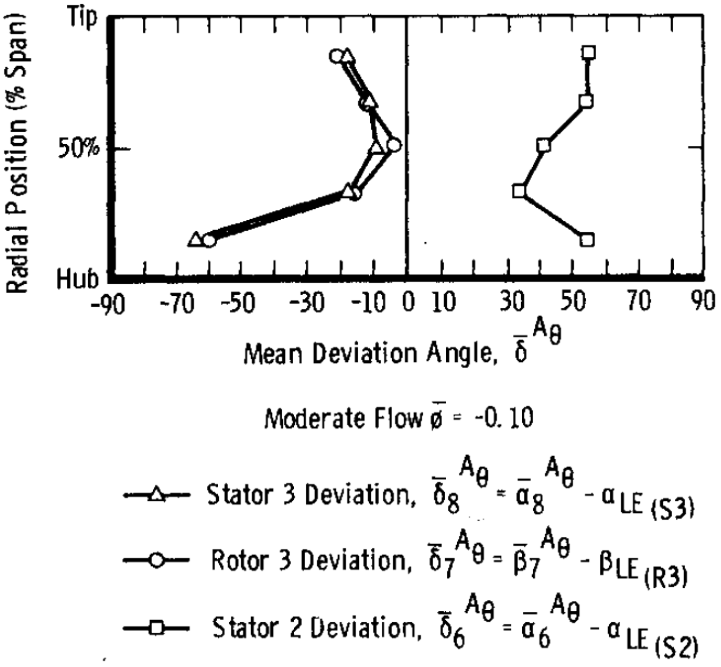

Figure 6.19: Mean flow-deviation angles at different axial stations at reverse flow conditions [41]

the flow is not following the established metal shape of the blades as in forward flow, small changes in the blade shape are not expected to modify the reverse flow performance. In following sections, it is shown the agreement of the CFD results with these observations and an extension to these assumptions regarding the variations of the stator stagger angle is presented.

The published work of Gamache [40] has allowed stating that the flow field observed at reverse flow conditions is very similar to that found within the stall cell at rotating stall conditions. This encourages the study of the reverse flow in detail since the understanding gained in that matter is applicable to the modelling of the rotating stall phenomena.

6.4.2 Methodology

The approach to model compressor reverse floe performance followed here has been thought to be robust and inexpensive. An experimental approach would be prohibitively expensive and a CFD study of the whole compressor is considered unattractive since the aim is to come up with a generic prediction methodology applicable to any multi-stage axial compressor. This generic methodology is based on the study of

single-stage performance in reverse flow by means of CFD analysis and the use of a mean-line Stage-Stacking Technique (SST) to build the overall compressor map. A SST encompasses the application of the continuity equation taking into account the velocity triangles at the inlet and outlet of each stage, as well as the momentum and energy equations that are represented by CFD derived correlations. Flow properties calculated at the outlet of a stage are used as inlet conditions for the next one. Details about both aspects of the methodology are given below in the present section. In the following paragraphs, the features and the assumptions used to define this methodology are presented being supported by the understanding of the reverse flow phenomenon given by the previous section.

The present model aims to be applicable to any multi-stage axial compressor. The only way to make it possible from an inexpensive approach in terms of time and computational cost is the use of a SST. The use of this technique is supported by the repeatability in terms of flow field which is derived from Gamache experimental tests [40].

The application of a SST requires to decide which is the minimum entity which is repeated along the axial layout of the compressor. In the present methodology, several reasons have invited to take the classical concept of stage (rotor + stator) as this minimum entity. This choice allows to avoid the problem of modelling the deviation at stator leading edges which was observed by Gamache and Greitzer [41] to be non-negligible. It is the section downstream of the rotor blade row the one which is taken in the SST to transfer the flow field values from one stage to the next one, and therefore, this choice avoid the analysis of the section downstream the stators which is taken into account by the CFD derived correlations. It has been shown previously that the deviation at rotor leading edge can be neglected. Therefore, this decision releases the SST from complex deviations models and relies the accounting of this effect on the CFD analysis.

The modelling of the single-stage performance by CFD analysis requires the built of a simulation domain which allows the analysis of this problem with guarantees. The domain chosen in the present analysis is a 2.5-stage domain including the sixth stage stator, the seventh stage and the eight stage of an 8-stage modern compressor whose geometry has been provided by the sponsor. More details of this domain are given below in this section. This choice is justified attending to the necessities of the model. Firstly, it is evident from the flow field analysis in the blade-to-blade plane that the last stage will exhibit a particular behaviour en terms of reverse flow performance. Secondly, the typical intermediate stage is represented in the

domain by the seventh stage of the compressor. Finally, the presence of the sixth stage stator completes the problem accomplishing a double purpose, namely, its presence is necessary to model the seventh stage as an intermediate stage and it allows deriving performance correlations for a typical Inlet Guide Vane (IGV).

The use of 3D CFD analysis to derive the single-stage performance maps is justified supported by several reasons. As has been proved by Gamache and Greitzer [41], the three-dimensional nature of the flow field in reverse flow cannot be neglected, and therefore, previous attempts to model reverse flow based on bi-dimensional losses model have been admitted unsuccessful. 3D CFD analysis has been proven successful in the analysis of the highly separated flow which dominates this event by comparing its results against experimental measurements in an annular cascade test [18]. Since the experimental approach was not an option due to its expensiveness, the task to build the generic single-stage performance maps required by this methodology has been tackle through high-fidelity 3D CFD simulations.

Modelling multi-stage axial compressors through a Stace Stacking Technique (SST)

The Stage-Stacking Technique (SST) is a well known methodology and it is widely used in the calculation of performance maps in turbomachinery. It is employed to build the overall compressor characteristic once the performance of each stage is known. In that case, the SST is applied as a mean-line technique so each thermodynamic property is represented by a single value at each section. The SST accounts for the mass flow conservation over the compressor, the velocity triangle at each section (rotor leading edge), and the momentum and energy equation through the information given by the correlations derived by CFD. At each stage, a system of non-linear equations is solved to calculate the flow properties at the stage inlet (station 1 in Figure 6.20) as a function of the known flow field at the stage outlet (station 2 in Figure 6.20). The system of equations that is solved is presented below.

$$\dot{m} = \rho_1 V_{x1} A_1 = \rho_2 V_{x2} A_2 \tag{6.16}$$

$$V_1 = \sqrt{V_{x1}^2 + \left(U + \left(V_{x1} \tan \beta_1\right)\right)^2} \tag{6.17}$$

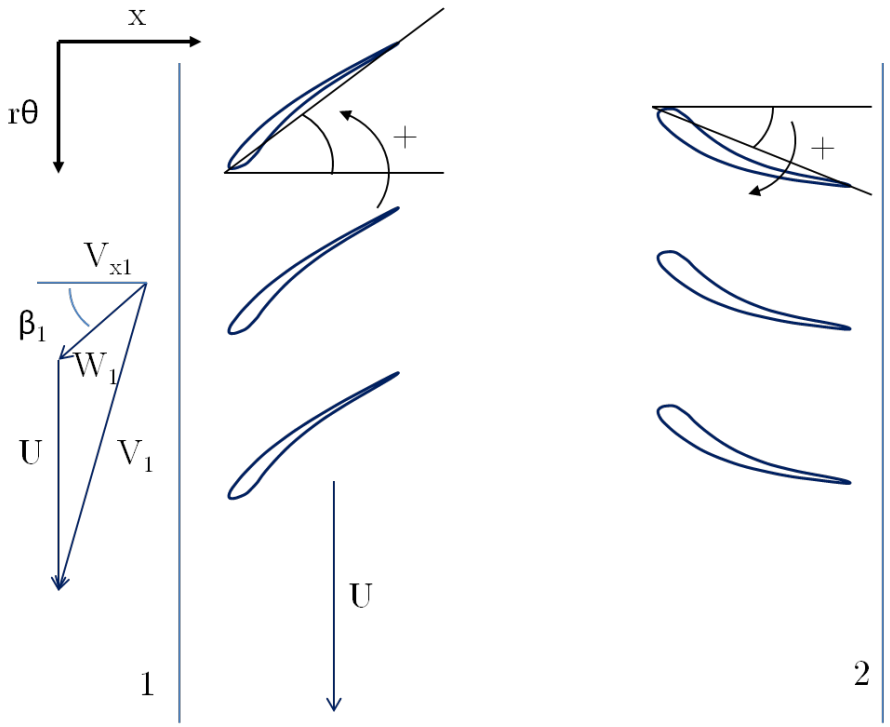

Figure 6.20: Blade-to-blade plane at reverse flow conditions - Sign convention

$$\psi_p(\phi_1) = \frac{p_2 - p_1}{\frac{1}{2}\rho_1 U^2} \tag{6.18}$$

$$\psi_\tau(\phi_1) = \frac{2C_{p1}\phi_1(T_{t2} - T_{t1})}{U^2} \tag{6.19}$$

$$\phi_1 = \frac{V_{x1}}{U} \tag{6.20}$$

$$\frac{P_{t1}}{p_1} = \left(1 + \frac{\gamma - 1}{2} M_1^2\right)^{\frac{\gamma}{\gamma - 1}} \tag{6.21}$$

$$\frac{T_{t1}}{T_1} = 1 + \frac{\gamma - 1}{2} M_1^2 \tag{6.22}$$

$$M_1 = \frac{V_1}{a_1} \tag{6.23}$$

$$a_1 = \sqrt{\gamma R T_1} \tag{6.24}$$

$$p_1 = \rho_1 R T_1 \tag{6.25}$$

It is necessary to establish here the sign conventions for the velocities and angles. Blade speed (U) is always positive. Axial velocity (V_x) is negative in reverse flow so the mass flow is negative too. Absolute velocity (V) and associated Mach number (M) are positive since absolute velocity is a vector modulus. Regarding angles, they are positive when measured in an anticlockwise sense for rotors and in a clockwise sense for stators (see Figure 6.20).

The heat capacity at constant pressure and the heat capacity ratio for air play a significant role in the system of equations. Since typical temperatures in a reverse flow scenario can be higher than 1500 K, it has been necessary to include a model to calculate C_p and γ accurately as a function of temperature. The model developed by Bucker [10] has been utilised. It is accurate below 3300 K.

The parameters used to correlate the single-stage performance are static-to-static pressure coefficient and torque coefficient as functions of flow coefficient. Equation 6.18 and Equation 6.19 show the definition of these non-dimensional groups. Flow coefficient is the measure of the mass flow through the compressor expressed as a velocity ratio using the rotor blade velocity to non-dimesionalise. Static pressure coefficient is the static pressure drop non-dimensionalised by the dynamic head based on the rotor blade velocity; torque coefficient is expressed in an equivalent manner. This expressions result from the application of the Π-Buckingham theorem to the problem of compressor stage performance. The advantage of using these non-dimensional groups is that the correlations obtained are independent of the compressor rotational speed and the flow conditions at the inlet of the stage.

Torque coefficient has been used as the property to evaluate the energy equations in place of other possible option such as a total temperature coefficient. The reason for that is to avoid another measurement which relies on an average value at interface planes. During the process of correlation derivation, it has been seen that torque coefficient correlations are more stable over the reverse flow operating region. Total temperature profiles along the circumferential coordinate show large variations around the average value while the integral of the pressure forces over the rotor blade wall has been seen to be more stable due to the fact that the flow pattern within the blade-to-blade region is much more stable than in the mixing region. Those reasons invite to use torque coefficient correlations as part of the SST methodology.

The SST, as described above, has been implemented using the programming language FORTRAN. The software consists of a main program, 3 subroutines dedicated to in/out procedures and 15 subroutines dedicated to calculations. It needs to be provided with 2 input files and produces a single output file. The only input file that has to be provided by the user is the same input file used by the in-house (sponsor) software VU59. As it was explained in Section 6.2.3, VU59 is a code for compressor performance analysis based on mean-line theory. Since the reverse flow SST software is also based on a mean-line approach, all the information needed is readily available within the input file of this code. Therefore, this software is completely compatible with data files available within the sponsor company and it has been thought to be user friendly and straight forward to be applied in the context of the industry. The input file contains the annulus geometry, compressor blading information and variable geometry schedule, among others. Apart from that, the user can define the non-dimensional rotational speed of the characteristics to be computed. The second input file provides the code with a 'library' of single-stage characteristics and it does not need to be modified by the user.

Figure 6.21 shows the block diagram which illustrates the structure of the code. The program starts reading, storing and converting to SI units the needed data from the input file. Once all this information is available, the subroutine GEOMETRY_ CALCULATION calculates all the derived geometrical data that the software needs during the whole process. Subsequently, the subroutine SINGLE_ STAGE_ MAPS reads the information related to single-stage performance contained in the file SINGLE_ STAGE_ CORRELATIONS.PRN. Then, the main calculation process of the program starts. A loop structure will repeat this process (same set of calculations) for as many speed lines as the user has requested in the input file. Firstly, the variable geometry schedule is applied to generate the compressor geometry which corresponds with the rotational speed that is going to be simulated. Secondly, the subroutine SPEED_ LINE_ CALCULATOR carries out the SST, calculating one operating point each time. Each operating point is defined by an imposed mass flow going through the compressor in reverse flow. Once the flow properties for every operating point of every speed line have been calculated, the subroutine MAPS_ CALCULATOR calculates the overall compressor performance and generates the maps. Finally, all the results are written in the output file by the subroutine WRITE_OUT.

The output file is divided into two parts: the first part gives the profile of thermodynamic properties over the compressor in reverse flow, characteristic by characteristic

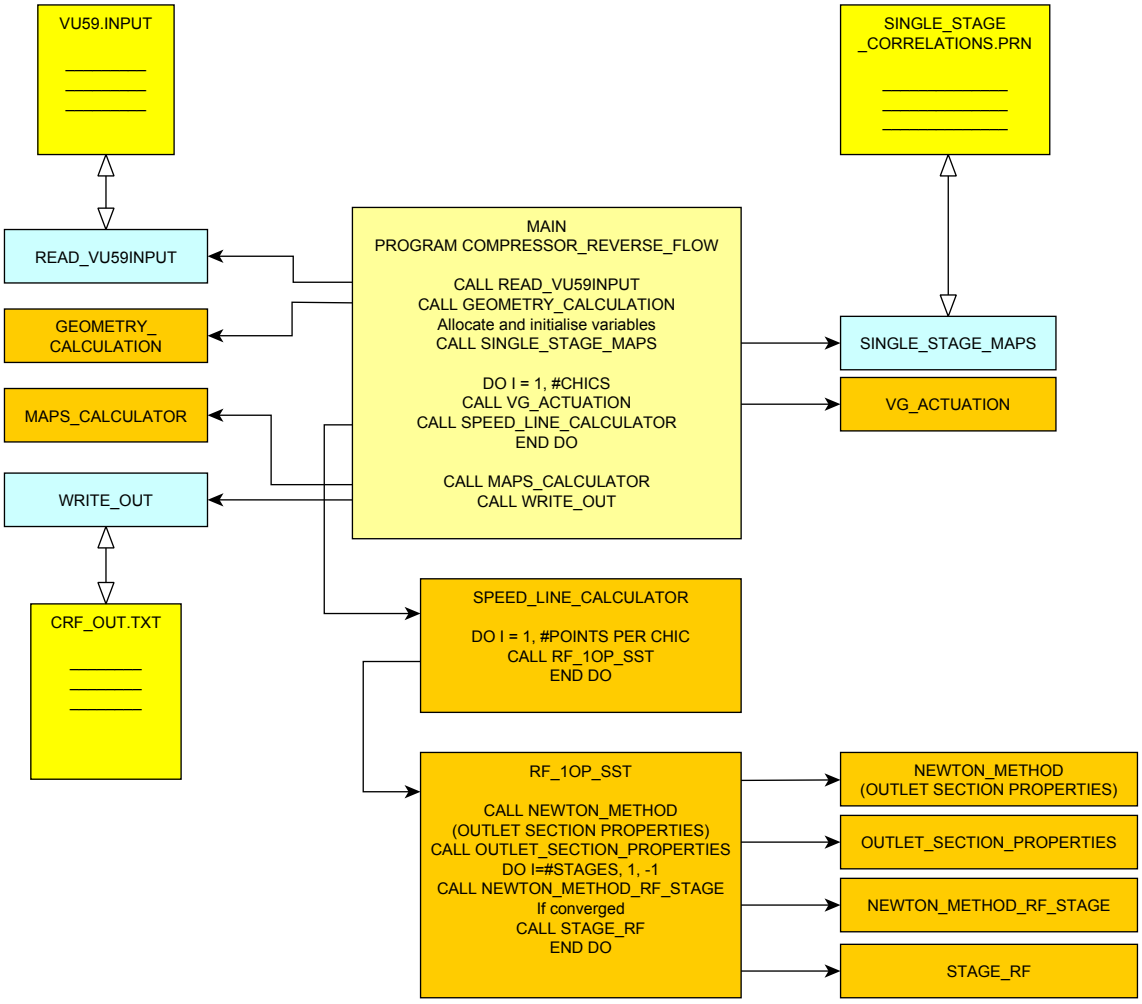

Figure 6.21: SST code structure

and one operating point each time; the second part offers the compressor map in two different ways, namely, pressure coefficient and torque coefficient as a function of flow coefficient, and pressure ratio and adiabatic efficiency as a function of non-dimensional mass flow. Note that the values used to non-dimesionalise the maps are the properties at compressor outlet since this is the inlet at reverse flow. Nevertheless, the blade speed used in the first set of maps is calculated with the radius at the mid-span of the first rotor.

Single-stage performance at reverse flow conditions by CFD analysis

CFD analysis has been decided, as explained above in this section, to be the most suitable approach to study the behaviour of the different compressor components (last stage, intermediate stage, IGV) at reverse flow conditions. The objective of this part of the research is the mapping of the single-stage performance by means of generic maps. Details about the CFD model, parametric analysis in terms of stage geometry and the derived single-stage maps are presented in this subsection.

The full three-dimensional geometry of a modern axial compressor provided by the sponsor was chosen to be modelled by means of 3D CFD. This geometry was considered to be a good example of a modern transonic axial compressor. This geometry was used as a baseline to carry out parametric analysis of those geometrical features that can affect reverse flow performance. Therefore, as it is shown below, this analysis aims to derive generic single-stage maps at reverse flow that are not stick to a particular geometry but can be applied to any stage geometry within the wide range explored during the parametric analysis performed.

The baseline compressor is an 8-stage intermediate pressure compressor utilizing four variable-geometry stages. The domain simulated includes the last two stages plus the stator of the sixth stage. This domain contains enough blade rows to extract the desired stage characteristics. More specifically, from this '2.5-stage' model, useful information was collected about the performance characteristics of a typical intermediate stage, a typical last stage and an IGV-like stator row.

The eighth stage behaves like a so-called last stage when the incoming flow through the compressor outlet section has no swirl velocity component. The seventh stage operates like an intermediate stage since it receives a flow with a high swirl component from the eight rotor and the flow leaving the stage is 'blocked' by the sixth stator which is also simulated. Therefore, the stator of the sixth stage is included

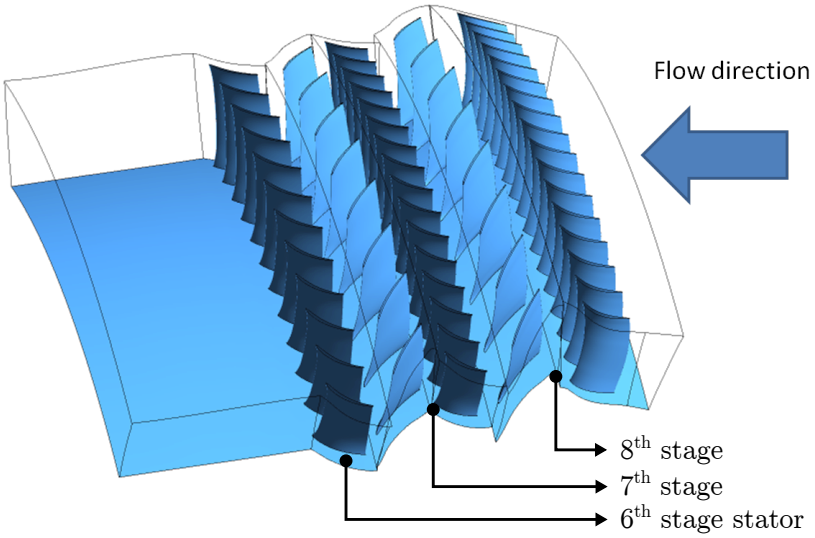

Figure 6.22: 3D CFD simulation domain

in the domain to fulfil a double purpose, i.e. it imposes a blockage to the seventh stage, which is necessary to extract realistic results, and also acts as an IGV from the point of view of performance (it 'sees' a high-swirl flow coming from the rotor and the flow is discharged downstream without being blocked by a blade row). Finally the domain is extended about three times of the chord of the blade so that the flow could stabilize and the influence of the boundary conditions could be avoided [6].

Regarding to the choice of the most suitable domain, an analysis of the effect of the number of passages simulated has been carried out. The reverse flow phenomenon is assumed to be periodic along the circumferential coordinate, nevertheless, the application of this assumption is not as certain as in the case of normal operation in forward flow. Reverse flow is dominated by highly separated flow and three-dimensional effects which provoke that the flow field changes with the relative position of rotor and stator along the rotor movement. From the point of view of CFD, the choice of number of passages included within the domain determines where the periodic boundary conditions are imposed. It has been observed that the imposition of these boundary conditions has an effect on the results when few passages are included in the domain. The present analysis tries to elucidate the number of passages that is necessary to simulate in steady state conditions to make the results independent of this parameter in terms of performance.

The simulation of a characteristic operating point in reverse flow has been carried out repeatedly with domains including a different number of passages from a single-

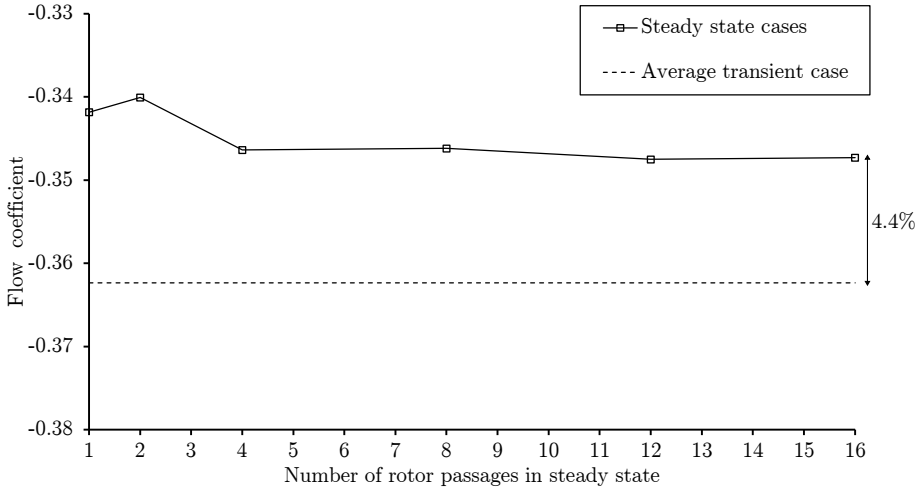

Figure 6.23: Number of passages independence study - Flow coefficient

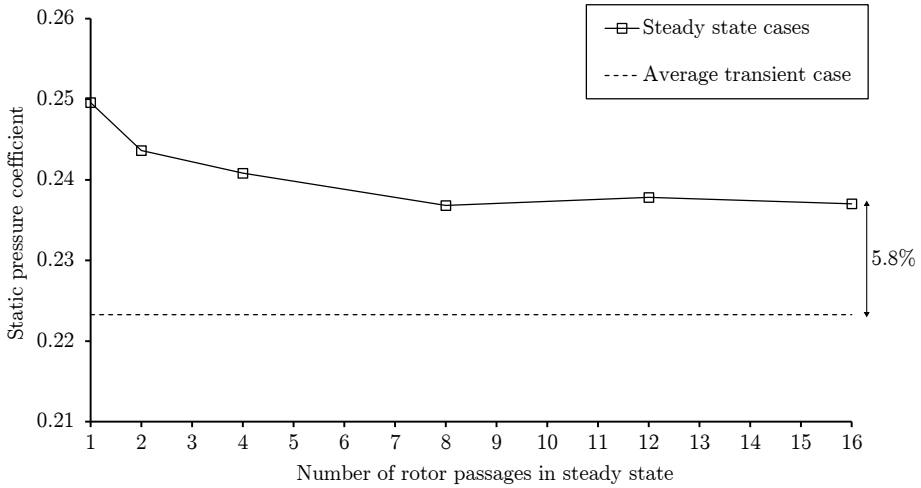

Figure 6.24: Number of passages independence study - Static pressure coefficient

passage simulation to 16 passages. The information obtained has been used to undertake the independence study of the number of passages.

Figures 6.23, 6.24 and 6.25 show the independence analysis for the three parameters used in the performance analysis, namely, flow coefficient, static pressure coefficient and torque coefficient. The results show that the asymptotic behaviour is reached when 8 or more passages are simulated. At that point, it has to be taken into account that the number of passages of the simulation domain determines the size of the computational model mesh and it has a direct impact on the computational resources and time needed. Since the number of simulations required to derive the generic maps is large (approx. 130 cases), it has been decided to choose a 4-passage domain as a trade-off between accuracy and computational cost. It can be observed in the figures that the 4-passage simulation produces values of flow coefficient and

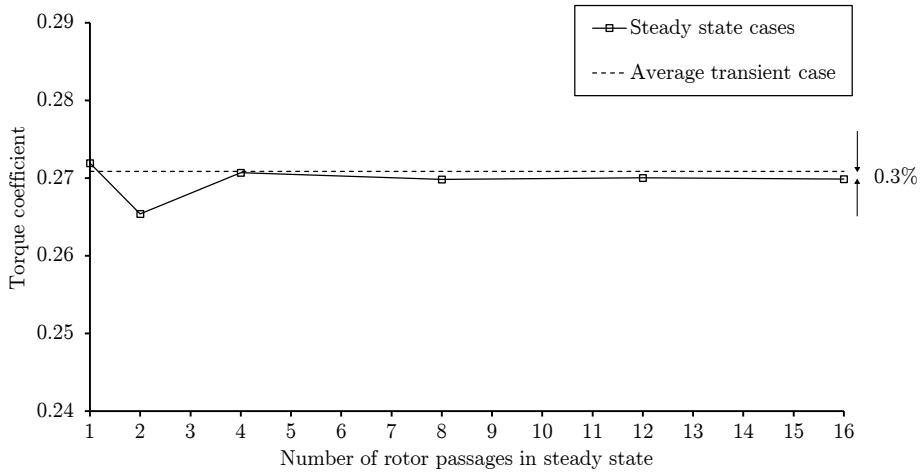

Figure 6.25: Number of passages independence study - Torque coefficient

torque coefficient which are already in the asymptotic region while provokes an error of only 1.5% in the static pressure coefficient. The right trade-off invites to pay this small error in pressure coefficient in order to reduce the computational cost to the half.

Once the domain geometry has been chosen, the next step is to create the mesh of this domain. Due to the complex flow pattern that characterises the reverse flow, high pressure gradients and velocities are expected and, as a consequence, a near-wall low Reynolds approach was followed. In terms of the grid structure, a structured O-Grid mesh was applied to the boundary layer region (around the blade), whereas a structure H-Mesh was preferred for the rest of the domain. Regarding the treatment of the boundary layer, a recommended value of y-plus of 2 has been obtained [98]. In order to ensure that the solution of the simulation do not depend on the size of the grid, a mesh sensitivity analysis has been carried out and three different grids were tested: a coarse grid of $2 \cdot 10^5$ elements, a fine mesh of $6 \cdot 10^6$ elements and an intermediate grid of $3 \cdot 10^6$ elements. The results of the sensitivity analysis are shown in Figure 6.26. The coarsest grid was obviously discarded as the solution it obtains is inaccurate and misleading. Then, the other two meshes were compared and the differences turn out to be 0.2% in the majority of the parameters and less than 0.8% in the rest. Taken into account these observation, the grid of $3 \cdot 10^6$ elements has been chosen as the best trade-off between accuracy and computational cost [80].

Regarding the turbulence model, the $k - \omega$ Shear Stress Transport model has been chosen. This model was specifically designed to provide a highly accurate prediction of the onset and the amount of flow separation under adverse pressure gradients [1]. Furthermore, it has proved also outstanding performance predicting flow separation

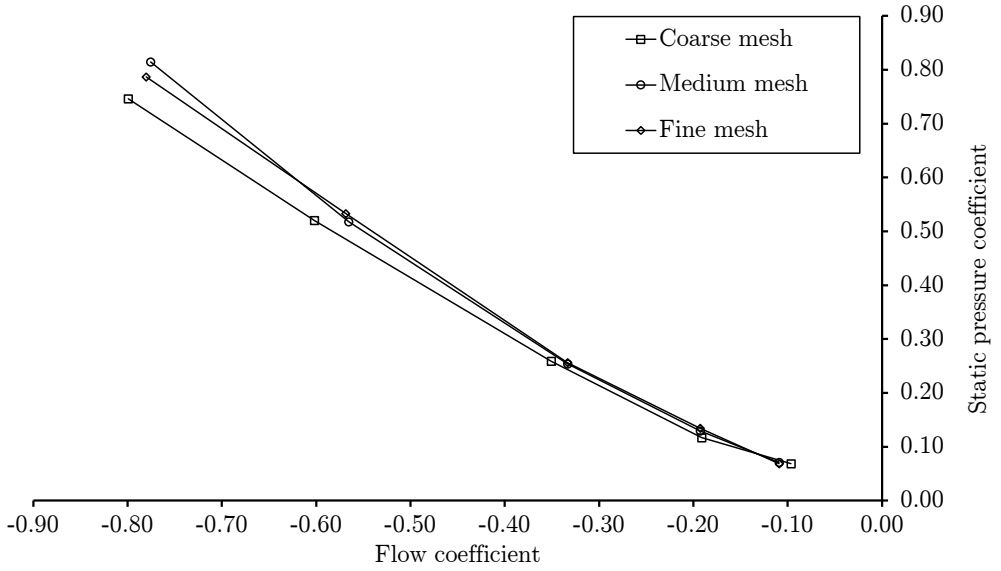

Figure 6.26: Mesh independence study - Pressure coefficient

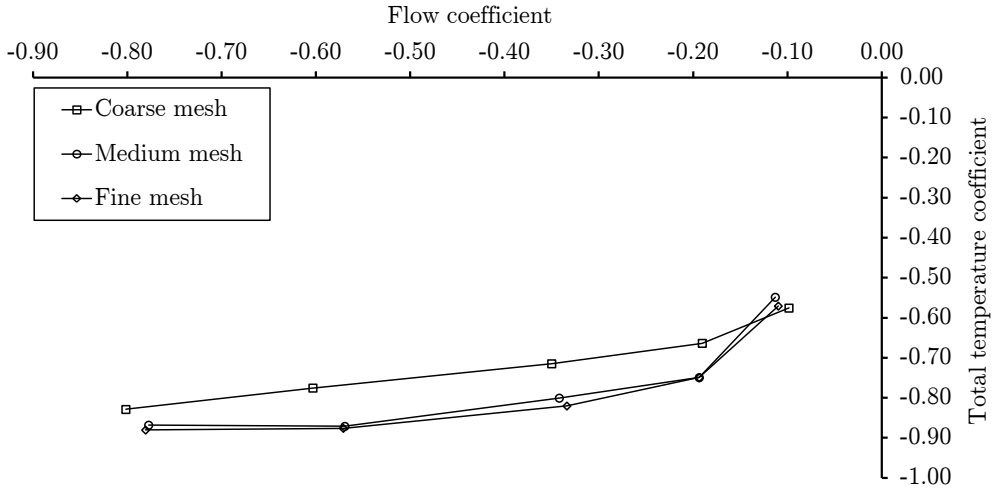

Figure 6.27: Mesh independence study - Temperature coefficient

and big separation bubbles in a large number of validation studies [9].

The selection of boundary conditions is an important step when setting up a CFD simulation. According to the recommended practices for turbomachinery, the selected conditions have been total pressure at the inlet of the domain and static pressure at the outlet [1]. To derive the single-stage maps, a wide range of operating points needs to be simulated. Values from 0.0 to -1.0 of the flow coefficient have been explored by changing the total pressure at the inlet of the domain (compressor outlet) while keeping constant the value of the static pressure at the outlet of the domain at ambient pressure.

Turbomachinery simulation in CFD requires to choose the interface model to allow the flow properties transition from a rotating frame to a steady frame. The options available in steady state mode are: 'frozen rotor' and 'stage'. The latter is based on performing a circumferential average of the flow properties at the interface and delivers a uniform flow to the next row [1]. This option is not acceptable at reverse flow conditions since the complete mixing of the flow cannot be assumed from one row to the next one. The former is the right choice for the present scenario. It consists of changing the frame of reference in the interface.

Frozen rotor interface model have several drawbacks that must be bear in mind: firstly, the results may be dependent on the relative position of the rotor respect to the stator; secondly, this methodology does not take into account the transient effects at the frame changing interface. A more accurate interface between two subdomains is available when the transient solver is used. This is known as the 'Transient Rotor-Stator' model. This model accounts for the transient interaction between rotor and stator. This model updates the location of the interface each time step as the relative position between components changes. However, this method requires very large computational resources and it will turn into an impossible task the derivation of generic single-stage maps at reverse flow conditions. Therefore, in order to make possible the achievement of the main objective of this research, a certain level of accuracy is sacrifice. Nevertheless, a transient simulations has been performed in the context of the present research with the objective of quantifying the error incurred when steady state approach is used to study the reverse flow performance.

Figures 6.28, 6.29 and 6.30 show the comparison between the results acquired through the transient simulation and the results of the different steady state simulations for different number of passages. The transient simulation has been run

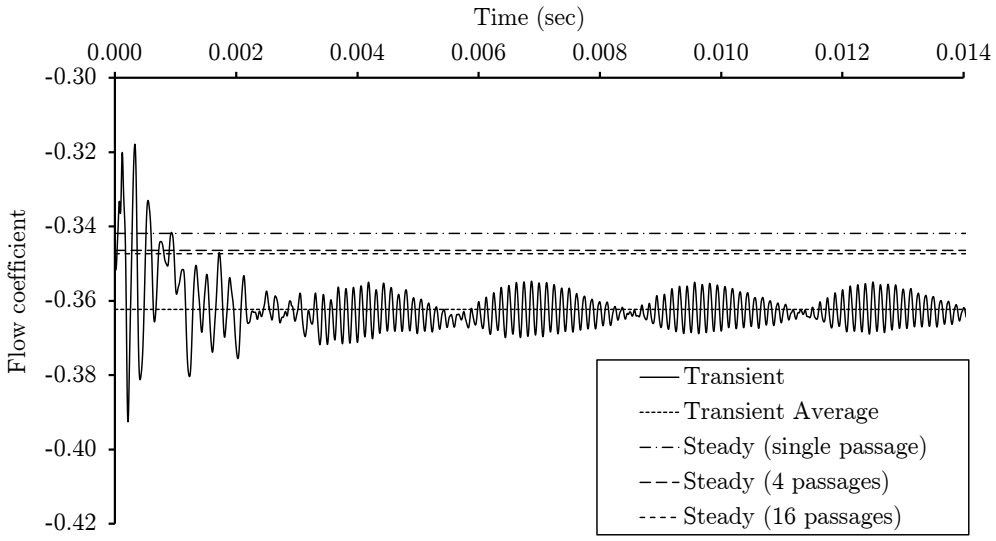

Figure 6.28: Flow coefficient at reverse flow - Transient vs steady state

during two rotor revolutions. It can be observed that this simulation time is enough to allow the solver to reach a periodic 'quasi-steady' solution.

Several conclusions can be drawn from the observation of these results. Firstly, the steady state solution for the static pressure coefficient improves with multiple passage simulations; secondly, regarding the flow coefficient, the same behaviour as in the case of the static pressure coefficient can be appreciated. In both cases the asymptotic behaviour leads to values which show a constant level of error when compared with the average of the transient simulation (see Figures 6.23 and 6.24). Therefore, this analysis allows to identify the magnitude of error provoked by the use of a steady state solver combined with the frozen rotor interface mode. On the other hand, these differences are not observed in the case of torque coefficient. In that case, the steady state analysis captures accurately the average value of the transient simulation. The careful observation of the flow field evolution in the transient simulations gives explanation to the particularities observed here. It has be observed that the flow pattern between stator vanes and in the interface change as a consequence of the movement of the rotor, while the flow pattern within the rotor blade row remains fairly constant. The difference between what is modelled by the steady and the unsteady CFD is the capability to capture the phenomena related to the relative movement between blades (rotor blades passing in front of stator blades). Therefore, taking into account that flow and pressure coefficients are calculated attending to flow properties measured/averaged in the interface plane while torque coefficient is calculated integrating the pressure field around the rotor blades, it is easy to explain the differences observed in the prediction capability

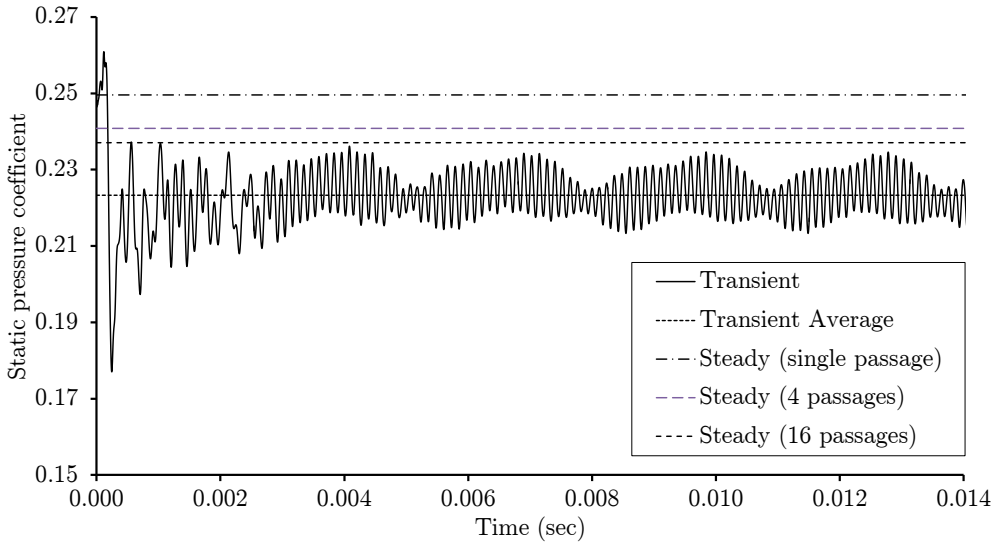

Figure 6.29: Pressure coefficient at reverse flow - Transient vs steady state

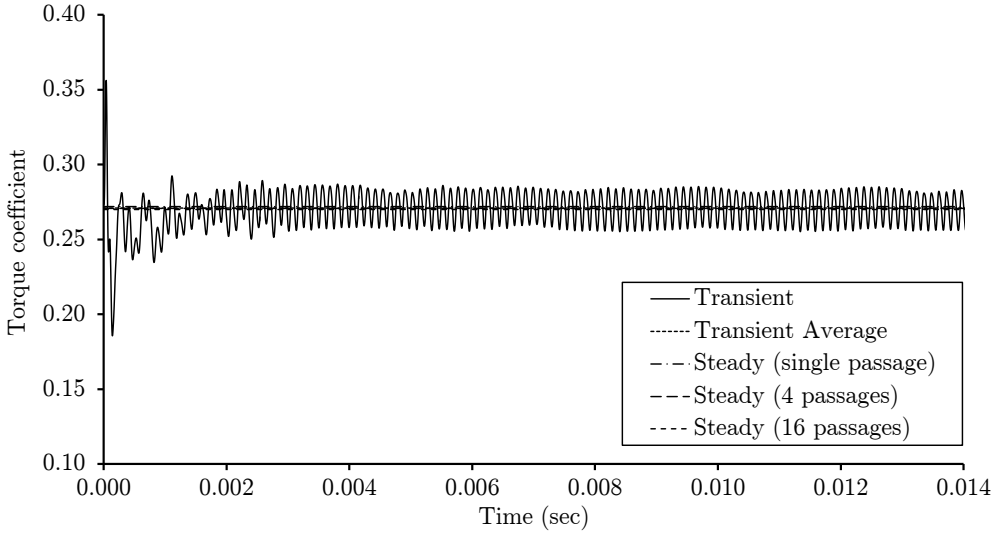

Figure 6.30: Torque coefficient at reverse flow - Transient vs steady state

using the steady state simulations.

It can be concluded that the errors incurred by a methodology based on steady state CFD simulations are given by the largest error among the performance coefficients. This parameter is the static pressure coefficient and the error when it is compared against a transient simulation is 7.3% for the case of 4 passages. This case has been chosen as the only feasible way to derive the generic single-stage maps needed by the SST to produce the generic capability which was aimed by the present research.

At that point, once the methodology to use 3D CFD analysis to derive reverse flow characteristics has been established, the results of this study are shown. As it has been said over the present section, it is aimed to reach a highly generic capability to predict any compressor reverse flow performance. Therefore, any geometry feature which could differentiate one axial compressor from another has been accounted and its effect has been studied. Although the analysis of reverse flow scenario has been shown here to be extremely complex in terms of flow pattern, it is going to be these facts, namely, highly separated and chaotic flow field, which will allow to reach general conclusions and generic correlations that could be widely applied to any compressor geometry. The stage geometry features that have been analysed are the solidity and the stagger angle of each blade row. The result of this parametric analysis invite to state that other parameters to define more in detail the shape of the blade profile such a camber angle, thickness, leading and trailing edge metal angles, etc, will not have any appreciable influence when they vary within the typical values used in axial compressor blades.

Extensive parametric analyses were carried out using as a baseline the real geometry of a modern axial compressor. Real geometry data from a wide range of axial compressors were collected in order to establish a range of variation for blade row solidity and rotor and stator stagger angles. Firstly, a set of simulations was undertaken to assess the effect of solidity on reverse flow performance. The number of blades was altered to change the solidity by +10% in the rotor and stator of the so-called intermediate stage. The comparison of the results is shown in Figure 6.31. The results confirm that changes in solidity within typical values have no effect on reverse flow performance.

Secondly, the effect of the rotor stagger angle was assessed. The variation of this angle that has been found within all the stages of all the compressors assessed is +/- 8 deg so this has been the range explored by means of the CFD simulations. The results derived from this analysis are shown in Figures 6.32 and 6.33.

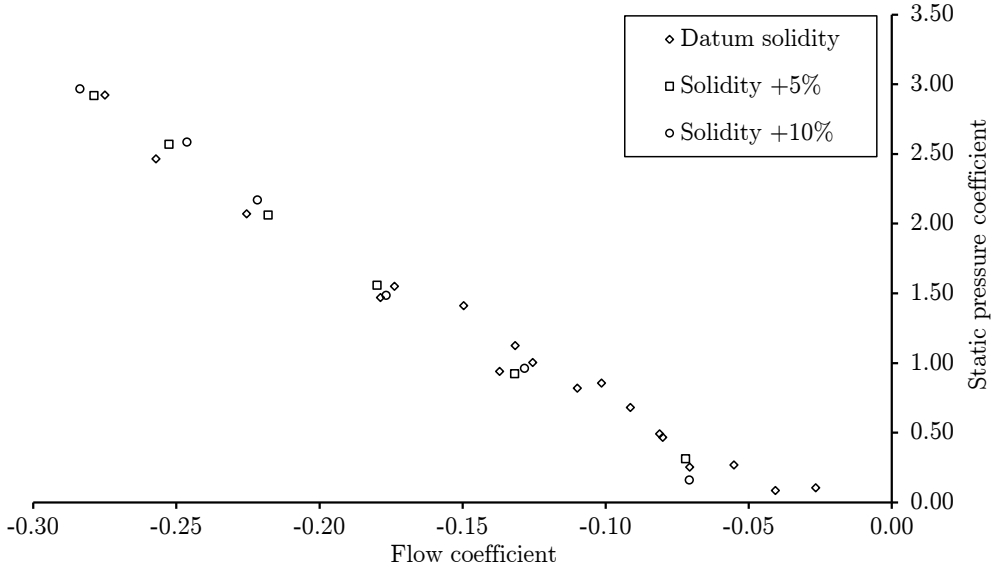

Figure 6.31: Effect of solidity on reverse flow performance

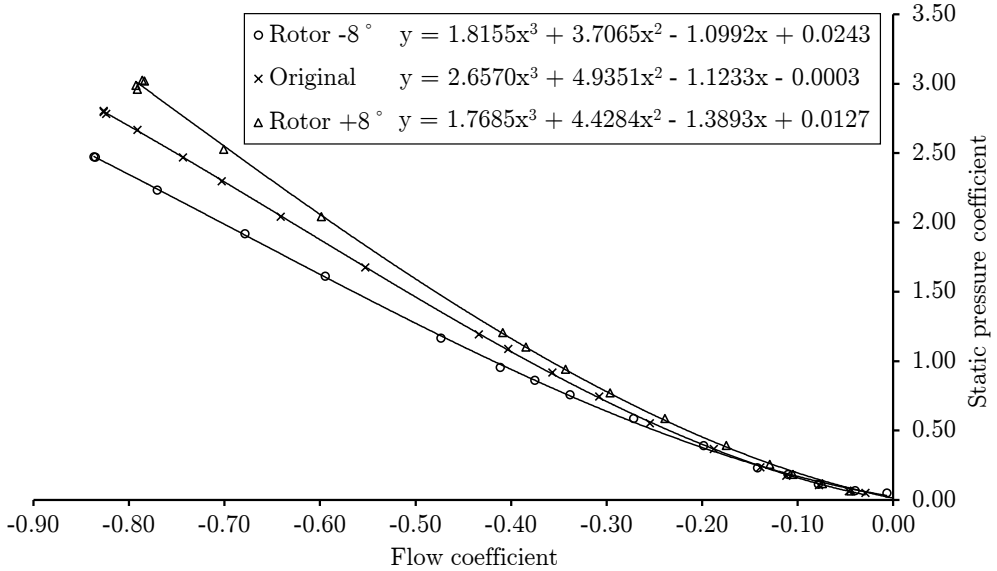

Figure 6.32: Single-stage map at reverse flow conditions - Influence of rotor stagger angle - Static pressure coefficient

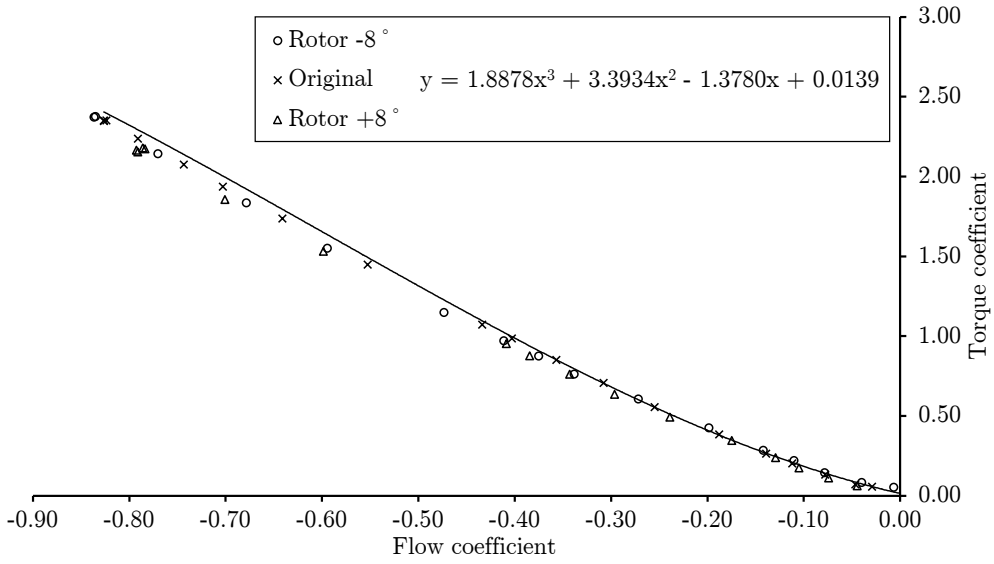

Figure 6.33: Single-stage map at reverse flow conditions - Influence of rotor stagger angle - Torque coefficient

It can be observed that variations in rotor stagger angle within the range tested have no effect on the compressor power consumption through the torque coefficient while the effect on pressure coefficient is noticeable at high flow coefficients.

Finally, the effect of the stator stagger angle has been assessed. In that case, the range of variation of this parameter has been chosen taken into account the possibility of variable geometry as is typically found in modern compressors. The results of this analysis are presented in Figures 6.34 and 6.35.

The general trends observed in the static pressure coefficient in both cases agree with the expected. Namely, pressure drop across a stage in reverse flow grows with the mass flow through the stage and also with the value of stagger angle (same effect in rotor and stator) which mean a higher blockage to the flow. On the other hand, torque coefficient plot in Figure 6.35 shows a particular behaviour for the lowest value of stator stagger angle while the rest of cases follow the same trend. This change in the trend can be explained attending to differences in blade loading provoked by changes in the flow pattern.

Figure 6.36 and Figure 6.37 show the velocity fields which correspond to the most 'open' case and one of the most 'closed' cases respectively. It is observed that, for high values of stator stagger angle, there is a high velocity jet impacting on the pressure surface of the rotor blade close to the trailing edge and, this jet is formed by the combination of two jets coming from the stator vane row. Nevertheless, this flow pattern is not present in the case with the lowest stagger angle. Figure 6.36

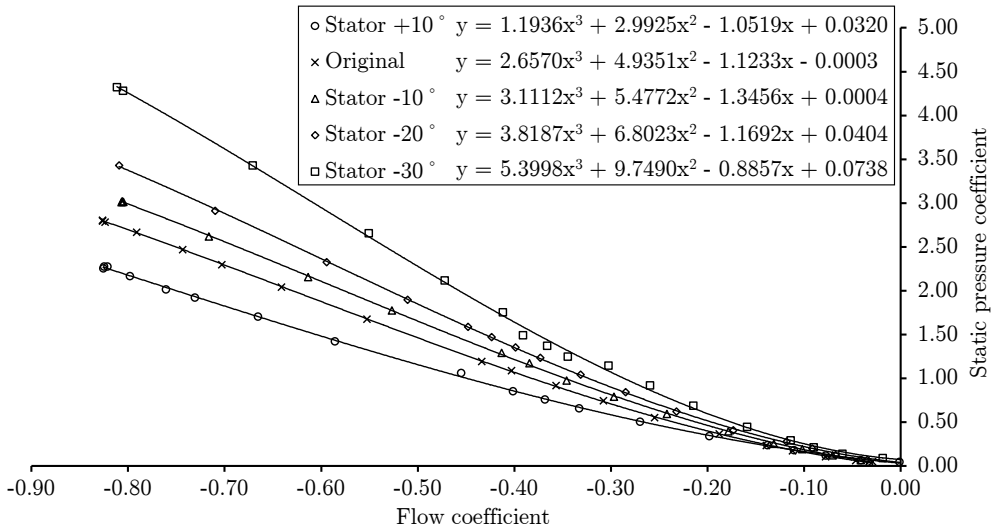

Figure 6.34: Single-stage map at reverse flow conditions - Influence of stator stagger angle - Static pressure coefficient

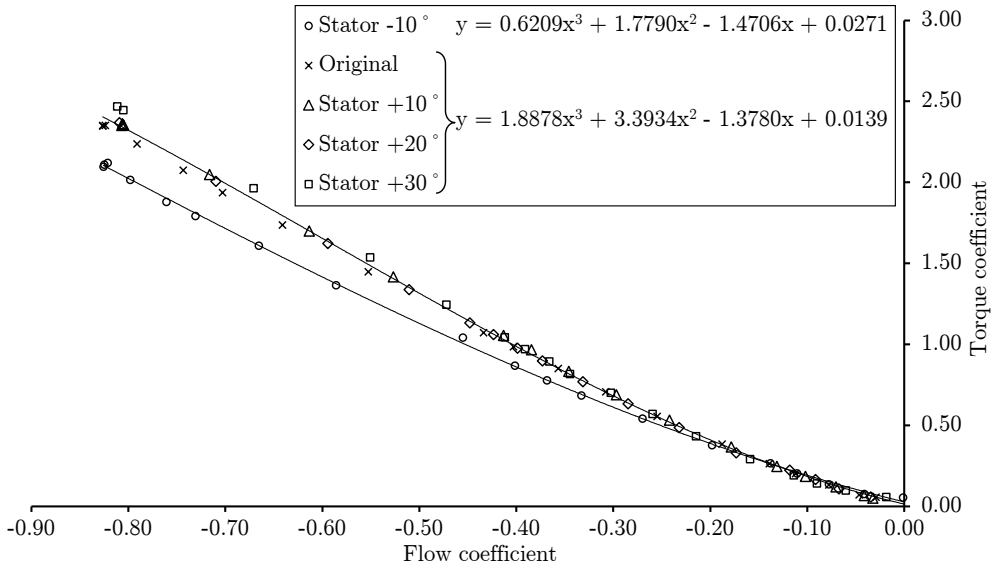

Figure 6.35: Single-stage map at reverse flow conditions - Influence of stator stagger angle - Torque coefficient

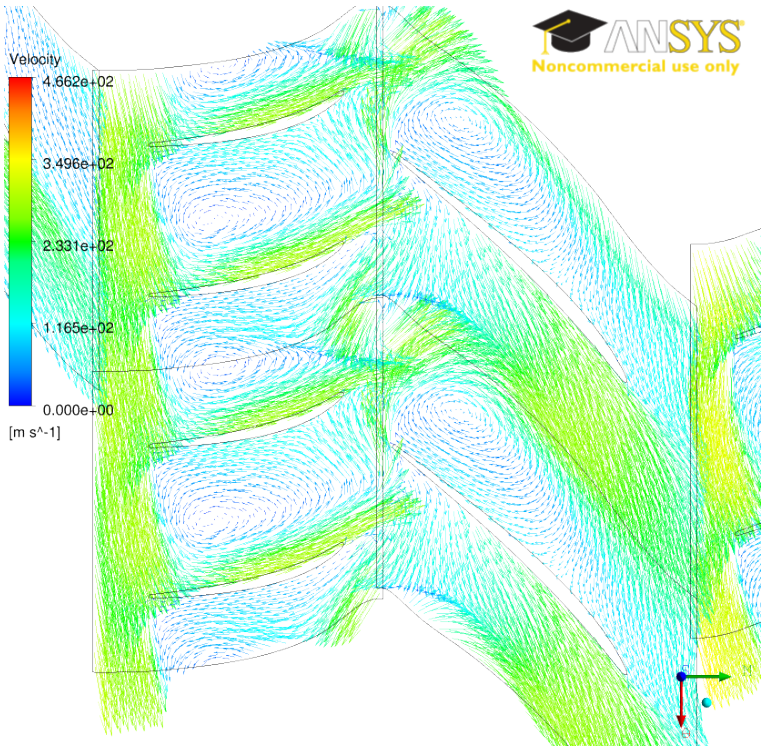

Figure 6.36: Effect of stator stagger angle on torque coefficient at reverse flow conditions - Stator open

shows how each stator vane jet penetrates the rotor blade row independently. One jet impacts against the rotor pressure surface and the next one penetrates in-between the blades, modifying the recirculation bubble structure. It can be concluded that a high stator stagger angle provokes a flow pattern where the jets coming from upstream stator vanes (reverse flow sense) are not able to penetrate into the bubble region but they are projected with a higher angle of incidence and combine together to impact the pressure surface of the rotor blade provoking a stronger stagnation point. The consequence of these differences in the flow patter in terms of blade loading can be observed in Figure 6.38. These differences in blade loading explain the lower torque coefficient experienced in the case with the lower stator stagger angle configuration.

Apart from the correlations presented above, the 2.5-stage domain also allows to derive correlations for pressure and torque coefficient for the last stage and for the IGV-like isolated stator. Figure 6.39 and 6.40 show these correlations. The trends are the same observed in previous plots.

The results shown above are coherent with the experimental evidences published by Gamache [40], namely, small variation in stage reaction has a negligible effect on compressor reverse flow performance. Nevertheless, the variations of stagger angles

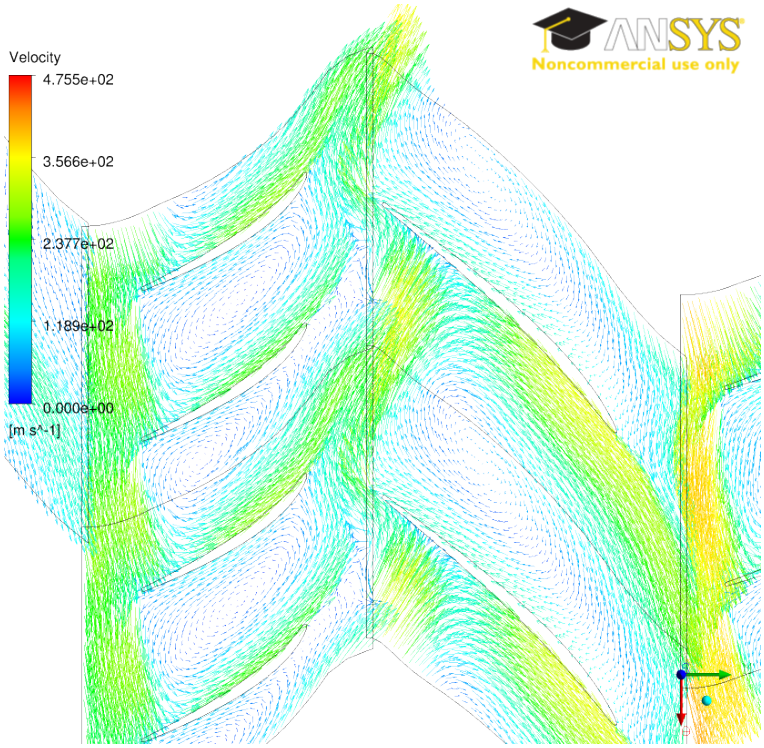

Figure 6.37: Effect of stator stagger angle on torque coefficient at reverse flow conditions - Stator closed

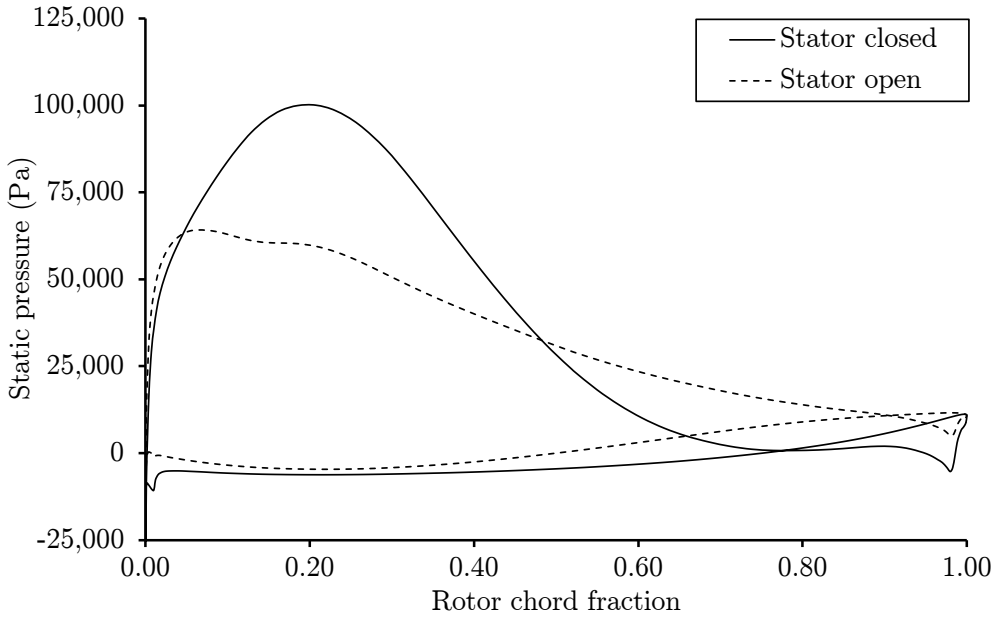

Figure 6.38: Effect of stator stagger angle on torque coefficient - Static pressure around the rotor blade

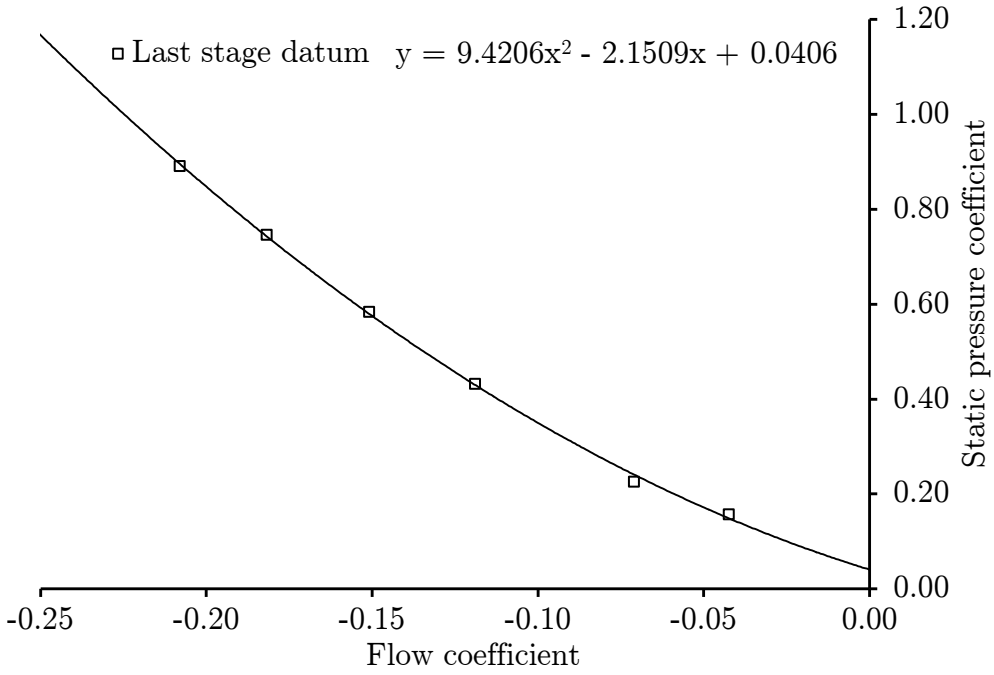

Figure 6.39: Last stage map at reverse flow conditions - Static pressure coefficient

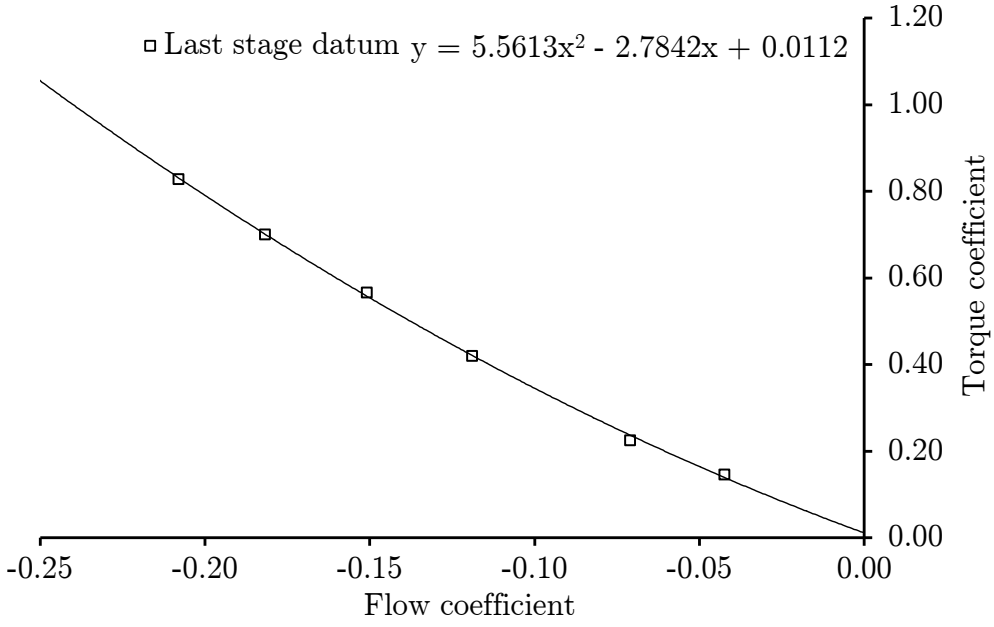

Figure 6.40: Last stage map at reverse flow conditions - Torque coefficient

tested by Gamache are within a narrower range than those tested in the present research. Furthermore, the flow coefficient tested in the low-speed compressor at MIT is lower than those where the influence of these parameters starts to be non-negligible.

The parametric analysis has shown the following functional relationships: static pressure coefficient is a function of flow coefficient, stator stagger angle and rotor stagger angle; torque coefficient is a function of flow coefficient and stator stagger angle but it is independent of the rotor stagger angle.

$$\psi_p = f\left(\phi, \gamma_r, \gamma_s\right) \tag{6.26}$$

$$\psi_\tau = f\left(\phi, \gamma_s\right) \tag{6.27}$$

In the case of torque coefficient, the information contained in the maps derived by CFD is complete, i.e. for a given stage geometry and flow coefficient, the value can be directly interpolated within the maps. The case of pressure coefficient is more complicated. It has been shown that this parameter is function of three variables, nevertheless, the information derived by CFD is given by two two-dimensional maps (see Equations 6.28 and 6.29). It means that the value of pressure coefficient cannot be directly interpolated for a given geometry and operating point. The problem has been linearised around the datum point.

$$\psi_p = g\left(\phi, \gamma_s\right)\big|_{\gamma_r^*} \tag{6.28}$$

$$\psi_p = h\left(\phi, \gamma_r\right)\big|_{\gamma_s^*} \tag{6.29}$$

$$\tilde{\psi_p} = g\left(\phi_1, \gamma_s^*\right)\big|_{\gamma_r^*} + \left.\frac{\partial g}{\partial \gamma_s}\right|_{\phi_1} \cdot \left(\gamma_{s1} - \gamma_s^*\right) + \left.\frac{\partial h}{\partial \gamma_r}\right|_{\phi_1} \cdot \left(\gamma_{r1} - \gamma_r^*\right) \tag{6.30}$$

Equation 6.30 shows the composition process to calculate the final value of pressure coefficient based on the linearization of the problem in the two variables rotor and stator stagger angles. This methodology is implemented within the SST to make possible the calculation of the coefficients for any given geometry under any operation conditions.

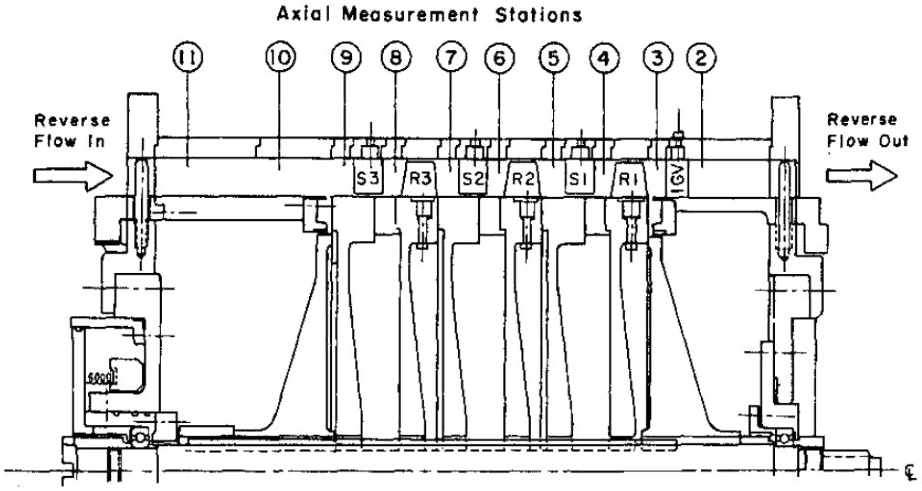

Figure 6.41: 3-stage low speed MIT compressor [40]

6.4.3 Validation

The overall reverse flow performance prediction methodology described in the present chapter, relies on the robust application of a Stage-Stacking Technique (SST), and the ability to accurately derive single-stage characteristics by means of 3D CFD analysis. Gamache's Thesis [40] contains information related to the behaviour of a low-speed 3-stage compressor with IGV, focusing on the performance of each stage, the evolution of the flow properties at various stations and the performance of the whole compressor during reverse flow operation.

The validation process presented here has been tackled from a global point of view, namely, the software tool has been directly applied to predict the reverse flow characteristics of a compressor that was experimentally tested. In other words, the input file containing the information of the 3-stage axial compressor at MIT, tested by Gamache, was prepared, and the SST, fed by generic maps derived through CFD simulations, was used to predict its reverse flow performance. A schematic of the compressor is shown in Figure 6.41.

The comparison between the experimental and the numerical results was based on the curves of total-to-static pressure coefficient and torque coefficient for the whole compressor. These coefficients were calculated using Equation 6.31 and Equation 6.32 (section's indexes related to Figure 6.41). From the point of view of the experimental measurements, it is attractive to choose this set of parameter because they were measured in places which minimise the possibility of error. The measurement of static pressure at section 9 is easy because the flow has not been affected

by the chaotic phenomena within the compressor. The static pressure radial profile exhibits a constant trend without radial gradients as observed in the inter-stage measurements [41]. This makes reliable the measurement taken by the static pressure probe at the casing. On the other hand, the measurement at section 0 is the total pressure in a plenum downstream the compressor so it can be considered a reliable measurement as well.

$$\psi_{p_{T-s}} = \frac{p_9 - P_{t0}}{\frac{1}{2}\rho U^2} \tag{6.31}$$

$$\psi_\tau = \frac{2C_p\phi_9\left(T_{t9} - T_{t0}\right)}{U^2} \tag{6.32}$$

Figure 6.42 and 6.43 show the result of this comparison exercise. The agreement of the total-to-static pressure coefficient characteristic is satisfactory having a Mean Relative Error (MRE) of 4.4%. The agreement for the torque coefficient characteristic is slightly worse having a MRE of 10%. This exercise confirms the reliability of the methodology and validates the tool developed. It is important to highlight that this validation shows the robustness of the methodology of the single-stage generic map approach. The single-stage characteristics were derived from CFD analysis of the geometry of a modern IPC (and variations of this) and they were subsequently successfully applied to model a compressor that is far from modern designs.

Static pressure profiles in reverse flow - Discussion

Apart from the validation presented above, the comparison exercise between the experimental results published by Gamache and the analysis of the results offered by the present methodology allows to extract other conclusions that are worth to be included here.

The compressor reverse flow analysis carried out by Gamache [40] presents the evolution of several thermodynamic properties over the compressor. Axial profiles of static pressure coefficient are shown based on measurements obtained by static pressure proves placed at the compressor casing. Figure 6.44 shows an example of one of these profiles, in particular, the case with flow coefficient -0.1.

Qualitatively, it can be inferred that the static pressure falls across stator rows, rises across rotor rows and falls greatly across the IGV. When these experimental results

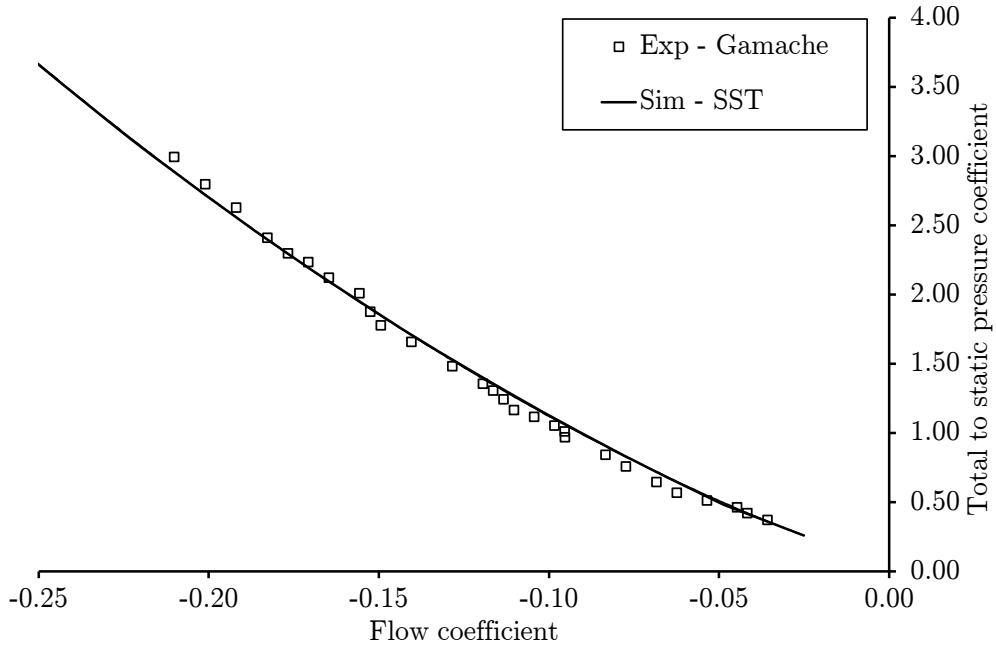

Figure 6.42: Reverse flow methodology validation - Static pressure coefficient

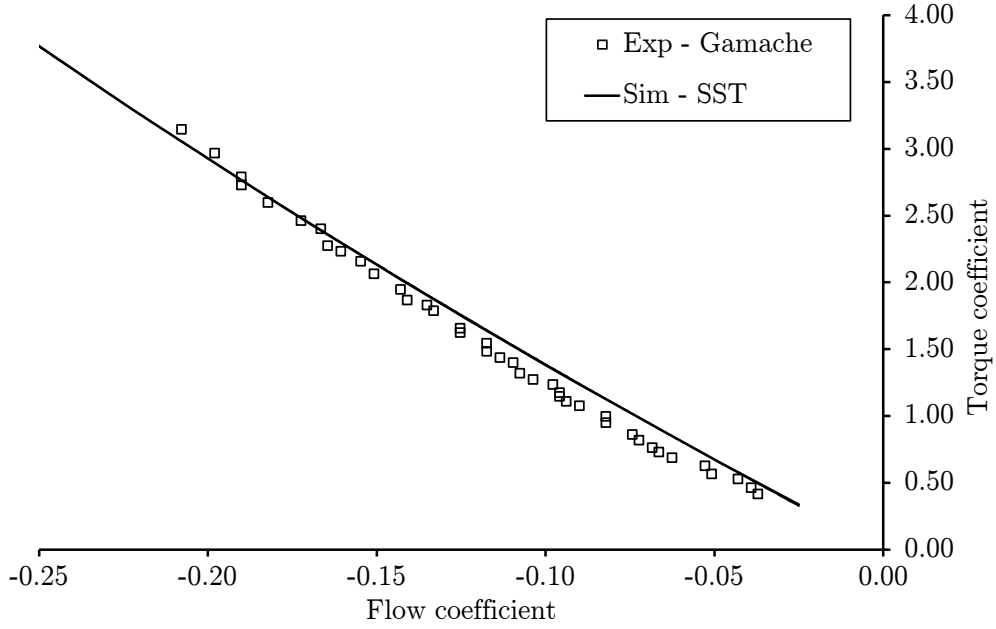

Figure 6.43: Reverse flow methodology validation - Torque coefficient

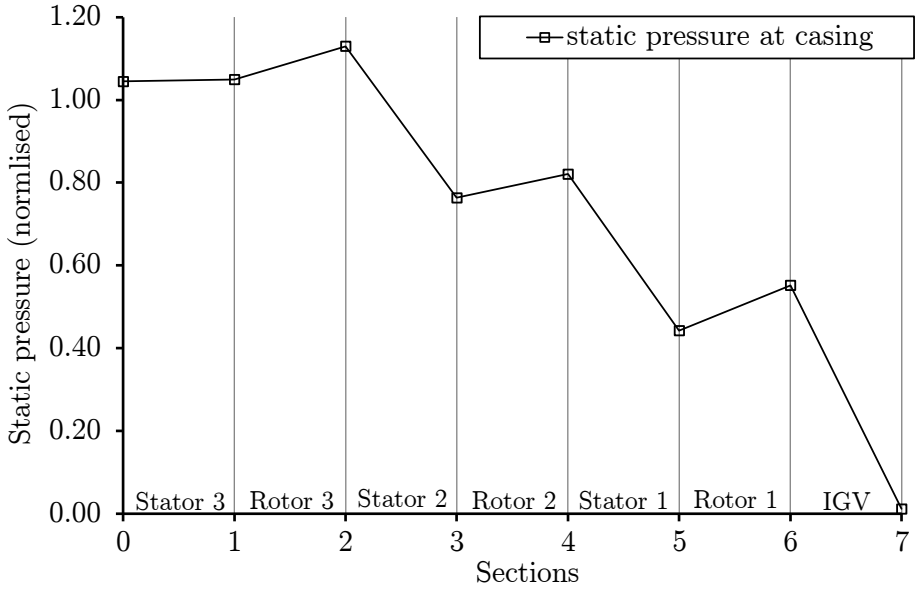

Figure 6.44: Static pressure profile at reverse flow - Gamache experimental measurements ($\phi = -0.1$)

are compared against the results of the CFD analysis, a qualitative disagreement is found. In that case, the profile of static pressure coefficient indicates that static pressure drops across stator and rotors in a similar fashion when the value is taken as area average at each section. Nevertheless, if the value of static pressure at the casing wall is taken, the qualitative evolution of the static pressure agrees with the trends presented by Gamache. In this author's opinion, it can be concluded that high pressure gradients in the radial direction provoke that the measurements of static pressure at the casing lead to misleading results. The compassion of these profiles can be observed in Figure 6.45.

6.4.4 Results - Modelling modern high speed multi-stage axial compressors

The compressor reverse flow performance prediction tool developed in the context of this research has been applied to calculate the map of two modern axial flow compressors. First example is a typical HPC and the second is a IPC. In this section results are presented and commented. The evolution of thermodynamic properties in compressors at reverse flow conditions, differences between compressors, and the effect of variable geometry mal-function are also discussed.

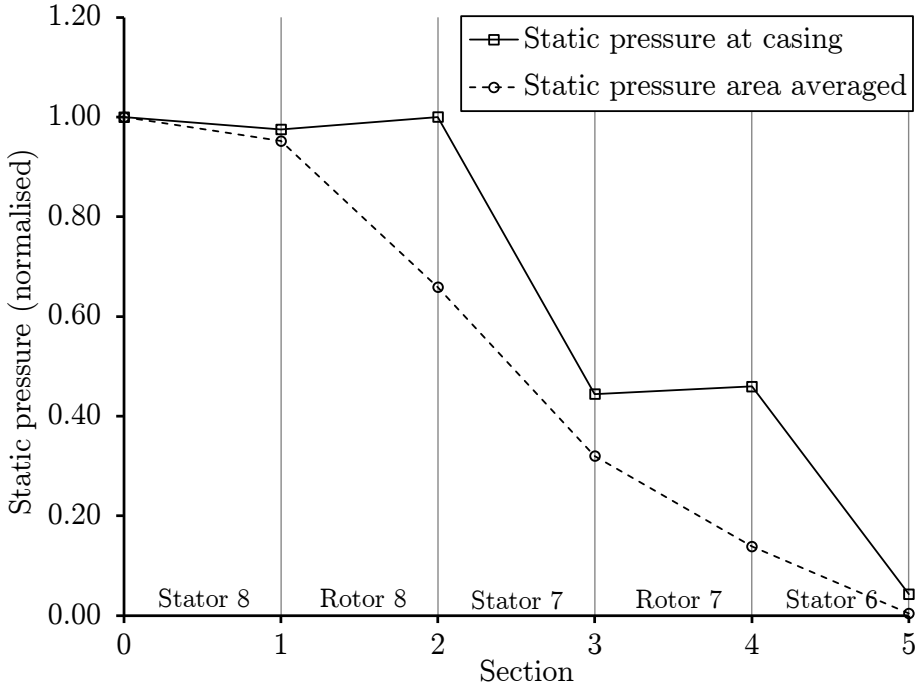

Figure 6.45: Static pressure profiles comparison - Misleading measurements in walls ($\phi = -0.13$)

HPC performance at reverse flow conditions

The compressor analysed is a 6-stage axial compressor without variable geometry. In the case of a hypothetical compressor surge, provoking reverse flow, the flow could enter the compressor straight from the combustion chamber through the compressor. Hence, it is assumed that the flow has no swirl velocity component and therefore, the last stage would behave as the last stage concept explained in Section 6.4.1.

The tool was used to calculate the reverse flow part of the compressor map and the characteristics have been plotted together with the compressor map at normal operation in Figure 6.46 and Figure 6.47. It must be taken into account that although both sets of curves, namely forward flow and reverse flow, have been plotted on the same map, the non-dimensonal parameters are defined differently for reverse flow, as explained in Section 6.4.2.

In Figure 6.46 it is useful to compare the compressor capacity in reverse flow with the normal capacity in forward flow. The slope of the reverse flow characteristic gives an idea of the 'opposition' or 'resistance' of the compressor to reverse flow. The mass flow range in reverse flow is one order of magnitude lower than in forward flow.

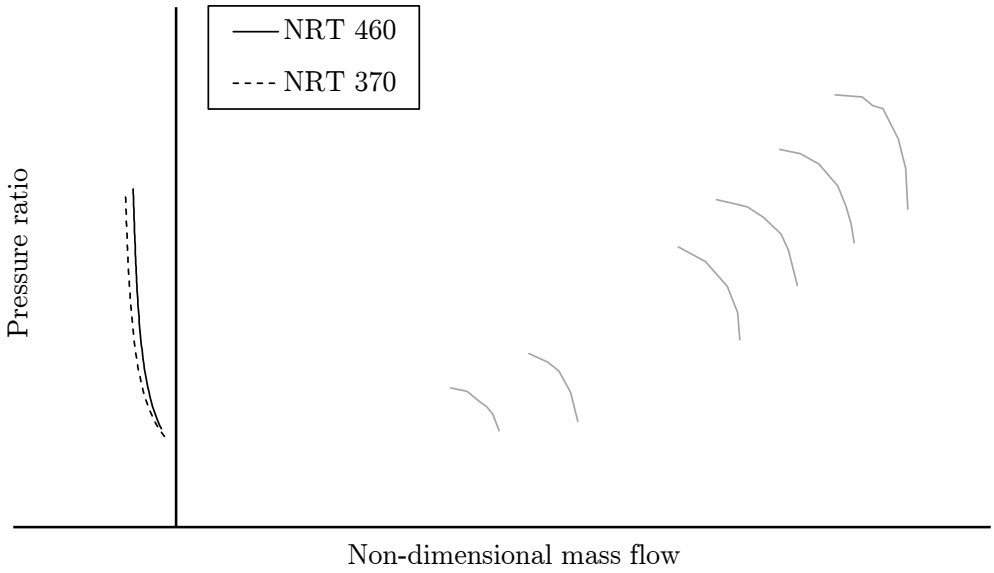

Figure 6.46: HPC map including reverse flow characteristics - Pressure ratio

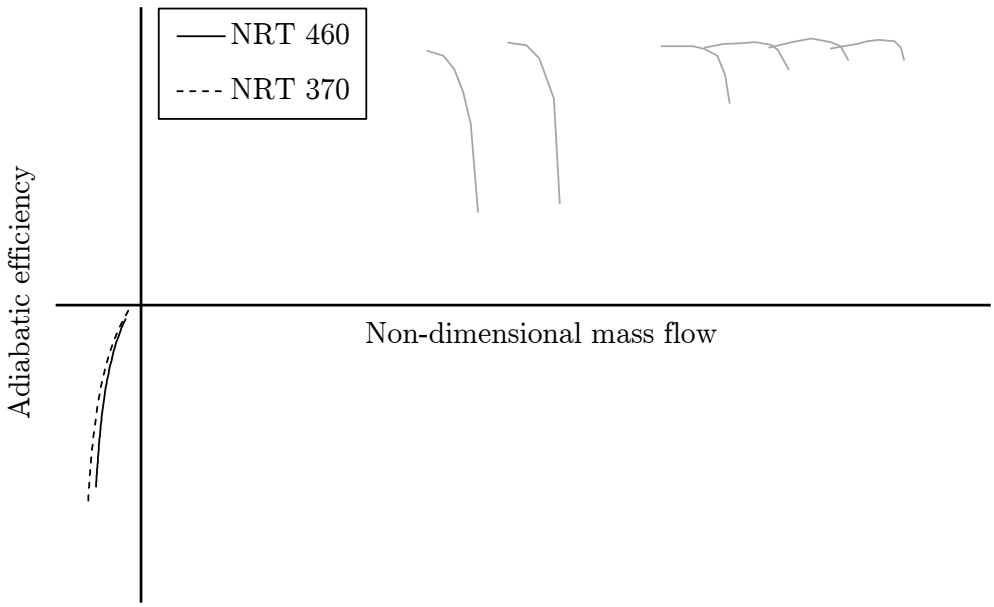

Figure 6.47: HPC map including reverse flow characteristics - Adiabatic efficiency

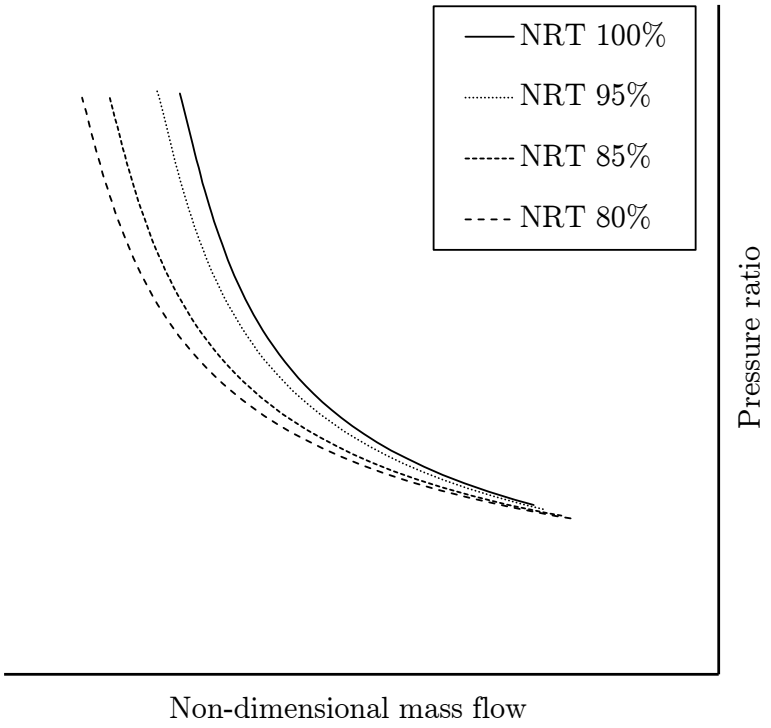

Figure 6.48: HPC reverse flow map - Pressure ratio

The adiabatic efficiency map has been included to complete the set of performance characteristics of the compressor. The value of efficiency lacks physical meaning but it can be used to calculate the total temperature at compressor inlet and so the power consumption of the compressor. For a similar value of power consumption, the total temperature increment through the compressor in reverse flow will be much higher than during forward flow since the mass flow is much lower.

The next figures show the reverse flow performance in detail. From Figure 6.48 it can be concluded that the compressor is more resistant to reverse flow at higher non-dimensional rotational speed. Figure 6.49 shows the characteristics of temperature ratio instead of adiabatic efficiency. Temperature ratio has been defined as $TR = \frac{T_{t_{inlet}}}{T_{t_{outlet}}}$ to obtain values over 1 and to give an idea of the temperature increment over the compressor at reverse flow. This figure shows that the temperature ratio is almost constant with the non-dimensional mass flow and that the most important parameter is the rotational speed. Temperature ratio is proportional to U^2.

The maps obtained for the IPC are not shown here since the results obtained are equivalent to the HPC which have been shown and commented. However, this compressor have variable geometry vanes, so the model of this compressor has been used to explore one of the capabilities of this prediction tool, namely, to assess the effect of variable geometry mal-schedule on reverse flow performance.

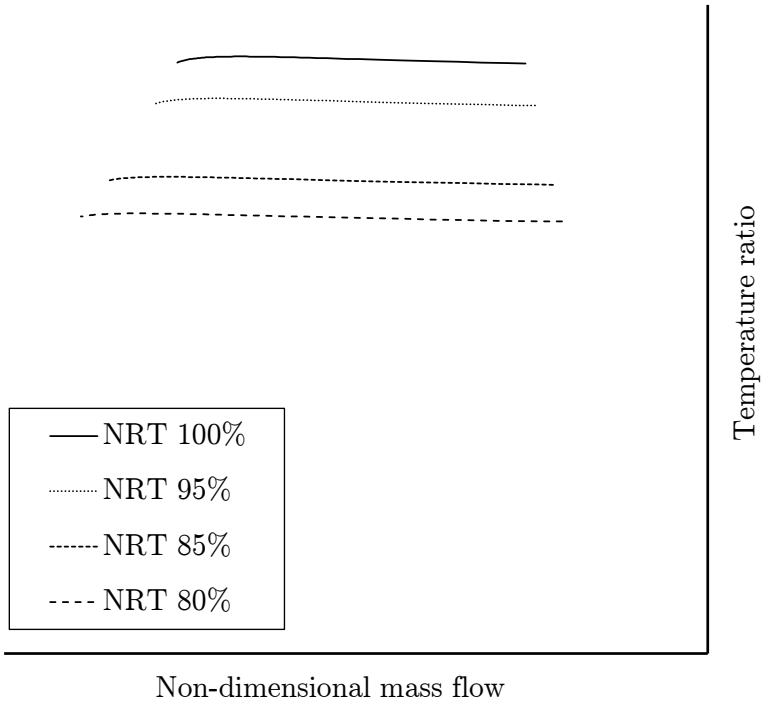

Figure 6.49: HPC reverse flow map - Temperature ratio

Variable geometry mal-schedule is expected to occur during any compressor surge event. This phenomenon is provoked by the differences in characteristic time between the compressor deceleration and the variable geometry actuation. When the compression system surges, the IPC may operate in reverse flow and/or in rotating stall during different parts of the unstable operating cycle. These two operating regions are characterised by a larger power consumption which decelerates the compressor. The time needed for the deceleration is lower than the reaction time needed by the variable geometry actuator to apply the right schedule which is a function of the rotational speed pre-implemented in the engine control system. Typically, compressor maps give one performance characteristic per non-dimensional rotational speed assuming that the variable geometry schedule follows the nominal schedule implemented in the engine control. What it is shown here is the change of a reverse flow characteristic if it is assumed that the variable vanes remain open in despite of the rotational speed reduction. This phenomenon has an even stronger effect in case of shaft failure. In case of an intermediate pressure shaft failure, the IPC will decelerate even faster since the power input coming from the turbine is not present any more.

Figure 6.50 shows the results of two different simulations, one has been carried out by allowing the re-stagger of the VSVs to the position which corresponds to its non-dimensional speed and the other represents a case where a variable geometry is lock

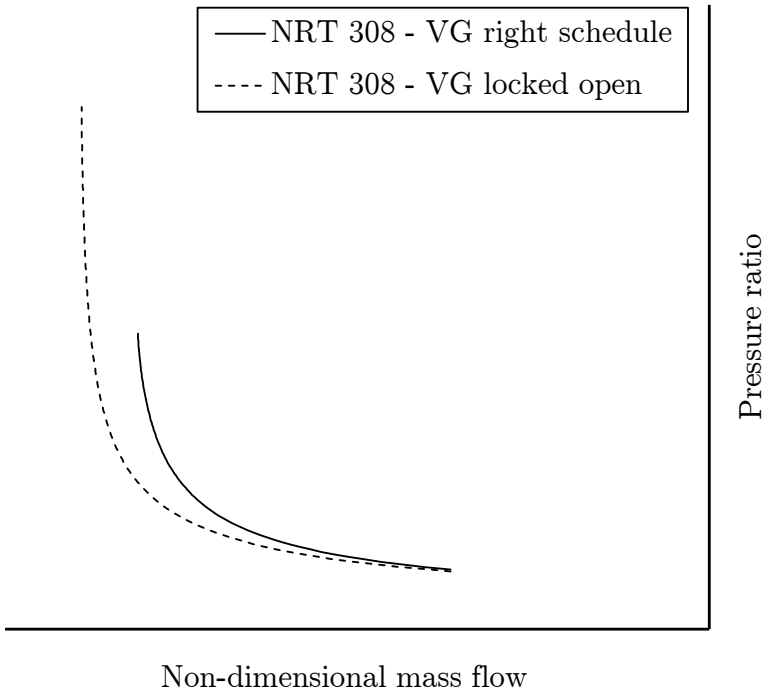

Figure 6.50: Effect of VG mal-schedule on compressor performance at reverse flow

in the open position corresponding to a higher rotational speed. As it was expected, the case with VSVs in the open position provokes a lower opposition to reverse flow.

Thermodynamic properties profile in a multi-stage axial compressor

The results obtained for the IPC are used here to characterise the thermodynamic properties evolution over a compressor at reverse flow conditions. The evolution of different values is shown section by section. The meaning of 'section' in the following figures is: Secton 0 is the compressor inlet, section 9 is the compressor outlet and section 1 to 8 refers to the inlets of the different stages (see Figure 6.51).

The profiles of thermodynamic properties shown here correspond with the design point rotational speed. Four curves are shown in each figure. Each curve is named after the value of flow coefficient at section 9. They are four representative values over the characteristic.

The static pressure evolution throughout the compressor is shown in Figure 6.52. Static pressure decreases across every stage in a similar fashion except across the VIGV which provokes a lower pressure loss because it is not a complete stage.

The evolution of total temperature can be observed in Figure 6.54. The values presented here correspond to the design rotational speed so this temperature incre-

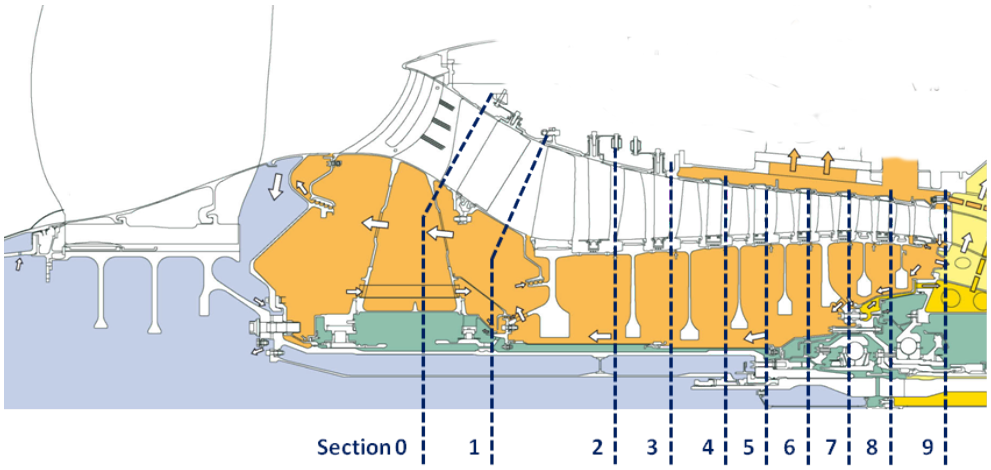

Figure 6.51: Scheme of an IPC - Sections numbering

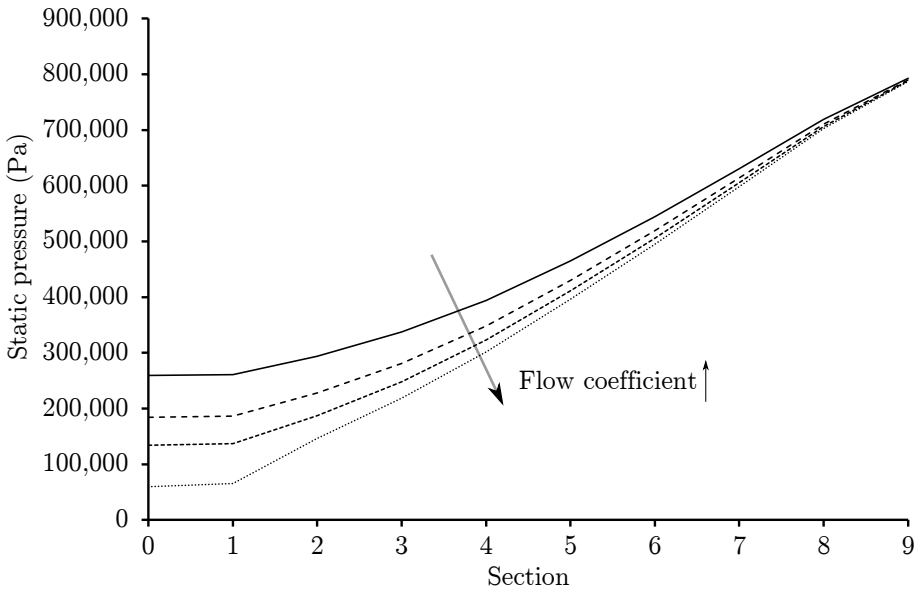

Figure 6.52: Static pressure profile over the compressor at reverse flow conditions

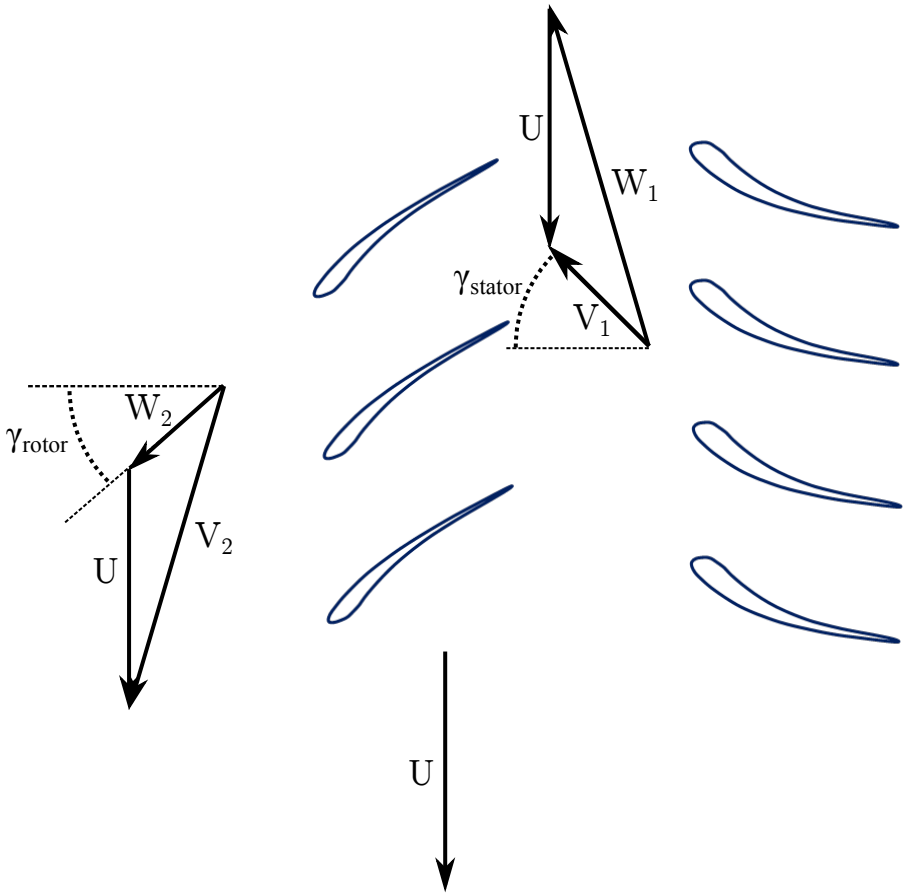

Figure 6.53: Velocity triangles at reverse flow conditions

ment is the highest achievable. This huge temperature rise is explained through the Euler equation for turbomachinery. Figure 6.53 shows the typical velocity triangle layout in reverse flow operation. If Euler equation is applied to the flow across the rotor and the energy equation is used to express the specific work as a function of total temperature increment, Equation 6.36 can be derived to express the total temperature increment as a function of flow coefficient and blade speed.

$$W = U\left(V_{\theta 2} - V_{\theta 1}\right) = C_p\left(T_{t2} - T_{t1}\right) \tag{6.33}$$

$$V_{\theta 1} = V_{x1} \tan \gamma_s \tag{6.34}$$

$$V_{\theta 2} = U - V_{x2} \tan \gamma_r \tag{6.35}$$

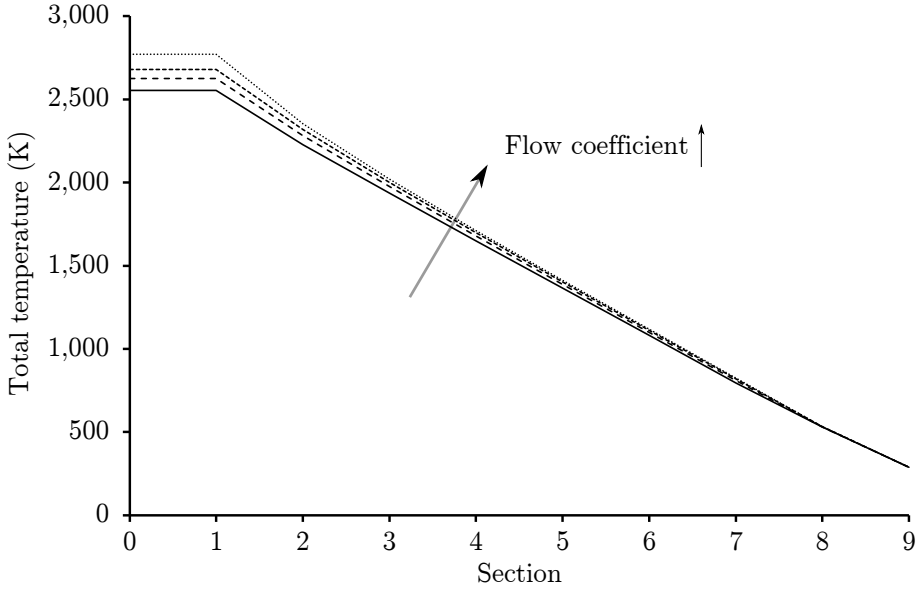

Figure 6.54: Total temperature profile over the compressor at reverse flow conditions

$$\triangle T_t = \frac{U^2}{C_p}\left(1 + |\phi|\left(\tan\gamma_r + \tan\gamma_s\right)\right) \tag{6.36}$$

If the flow angles in Figure 6.53 are assumed to be similar to the metal angle at rotor and stator leading edge respectively, the term in brackets () of Equation 6.36 takes a value from 2 to 3 approximately. If a flow coefficient of -0.5 and a blade speed of 350 m/s are assumed to be representative of an intermediate stage in the compressor, the value obtained for the total temperature increment is about 300 K. This value agrees with the results shown in Figure 6.54. The Euler equation has been used here to give a physical meaning to the order of magnitude of the total temperature increment in one stage. Nevertheless, strong assumptions are made in the process and therefore, it can only be used with qualitative purposes.

Figure 6.55 shows the evolution of the density. The important drop in density observed is caused by the large increase in temperature explained above. This density reduction itself causes the increase in axial velocity which is observed in Figure 6.56. Although the annulus is a divergent duct in the reverse flow sense, this area change is not enough to 'contain' the large increase in axial velocity since it has been designed to work in forward flow. In forward flow, the density goes up since there is a compression process associated to the work input while, in reverse flow, there is an expansion process added to the work input.

In Figure 6.56, the curve for the highest flow coefficient shows a dramatic increase in axial velocity at section 1. This is provoked by extremely low values of density.

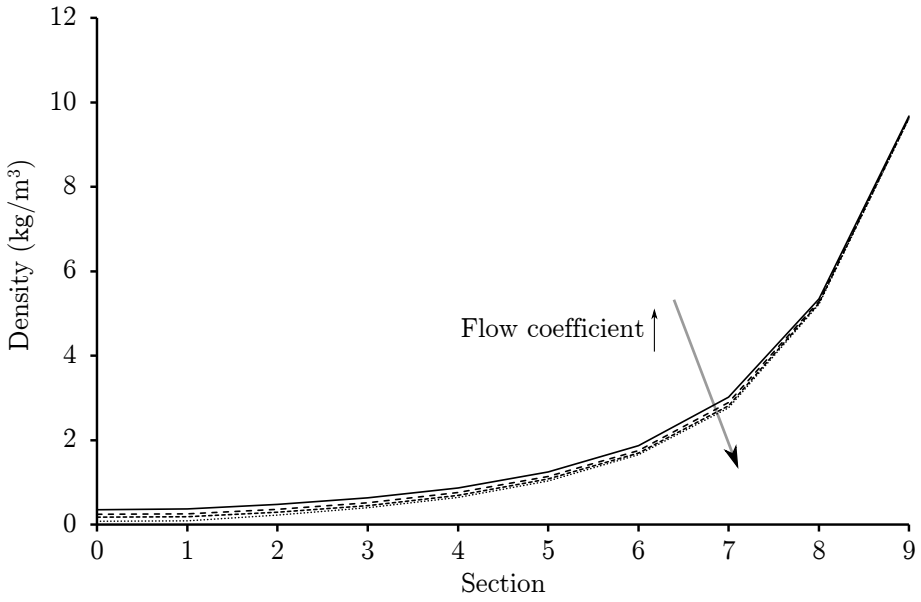

Figure 6.55: Density profile over the compressor at reverse flow conditions

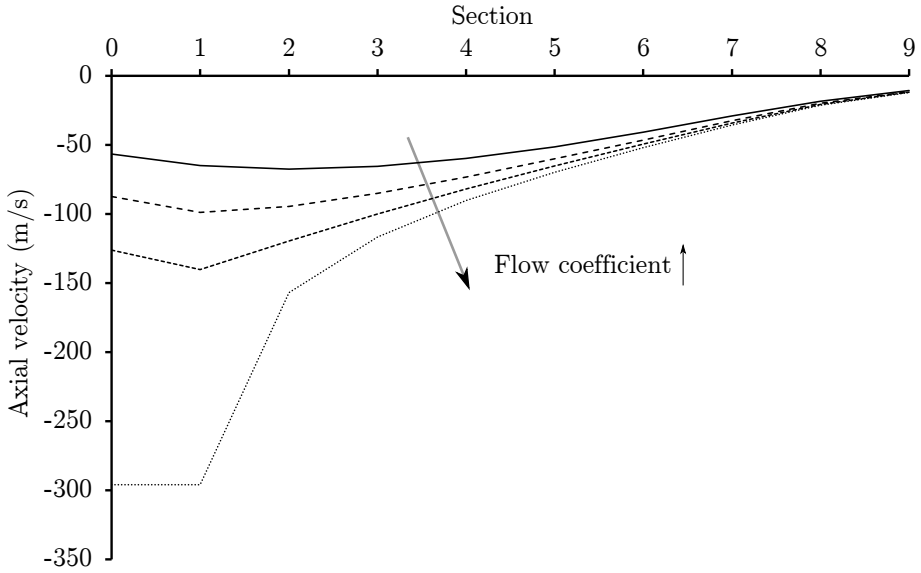

Figure 6.56: Axial velocity profile over the compressor at reverse flow conditions

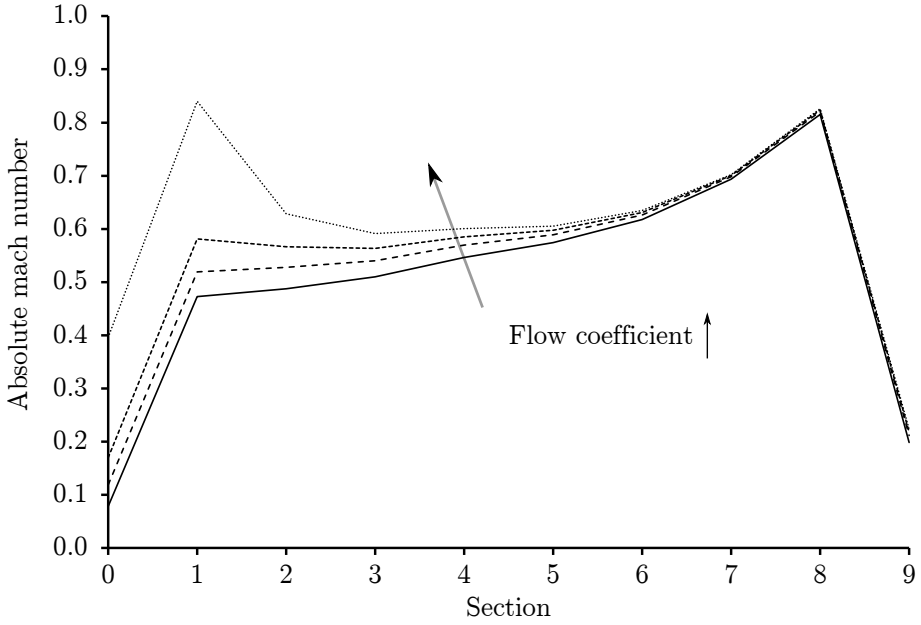

Figure 6.57: Mach number profile over the compressor at reverse flow conditions

Although it cannot be seen in Figure 6.55, the value of density is below 0.1 kg/m^3. Taking into account that the axial velocity is directly proportional to the mass flow (flow coefficient) and inversely proportional to density, a linear trend in the reduction of density provokes a hyperbolic trend in the increment of axial velocity.

The evolution of Mach number, observed in Figure 6.57, is of paramount importance. This is the Mach number associated to the absolute velocity at the outlet of each rotor. Section 9 is the Mach number at the outlet of the compressor (reverse flow domain inlet) and Section 0 is the Mach number of the flow leaving the VIGV. This value is below 1.0 at every section across the compressor and therefore, it reveals that supersonic effect during reverse flow are not going to be encountered despite the extremely high velocities experienced. That is the consequence of the extremely high temperature increase along the compressor.

6.5 Conclusions

1D modelling of compressor instability needs of information about the 'steady' compressor performance over the three regions of the compressor map, namely: forward flow, rotating stall and reverse flow. Experimental information regarding the stable (forward flow) operation has been provided by Rolls-Royce, nevertheless, the compressor characteristics over the other two regions are not available and therefore,

they need to be predicted / modelled.

Regarding rotating stall characteristic, a simple preliminary model has been developed based on the understanding of the phenomenon through public domain publications and experimental information provided by the sponsor company. The model implemented in CERVANTES assumes that the rotating stall line is horizontal and its pressure level is independent of the rotational speed following the conclusions derived from the analysis of the experimental information available.

Extensive work has been undertaken to model compressor reverse flow performance. The methodology developed is generic and robust; it has been implemented in a standalone FORTRAN code thought to be user friendly for its internal use in Rolls-Royce. The methodology relies on the use of 3D CFD to derive single-stage performance maps. Numerous CFD simulations (steady and unsteady) and sensitivity analysis have been undertaken to explore the capabilities of applying CFD techniques to the reverse flow problem. These CFD-derived maps are generic and applicable to any compressor stage within reasonable margins for the different geometrical parameters. The prediction of multi-stage axial compressor reverse flow maps is carried out using a SST fed by the single-stage maps. This performance prediction tool has been validated against experimental data and applied to several modern compressors in order to derive the reverse flow maps needed by CERVANTES.

Chapter 7

Turbine performance

7.1 Background

A shaft over-speed event in the context of a multi-shaft gas turbine provokes the distortion of the velocity triangle at the inlet of the turbine placed downstream the over-speeding rotor. Along the present chapter, the case study analysed corresponds to the over-speed of the intermediate pressure shaft of a 3-spool gas turbine and therefore, the turbine affected by this distorted inlet conditions is the Low Pressure Turbine (LPT). Nevertheless, the methodology developed and presented herein is generic enough to be applied to a case of high pressure shaft over-speed; in that case, the turbine affected by the velocity triangle distortion would be the Intermediate Pressure Turbine (IPT).

The distortion is caused by two different effects, namely, the over-speed process itself by increasing the velocity of the relative frame and the reduction of the axial velocity which is a consequence of the drop in mass flow caused by the compression system instability which is usually linked to the shaft breakage scenario as has been explained in previous chapters. A graphical representation of this effect is shown in the Figure 7.1.

Turbine maps are usually experimentally derived by means of test rig where inlet gas velocity is imposed to reach the first NGV with an incidence angle close to the design one. Moreover, turbine NGVs are able to work within a high efficiency region even if the flow incidence deviates slightly from the nominal conditions due to two main reasons: their leading edge is thick and rounded so it is able to avoid separation

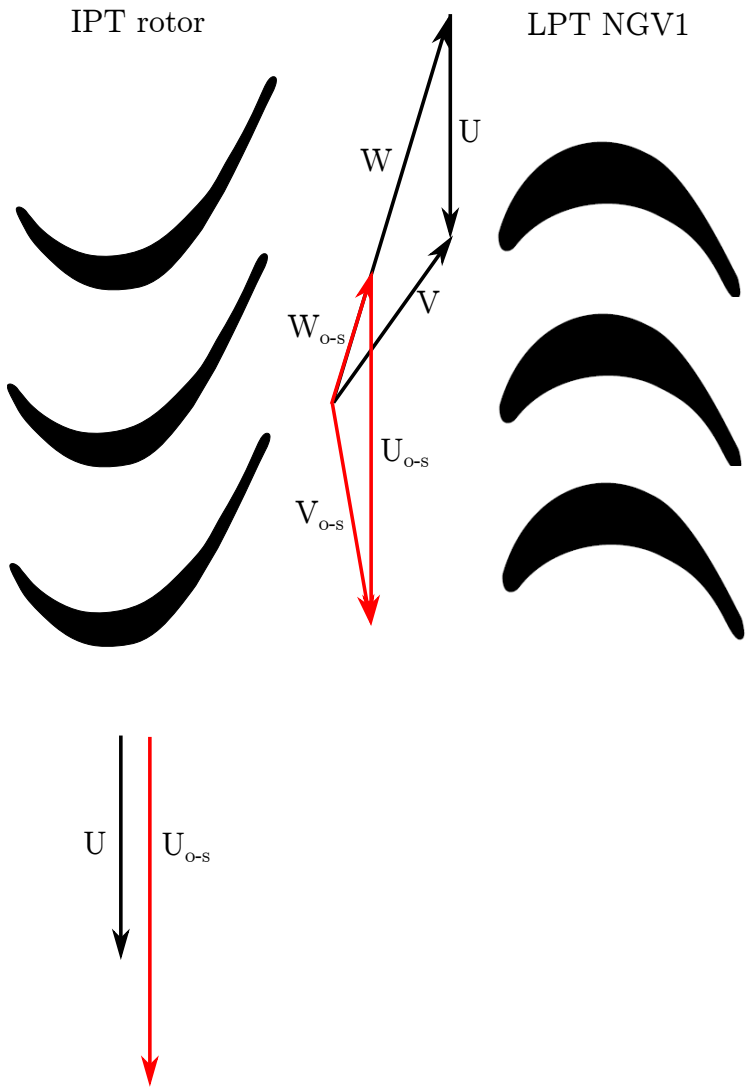

Figure 7.1: LPT NGV1 velocity triangles at over-speed conditions

within a relatively wide range of incidences and, in contrary to compressor blading, the flow is expanding across turbine blades so the pressure gradient is favourable to keep the flow attached. For that reasons, incidence angle has never been considered an important variable in the process of mapping turbine performance. Nevertheless, in case of shaft over-speed, the incidence angle can reach values up to -100 deg provoking a dramatic separation of the flow across the NGV and the consequent increment in pressure losses and reduction in turbine capacity.

The application of dimensional analysis to the turbine system shows the non-dimensional groups that must be considered in the turbine mapping process. It is usual to choose as dependent variables the mass flow ($\dot{m}$) and the total temperature drop (ΔT_t) and to express them as functions of the independent variables.

$$\dot{m}, \Delta T_0 = f\left(P_{t_1}, P_{t_2}, T_{t_1}, N, D, R_g, \gamma, \mu\right) \tag{7.1}$$

P_{t1}, P_{t2} and T_{t1} are boundary conditions, N is the rotational speed that represents the operating point of the machine, D represent a characteristic dimension of the turbine and R_g, γ and μ contain the properties of the working fluid.

Applying the Π theorem, these nine-variable relations can be reduced to relations between five non-dimensional quantities.

$$\frac{\dot{m}\sqrt{RT_{t1}}}{P_{t1}D^2}, \frac{\triangle T_t}{T_{t1}} = f\left(\frac{ND}{\sqrt{R_g T_{t1}}}, \frac{P_{t1}}{P_{t2}}, \frac{\dot{m}}{\mu D}, k\right) \tag{7.2}$$

If it is assumed that the working fluid and the machine are fixed and that the effect of Reynolds number is negligible, these five non-dimensional quantities can be reduced to three so-called 'non-dimensional' groups although, in that case, the variables are not strictly non-dimensional any more [54].

$$\frac{\dot{m}\sqrt{T_{t1}}}{P_{t1}}, \frac{\triangle T_t}{T_{t1}} = f\left(\frac{N}{\sqrt{T_{t1}}}, \frac{P_{t1}}{P_{t2}}\right) \tag{7.3}$$

Equation 7.3 shows the most common way to express turbine maps. As it was explained in Chapter 5, the all-in-one simulation tool CERVANTES solves the expansion side of a gas turbine by means of a quasi-steady methodology consisting in matching the different operating points of each turbine for given boundary conditions (combustor outlet and nozzle discharge pressure) and using the turbine maps

as input data. Since the objective of this tool is to acquire simulation capability for the shaft over-speed event, the maps provided as input must contain not only the nominal information but also the turbine behaviour under extreme negative incidence angles.

Therefore, the objective of the work presented in the present chapter is to develop a methodology to predict turbine maps as a function of the well known non-dimensional group and an extra variable (incidence angle) to take into account the over-speed effect.

$$\frac{\dot{m}\sqrt{T_{t1}}}{P_{t1}}, \frac{\triangle T_t}{T_{t1}} = f\left(\frac{N}{\sqrt{T_{t1}}}, \frac{P_{t1}}{P_{t2}}, \hat{i}\right) \tag{7.4}$$

The objective is to capture the first order effects, to develop a generic and robust methodology applicable to any turbine requiring the minimum amount of information and, to implement it as a standalone piece of software thought to assist CERVANTES by providing the needed three-dimensional turbine maps.

The present study and the achievement of the final prediction tool are supported by an extensive previous work carried out at Cranfield University about this topic. L. Gallar [38] carried out 3D CFD analysis using the particular geometry and boundary conditions of a documented case of over-speed. Furthermore, experimental tests were undertaken at Cranfield University by the same author with the main purpose to validate the CFD techniques in the study of highly separated flows across turbine NGVs. The comparison between CFD and experimental results were successful in the context of performance analysis. The work of L. Gallar is paramount to support the use of CFD as part of the methodology implemented.

7.2 Methodology

The necessity of predicting turbine performance affected by extremely negative incidence angles has been established in the previous section. Attending to results produced in previous work [38], it can be stated that only the performance of the first stage of the downstream turbine is affected by the velocity triangle distortion. In particular, the effect can be confined to the first stage NGV. Figure 7.2 shows the evolution of the incidence angle for the NGV and the rotor of the first stage during one of the documented cases of shaft failure. It can be noticed that, even when the

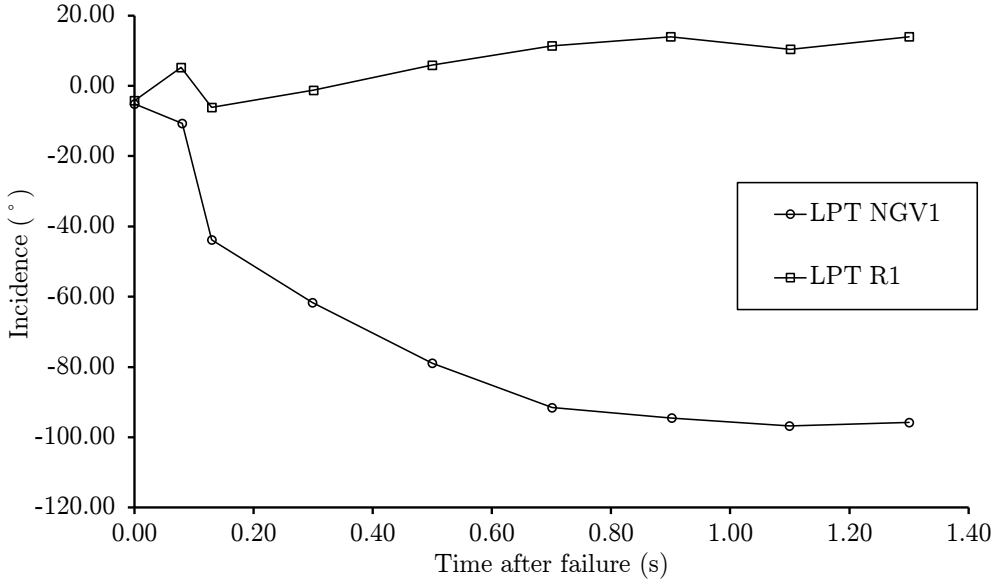

Figure 7.2: Evolution of the LPT NGV1 relative incidence angle [38]

NGV is working with highly distorted flow, it is able to readapt the flow delivering acceptable incidence angle to the next rotor blade.

This conclusion is essential to support the methodology chosen. In case of a multi-stage turbine, it is assumed that all the stages except the first one are not affected by the distorted inlet conditions so the turbine map is split into two parts, namely, stage 1 and virtual stage 2. The latter comprises the rest rearward stages. In this case, the LPT consists of four stages so the part called 'virtual stage 2' comprises the last three stages. The methodology consist in splitting the turbine map into these two parts, substitute the first stage map by a wider version which includes de effect of the incidence angle and finally stack again both parts obtaining the overall map as a function of the incidence as an additional variable.

The first step, needed to carry out the map splitting process, is the prediction of the isolated first stage map. Only the map in nominal conditions (excluding over-speed) is needed to produce the map of the virtual stage 2 but, since the complete map as a function of incidence is needed in the final part of the process, the map of the stage 1 including over-speed conditions is calculated at this first step of the process. This is done by applying meanline theory, calculating the velocity triangles and using losses correlations as a function of incidence for both turbocomponents. Once the map of the first stage is available, a stage splitting technique is applied to calculate the map of the stage 2 which is only a function of the classic non-dimensional groups. Finally a stage stacking technique is applied to produce the overall turbine map which now has the incidence as an extra variable.

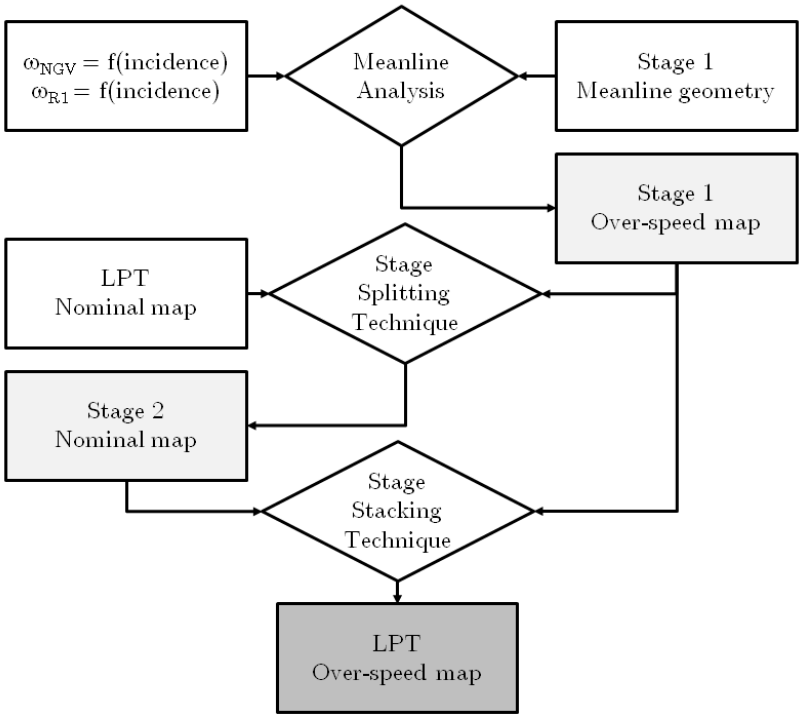

Figure 7.3: Methodology scheme

7.2.1 Mean line analysis - First stage map prediction

A turbine stage consists of two turbocomponents, firstly, the NGV increases the tangential velocity of the flow and produces a reduction in static pressure; secondly, the rotor reduces the tangential velocity while produces torque. In axial flow turbines, the most important gas velocity components are axial and tangential while the radial velocity can be neglected if only first order effects are intended to be captured. Meanline analysis assumes a 2D approach by solving the velocity triangles using blade geometry at midspan section and constant flow properties over the whole cross sectional area. That is considered a good assumption to be applied in turbines with a hub to tip ratio close to unity [54].

The objective is to build the map of the first stage of the turbine. Since a map covers the whole operating range of a turbine, the repeated calculation of a big amount of operating points is needed. Here, the process to calculate one operating point is stated. This process has been implemented in a software tool that is able to explore the whole turbine operating region and produce the map automatically.

The geometry of the annulus is known so the cross sectional area in (1), (2) and (3) are data. The blade geometry at midspan is also known so β_2 and β_3 are data. For

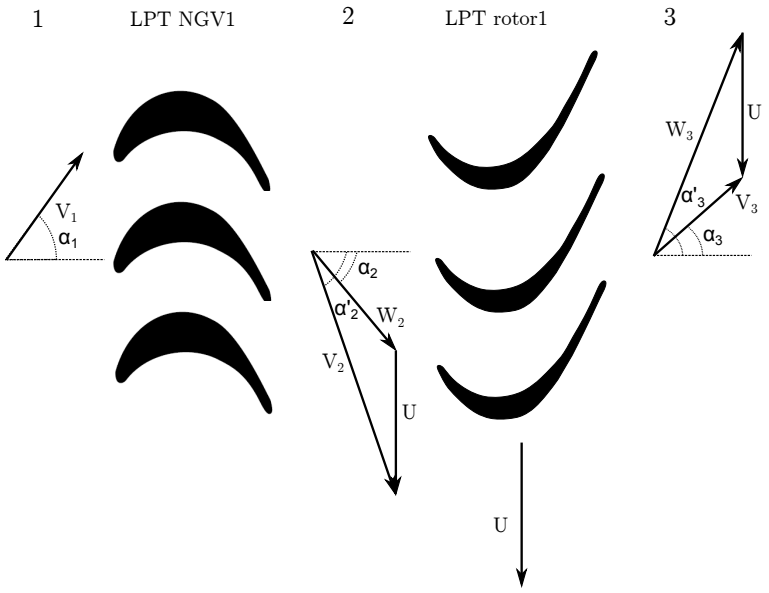

Figure 7.4: Meanline velocity triangles in a turbine stage

the purpose of this study is going to be assumed that the deviation at the outlet of rotor and stator are negligible. This is a reasonable assumption in turbines [54].

$$\alpha_2 \simeq \beta_2 \tag{7.5}$$

$$\alpha'_3 \simeq \beta_3 \tag{7.6}$$

Regarding the energy equation, it is assumed that there is no energy exchange in the relative frame.

$$T_{t1} = T_{t2} \tag{7.7}$$

$$T'_{t3} = T'_{t2} \tag{7.8}$$

Regarding the momentum equation, it is substituted be the expressions of pressure losses as a correlation for the incidence. These correlations are treated as inputs from this part of the methodology, nevertheless, the production of these correlations has been an important part of this project and it is described in detail in the next section.

$$\omega_{NGV} = \frac{P_{t1} - P_{t2}}{P_{t1} - p_1} \tag{7.9}$$

$$\omega_{rotor} = \frac{P'_{t1} - P'_{t2}}{P'_{t1} - p_1} \tag{7.10}$$

The mass flow conservation provides a relation between the axial velocity and the density along the turbine.

$$\dot{m} = \rho_1 A_{\perp 1} V_{x1} = \rho_2 A_{\perp 2} V_{x2} = \rho_3 A_{\perp 3} V_{x3} \tag{7.11}$$

The velocity triangles link the different velocity components (see Figure 7.4). To close the problem, it is necessary to establish a gas model, the definition of total properties and the definition of Mach number.

$$p = \rho R T \tag{7.12}$$

$$\frac{P_t}{p} = \left(1 + \frac{\gamma - 1}{2} M^2\right)^{\frac{\gamma}{\gamma - 1}} \tag{7.13}$$

$$\frac{T_t}{T} = 1 + \frac{\gamma - 1}{2} M^2 \tag{7.14}$$

$$M = \frac{V}{\sqrt{\gamma R T}} \tag{7.15}$$

This set of equations is solved to calculate all the fluid properties in the three sections along the turbine stage specified in Figure 7.4. To define each operating point, it is necessary to specify the total properties at the inlet, the rotational speed of the machine, the incidence angle and the mass flow. Since the turbine maps are independent of the total properties, they can be fixed to arbitrary values. The variation of the mass flow allows exploring each characteristic line which is defined by fixed values of rotational speed and incidence angle.

Figure 7.5: Differences in LPT NGV1 geometries

7.2.2 Turbine NGV aerodynamics under over-speed conditions

The meanline approach applied to derive the turbine map of the first stage affected by over-speed conditions relies on the correlation of pressure losses as a function of incidence obtained for an specific geometry of NGV. These correlations are derived by means of 3D CFD analysis for each different geometry since the models available in the public domain do not cover the operating region experienced during a shaft failure event [38, 87].

The CFD analysis of two different geometries has been carried out in order to assess the different behaviour of the LPT NGV1 geometry in case of shaft failure. The geometry named as 'Engine A' exhibits the classic geometry used in this family of engines while the geometry named 'Engine B' means a rupture with the previous designs. The differences are patent just observing the blade profile shown in Figure 7.5. Classic geometry is more cambered and has a positive metal angle at the leading edge while this angle is negative in the modern geometry. These differences in geometry provoke differences in the behaviour under highly negative incidence flows and therefore, the assessment of both geometries is paramount for the completeness of the present study.

The domain meshed extends from approximately one chord upstream the NGV leading edge to three chords downstream the NGV trailing edge. The set-up of the simulations has been done in accordance with the conclusions extracted by Gallar [38] which carried out the validation of the CFD results against the experimental rig tested at Cranfied. Apart from that, a mesh independence analysis has been carried out following the Roache method which is an extension of the Richardson extrapolation [16, 85]. The results of this study are shown in Figure 7.6.

The CFD model has been used to simulate a wide range of incidence angles. The calculation of the pressure loss coefficient has been carried out using area-averaged

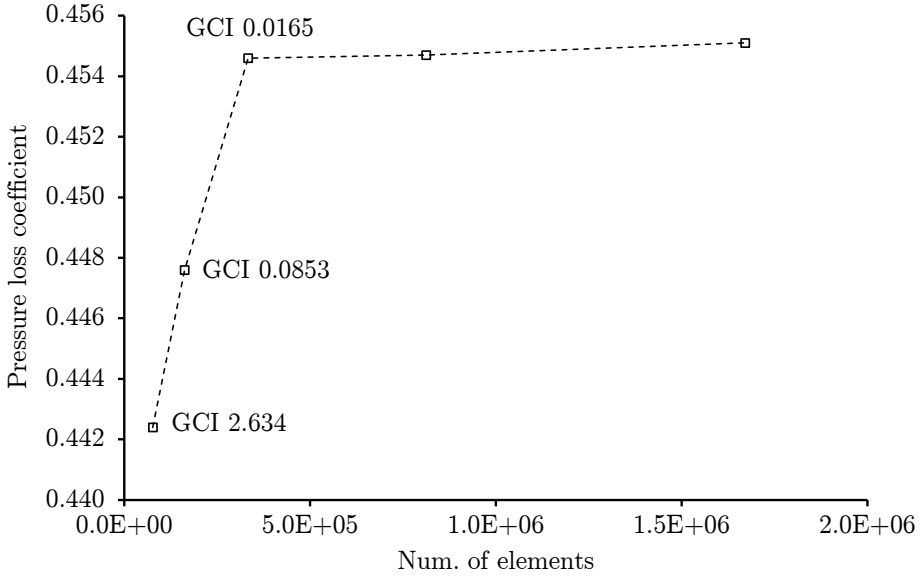

Figure 7.6: Mesh independence analysis

properties so it is compatible with the assumptions of the meanline approach. The measurements have been taken one chord upstream the leading edge (inlet) and half a chord downstream the trailing edge (outlet). Next, the results obtained are shown and compared by means of visual flow field descriptions and plots of the evolution of the pressure loss coefficient with the incidence angle for the two different geometries assessed.

As expected, it is observed that the NGV is able to accommodate the flow with low pressure losses for a wide range of incidence angle around the one of minimum losses. Finally, when the separation of the flow starts, the change in slope is patent and the desired behaviour, namely, the reduction in capacity that throttle the upstream turbines to a lower power extraction operating point, takes place.

Plots show in Figure 7.7, although useful to extract correlations needed by the meanline method to derive the first stage turbine map, are meaningless in terms of comparison. This is due to the difference between geometries in the leading edge metal angle. To compare these two geometries in terms of their behaviour during an over-speed scenario, it is more suitable to attend to a representation of the pressure losses as a function of the absolute flow angle which, at the end of the day is the direct consequence of upstream turbine over-speed and the possible mass flow reduction due to compressor surge.

Figure 7.8 shows the curve of the geometry correspondent to Engine B is below the curve for Engine A over the whole range of flow angles. Therefore, if it is

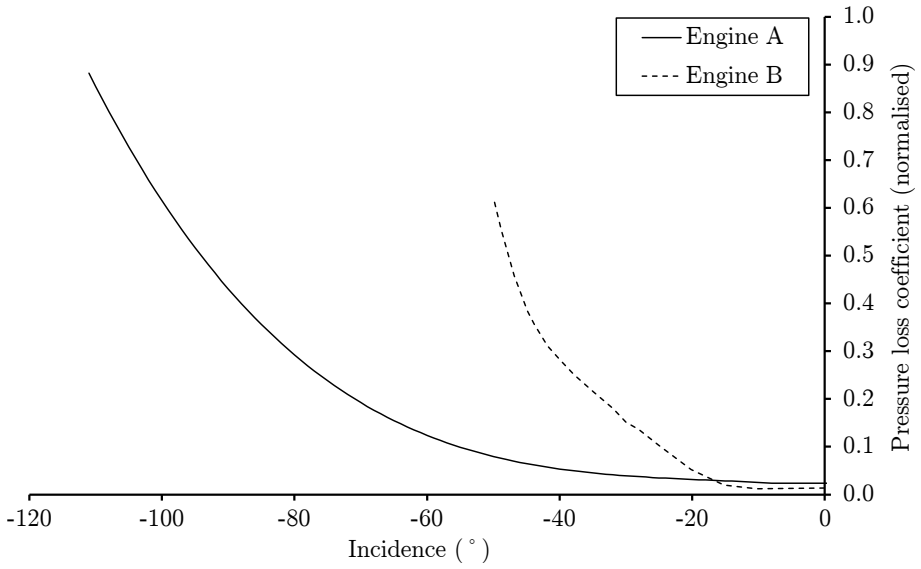

Figure 7.7: NGV pressure loss coefficient - Geometry comparison

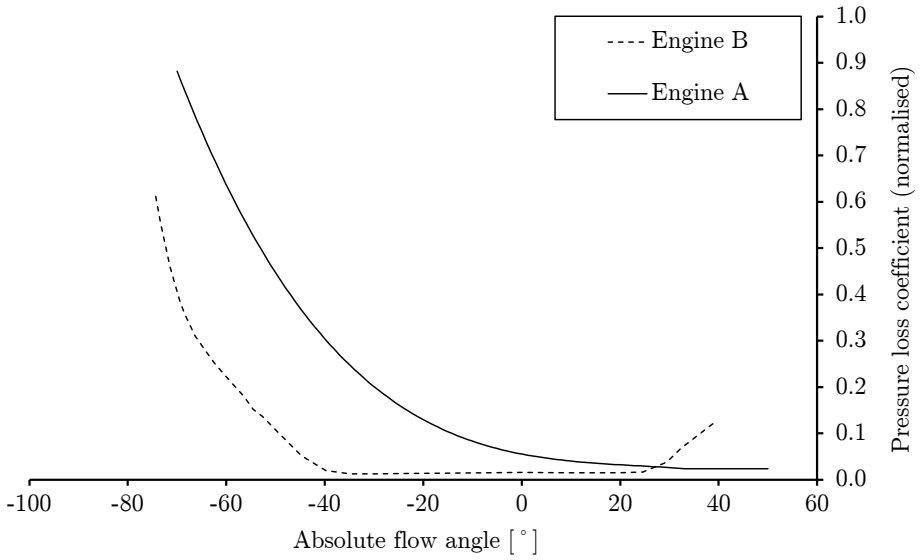

Figure 7.8: NGV pressure loss coefficient - Geometry comparison

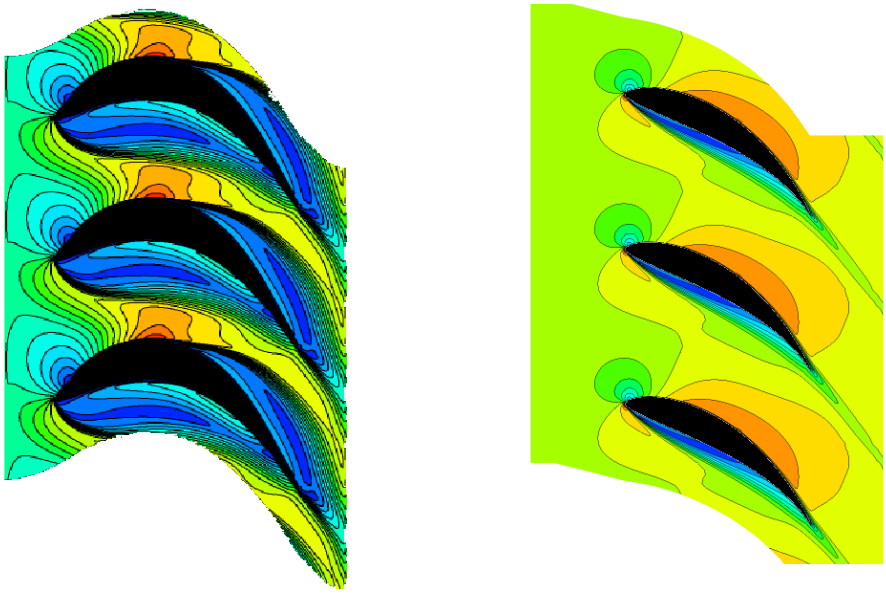

Figure 7.9: Mach number contours (flow angle -40 deg) - Geometry comparison

assumed that the evolution of this flow angle is similar for both engines during a shaft failure scenario, geometries similar to Engine A present a higher pressure loss and consequently a higher capacity reduction contributing more to avoid the acceleration of the free-running turbine. The same conclusion can be drawn from the observation of the flow pattern (Mach number contours) presented in Figure 7.9. It is obvious that the more cambered profile correspondent to the Engine A provokes a more complex separation phenomena and a higher blockage when the absolute flow reaches the highly negative angles typical of the over-speed phenomena.

7.2.3 Stage splitting technique

The stage splitting technique is the methodology proposed to derive the map of the virtual 'stage 2'. The data needed for that calculation are the overall turbine map provided by the sponsor and the map of the stage 1 that is now available after the methodology explained in the previous sections.

As it has been demonstrated in Section 7.2, it can be assumed that the performance of this virtual stage 2 are independent of the incidence angle since the first stage was the only affected by these far off-design conditions. Therefore, this map is only given by the classical non-dimensional groups.

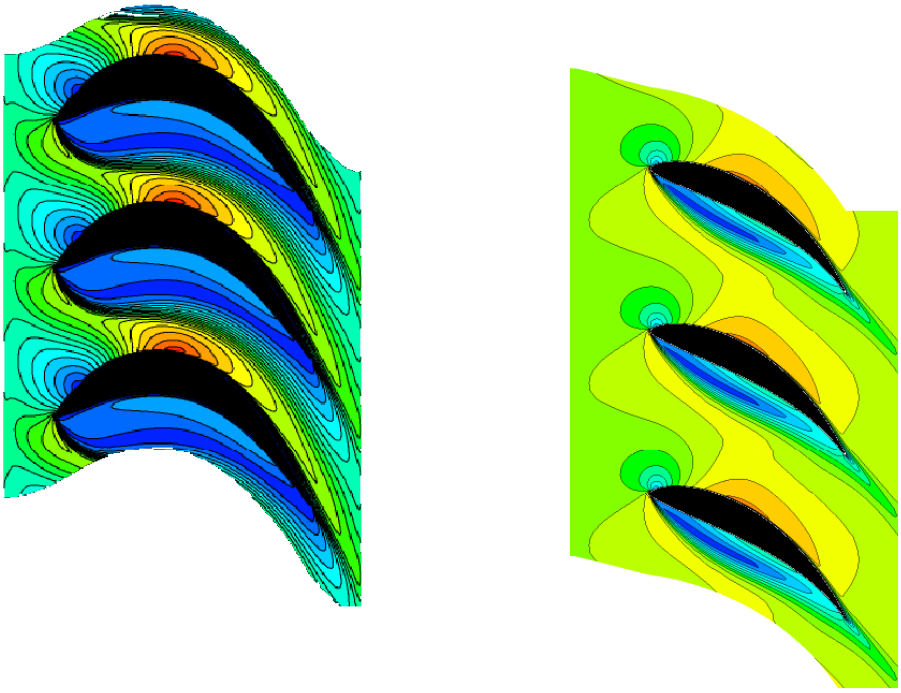

Figure 7.10: Mach number contours (flow angle -50 deg) - Geometry comparison

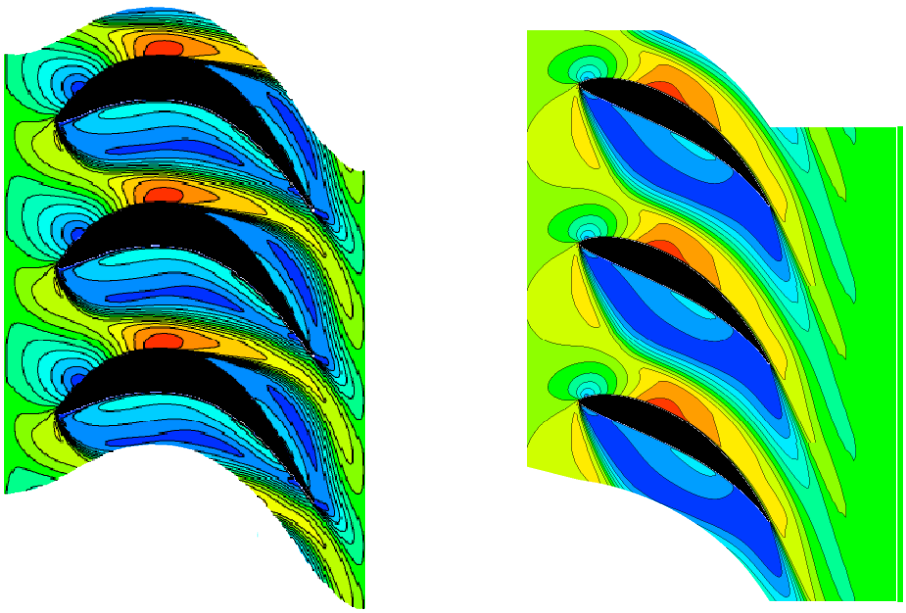

Figure 7.11: Mach number contours (flow angle -60 deg) - Geometry comparison

$$\frac{\dot{m}\sqrt{T_{t2}}}{P_{t2}}, \frac{\triangle T_t}{T_{t2}} = f\left(\frac{P_{t2}}{P_{t3}}, \frac{N}{\sqrt{T_{t2}}}\right) \tag{7.16}$$

Here, section 2 is the inlet of the virtual stage 2 and section 3 is the outlet which is coincident with the outlet of the overall turbine. Subscript 1 is used to refer to the stage 1 inlet which is coincident with the inlet of the overall turbine.

The speedlines of this map correspond to constant values of NRT_2 and therefore, it is necessary to define an iterative loop in the calculation of this map. As it has been said, the data available are the map of the first stage and the overall turbine map, those are given by the next expressions.

$$\frac{W\sqrt{T_{t1}}}{P_{t1}}, \frac{\triangle T_{t1-2}}{T_{t1}} = f\left(\frac{P_{t1}}{P_{t2}}, \frac{N}{\sqrt{T_{t1}}}\right) \tag{7.17}$$

$$\frac{W\sqrt{T_{t1}}}{P_{t1}}, \frac{\triangle T_{t1-3}}{T_{t1}} = f\left(\frac{P_{t1}}{P_{t3}}, \frac{N}{\sqrt{T_{t1}}}\right) \tag{7.18}$$

The calculation process to follow for each operating point is the next. Values of total pressure at 1 (P_{t1}), rotational speed (N), mass flow ($\dot{m}$) and total temperature at 2 (T_{t2}) are imposed. The value of total temperature at 1 (T_{t1}) is guessed and it will be used to iterate. Known those variables, the map of the stage 1 can be read to obtain the total pressure at 2 (P_{t2}) and the total temperature at 2 (T^*_{t2}). Now, the Newton-Raphson method is used to iterate in T_{t1} until both values of the total temperature at 2 are coincident. Once this process has been converged the process continues by reading the overall turbine map to calculate P_{t3} and T_{t3}. Finally, all the properties needed to identify the operating point in the map of the virtual stage 2 are known. Next, the rest of the speedline is explore by changing the mass flow and, once the speedline is completed, the rotational speed can be changed to explore the rest of the speedlines.

7.2.4 Stage stacking technique

The stage stacking technique is the last step in the process to build the overall turbine map with the incidence angle as additional variable. This method is commonplace in performance analysis and the application is straightforward once the maps of the stage 1 and the virtual stage 2 are known.

The objective is to recompose again the overall turbine map, now with the incidence at the inlet as additional variable. The process to calculate one operating point is the following:

- Impose N, incidence, T_{t1}, P_{t1} and $\dot{m}$
- Calculate $\frac{N}{\sqrt{T_{t1}}}$ and $\frac{\dot{m}\sqrt{T_{t1}}}{P_{t1}}$
- Read the stage 1 map to obtain P_{t2} and T_{t2}
- Calculate $\frac{N}{\sqrt{T_{t2}}}$ and $\frac{\dot{m}\sqrt{T_{t2}}}{P_{t2}}$
- Read the virtual stage 2 map to obtain P_{t3} and T_{t3}
- Calculate $\frac{P_{t1}}{P_{t3}}$ and $\frac{T_{t1}-T_{t3}}{T_{t1}}$
- The operating point of the overall turbine map is known

$$\frac{\dot{m}\sqrt{T_{t1}}}{P_{t1}}, \frac{\triangle T_t}{T_{t1}} = f\left(\frac{P_{t1}}{P_{t3}}, \frac{N}{\sqrt{T_{t1}}}, \hat{i}\right) \tag{7.19}$$

- Explore the whole speedline ($\hat{i}$ = cte and $\frac{N}{\sqrt{T_{t1}}}$ = cte) by varying $\dot{m}$
- Explore the effect of incidence ($\frac{N}{\sqrt{T_{t1}}}$ = cte) by varying $\hat{i}$ and using $\dot{m}$ to explore the characteristic
- Repeat the process varying N to complete the map with all the desired speedlines

7.3 Results - Engine A LPT over-speed analysis

The methodology discussed in the previous section was implemented in a standalone software tool. The simplicity and robustness of this tool allows its application to different turbine geometries requiring a minimum amount of information. In the present section, the results of the application of this tool to the LPT of the Engine A are shown. This engine model is representative of most of the engines within the same family so the conclusions derived from this analysis can be extended to other similar engines. Furthermore, the validation of the methodology is presented.

7.3.1 Methodology validation

The methodology used is based on three mayor steps, namely, the prediction of the stage 1 over-speed map, the calculation of the map of the virtual stage 2 by means of a stage splitting technique and the final built of the overall turbine map as a function of the incidence by means of a stage stacking technique. The key step in this process is the calculation of the stage 1 map since this is used as input in the other two steps. The application of the stage splitting and stage stacking techniques does not add any error to the process since they are just straight performance calculation without involving any additional modelling. Therefore, the validation of the meanline approach to model the performance of the first stage is of paramount importance for the reliability of the entire model.

A first approach to the modelling of the first stage performance in over-speed conditions was carried out by Gallar [38]. The methodology in this case relies on the full 3D CFD analysis of the whole stage. The CFD model includes the over-speeding rotor of the IPT, the first NGV and the first rotor of the LPT. The methodology used by Gallar has been superseded by the one developed herein due to its robustness and the easier applicability to different geometries. Nevertheless, the CFD study carried out by Godino as part of the research of Gallar [97] are suitable for validation purpose. The methodology based on meanline analysis and pressure losses correlations is first-principles-oriented and more basic than the direct CFD analysis of the whole domain so the former can be compared with the latter with validation purpose. It must be taken into account that the work of Gallar included the validation of the CFD techniques against experimental data extracted from the rig test built at Cranfield University. Therefore, the present validation is indirect supported by this experimental work.

The validation has been carried out by comparing the operating points simulated by Godino with the results given by the present methodology for these exact operating points. The same inlet conditions and rotational speed imposed in the CFD are given to the meanline tool and the values of the flow properties at the stage outlet are compared. Figure 7.12 shows the magnitude of the error in total pressure and total temperature. All the properties have been area-averaged in the CFD. It can be concluded that the prediction capability for the first stage performance in over-speed of the present methodology is validated with a maximum error of 4% in total pressure.

The validation of this simplification of the methodology has been satisfactory. A

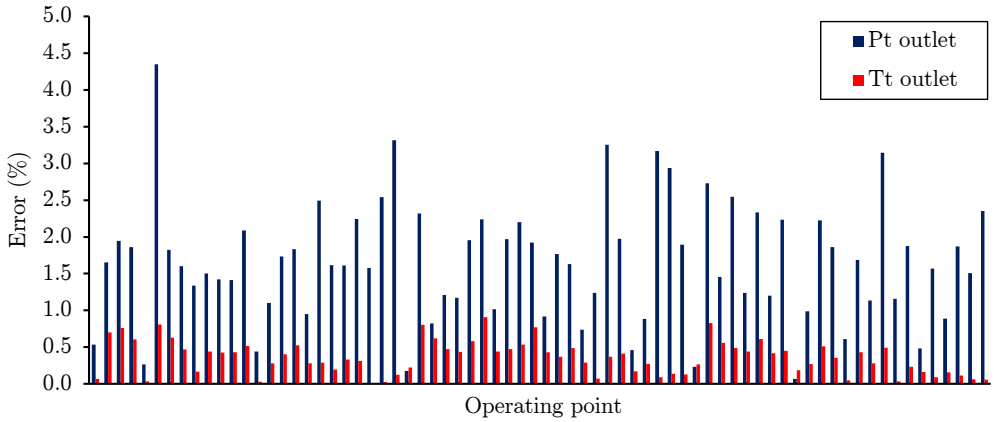

Figure 7.12: Verification of the meanline method - Comparison against full-stage CFD model

fully CFD approach requiring the simulation of three turbo components and a huge amount of operating point to derive a map has been substituted by a model based on first principles and a CFD derived correlation for losses which is only dependent on the incidence angle. Simplicity, robustness and computational time have been gained and it was shown than the differences between both methods are low enough to be acceptable.

A second stage of validation has been carried out in order to check the proper implementation of the stage splitting technique and the stage stacking technique. The results produced by the tool for the nominal incidence operation have been compared against the overall nominal map provided by the sponsor. The differences in the worst case are lower than 1% in the map variables non-dimensional mass flow and non-dimensional torque. That comparison is useful to validate the implementation of the stage splitting and stacking techniques.

7.3.2 Engine A LPT over-speed maps

The software developed has been applied to the LPT of the Engine A to derive the maps needed by the 'all-in-one' simulation tool CERVANTES. The input data needed to carry out this case study are the followings: nominal LPT map, meanline geometry of the first stage (blade metal angles) and the correlation of the pressure loss coefficient with the incidence for the first stage NGV.

The results of this analysis are the maps shown in Figure 7.13 and Figure 7.14. These figures are four-dimension maps showing the dependent variable, non-dimensonal mass flow and non-dimensional torque respectively, as a function of the pressure

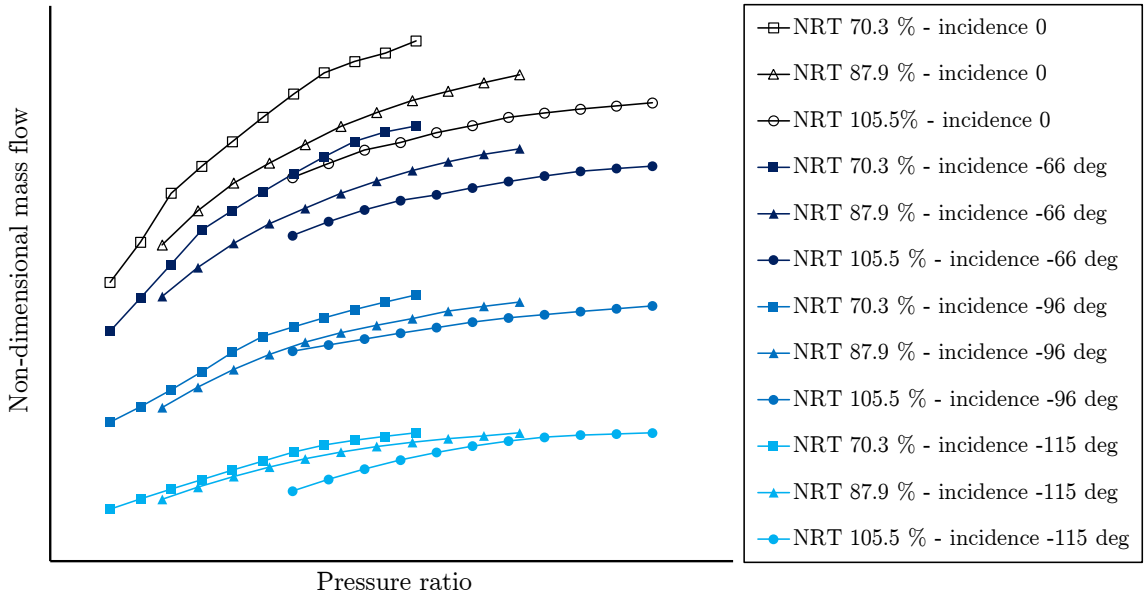

Figure 7.13: LPT map under over-speed conditions - Capacity

ratio, non-dimensional rotational speed and incidence angle. The maps are organised presenting four families of curves corresponding to different incidence angle (0 deg, -66 deg, -96 deg and -115 deg), each family is a turbine map represented by three characteristics or speedlines (70.3%, 87.9% and 105.5%).

These maps are used by interpolating in three variables. Pressure ratio and non-dimensional rotational speed are known or guessed during the turbine matching process while the incidence angle is calculated by solving the complete velocity triangle at each station across the turbine.

The observation of the maps confirms the phenomenon that has been explained previously in this chapter. During an over-speed event, the combined effect of mass flow reduction due to compressor surge and the acceleration of the upstream turbine rotor due to the shaft breakage provoke the distortion of the velocity triangle at the inlet of the LPT in that case. This distortion is noticed as an increment of the incidence angle in the negative sense provoking the separation of the flow across the NGV and the consequent reduction in effective area. This scenario explains the reduction in capacity observed in the maps. This reduction in capacity leads to a lower torque absorption which is patent in the Figure 7.14.

From the point of view of the outcome of an intermediate pressure shaft failure event, this change in performance in the LPT is positive. The reduction in capacity in the LPT throttles the upstream turbines for a lower pressure ratio and therefore the power absorption is also reduced, limiting the over-speed [87].

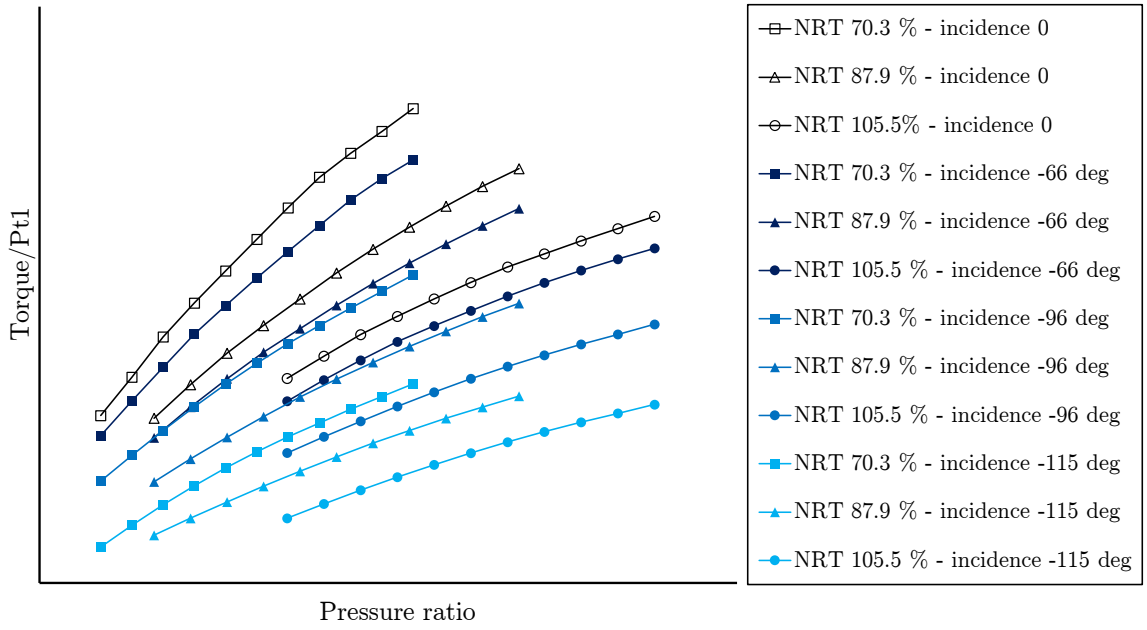

Figure 7.14: LPT map under over-speed conditions - Torque

A second effect observed in the maps is the trend to converge of the different speedlines with the increase in negative incidence. The three speedlines plotted in the map tend to overlap showing the same behaviour as in the single-stage high-pressure turbine maps, namely, the rotational speed has no effect on the capacity which now is given by the choke of the minimum effective area across the NGV provoked by the highly separated flow. This effect of convergence due to the new throat caused by the separation is clearly presented in Figures 7.15. Figure 7.15 shows how the capacity can be reduced by 33% during an over-speed event and the clear convergence pattern independent of the non-dimensional rotational speed.

7.4 Conclusions

The objective of the work presented in the present chapter was to derive a methodology to predict the performance of a turbine affected by the over-speed of the upstream turbine. It has been seen how the over-speed event and, in particular, the shaft failure scenario provokes the distortion of the velocity triangles at the inlet of the turbine downstream the over-speeding rotor.

The methodology described above intended to the spread of the existing turbine maps to cover the influence of an additional variable playing an important role in over-speed operation, namely, the incidence angle at the first NGV of the turbine

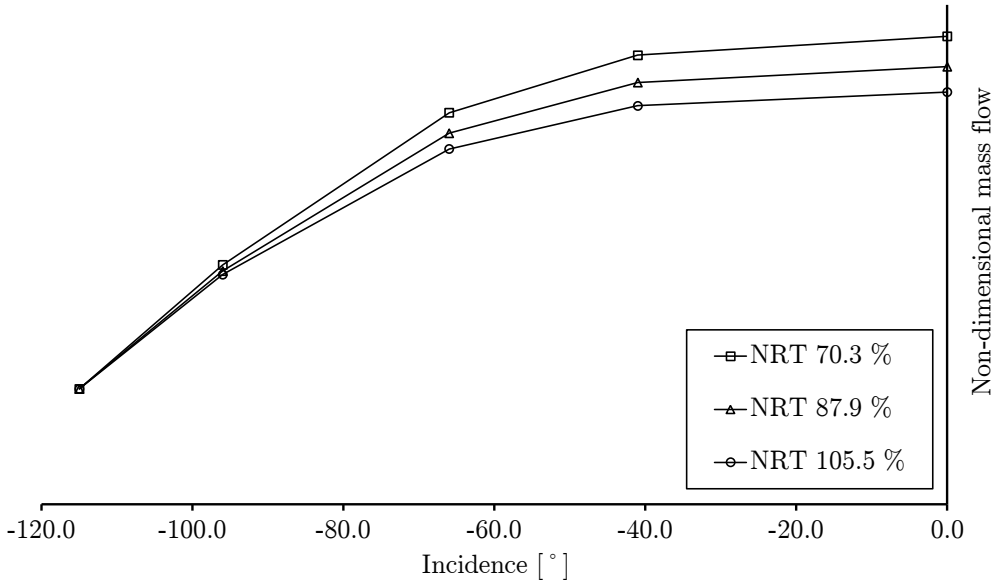

Figure 7.15: Effect of incidence in capacity at over-speed conditions

in question. The methodology, as explained above, lays on the prediction of the stage 1 map under over-speed conditions assuming that this effect is confined or influencing only this first stage. The knowledge of this predicted map of the stage 1 and the overall nominal map of the turbine allows to rebuild the overall map now including the additional variable by means of the application of a stage splitting and stacking technique in order to substitute the performance of the first stage by a more complete map which is a function of the incidence angle.

The prediction of the stage 1 performance is based on the meanline analysis of the stage. This analysis relies on the characterisation of the pressure losses across the NGV by means of CFD. Two engine geometries with fundamental differences in the blade shape have been assessed by CFD analysis and the impact of their geometrical features on the behaviour of the vane under over-speed conditions have been evaluated.

The methodology developed here was implemented as a standalone piece of software that requires a small amount of information. Once the nominal map of the turbine, the geometry of the first stage at midspan and the function of the pressure loss coefficient of the first NGV are available, this tool is able to calculate the overall turbine map in over-speed conditions. This tool was developed to assist the overall engine simulation tool CERVANTES which needs to be provided with turbine maps as a function of the incidence in order to allow the simulation of the over-speed scenario.

The methodology was validated in two different steps. Firstly, the modelling of the first stage performance was compared against the results obtained by Godino [97] which carried out the fully 3D CFD study of an over-speeding rotor and the first stage of the downstream turbine. It was shown how the present methodology, based on first principles and a unique correlation of the NGV pressure losses, is able to produce results with errors lower than 4%. The second step of the validation is the verification of the stage splitting and stacking technique. The nominal region of the overall turbine map produced by this method was compared with the initial nominal map provided by the sponsor with differences lower than 1%.

The observation of the results plotted in the overall turbine maps arises several conclusions. The over-speed conditions at the inlet of the LPT provoke the reduction in capacity and consequently a reduction in the torque absorption. The reduction in capacity can reach the 33% while the reduction in non-dimensional torque is more important and could reach the 60%. This mal-function of the turbine downstream the over-speeding rotor has positive consequences limiting the terminal speed of the free-running turbine since the reduction in capacity in this turbine throttles the upstream turbine for lower pressure ratio decreasing the torque absorption so its acceleration capability.

Chapter 8

Validations and results

The methodology developed over this doctoral research, consists of different parts which was finally integrated within the 'all-in-one' simulation tool CERVANTES with the objective to simulate the overall complexity of the shaft failure event in gas turbines. The development process was designed to allow the partial validation/verification of the code at the different stages of the development process. This allowed assessing few new functionalities at each time making feasible the debugging process.

The objective of the present chapter is to go over the validation process showing the most important milestones in terms of validation and the final results and capabilities of the integrated tool. The chapter focuses on the development of the MGP simulation tool and the final integrated tool. The development of the SAS simulation tool was undertaken in parallel. Its development process and the last stages of validation have been shown in Section 5.4.

The development process started with the implementation of the numerical solver for the quasi-1D Euler equations. This solver is able to predict the transient behaviour of the flow field inside a variable area duct. The mesh independence analysis, the verification of the numerical solver, and the validation with a benchmark case widely used for that sort of solvers is presented in Section 8.1. The second step was the implementation of the source term to model the presence of compressors. The validation of the capability to model the different phenomena involved in the unstable operation of the compressor is shown in Section 8.2. Finally, the MGP was completed by adding the turbine matching solver and this was integrated with the SAS and with the subroutine which calculates the friction torque. The 'all-in-one'

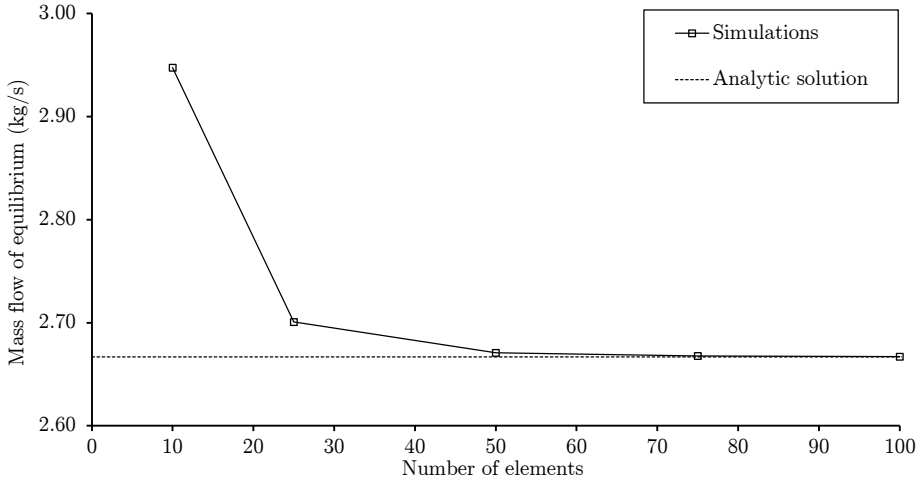

Figure 8.1: Mesh independence analysis

simulation tool was applied then to model a shaft failure case for validation, the results of this study are shown in Section 8.3. Furthermore, CERVANTES has been used to simulate a different case study whose results are shown in Section 8.5.

8.1 Euler solver - Numerical scheme validation

The backbone of the simulation tool which models the compression side of the MGP is a solver of the quasi-1D Euler equations (Equation 5.54). This first stage of development and validation comprises the implementation of the numerical solver and the different types of boundary conditions at the inlet and outlet of the domain. The steady state solution of the code has been validated by modelling cases such as: a straight tube, a convergent nozzle and a convergent-divergent nozzle. It has allowed testing the different boundary condition possibilities, namely, subsonic inlet, subsonic outlet and supersonic outlet. The convergent nozzle geometry has been used to carry out the mesh independence analysis. The solution of this problem can be calculated analytically, in particular, the mass flow through the nozzle for a given pressure gradient. Figure 7.6 shows the result of the mesh independence analysis. It shows the right asymptotic behaviour for grids with more than 50 elements.

Once the solver was verified in terms of steady state solution, the transient capability was tested. For that purpose, the well documented case of the shock tube has been modelled. This test case involves a long pipe which is initially divided into two regions by a diaphragm, each region having a different pressure level. The test starts breaking the diaphragm so a transient evolution occurs until the new stable

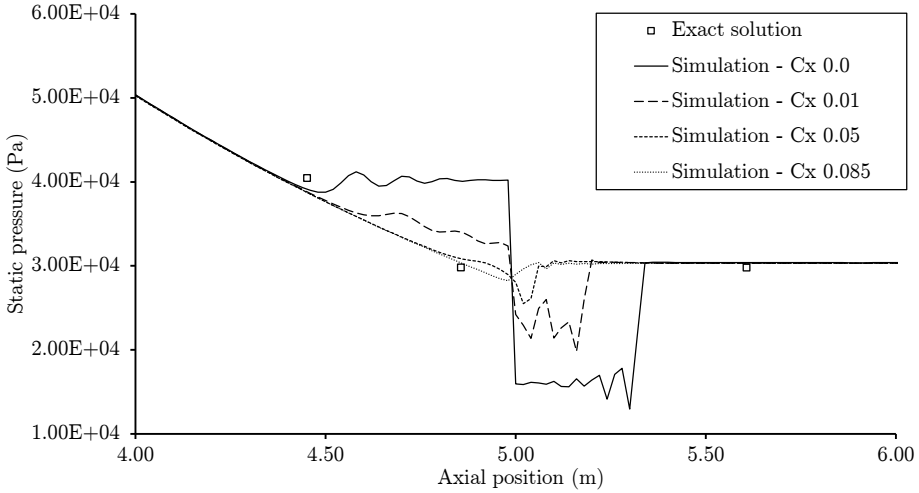

Figure 8.2: Exact solution validation - Effect of artificial viscosity

steady state is reached. This test involves an initial discontinuity and its evolution which is given by the transmission of information by means of sound waves over the domain. In order to allow this sort of solvers to deal with discontinuities in a realistic way, it is necessary to implement a numerical concept known as artificial viscosity whose objective is to introduce a numerical dissipation. Euler equations assume that the flow is inviscid which is a valid assumption 'macroscopically' speaking, nevertheless, the artificial viscosity concept is necessary to add realism within the regions with discontinuities such as the initial conditions of the shock tube case and flow fields involving shock waves typically occurring in supersonic flows. As has been explained in Section 5.2.1 the strength of this numerical viscosity has to be adjusted by a parameter (C_x). Figure 8.2 shows the effect of this parameter on the solution around problematic regions. This parametric analysis allowed choosing a value of 0.085 to guarantee the smoothness of the solution.

Once the value of artificial viscosity has been adjusted, the shock tube case allows verifying the numerical scheme. This test case has been widely modelled by a big variety of numerical schemes and the results are available in the public domain. Hirsch's book [52] offers a complete comparison of results depending on the sort of numerical scheme used. This benchmark problem consists in a 10 metres long tube which is initially divided into two regions. The left-hand half has a pressure of 100 KPa while the right-hand half has a pressure of 10 KPa. The subsequent transient evolution can be explained by the presence of a compression wave travelling from x = 5 m towards the right and a expansion wave travelling from the same initial point towards the left. Figures 8.3, 8.4 and 8.5 show snapshot pictures of the profiles of pressure, density and velocity respectively, 6.1 ms after the initialisation. In the

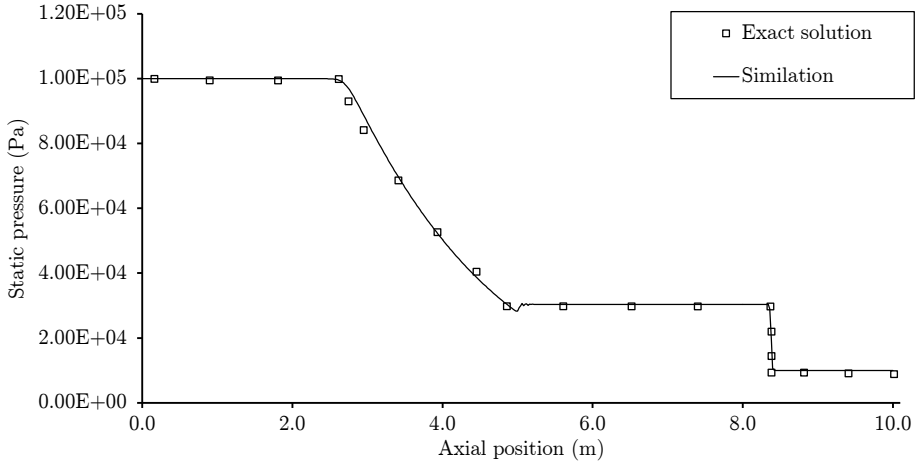

Figure 8.3: Exact solution validation - Pressure profile at t=6.1 ms

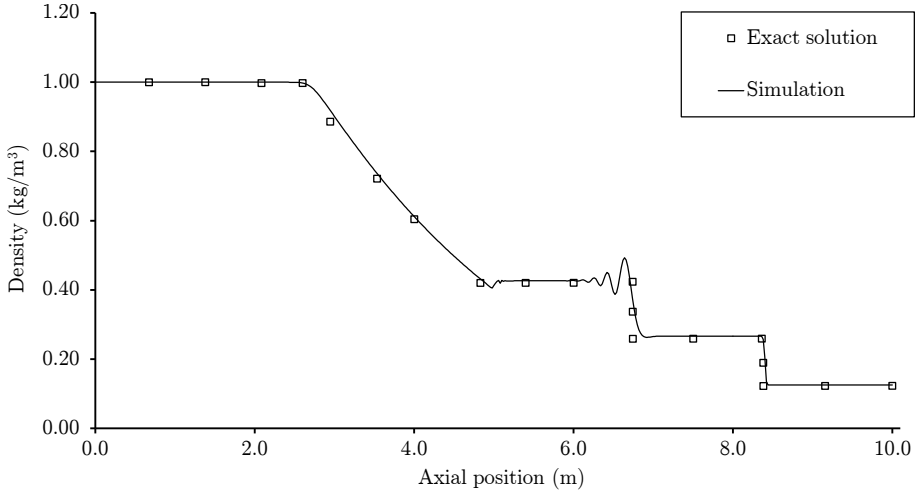

Figure 8.4: Exact solution validation - Density profile at t=6.1 ms

figures, the comparison between the solution obtained with a McCormack scheme by Hirsch [52] and the solution of CERVANTES is shown. The purpose of this exercise is the verification of the numerical scheme implementation since the comparison is done against a solution produced by the same numerical scheme. The good agreement observed guarantees the proper implementation in the solver at that point of the development process.

Besides the verification of the coding process, it is necessary to guarantee that the chosen methodology, and in particular this numerical scheme, is suitable to model the reality. Thus, a similar experimental test is available in the public domain [37] to be used for validation purposes. Figure 8.6 shows the layout of the experiment. The shock tube is 6.759 m long and it is initially divided into two regions with different initial pressure by a diaphragm. Two pressure transducers are installed along the

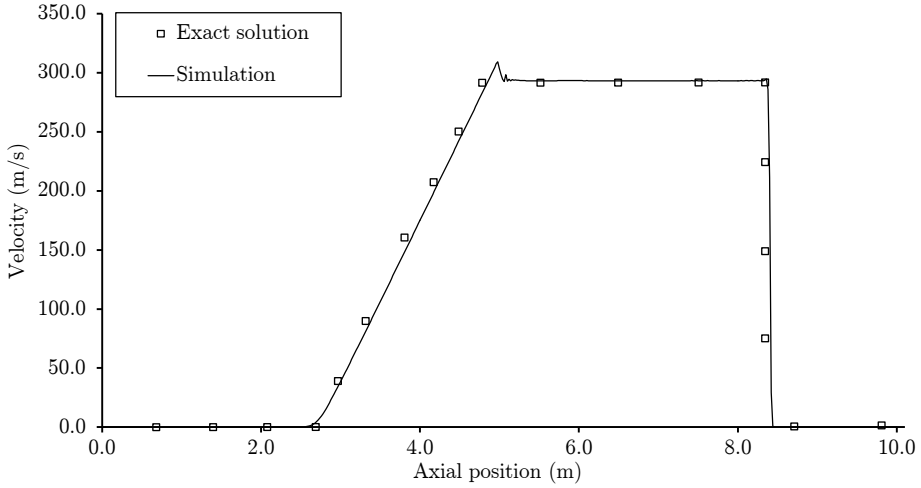

Figure 8.5: Exact solution validation - Velocity profile at t=6.1 ms

tube. The measurement of these transducers will allow the comparison with the simulated version.

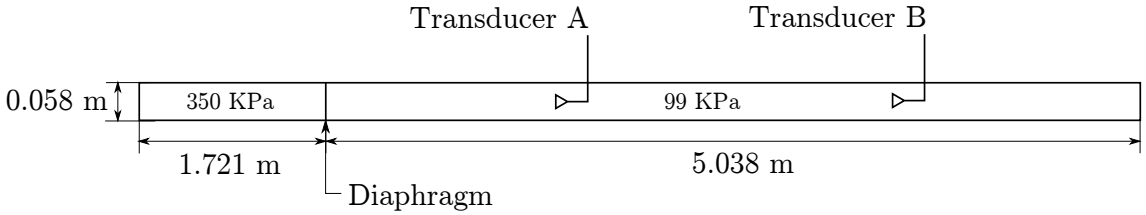

Figure 8.6: Shock tube experiment layout

Figure 8.7 and 8.8 show a comparison between the experimental results published by Felling [37] and the simulations. In that case, the evolution of the static pressure captured by the transducers is plotted against the time, being time 0.0 sec the breakage of the diaphragm. Figure 8.7 shows the comparison at the position of the transducer A. The poor agreement to capture the first pressure wave is caused by three-dimensional effects related to the breakage system of the diaphragm. The agreement is satisfactory for the second wave. Figure 8.8 shows the level of agreement for the transducer B.

The three verification/validation cases shown here allow trusting in the numerical scheme implemented and in its functionality capturing transient phenomena in quasi-1D problems.

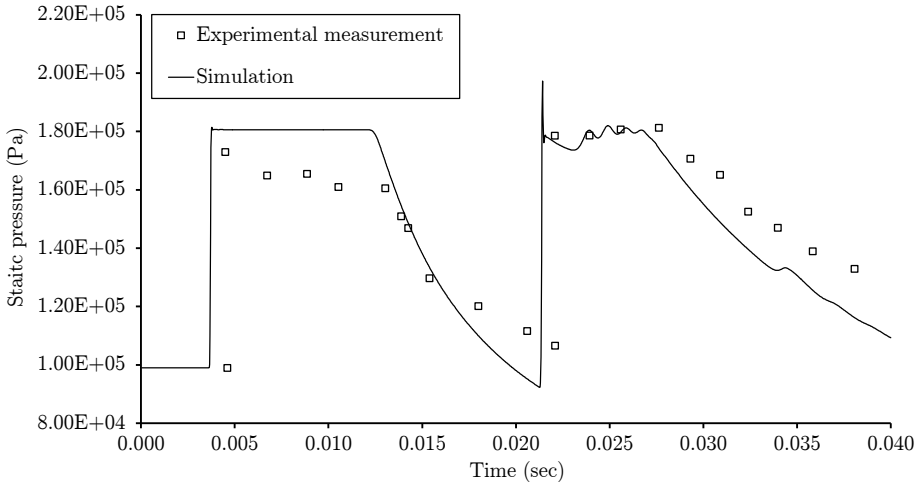

Figure 8.7: Shock tube experiment validation - Pressure evolution at station A

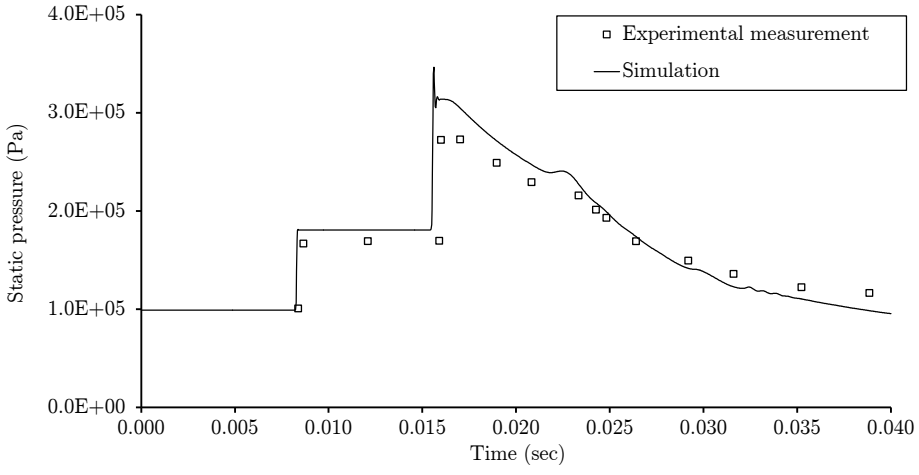

Figure 8.8: Shock tube experiment validation - Pressure evolution at station B

8.2 Compressor model validation at stall conditions

The next step in the development process was the implementation of the source terms which allow the simulation of compressor forces. At that point, it was necessary to validate the compressor model and to show the suitability of this methodology to deal with unstable compressor operation. The classic study of Greitzer [45, 46] for compressor surge and rotating stall was used to carry out the validation.

CERVANTES was used to model the 3-stage axial compressor that Greitzer used at MIT to study the compressor instability. The experiment layout consists of a compressor, a plenum and a throttle valve. The compressor is installed in a constant area pipe which discharges into a plenum which discharges itself to the ambient through a throttle valve. An equivalent system was modelled with CERVANTES as can be seen in Figure 8.9. In that case, a quasi-1D version has been built where the plenum is just a region of the pipe with very high cross sectional area and the throttle is a convergent nozzle. Apart from the definition of the domain, CERVANTES needs to be given the complete steady state compressor map which is available in this case..

Following the nomenclature of Greitzer, unstable phenomena in that compressor can be classified as: rotating stall, classic surge and deep surge. The compressor will experience these different patterns depending on the value of the Greitzer B parameter (see Equation 8.1) and the position of the throttle. In the experiment, different values of B are imposed by modifying the volume of the plenum and the compressor's rotational speed. In the case of the simulation the domain geometry remained constant and the effect of B was captured by modifying only the rotational speed.

$$B = \frac{U}{2a}\sqrt{\frac{V_p}{A_c L_c}} \tag{8.1}$$

Modelling compressor rotating stall with a quasi-1D model is 'unphysical', in particular during the first instants after the operating point crosses the surge line. At those moments, the phenomenon is dominated by the process of formation of the rotating stall cell which involves the compressor dynamics along the circumferential coordinate. Although Greitzer [45, 46] showed that a quasi-1D model can be used to predict the evolution of the area-averaged properties during this event, a mathematical artefact is still needed to be added to this solvers to deal with the initial phenomenon which is eminently two-dimensional. To model the process of formation of the stall cell, a first order lag is applied on the calculation of the compressor

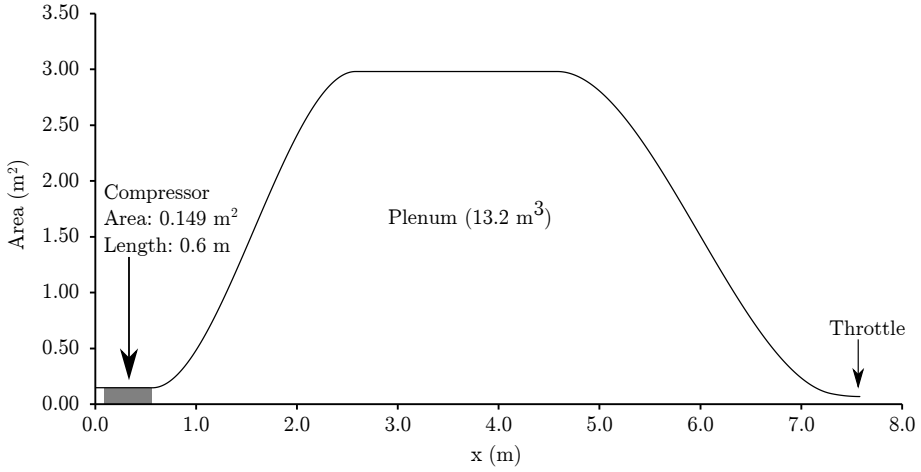

Figure 8.9: Compressor surge simulation - Domain geometry

forces. This lag represents the time needed by this stall cell to grow and reach an equilibrium size. The effect of this parameter on the prediction of compressor surge has been analysed. Figure 8.10 shows the variation of the operating point trajectory over the compressor map for different values of the lag parameter (τ), the legend of the graph shows the value in rotor revolutions. Low values of τ provoke a more abrupt and faster reduction in mass flow and in compressor pressure delivery. Although the evolution with time cannot be observed in the figures, it is clear how the trajectory for the lowest value of τ departs from the throttle characteristic following an under-dumped trajectory towards the new 'stable' point on the stall characteristic. The effect of this parameter on the damping process of the system affects ultimately to the surge type. Figure 8.11 shows a case with a slightly higher value of the B parameter. In that case, it can be observed how the surge phenomenon can change from rotating stall to classic surge depending on the value of τ.

The experiments of Greitzer allowed measuring the time needed by the stall cell to grow. It was seen that the complete development of the stall cell occurs after 7 rotor revolutions. From a numerical point of view, Greitzer observed that a value of 2 revolutions for the time constant of the first order lag equation allowed the modelling of this growth phenomenon. In the following, this value has been adopted for the simulations carried out with CERVANTES.

Once the choice of the value of τ and its effect on compressor surge simulation has been determined, the effect of the most important parameter (B) can be assessed. As shown in Equation 8.1, the B parameter takes into account the geometry of the system and the operating conditions of the compressor. The work of Greitzer demonstrated that the effect of all this variables can be grouped under this unique

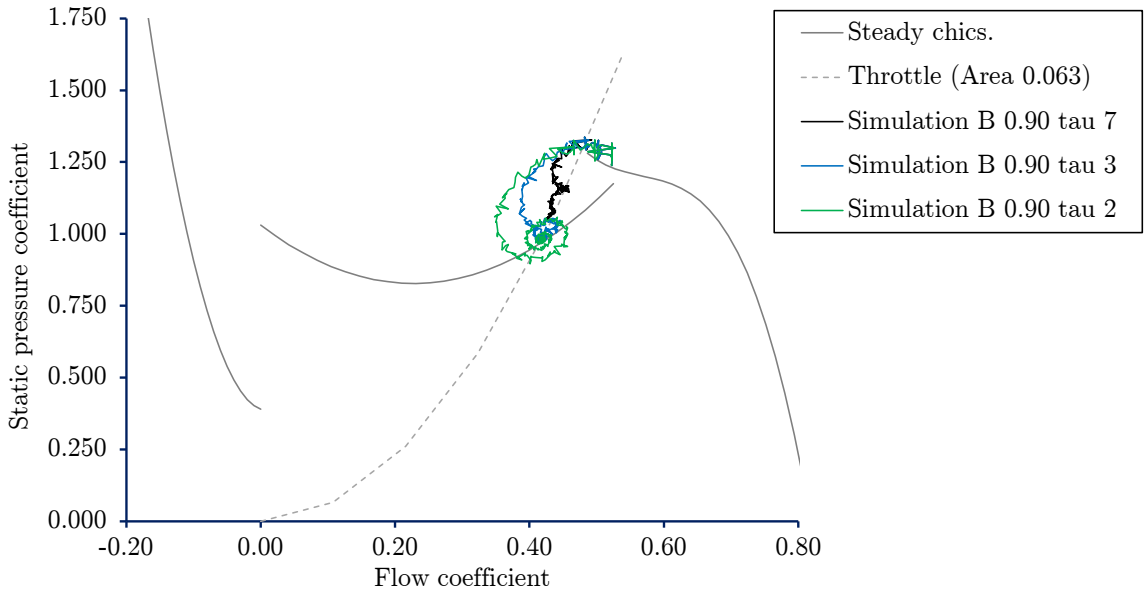

Figure 8.10: Compressor surge simulation - Effect of lag parameter ($B = 0.9$)

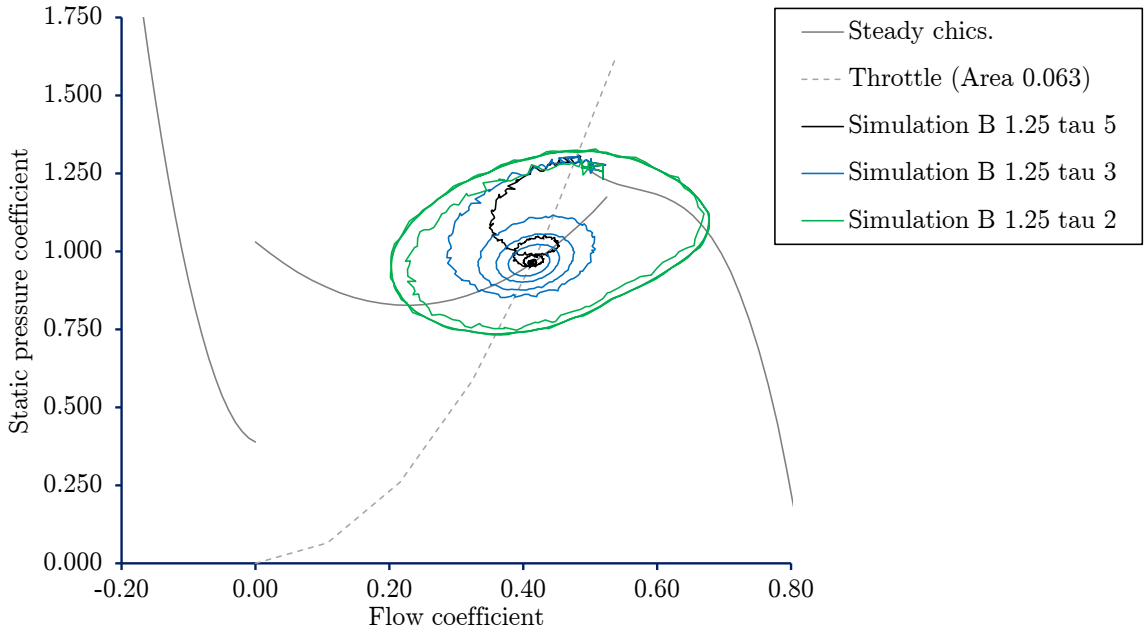

Figure 8.11: Compressor surge simulation - Effect of lag parameter ($B = 1.25$)

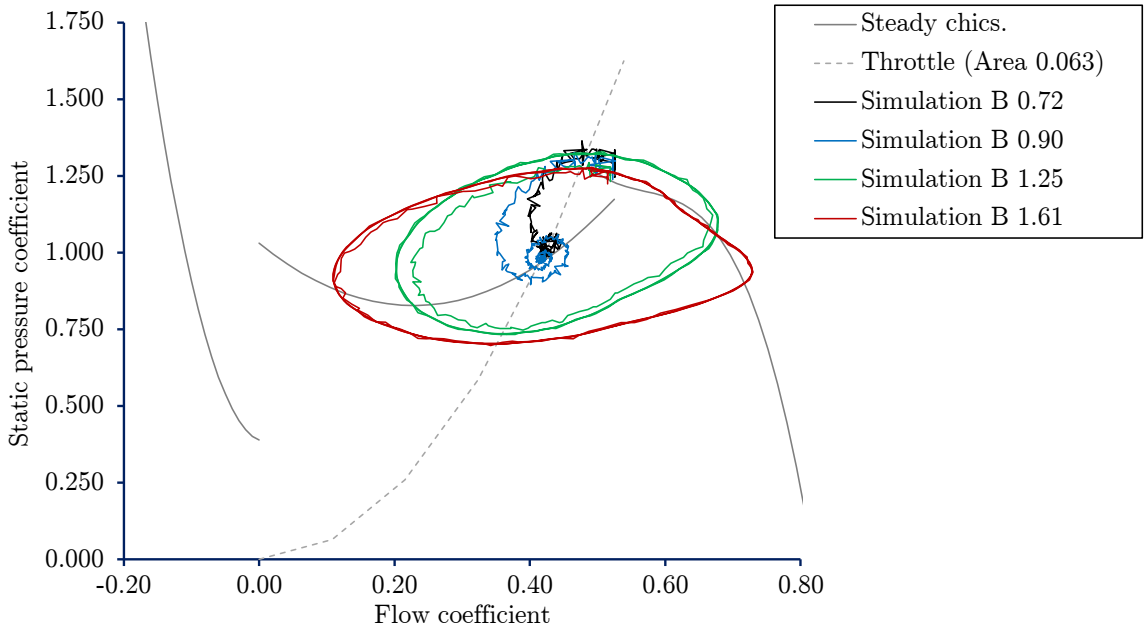

Figure 8.12: Compressor surge simulation - Effect of B parameter

non-dimensional group. Figure 8.12 shows the results of the parametric analysis carried out to show the effect of this parameter. As expected based on Greitzer's work, a critical value of B exists which changes the behaviour of the system from rotating stall to classic surge.

Finally, the comparison of the simulation results against the experimental measurement obtained by Greitzer has been carried out. The rotational speed of the compressor has been modified to produce similar values of the B parameter in order to make possible the direct comparison with the test results. The three different compressor behaviours observed by Greitzer has been reproduced, namely, rotating stall, classic surge and deep surge.

The operation in rotating stall is characterised by a 'stable' point which is located where the stall characteristic is crossed by the throttle line. The compressor operation tends to stabilise at this point after a short transient trajectory. Figure 8.13 shows the agreement between the simulation and the experimental results. The picture shows a compressor map given by three characteristic lines: the stable line (forward flow), the stall line and the reverse flow line. The throttle characteristic has been also plotted in order to identify the new equilibrium point. The simulation is initialised with the compressor operating in a stable point close to the surge line, then the throttle area is suddenly closed from 0.07 m^2 to 0.063 m^2. This change provokes the movement of the throttle line pushing the operating point over the surge line and giving place to the new 'stable' operating point on the stall charac-

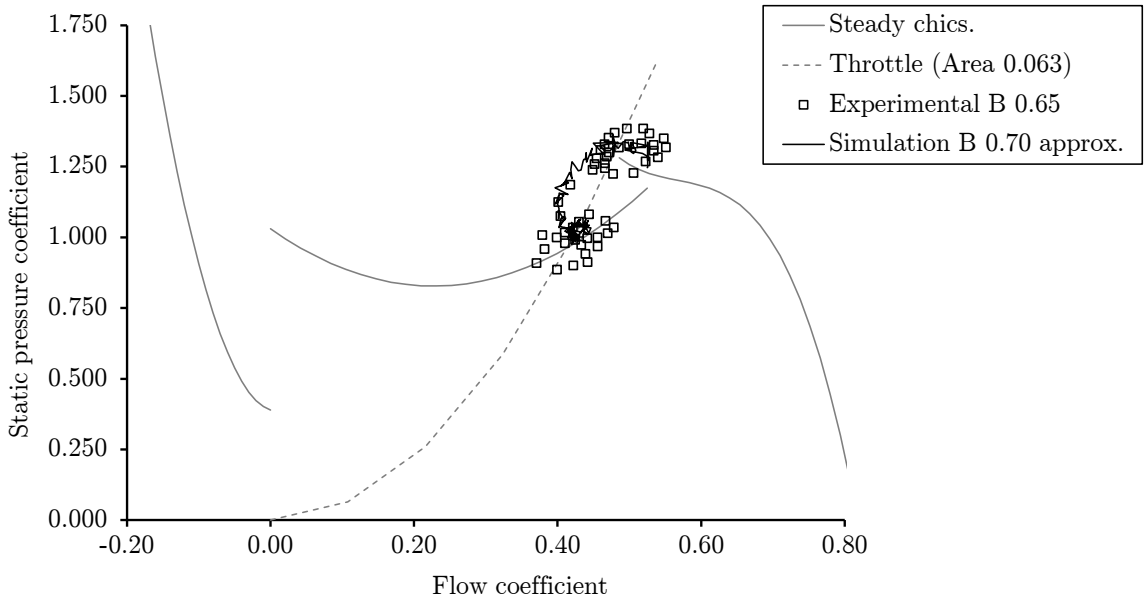

Figure 8.13: Compressor surge validation - Rotating stall

teristic. The operating point departs from the stable line and follows a trajectory given by the decrease of the compressor delivery pressure and a reduction in mass flow. Finally, it oscillates and stabilises in the new 'stable' point. The agreement between the simulation and the experiments is satisfactory.

If the B parameter is increased above a critical value the compressor's response changes from rotating stall to classic surge. The main difference is the absence of a stable point, and therefore, the compressor continues operating in the way observed in Figure 8.14 while the cause that provoked the surge in the first place (throttle closing in that case) is still in place. Although the crossing point between the stall characteristic and the throttle line is the same than in the previous example, a higher B parameter changes the dynamic of the system provoking in that case an oscillation that is not damped. When a compressor is operating following this behaviour, a change in the throttle which would allow the possibility of a stable point in the forward flow characteristic would make possible the recovery of the compressor. The agreement between both curves can be considered satisfactory given the simplicity of the model and the final purpose of the overall tool.

The word 'approx.' can be read in the legend of the figures which show the validation of the different surge phenomena. The reason for that is the difficulty to calculate the exact value of B parameter for the domain given by Figure 8.9. In a theoretical system, the values of plenum volume and compressor length would be unambiguous but given the nature of the domain used here (continuous variable-area duct) this

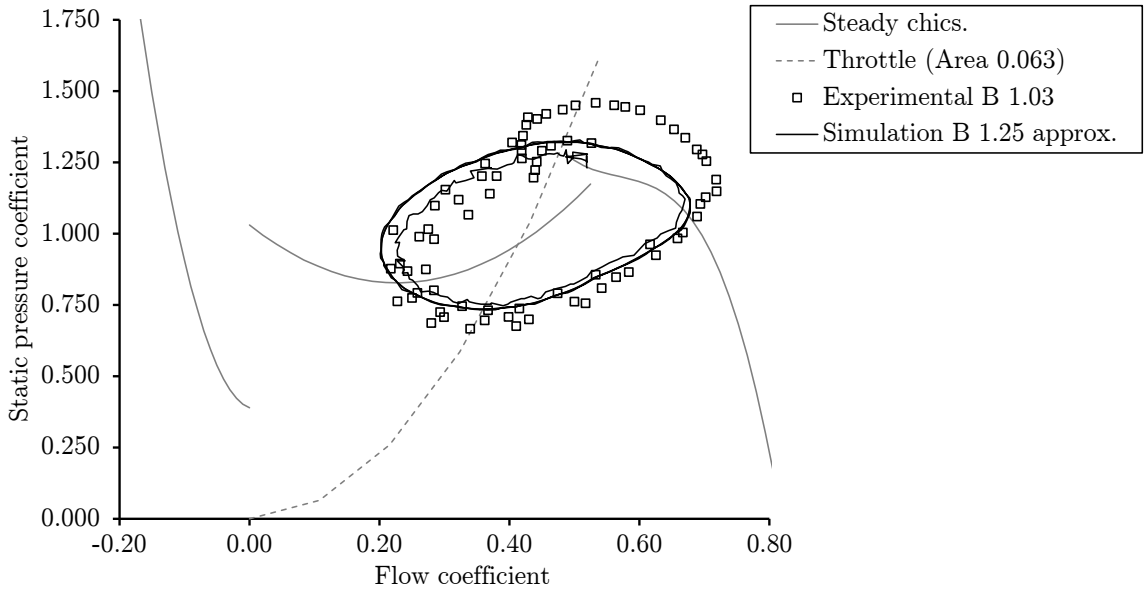

Figure 8.14: Compressor surge validation - Classic surge

calculation can only be done in a approximative way.

The deep surge is a transient response which is provoked by reducing the nozzle area even more, while keeping the B parameter constant. This pushes the compressor to work in reverse flow because the mass flow through the discharge nozzle is not enough and the compressor is forced to act like a throttle in the negative sense of the flow. Figure 8.15 shows the comparison between the simulation and the experimental results. In that case the throttle has been closed from 0.07 m^2 to 0.046 m^2 following the same procedure than in the previous cases.

The results shown over the present section demonstrate the suitability of the methodology chosen to predict the performance of a compression system including its in-stall operation. Although rotating stall exhibit two-dimensional features which dominates the stall cell growth, models based on a quasi-1D approach can be applied when the interest of the analysis focus on the area-averaged evolution of the flow properties as is the case of the overall engine transient performance analysis which is the main concern of the present doctoral research.

8.3 CERVANTES validation - Shaft failure Case 1

The simulation tool CERVANTES, whose methodology and development process has been explained in the present manuscript, was developed with the objective

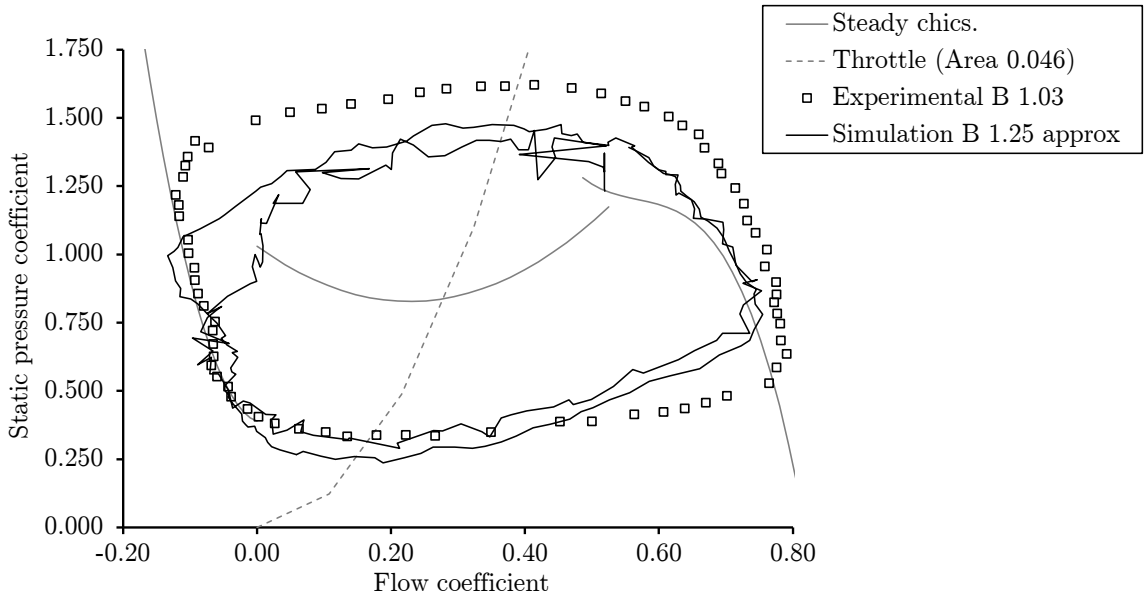

Figure 8.15: Compressor surge validation - Deep surge

of simulating gas turbine shaft failure events. The compression side simulation tool was coupled with the expansion side solver, the SAS transient model, and the turbine interaction model, to obtain a fully-integrated, transient simulation software. This tool includes all the necessary features to produce reliable predictions of the behaviour of any gas turbine in case of shaft failure.

'Case 1' is a shaft failure event occurred in a test engine while a fuel spiking test at maximum power was being performed. The engine had been provided with a thinner version of the IPS and it failed by fatigue when it was running close to the top of the fuel ramp. Figure 8.16 shows the law for fuel injection used in this case. The simulation tool CERVANTES has been used to build a model of the Engine A. The fuel flow shown in Figure 8.16 has been given as boundary condition and the IPS failure has been triggered at 0.22 sec in the time scale used by the plots included in the present section. The objective of this section is to show the comparison between the real data recorded in the event and the simulation carried out by the 'all-in-one' simulation tool with validation purpose.

During the first 0.2 seconds of the event the engine accelerates while the operating point departs from the stable running line towards the surge line which is the objective of a fuel spiking test. In that case, the IPS failed before the surge line was crossed. The vibration provoked by the failure triggered the HPC surge due to the increase of tip clearances. Figure 8.18 shows the evolution of the total pressure at the outlet of the HPC (PT30). The dynamic model captures successfully the slop of the pressure drop after the surge and the level of pressure in stall. Figure 8.19

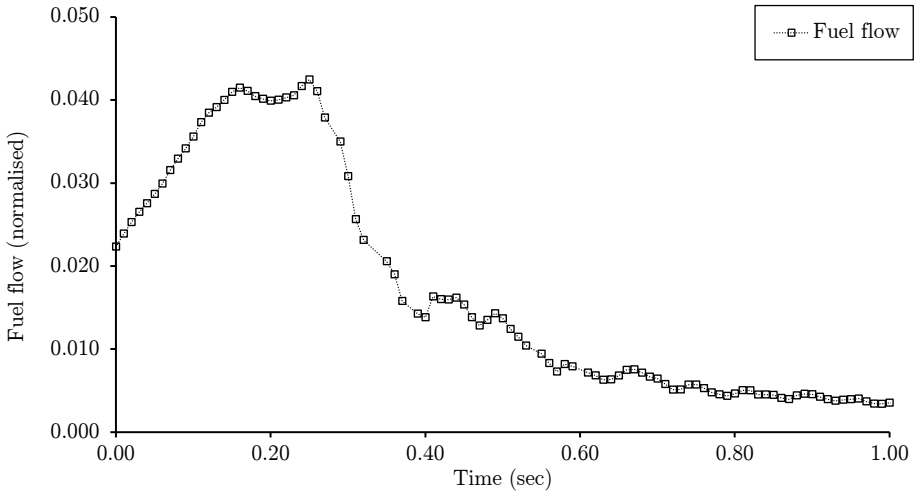

Figure 8.16: Fuel flow (fuel spike) - Shaft failure Case 1

shows a detail of the previous figure. It shows a difference in the trend towards the end of the event. The model seems unable to capture the rundown of the engine. This is a consequence of two assumptions that can be relaxed in future versions of the tool. The model of stall, based on observation of experimental data, assumes that the pressure ratio in stall is independent of the rotational speed. It seems to be correct when analysing the final pressure level in stall in experiments from 65% to 85% of rotational speed. Nevertheless, in the case of shaft break the IPC is not only in stall but also it lacks power input. The second assumption that can be affecting this fact is the model used to calculate the compressor work consumption in surge and rotation stall. This model is based on the application of the energy equation following a one-dimensional approach. It means that the work is proportional to the average mass flow which tends to be very small, even close to zero, in the first instant. It tends to underestimate this value. Other approach closer to reality would be to divide the compressor into two regions as is done in a parallel compressors model. These two regions could have non-zero absolute values of mass flow in different senses (forward flow and reverse flow) and both of them would contribute positively to the work consumption avoiding the value close to zero resultant of the use of the average mass flow. The consequences of this assumption can be observed in Figure 8.32. The IPC rotational speed predicted by the simulation does not follow the steep slop of the first instant leading to a final overestimation of the rotational speed. It is thought that the correction of these assumptions would allow the simulation of the IPC rundown improving the prediction of P30 evolution.

Figure 8.20 shows the evolution of the total pressure at the inlet of the HPC (PT26). It can be observed how the dynamic model is able to capture the pressure rise at

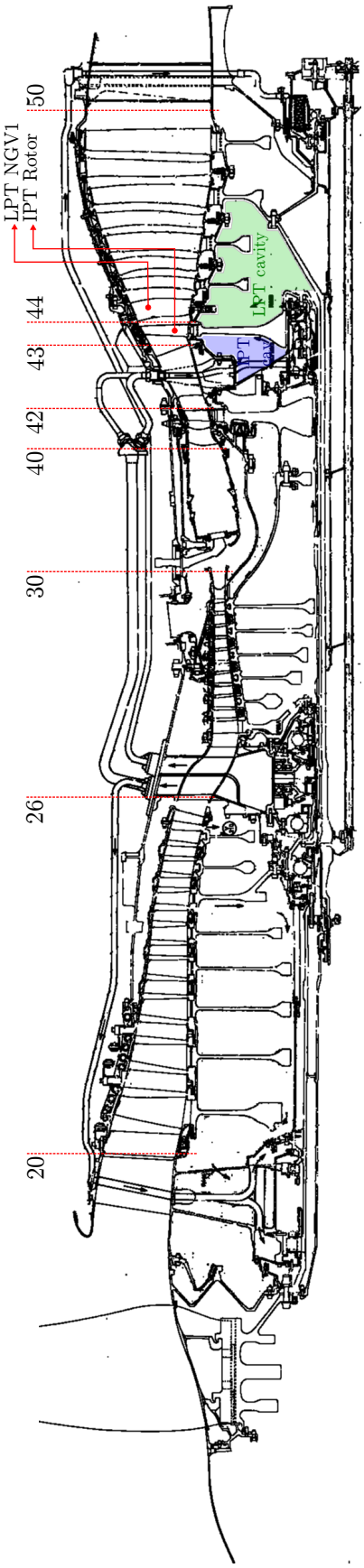

Figure 8.17: Engine A cutaway

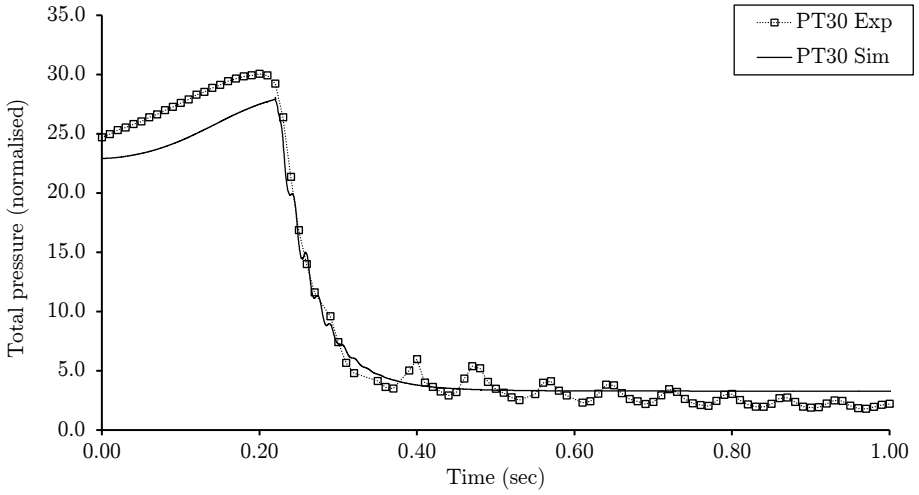

Figure 8.18: HPC delivery pressure evolution - Shaft failure Case 1

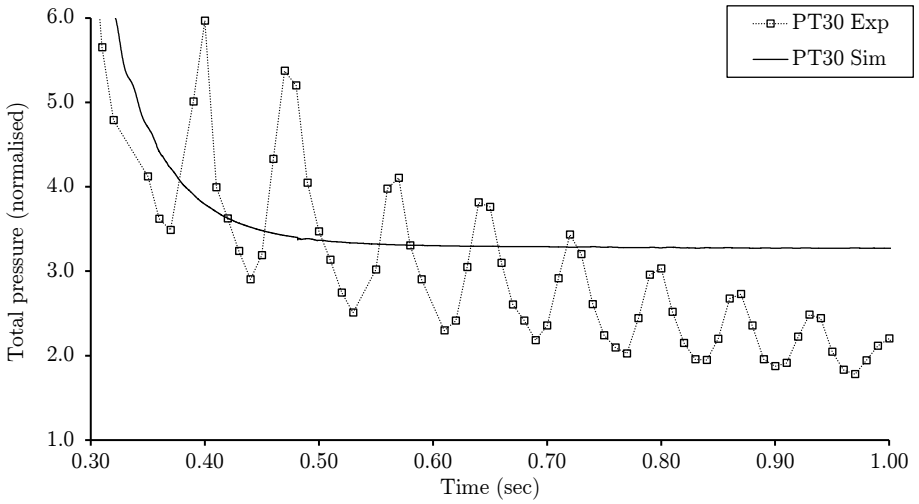

Figure 8.19: HPC delivery pressure evolution (detail) - Shaft failure Case 1

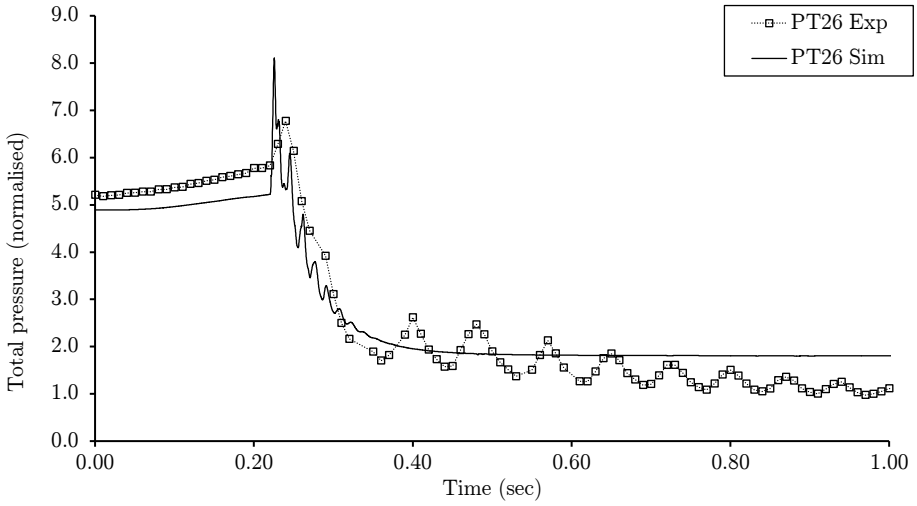

Figure 8.20: IPC delivery pressure evolution - Shaft failure Case 1

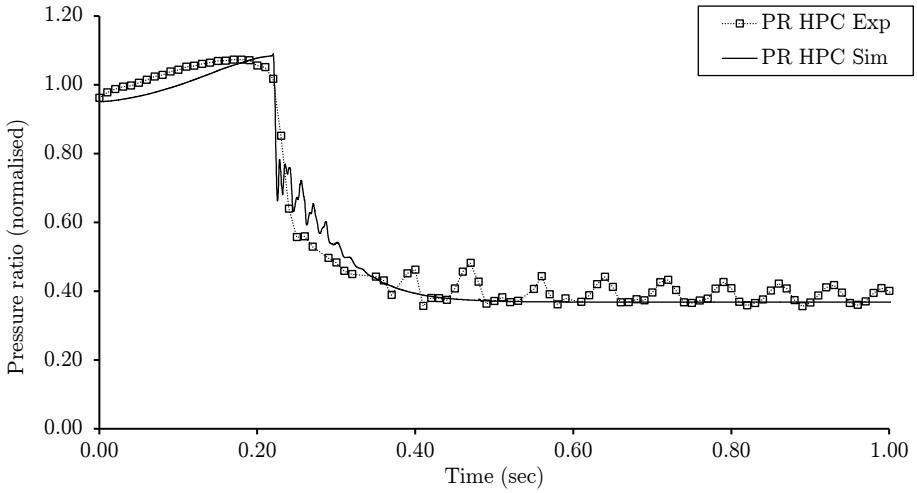

Figure 8.21: HPC PR evolution - Shaft failure Case 1

this point just in the moment of surge. This pressure rise is provoked by the sudden reduction in mass flow at the inlet of the HPC at the moment of surge which occurs earlier than the IPC surge. Apart from that, the rate of pressure decrease is captured with a good agreement and the same effect relative to the engine rundown is observed towards the end of the simulation as in the previous figure. For completeness, Figure 8.21 shows the evolution of the HPC PR.

The evolution of the non-dimensional mass flow at the inlet of the HPC (NDMF26) is shown in Figure 8.22. It can be observed that the model captures accurately the sudden drop in mass flow in the moment of surge and it reproduces fairly well the average level of this value in stall. The simulation predicts an initial oscillation in a frequency that is two high to be expected to appear in the experimental measurements due to the sampling rate used at the moment. Nevertheless, it is thought

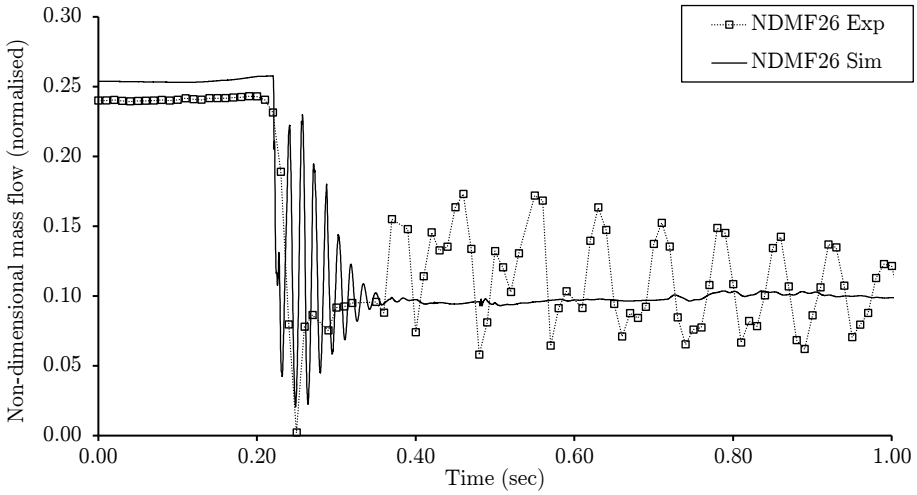

Figure 8.22: HPC inlet non-dimensional mass flow evolution - Shaft failure Case 1

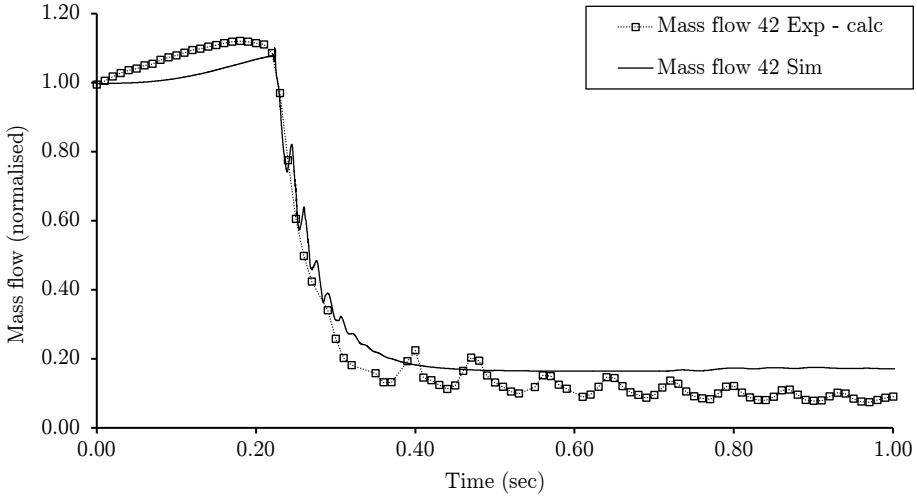

Figure 8.23: IPT inlet mass flow - Shaft failure Case 1

that this behaviour is realistic and it has been observed in other engines [50, 69].

Figure 8.23 shows the agreement in the prediction of mass flow at the inlet of the IPT. The model allows comparing the mass flow at both sides of the combustor in order to assess the dumping effect that this volume introduce to the event. Figure 8.24 shows the comparison of the mass flow at the inlet of the HPC (section 26) and at the inlet of the IPT (section 42). A good agreement is observed with experimental measurements too.

For completeness and to finish with the comparison of the evolution of thermodynamic properties, Figure 8.25 shows the evolution of the total temperature at the inlet of the HPT (TET). The model overestimates the slope of the first evolution prior to surge. It is provoked by the combustion model. Although a first order lag

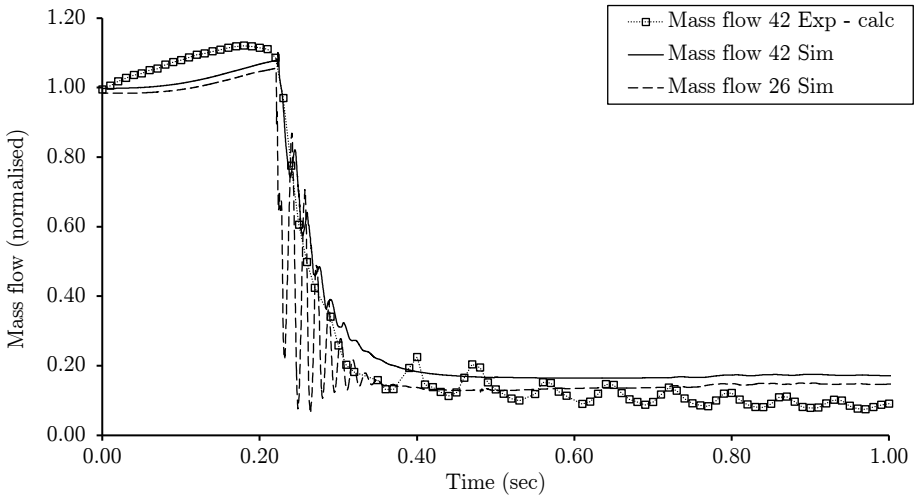

Figure 8.24: Combustor volume damping effect on mass flow - Shaft failure Case 1

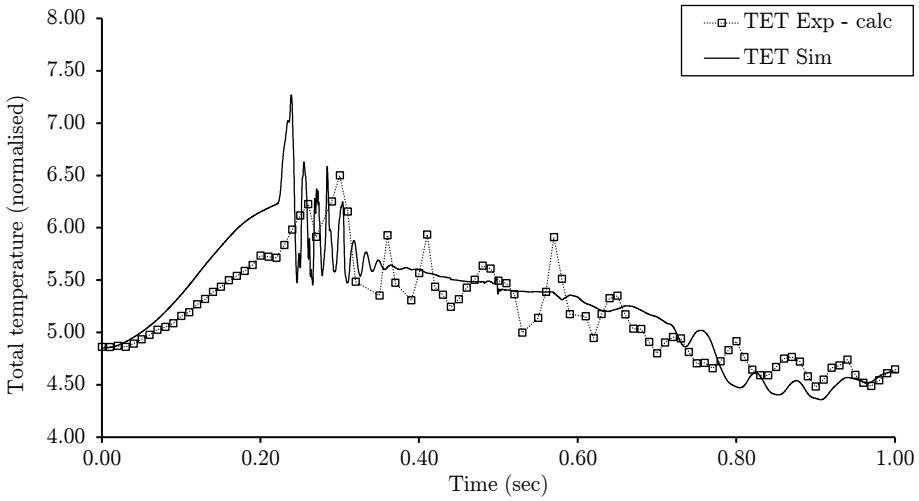

Figure 8.25: TET evolution - Shaft failure Case 1

has been implemented to delay the heat release in this kind of situations, improvements in the model are needed. Recommendation to improve the combustor model are included in Section 9.2. Beside that, the model captures the strong oscillations provoked by the surge and the temperature level over the event with acceptable accuracy.

Figure 8.26 shows the trajectory followed by the operating point plotted on top of the HPC map. Apart from the small error predicting the initial operating point, the trajectory agrees with the measurements. Given the final objective of this simulation tool, namely, the prediction of the overall performance after a shaft breakage, the slight disagreement in the prediction of the initial stable operating point does not raise special concern. This agreement could be improved by using more accurate values for the port areas connecting the MGP with the SAS. The lack of a heat

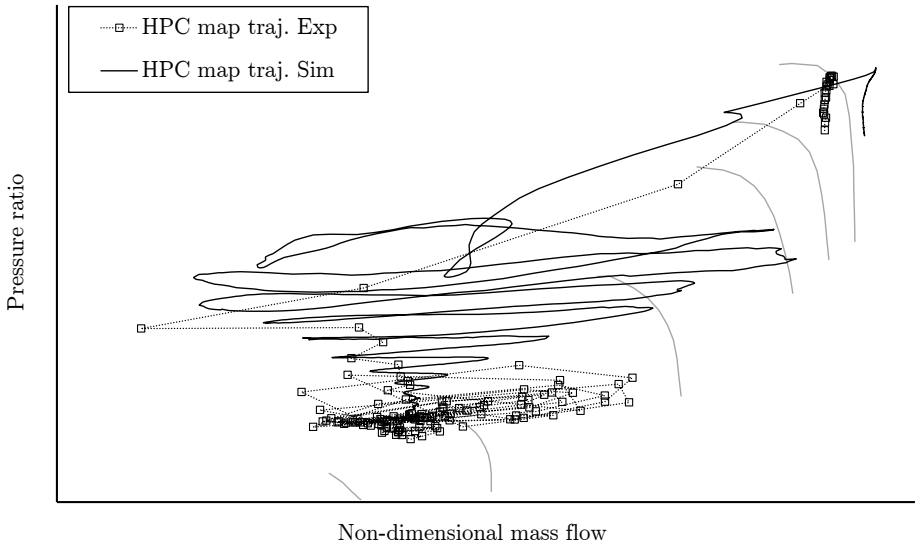

Figure 8.26: Operating point trajectory over HPC map - Shaft failure Case 1

transfer model over the MGP may also provoke misalignment in the steady state operating point. This functionality has not been implemented in this version of the solver since its main objective is the simulation of fast transient event where the heat transfer is a negligible phenomenon. Nevertheless, the equilibrium of the engine is affected by the energy transferred from the working fluid to the ambient. If the prediction of the initial operating point needs to be improved in the future, it is recommended to model heat transfer effects by means of the source terms available in Euler equations. Regarding the rest of the trajectory, the differences observed have been already discussed above through the comments to Figure 8.22. The agreement is satisfactory in terms of overall trajectory towards the stall point. The high frequency oscillation in non-dimensional mass flow which are not visible in this set of experimental data has been observed in other engines and they are given the name of 'Tornado' [50] following the pattern that can be observed in Figure 8.26.

The operating point trajectory, in that case on top of the IPC map, is shown in Figure 8.27. It can be observed how the IPC is pushed to surge by a sudden increase in pressure at the outlet provoked by the reduction in mass flow through the HPC consequence of the surge. The rest of the trajectory is very similar to previous one describing the same 'Tornado' pattern while the operating point falls down into the rotating stall region.

The same operating point trajectory can be plotted on top the turbine maps. Figure 8.28 shows the comparison of trajectories regarding the HPT map. The objective of this plot is the check of one of the assumptions of the model, namely, the choking conditions at the HPT at any moment after the failure. It can be observed how the

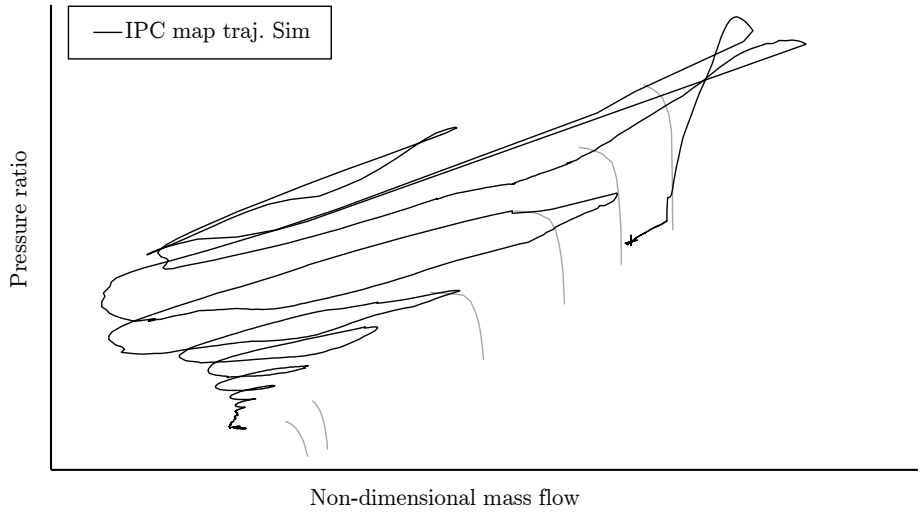

Figure 8.27: Operating point trajectory over IPC map - Shaft failure Case 1

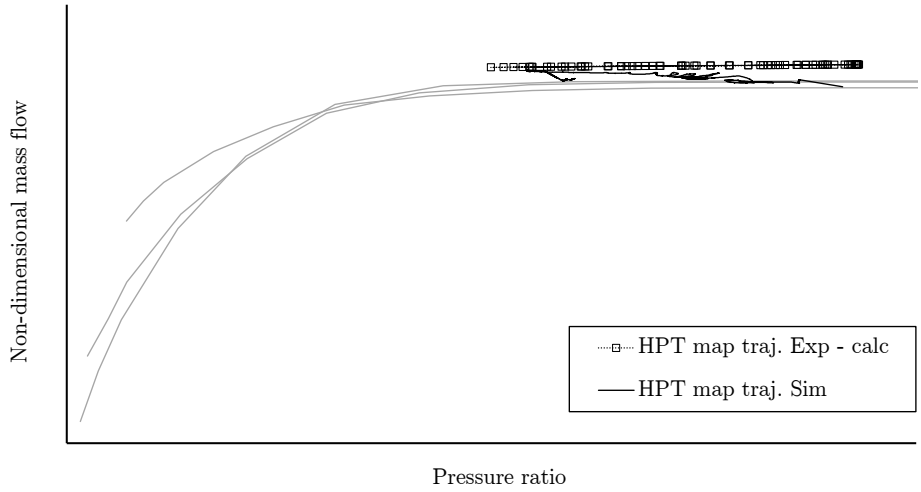

Figure 8.28: Operating point trajectory over HPT map - Shaft failure Case 1

operating point stays within the horizontal region of the turbine map confirming the choke operation of the HPT.

Figure 8.30 illustrates one of the special capabilities of this simulation tool. An important effort has been invested over the years in the modelling of the LPT performance when it is affected by inlet velocity triangle distortion provoked by the combined effect of IPT over-speed and compressor surge. The figure shows the trajectory of the operating point plotted on top of the LPT map. Apart from the two trajectories the figure shows as a reference two sets of turbine characteristics, the top three characteristics are those for nominal incidence while the other three correspond to the same rotational speed for an absolute incidence of -50 deg. The trajectory followed by the simulation goes from one map to the other during the event. In that case, the experimental trajectory is just a reference, it was not measured but

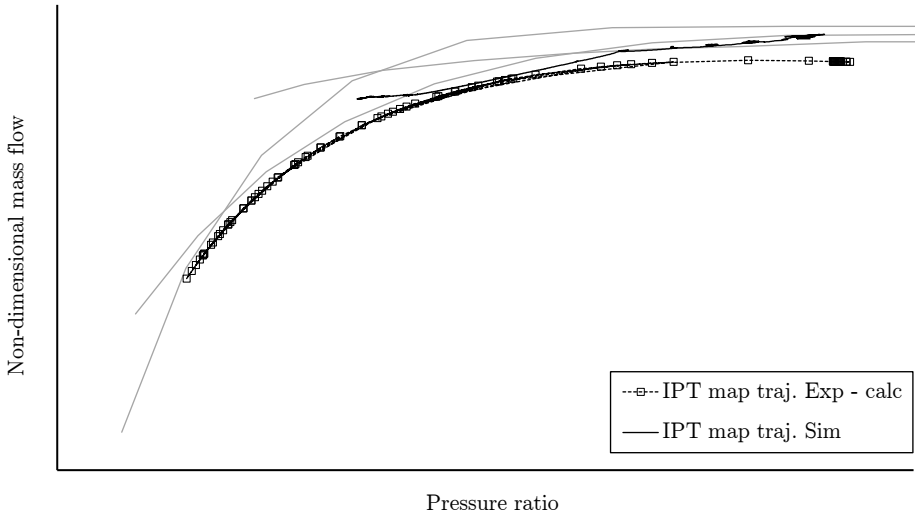

Figure 8.29: Operating point trajectory over IPT map - Shaft failure Case 1

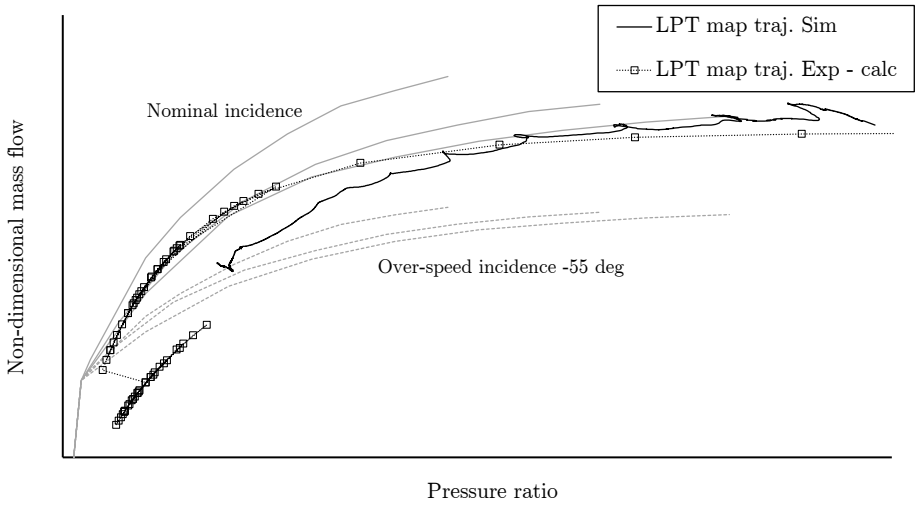

Figure 8.30: Operating point trajectory over LPT map - Shaft failure Case 1

calculated. The discontinuity observed is explained by the use of a coefficient to reduce the turbine capacity in a attempt to take into account the effect explained previously in this paragraph [87].

Previous figures have shown the agreement obtained in the simulation of the evolution of the thermodynamic properties over the MGP of the engine. The knowledge of the evolution of these properties allows the calculation of the torque extracted by the turbines and consumed by compressors and the integrator of the Newton's second law for angular acceleration can be used to calculate the evolution of the rotational speed of the different shafts. Figure 8.31 shows the prediction of the evolution of the rotational speed for the HPS and the LPS. The agreement in the HPS is relatively good while the prediction of the LPT speed underestimates the

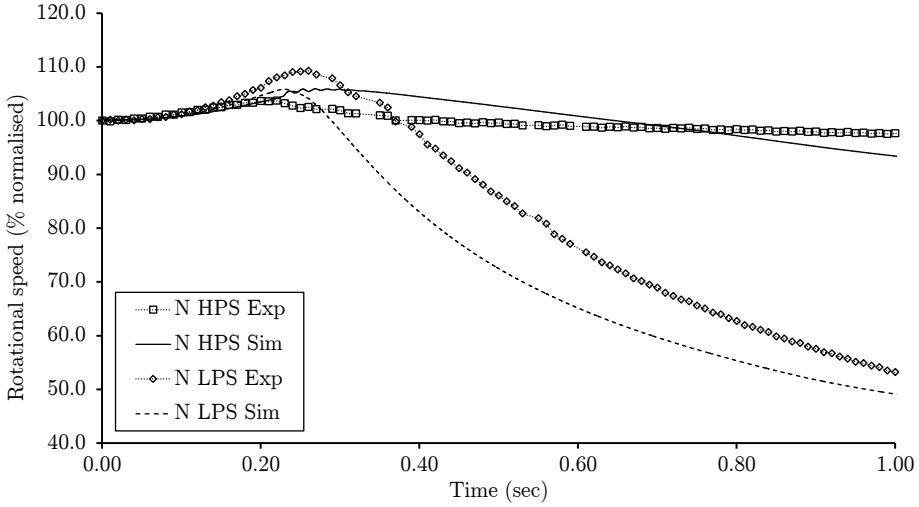

Figure 8.31: HPS and LPS speed evolution - Shaft failure Case 1

real measurement although the trend is captured. An important part of the torque acting on the LPS is the part consumed by the outer part of the fan (bypass side). As it has been explained in Chapter 5, the bypass of the engine has not been included in the simulation and the torque consumed by this part of the fan has been approximated as a function only of the rotational speed and assuming that it is not affected by the surge of the compression system. The disagreement observed in Figure 8.31 can be explained through this simplification of the problem. However, the error incurred as a consequence of this simplification does not have an important effect on the simulation of a shaft failure event. The agreement shown by Figure 8.31 is considered satisfactory for the purpose of this simulation tool.

The main objective of this simulation tool is the prediction of the terminal speed of the over-speeding turbine. Figure 8.32 shows the prediction of the evolution of rotational speed for the IPS. A unique line can be observed over the first 0.22 seconds, then the shaft breaks and the figure shows the evolution of the turbine and compressor speed separately. The test engine which suffered the shaft failure was not instrumented with that purpose and therefore, measurement of rotational speed are only available at the compressor side. Experimental data regarding the turbine speed plotted in the figure were extracted from the experimental evidences derived from the radial growth of the disc after the event. This hardware evidence offered an accurate estimation of the terminal speed. Figure 8.32 shows the rapid initial acceleration of the IPT rotor immediately after the failure. Although the compressor surge is triggered at the moment of failure, the energy stored in the combustor volume provokes the dramatic acceleration that is observed in the first tenth of a second. Then, the acceleration ratio falls due to the reduction in pressure and mass

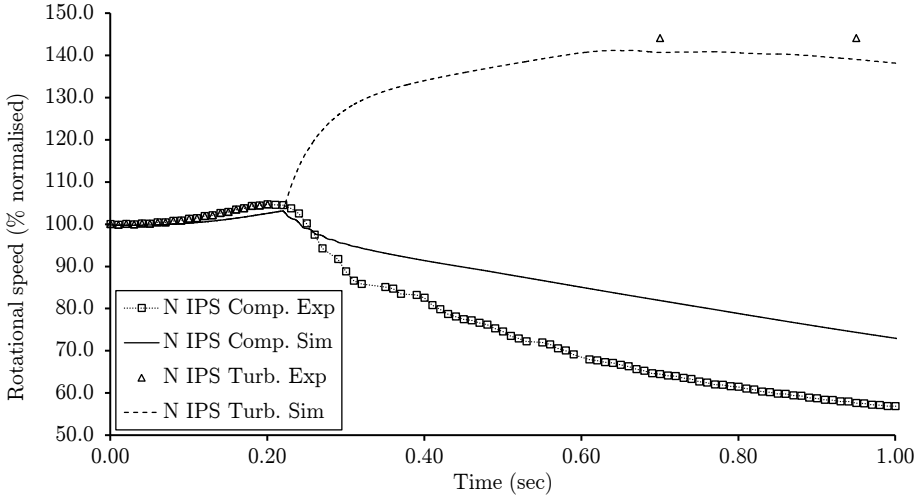

Figure 8.32: IP shaft speed evolution - Shaft failure Case 1

flow consequence of the compressor surge. The rotational speed continues increasing until 4 tenths of a second after the failure when the software predicts the first blade-to-vane contact whose deceleration torque leads to a plateau in the rotational speed signature. The difference observed between the experimental evidence of terminal speed and the speed predicted by CERVANTES is approximately 1.4%.

Regarding the deceleration of the compressor, an important disagreement is observed as a consequence of not capturing properly the high deceleration ratio over the first tenth of a second. The trend and the deceleration ratio during the rundown in stall is correct but the misalignment provoked by the difference in the first instant leads to an error of 29% in rotational speed at the end of the event. The reasons for this disagreement has been commented above in this section. The model used to calculate the power consumption of the compressor is based on a 1D approach which tends to underestimate the torque when the averaged mass flow is close to zero although, in the reality, this near-zero flow conditions is a consequence a 2D effect. Part of the compressor is working in reverse flow and the rest in forward flow, both sectors consuming power, but this effect is not captured by the actual model. The consequences of this simplified model are those observed in Figure 8.32. The error in IPC speed has no further impact on other variables since the force model used for compressor stall is independent of the rotational speed. Nevertheless, this inaccuracy can be solved in future versions of CERVANTES. Direction and suggestions to improve this part of the code are included in Chapter 9

The evolution of the rotational speed of the over-speeding turbine in case of un-located failure is affected by both, the power available in the MGP flow and the effect of friction and tangling due to the impact between the rotor disc and the

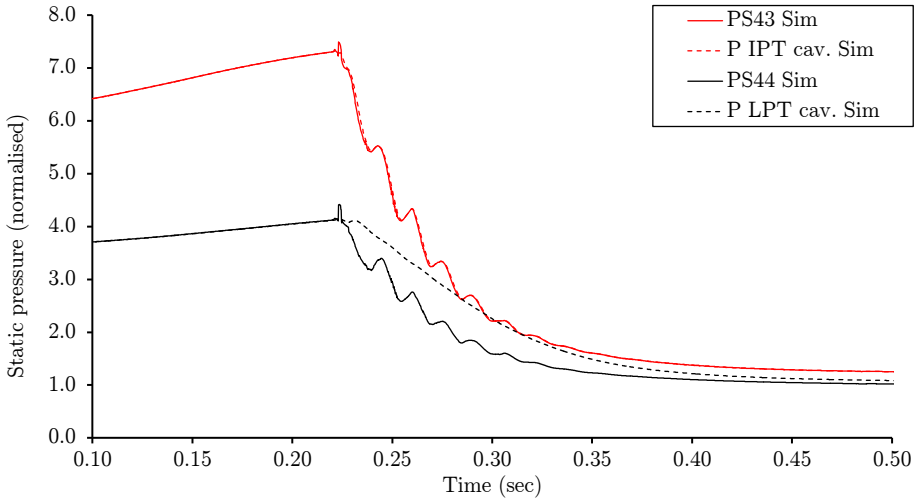

Figure 8.33: SAS cavity pressures evolution - Shaft failure Case 1

downstream static structure. The shaft failure case that is being analysis over this section was unlocated and the experimental evidences available clearly showed that the IPT rotor eroded the LPT NGV1 platform and penetrated on this structure leading to blade tangling. The simulation of the SAS is paramount to simulate that phenomena. The over-speeding disc is affected by the pressure of two cavities of the SAS, namely, IPT cavity (left-hand side in the cutaway) and LPT cavity (right-hand side in the cutaway). Figure 8.33 shows the evolution of the cavity pressures compared against the pressure in the MGP where the major port of each cavity is discharging. The figure shows how the pressure in the IPT cavity matches perfectly the static pressure in the section 43 of the engine (see cutaway Figure 8.17) while the pressure in the LPT cavity departs from the static pressure at the other side of its major port. This phenomena can be explained attending to two effects, namely, the axial displacement of the turbine which modifies the area of the ports and the size of each cavity. Since the free-running turbine is moving axially towards the LPT, the port which connects the IPT cavity with the MGP is going to open in the process while the LPT major port is going to close. It makes easier the pressure in the IPT cavity to equalise with the pressure in the MGP. Adding this effect to the fact of a smaller volume explains the evolution shown in Figure 8.33.

The effect observed in Figure 8.33, namely, the pressure increment inside the LPT cavity with respect to the pressure evolution over the MGP, has a negative effect from the point of view of the shaft failure outcome. This overpressure reduces the axial force acting on the free-running disc and therefore, limits the friction torque promoting the over-speed and delaying blade tangling. Figure 8.34 and 8.35 show the evolution of the two components of the pressure difference across the IPT

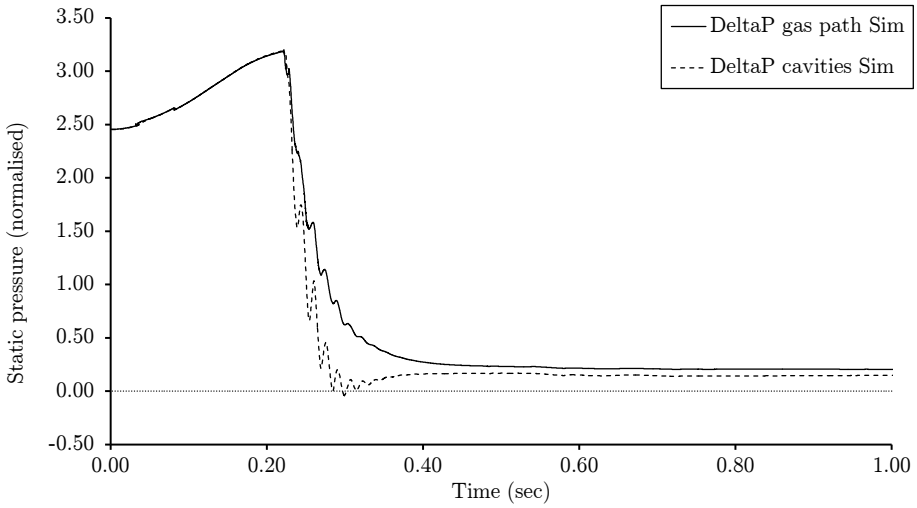

Figure 8.34: Pressure gradient across IPT blades and disc evolution - Shaft failure Case 1

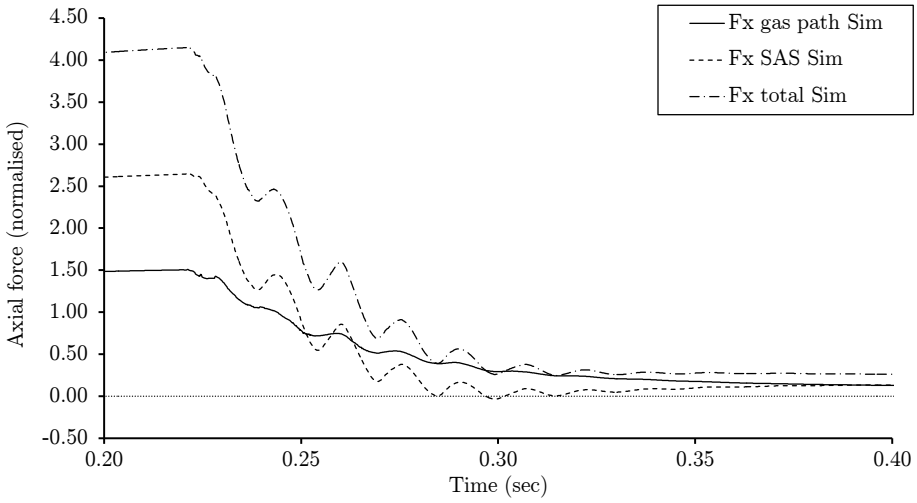

Figure 8.35: Axial force components evolution - Shaft failure Case 1

rotor (MGP and SAS) and the consequences in terms of axial force. The effect explained above can be observed more clearly here. The transient behaviour of the SAS provokes a valley in the pressure gradient which reduces the axial force. The accurate calculation of the different component of the axial force determines the capability to predict the terminal speed of the turbine which is highly dependent of the occurrence of blade tangling. It justifies the necessity to build a fully transient simulation tool for the SAS in addition to the solver of the MGP and the necessity to integrate both to capture the observed transient effect. This phenomenon is analysed in depth in Section 8.4.

The most important consequence of the axial force acting on the free-running turbine is the rate of material worn and ultimately the time to tangling. Although

there is a friction torque associated to the contact between the lock plate and the NGV platform, the capability to dissipate energy of this mechanism is by far lower than the deceleration provoked by blade tangling. Blade tangling is a more violent phenomenon involving impacts and, in addition, it occurs at higher radius with the consequent increment in torque. Figure 8.36 shows the evolution of the axial displacement of the over-speeding turbine, in addition, the length where the blade tangling starts has been indicated. Immediately after the breakage, the wear rate is very high due to the high value of pressure acting on the turbine. Half of the distance to tangling is covered over these first hundredths of a second. Then, apart from 0.26 - 0.28 seconds, a dramatic reduction in the wear rate can be observed. This can be explained attending to two different reasons, namely, the pressure drop provoked by the compressor surge and the overpressure experienced in the LPT cavity which reduces the net axial force acting on the disc. Finally, a slight increment in the slope is observed when the pressure within the LPT cavity reduces. The final level of axial force is sufficient to promote a continuous material erosion which leads to blade tangling 0.38 seconds after the failure. This description of the phenomenon can be linked with Figure 8.32 where it is observed that the turbine acceleration stops reaching a plateau after 0.6 seconds of simulation which is the moment when blade tangling starts.

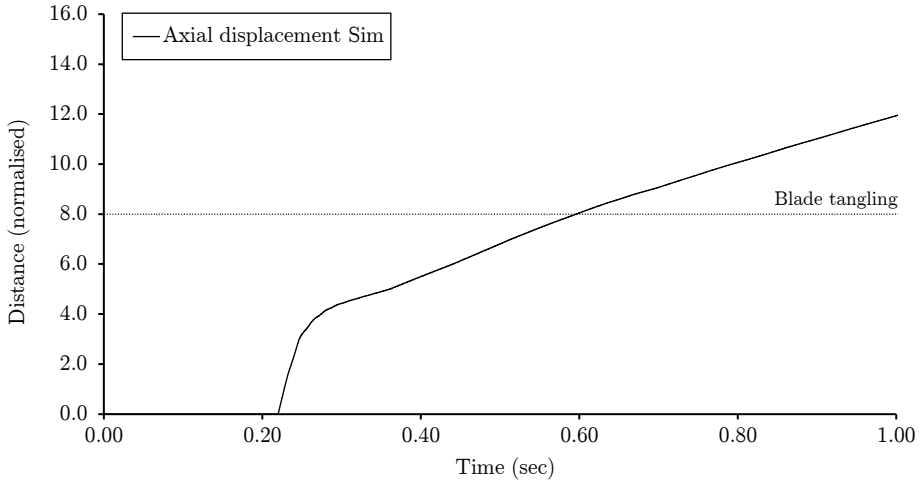

Figure 8.36: IPT disc axial displacement evolution - Shaft failure Case 1

8.4 Case study - Effect of the SAS

The previous section has shown the capabilities of CERVANTES to simulate a shaft failure scenario. The conditions of the shaft failure Case 1 have been reproduced

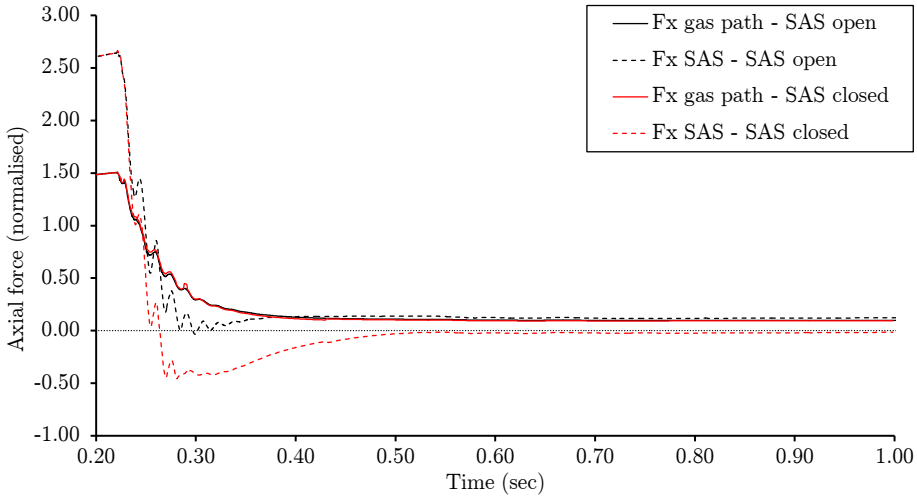

Figure 8.37: Axial force components evolution - SAS open vs closed

and the simulation has been shown to compare satisfactorily with the measurements. The objective of the present section is to undertake a sort of sensitivity analysis to assess the effect of the SAS on the event, in particular, its effect on the terminal speed. It is known that the axial displacement of the free-running turbine disc, in case of unlocated failure, can lead to the closure of the major port of the LPT cavity. Nevertheless, observations of different scenarios indicate that the total closure of the port is unlikely, presumably due to three-dimensional effects such as disc orbiting which would allow the contact and the wear of material without closing completely the port and therefore, allowing the LPT cavity pressure to equalise with the pressure in the MGP. That said, the purpose of this section is to show the capabilities of CERVANTES modelling different scenarios. Using the starting conditions of Case 1, two simulations have been performed, namely, the equivalent located failure and the hypothetical case with complete closure of the major port of the LPT cavity.

Figure 8.37 shows the comparison for the different components of the axial force between the reference case (Case 1) and the case with complete closure of the port (SAS closed). It can be observed that the axial force derived from the MGP does not suffer any important variation. On the other hand, the impact on the component derived from the SAS is clearly visible. As expected, in case the LPT cavity port closes completely, the overpressure within the LPT cavity is higher and more prolonged in time than in the reference case. In that case, the SAS component of the force becomes negative over a long period of time. The total axial force can be observed in Figure 8.38. The negative peak in the SAS component of the axial force is enough to provoke an overall change in the direction of the axial force which would provoke the reopening of the port.

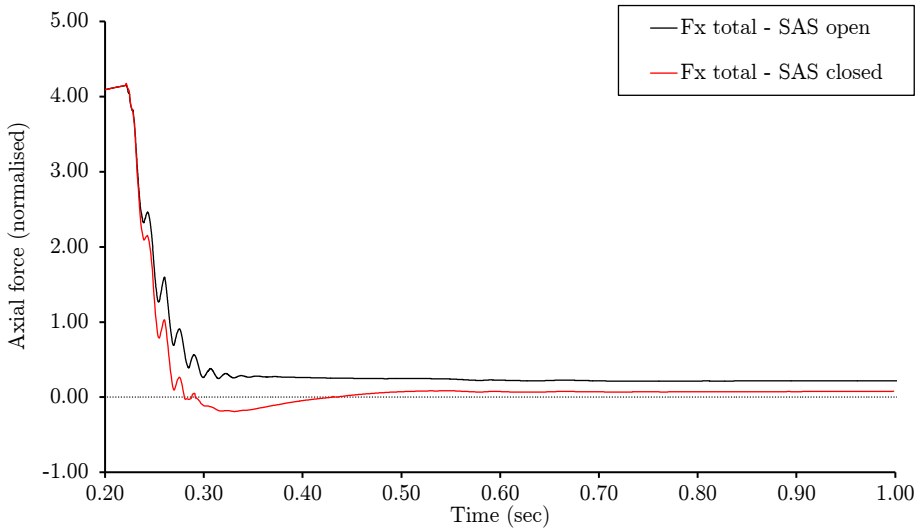

Figure 8.38: Total axial force evolution - SAS open vs closed

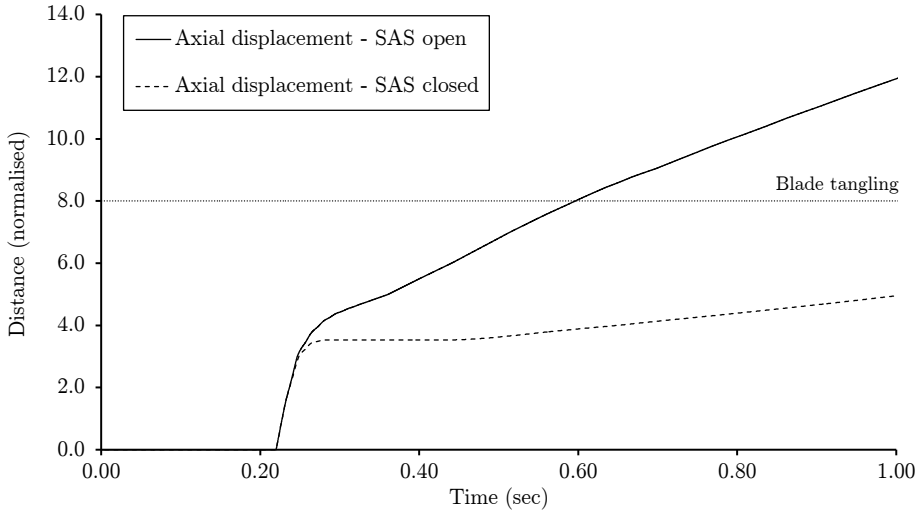

Figure 8.39: IPT disc axial displacement evolution - SAS open vs closed

The direct consequence of the axial force signature observed in Figure 8.38 is the reduction in the rate of material worn. Figure 8.39 shows the comparison between the axial displacement of the free-running turbine disc in both cases. The overpressure within the LPT cavity lead to a long plateau in the axial displacement signature after the first instant where both curves follow the same path. Although after 0.5 seconds the axial force become positive again, its value is always lower than in the reference case; the consequence of that can be observed in Figure 8.39 where the slope of the curve is lower than the reference case and does not allow the event to reach the tangling distance.

As it has been explained in the previous section, the friction torque derived from the contact in the platform is not enough to compensate the torque extracted from

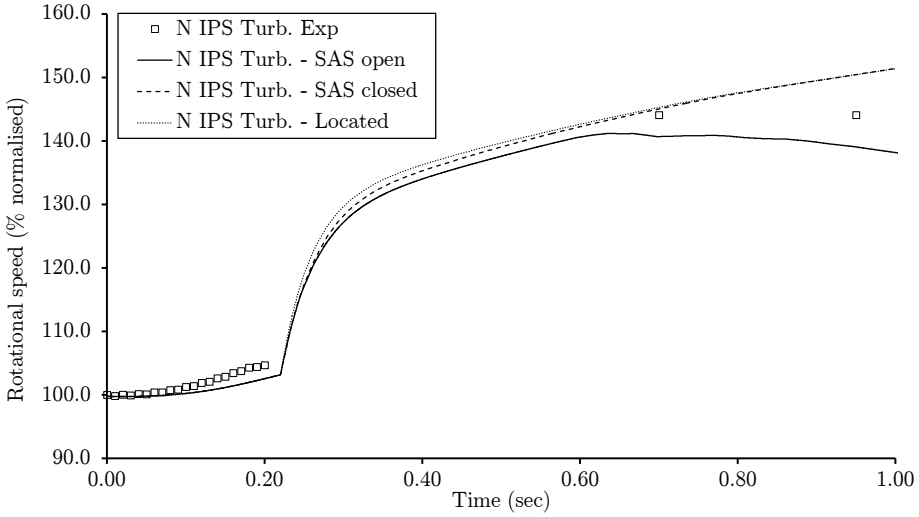

Figure 8.40: IPT speed evolution - SAS open vs closed

the gas path in that shaft failure scenario. The contribution of the blade tangling was paramount to arrest the acceleration rate. Since, in that case, blade tangling never occurred, the IPT continues accelerating as can be observed in Figure 8.40. In this figure, three different scenarios are compared. The reference curve is the Case 1 named as 'SAS open'. The same case has been simulated assuming that the turbine remains axially located after the failure, this simulation is named as 'Located' in the picture. The case 'Located' illustrate an upper limit in terms of terminal speed for a particular thermodynamic evolution / surge sequence. Apart from that, the case 'SAS closed' has been included. It can be observed that the case 'SAS closed' would be very similar to the worst possible scenario because the LPT cavity overpressure acts preventing friction and tangling in a similar way as would happen in a located case.

The main conclusion that can be derived from this analysis is the importance of blade tangling to arrest the turbine acceleration. Compressor surge may not be sufficient to arrest the over-speed in certain engines if the failure is located or if any other event prevents the axial displacement and the blade tangling. The presence of more material between the IPT rotor and the LPT NGV (longer platform) could have a similar effect on the rotor acceleration signature.

8.5 Case study - "Clean" failure demonstrator

Depending on the cause of failure and its location over the shaft, the level of vibration may change. The robustness of the developed simulation tool allows its application

to different scenarios. In this case, a simulation has been carried out assuming that the initial vibrations after the failure are not strong enough to trigger the compressor surge. If this is the case, surge will be triggered by VG mal-schedule. The IPC will decelerate rapidly. The time scale of this deceleration is much lower than the time needed by the variable geometry actuation system to adapt the position of the VSVs to the new rotational speed. This fact provokes a mal-schedule of the variable geometry which changes the compressor map. Nominal compressor maps are derived assuming that the schedule of the variable geometry is the one that has been pre-implemented at each rotational speed. The mal-schedule provokes a change in the map that, in that case, tend to reduce the surge margin and, ultimately, trigger the IPC surge. Since compressor surge is not initiated immediately after the failure, the occurrence of surge in that case has a delay associated to the mal-schedule process that is going to affect greatly to the shaft failure outcome. The simulation has been initialised using the same conditions than in Case 1 but keeping the fuel flow constant (without fuel spike). This conditions are close to the maximum power conditions of the engine. Then a IPS break has been simulated after 0.1 seconds. The most relevant results of this simulations are shown and analysed in the present section.

Figure 8.41 shows the evolution of the IPC and HPC delivery pressures. It can be seen that no sing of surge is observed at the moment of failure but slightly later. The pattern of pressure decay is the same observed in Case 1, the engine runs down in stall. More interesting is to observe the detail around the failure to understand the surge sequence which is shown in Figure 8.42. The overall compression system surge is delayed almost 5 hundredths of a second which is the time needed by the combined effect of compressor deceleration and variable geometry mal-schedule to trigger the surge. The surge sequence occurs as follows: the IPC surges 0.045 seconds after the failure, then, the sudden reduction in mass flow due to the IPC surge triggers the HPC surges which occurs 5 miliseconds after the IPC surge. Figure 8.42 clearly shows the HPC surge through a bump in PT26. After that sequence, both compressors evolve towards stall conditions.

The operating point trajectory of this event can be plot on top of the compressor maps. Figure 8.43 shows the trajectory on top of the HPC map. The surge inception process can be observed. The initial stable operating point is suddenly modified following a horizontal trajectory towards the surge line provoked by the rapid drop in mass flow at the inlet as a consequence of the IPC surge. The later trajectory towards the stall point describes the 'Tornado' pattern already observed in Case

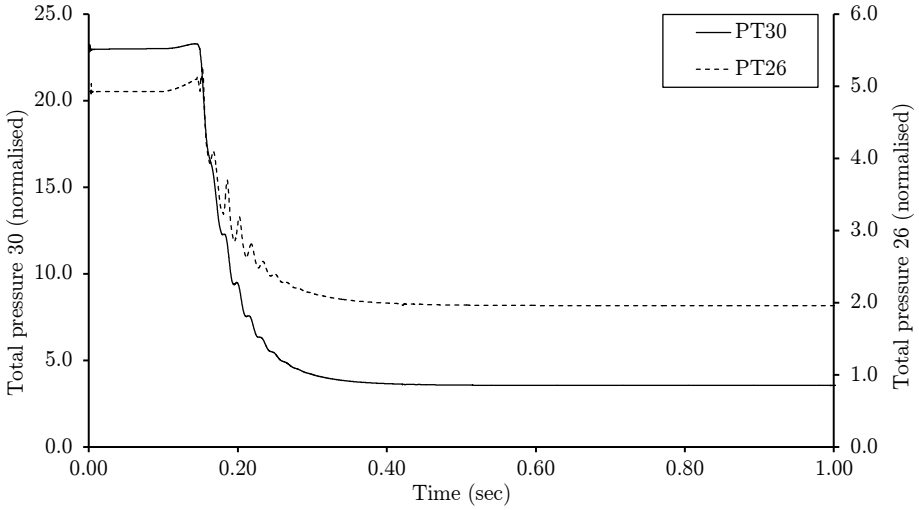

Figure 8.41: HPC and IPC delivery pressures evolution - "Clean" failure case

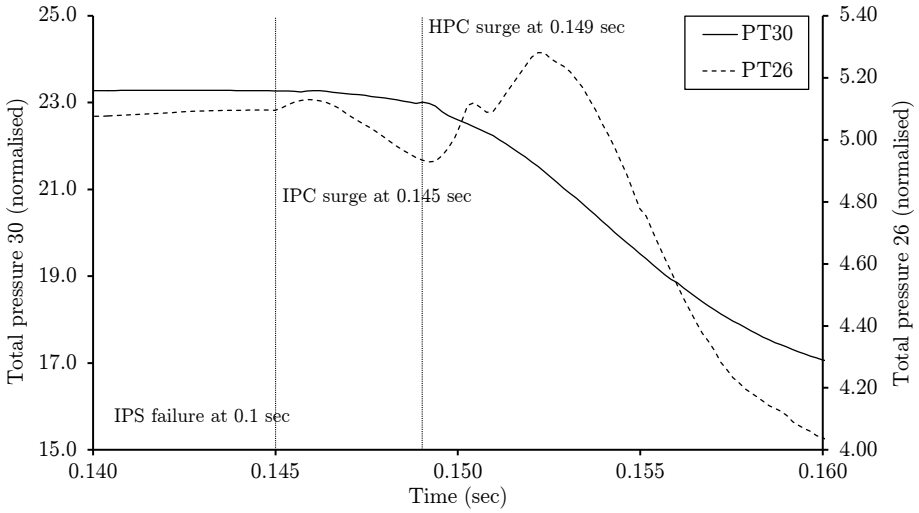

Figure 8.42: Compressor surge sequence - "Clean" failure case

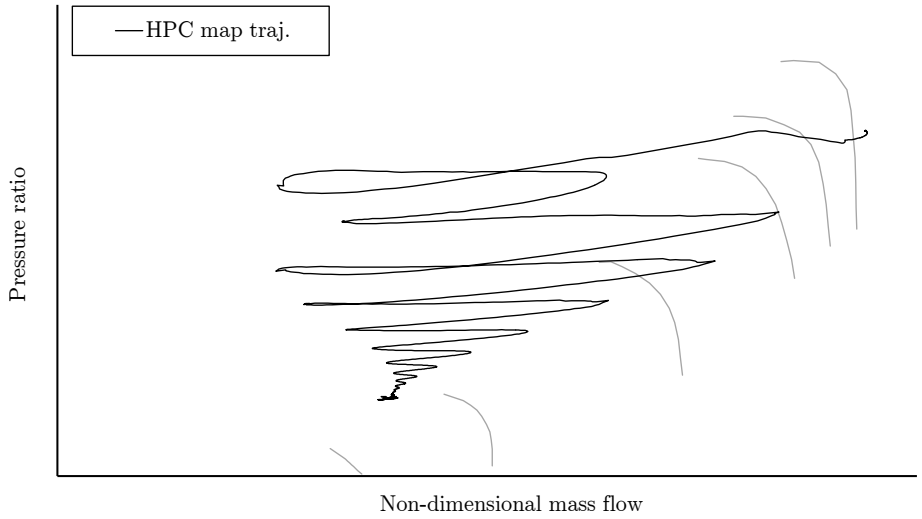

Figure 8.43: Operating point trajectory over HPC map - "Clean" failure case

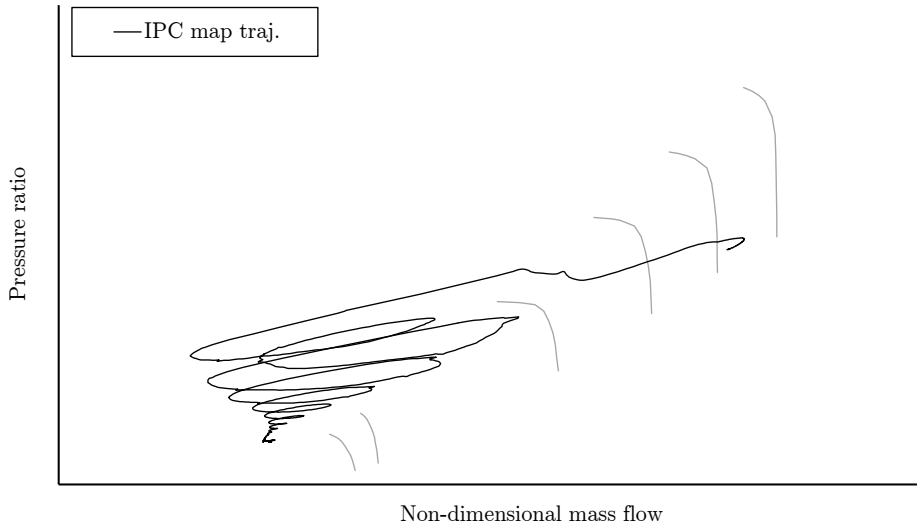

Figure 8.44: Operating point trajectory over IPC map - "Clean" failure case

1. Figure 8.44 shows the trajectory on top of the IPC map. The operating point follows a horizontal descending trajectory while the compressor is decelerating which finally crosses the surge line and continues towards the stall point following a pattern similar to the one observed in the rest of the plots.

Besides the analysis of the differences in terms of compressor surge sequence, the evolution of the rest of thermodynamic properties is similar to those observed in Case 1, both cases are dominated by the consequences of compressor surge. For completeness, the evolution of the IPC rotational speed can be seen in Figure 8.45. It has been plotted compared against the evolution if the HPS speed. The instant of failure can be observed in the figure by the steep change in IPC rotational speed. The deceleration slope changes when the IPC surges. A deceleration of approximately

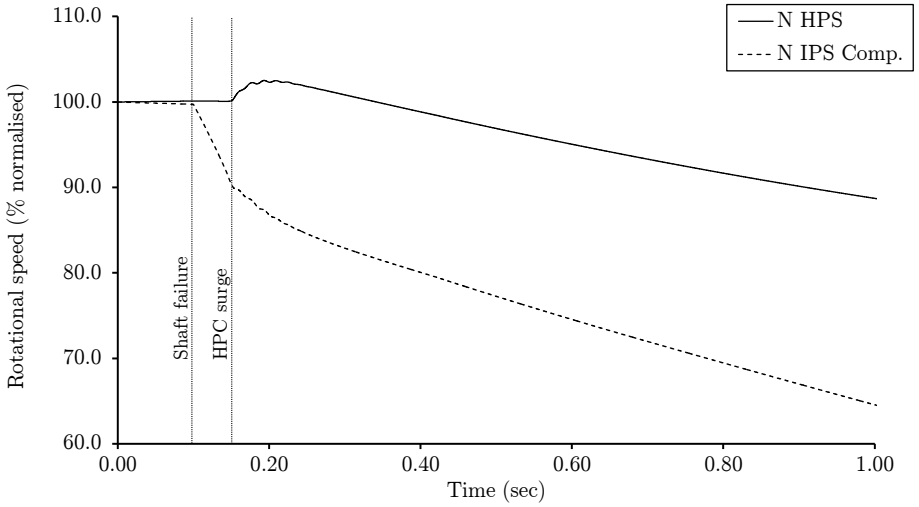

Figure 8.45: IPT speed evolution - "Clean" failure case

of 10% is sufficient to push the compressor to surge assuming the variable geometry to be frozen. This assumption is perfectly valid for the time scale of the event given by the deceleration rate.

Finally, the analysis of the over-speed outcome in that case can be summarised by Figures 8.46 and 8.47. Figure 8.46 shows the evolution of the IPT rotational speed. The evolution of the rotational speed in Case 1 has been included as a reference (the curve has been moved to make coincident the failure instants). The last simulation has been labelled with the name 'Clean'. In addition, the same simulation has been run assuming located failure in order to explore the worst possible scenario for the given surge sequence. The first conclusion that can be extracted from Figure 8.46 is that the terminal speed in the 'Clean' case is higher than in Case 1. The reason for that is the delay of the compressor surge. This is not triggered immediately, provoked by the failure as in Case 1, but occurs later due to the fast deceleration and the consequent variable geometry mal-schedule in the IPC. The consequence of that can be clearly observed in the plot. The first acceleration period, the one with the highest slope, is slightly longer in time leading to a higher rotational speed when surge, turbine friction and, in particular blade tangling, contribute to arrest the acceleration process. Since the level of pressure is higher during a longer period of time after failure, the material erosion process is faster and reaches the tangling distance 0.18 seconds earlier than in Case 1 as can be observed in Figure 8.47. Nevertheless, although blade tangling occurs earlier, the dominant effect is the acceleration over the first instants and the terminal speed predicted is a 4% higher.

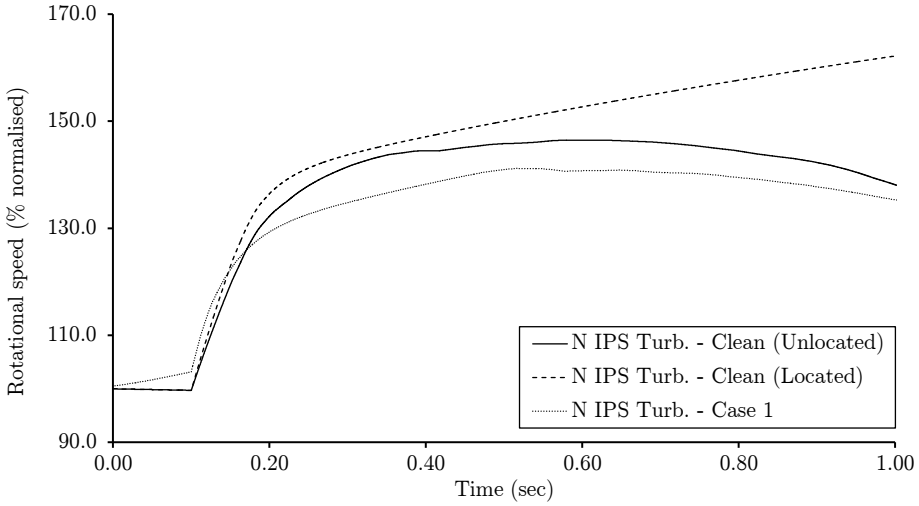

Figure 8.46: Compressors' rotational speed - "Clean" failure case

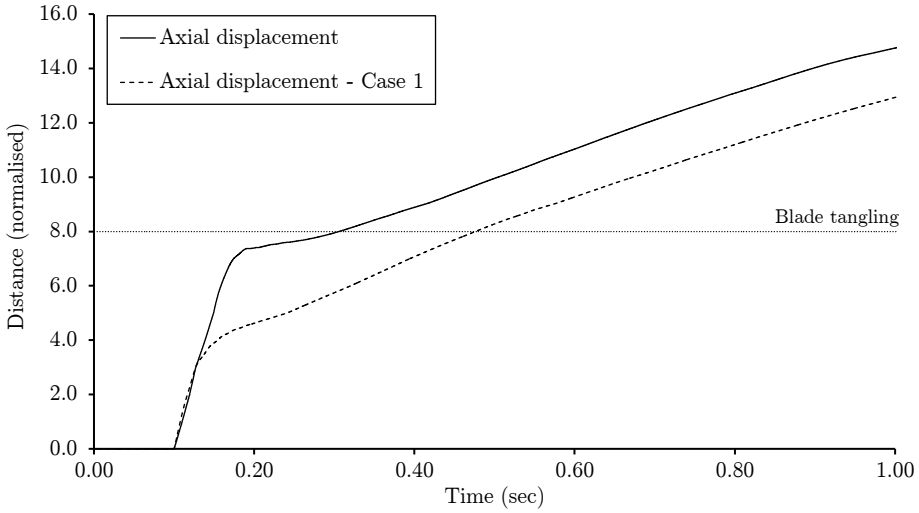

Figure 8.47: IPT disc axial displacement evolution - "Clean" failure case

8.6 Conclusions

The building process of the 'all-in-one' simulation tool CERVANTES followed different stages of programming and validation. Firstly, the core of the program, the numerical solver, was validated against several exact solutions including steady-state solutions and complex transient evolutions such as the shock tube case. Once verified the numerical solver, its capability to model the reality was checked against the experimental measurements of the shock tube problem. Satisfactory agreements were found at all the stages of this process which allowed certifying the capability of the solver to simulate transient 1D flows.

The most important feature of CERVANTES is the reliability in the simulation of

compressor instability. The classic experiment carried out by Greitzer in the 70s' at MIT was modelled with CERVANTES to assess the capability to predict the different behaviours regarding compressor surge. The influence of the lag parameter and the B parameter of Greitzer was assessed and three specific transient trajectories (rotating stall, classic surge and deep surge) were compared against the experimental measurements obtaining satisfactory results. This test allowed confirming the capability of this methodology to deal with compressor surge within the context of a 1D approach.

CERVANTES is the integration of different functionalities with the objective of simulating gas turbine shaft failure events. The integration of the tool includes the coupling of the compression side with the expansion side to build the MGP, the connection of the latter with the SAS simulation tool, the model of friction and wear and the shaft speed integrator. Once the 'all-in-one' simulation tool was built, it was applied to model a documented case of shaft break. The level of agreement achieved in the simulation of thermodynamic properties and shaft speeds was shown along this chapter. The agreement is acceptable in most of the important variables such as P30, TET and the free-running turbine speed. The error in terminal speed was shown to be below 2%. Nevertheless, some weaknesses were identified which will determine the further work to continue to improve this simulation tool.

The analysis of the different case-studies was used to show the most important capabilities of CERVANTES:

- Compressor surge modelling.
- Modelling of the mal-function of the LPT after a IPS failure by means of turbine maps depending on the incidence angle.
- Integration with friction/wear model allows predicting the time to tangling and its effect on turbine acceleration.
- Reaction of the SAS to fast changes in the flow properties over the MGP and changes in the geometry of cavities and ports.
- Assessment of the effect of the SAS on the turbine friction process.
- Capability to predict compressor surge triggered by VG mal-schedule.

The sensitivity analysis carried out, in particular the case with closure of the LPT cavity major port, confirms that blade tangling is essential in the process of limiting

the terminal speed of the free-running turbine. The compressor surge sequence is the most influencing fact on the acceleration of the turbine but the combined effect of the friction consequence of blade tangling is necessary to guarantee the safe rundown of the engine.

In summary, CERVANTES was shown to be a reliable and inexpensive method to assess the behaviour of an engine after a shaft failure achieving accuracy below 2% of error in the prediction of free-running turbine terminal speed.

Chapter 9

Conclusions, contribution and way forward

Shaft over-speed, particularly when it is provoked by a shaft failure, has been pointed out as a major certification issue for aero engine manufacturers. The opportunity to satisfy certification authorities by means of reliable simulation tools has motivated the present research project with the objective of supporting the sponsor company in the certification process avoiding expensive experimental demonstrations.

The shaft over-speed event cannot be tackled unless engine component interactions and fast transient effects are taken into account in a global manner. The high vibration level, consequence of a shaft breakage, is enough to push the compressor into surge. This provokes unstable transient operation which affects the performance of every engine component. The accurate prediction of the evolution of the fluid properties within the main gas path determines the power available to over-speed the free-running turbine, and therefore its acceleration rate. On the other hand, the axial movement of the free-running turbine is influenced by the pressure within the secondary air system where the disc is immersed. Therefore, the evolution of the flow properties within both systems, namely, main gas path and secondary air system, is needed to calculate the rotational speed of the free turbine and determine its terminal speed.

The methodology to simulate the main gas path dynamics is based on the one-dimensional transient Euler equations of fluid dynamics applied within the fluid domain which represents the gas path. Source terms in the equations simulate the effects of engine components such as the compressor and combustor. The secondary

air system is modelled through a network of tanks and tubes where the flow evolves affected by the changes in boundary conditions which are the connections with the main gas path. Both solvers have been integrated and run coupled within the same time marching scheme. The module to simulate the mechanical interaction of the turbine with the rear static structure developed by Aleixo González has also been integrated and therefore, the tool allows the simulation of all the particularities involved in a shaft failure event.

The 'all-in-one' simulation tool has been used to build a model of the a real engine which suffered a shaft failure event. This event has been simulated with CERVANTES to carry out the first validation of the tool. This exercise has shown promising results, in particular, accurate prediction of aero-thermal properties and free-running turbine rotational speed evolution. The influence of the secondary air system on the outcome of the event has been assessed showing its impact on the friction and wear process and the subsequent evolution of the free-running turbine rotational speed. Furthermore, a case study simulating a clean failure where the compressor surge is triggered by the compressor variable geometry mal-schedule has been performed for demonstration purposes.

Besides the development of the overall engine simulation tool, the investigation has focused on the understanding of the performance of key engine components during the extreme conditions experienced during a shaft failure event:

- Shaft failure triggers compressor surge which leads the compressor to operate at reverse flow conditions. Extensive CFD analysis has allowed the mapping of the single-stage performance at reverse flow conditions as a function of its geometry. Moreover, a methodology based on the stage-stacking technique and the generic single-stage maps has been developed which allows the prediction of the reverse flow map of any compressor.

- The drop in mass flow due to compressor surge and the increment in swirl velocity due to the over-speed of the free turbine provoke extremely distorted velocity triangles at the inlet of the downstream turbine. The change in performance of the first NGV under this conditions has been assessed by means of 3D CFD and a methodology has been developed to derive the overall turbine map adding the incidence angle as an extra variable.

9.1 Contribution to knowledge

Main gas path simulation

- Development of a fully-transient gas turbine performance solver.
- Capability to model compressor post-stall behaviour validated against experimental results.
- Capability to model distorted inlet flows in turbines.

Secondary air system simulation

- Development of a fully-transient secondary air system network solver.
- Capability to model the effect of variable geometry in cavities and ports due to the axial displacement of the free-running turbine.
- Implementation of heat transfer effects in cavities which allowed reducing the errors below 2% in the steady-state solution.
- Modelling of turbulence pressure loss in long pipes of the secondary air system.
- High level of readiness achieved: Software delivered as standalone tool to Rolls-Royce.

Integration and shaft failure modelling

- Development of the 'all-in-one' simulation tool by the coupling of different solvers: MGP + SAS + Friction/wear.
- Capability to capture the systems' interaction during a shaft failure event.
- Simulation of a shaft failure event using an integrated standalone tool by the first time (only ambient conditions, fuel flow, component maps and geometry are given as input data / boundary conditions).
- Assessment of the impact of the SAS behaviour on the outcome of the shaft failure event.
- Assessment of the impact of different surge sequence on the outcome of the shaft failure event.

Compressor reverse flow performance

- Extensive CFD analysis of the flowfield at reverse flow conditions and identification of the geometrical features affecting the performance.
- Derivation of universal single-stage maps at reverse flow conditions only function of stage geometry.
- Development, implementation and validation of the methodology/software to calculate multi-stage compressor maps at reverse flow conditions: SST + single-stage maps.
- Application of the prediction tool to calculate the reverse flow maps of several modern compressors.
- High level of readiness achieved: Software delivered as standalone tool to Rolls-Royce.

Turbine performance at high negative incidence angles

- Establishment of a simple and robust methodology to derive turbine maps affected by the high negative incidence angles typically observed in a shaft over-speed event.
- Aerodynamic assessment of a novel design of NGV at high negative incidence angles by 3D CFD.

New technologies to improve VIGV performance

- Aerodynamic assessment of the Variable Camber Vanes to establish the potential improvement in VIGV performance.
- Development and aerodynamic assessment of a novel idea for high-performance VIGV of simple implementation (Split Variable Guide Vanes). In process to be patented with Rolls-Royce.

The majority of the achievements listed above can be classified as industrial contribution. Most of them have contributed to enhance the performance prediction

methods of the sponsor. Nevertheless, being the sponsor's business the cutting-edge technology within the aero engine industry, some of the advances carried out in the context of this doctoral research are state-of-the-art scientific contributions. In particular, the development of the 'all-in-one' simulation tool and the study of compressor reverse flow performance. The former is, to the best of the knowledge of the author, the first fully integrated tool to simulate the shaft failure event taking into account the transient effects in the SAS and counting with an advance model of friction and blade tangling. The latter has led to the development of a truly generic prediction capability of compressor reverse flow performance unavailable in the public domain. The extensive CFD analysis has allowed the generalisation of the phenomenon identifying the stage geometry features involved and mapping the reverse flow performance of any compressor stage.

9.2 Way forward

The shaft over-speed research started at the Cranfield UTC with the work of Luis Gallar in 2007 [38]. The present thesis has covered the progress in this research project for the last 3 years and the interest of Rolls-Royce guarantees the continuation of the project in future years.

The sponsor company has expressed its interest in the application of the 'all-in-one' simulatione tool to other engines and also in modelling HPS failures. The continuous use of this methodology in future projects will help to identify the limitations and weaknesses of the models leading to their improvement and the reliable application to aero engine certification.

So far, some weaknesses and room for improvement have been identified which allow suggesting the immediate way forward of the research:

Combustor modelling

The impact of combustion modelling on the throttling of the engine makes its reliability of paramount importance. The choke condition at the HPT NGVs regulates the mass flow through the engine which is a consequence of the compression system delivery presser and the turbine entry temperature, being the latter directly affected by the model of the combustion process.

The actual model of combustor is based on:

- Stoichiometric burnt inside the primary zone
- Efficiency degradation at high FAR vales
- Moderation of the heat release by a first order lag equation

Engine recovery from surge is determined by the throttling of the engine. Since the accurate modelling of surge recovery is essential to rely on shaft failure predictions, it is recommended the implementation of a combustion heat release model based on the physics of the process able to take into account, among others:

- Changes in fuel evaporation time
- Combustor blow out and reignition
- Changes in evaporation efficiency

The future combustor model should be developed and validated as an independent tool, being highly recommended to use real shaft failure data or measurements from fuel spiking tests for its validation since the most important objective is to capture the reaction of the combustor to the compressor surge.

Prediction of the free-running compressor deceleration

Differences around 30% have been observed in the capability of CERVANTES to predict the evolution of the rotational speed of the free-running compressor which decelerates fast after the breakage. This error is a consequence of the 1D model used to calculate the shaft work which gives values proportional to the average mass flow through the compressor. This mass flow reduces rapidly to values close to zero in the first instants of the compressor surge leading to low values of power consumption for the compressor. In reality, the compressor deceleration is much faster because the stall inception phenomenon is two-dimensional. It can be considered that the circumferential dimension of the annulus splits into two regions, one working with forward flow and other working with reverse flow. If a 2D approach is applied to calculate the shaft work, both parts of the annulus would contribute positively adding their effects instead of cancelling them as a consequence of dealing with the

low value of average mass flow. This issue might be tackle by a model able to associate an 'equivalent 2D flowfield' to the 1D state calculated by the solver and then higher values of shaft work would be obtained improving the accuracy of the shaft speed evolution over the first instants after surge.

This explanations agrees with engine observations during deep surge events [86]. Observations indicate that deep surge in modern aero engines develops as a two-dimensional phenomenon where the flow is able to reverse from the combustor to the engine inlet following a helicoidal path instead of an axisymmetric one.

In summary, significant milestones have been accomplished over the last 3 years, namely: the development of the compression side model with post-stall capability; the mapping of compressor reverse flow performance; and the integration of the different modules which has produced the 'all-in-one' simulation tool CERVANTES. The first simulation of a real shaft failure scenario carried out with the developed software has shown promising results, establishing a solid backbone for future developments and improvements. The sponsor company has expressed its intention of applying this methodology to other shaft failure scenarios and support this research in future years.

Bibliography

[1] *ANSYS CFX-Solver Modelling Guide, Release 14.5.*

[2] VV. AA. Certification specifications for engines CS-E - Amendment 3. Technical report, European Aviation Safety Agency, 2010.

[3] VV. AA. In-flight uncontained engine failure Airbus A380-842, VH-OQA. Technical report, Australian Transport Safety Bureau, 2010.

[4] VV. AA. Certification memorandum - turbine over-speed resulting from shaft failure. Technical report, European Aviation Safety Agency, 2012.

[5] A. Alexiou, H. J. Hills, C. A. Long, A. B. Turner, and J. A. Millward. Heat transfer in high-pressure compressor gas turbine internal air system: a rotating disc-cone cavity with axial throughflow. *Experimental Heat Transfer: A Journal of Thermal Energy Generation, Transport, Storage and Conversion*, 2000.

[6] J. D. Anderson. *Computational Fluid Dynamics - The Basics with Applications.* McGraw-Hill, 1995.

[7] F. Andreu. Secondary air system and turbine friction/wear model integrated tool. Master's thesis, School of Engineering (Cranfield University), 2012.

[8] M. Arias. Compressor VIGV and VSV schedule optimisation. Master's thesis, School of Engineering (Cranfield University), 2008.

[9] J. E. Bardina, P. G. Huang, and T. J. Coakley. Turbulence modelling validation testing and development. *NASA Technical Memorandum no. 110446*, 1997.

[10] D. Bücker, R. Span, and W. Wagner. Thermodynamic property model for moist air and combustion gases. *Journal of Engineering for Gas Turbines and Power*, 2002.

[11] T. Breuer. Compressor flow instability - Part I: Multistage environment, modelling approaches. In *Unsteady Flows in Turbomachinery - von Karman Institute for Fluid Dynamics Lecture*, 1996.

[12] T. Breuer and S. Servaty. Stall inception and surge in high-speed axial flow compressors. *AGARD-CP-571*, 1995.

[13] C. Calcagni. Secondary air system dynamics modelling during shaft failure. Master's thesis, School of Engineering (Cranfield University), 2008.

[14] J. P. Carneal. Experimental investigation of reverse flow in a compressor cascade. Master's thesis, Virginia Polytechnic Institute and State University, 1988.

[15] A. Caro. Secondary air system dynamics modelling during shaft failure. Master's thesis, School of Engineering (Cranfield University), 2011.

[16] B. I. Celik. Procedure for estimation and reporting of discretization error in CFD applications. *Journal of Fluids Engineering*, 2008.

[17] M. W. Chase. NIST-JANAF Thermochemical tables. *Journal of Physical and Chemical Reference Data Monographs*, 1998.

[18] V. A. Chenaux, H. Schönenborn, and P. Ott. Experimental investigation of an oscillating annual compressor cascade at reverse flow conditions. *ISUAAAT13-S5-7*, 2012.

[19] J. W. Chew. Development in turbomachinery internal air systems. *Proceedings of the Institution of Mechanical Engineers, Part C: Journal of Mechanical Engineering Science*, 2009.

[20] P. R. N. Childs. *Rotating Flow*. Butterworth-Heinemann, 2011.

[21] W. W. Copenhaver. Rotating stall performance and recoverability of a high-speed 10-stage axial flow compressor. *Journal of Propulsion and Power*, 1993.

[22] W. G. Cornell. The stall performance of cascades. In *Proceedings of the second U.S. national congress of applied mechanics*, 1954.

[23] N. A. Cumpsty. *Compressor Aerodynamics*. Longman Scientific & Technical, 1989.

[24] D. K. Das and H. K. Jiang. An experimental study of rotating stall in a multistage axial-flow compressor. *Journal of Engineering for Gas Turbines and Power*, 1984.

[25] M. W. Davis, A. A. Hale, K. A. Shahrokhi, and G. D. Garrard. Euler modelling technique for the investigation of unsteady dynamic compression system behaviour. *AGARD CP-571*, 1995.

[26] M. W. Davis and W. F. O'Brien. A stage-by-stage post-stall compression system modelling technique. *AIAA-87-2088*, 1987.

[27] I. J. Day. Axial compressor performance during surge. *Journal of Propulsion and Power*, 1994.

[28] I. J. Day. The fundamentals of stall and surge in axial compressors. In *Unsteady Flows in Turbomachinery - von Karman Institute for Fluid Dynamics Lecture*, 1996.

[29] I. J. Day. Stall and surge in high-speed compressors and the prospects for active control. In *Unsteady Flows in Turbomachinery - von Karman Institute for Fluid Dynamics Lecture*, 1996.

[30] I. J. Day, E. M. Greitzer, and N. A. Cumpsty. Prediction of compressor performance in rotating stall. *Journal of Engineering for Power*, 1978.

[31] C. Depcik, B. van Leer, and D. Assanis. The numerical simulation of variable-property reacting-gas dynamics: new insights and validation. *Numerical Heat Transfer, Part A: Applications*, 2005.

[32] R. J. Donnelly and D. Fultz. Experiments on the stability of viscous flow between rotating cylinders: II Visual observations. *Proceedings of the Royal Society A*, 1960.

[33] J. F. Dugan. Component operating trends during acceleration and deceleration of two hypothetical two-spool turbojet engines. *NACA RM E54L28*, 1955.

[34] H. W. Emmons, C. F. Person, and H. P. Grant. Compressor surge and stall propagation. *Transactions of the ASME*, 1955.

[35] J. F. Escuret and V. Garnier. Numerical simulation of surge and rotating stall in multi-stage axial-flow compressors. *AIAA-94-3202*, 1994.

[36] A. J. Fawke and H. I. H. Saravanamutto. Digital computer methods for prediction of gas turbine dynamic response. *SAE Paper 710550*, 1971.

[37] M. M. Felling, R. H. Page, H. H. Korst, and R. A. White. An experimental analysis and demosnstration of the non-steady flow in a shock tube. *International Journal of Engineering Education*, 1998.

[38] L. Gallar. *Gas Turbine Shaft Over-Speed / Failure Performance Modelling.* PhD thesis, School of Engineering (Cranfield University), 2010.

[39] L. Gallar, I. Tzagarakis, V. Pachidis, and R. Singh. Compressor performance 2D modelling at reverse flow conditions. In *Proceedings of ASME Turbo Expo 2010: Power for Land, Sea and Air - GT 2010*, 2010.

[40] R. N. Gamache. *Axial Compressor Reverse Flow Performance.* PhD thesis, Massachusetts Institute of Technology, 1985.

[41] R. N. Gamache and E. M. Greitzer. Reverse flow in multistage axial compressors. *Journal of Power and Propulsion*, 1990.

[42] A. Garbo. Performance improvement assessment of a new technology for VIGVs. Master's thesis, School of Engineering (Cranfield University), 2012.

[43] D. Garrard, M. Davis, A. Hale, J. Chalk, and S. Savelle. Analysis of gas turbine engine operability with the aerodynamic turbine engine code. *ISABE 91-7034*, 1997.

[44] A. Gonzalez. Phd thesis (2014). Unpublished, 2014.

[45] E. M. Greitzer. Surge and rotating stall in axial flow compressors, Part I: Theoretical compression system model. *Journal of Engineering for Power*, 1976.

[46] E. M. Greitzer. Surge and rotating stall in axial flow compressors, Part II: Experimental results. *Journal of Engineering for Power*, 1976.

[47] E. M. Greitzer and F. K. Moore. Theory of post-stall transient in axial compression systems: Part II - Aplication. *Journal of Engineering for Gas Turbines and Power*, 1986.

[48] M. Haake, R. Fiola, and S. Staudacher. Multistage compressor and turbine modelling for the prediction of the maximum turbine speed resulting from shaft breakage. *Journal of Turbomachinery*, 2010.

[49] A. A. Hale and M. W. Davis. Dynamic turbine engine compressor code (DYNTECC) theory and capabilites. *AIAA-92-3190*, 1992.

[50] J. Harvell. Private conversation.

[51] J. A. Hernández. *Cálculo Numérico en Ecuaciones Diferenciales Ordinarias.* Aula Documental de Investigación, 2001.

[52] C. Hirsch. *Numerical Computation of Internal and External Flows*. John Wiley & Sons, 1990.

[53] J. H. Horlock. *Axial Flow Compressors - Fluid Mechanics and Thermodynamics*. Robert E. Krieger Publishing Company, 1973.

[54] J. H. Horlock. *Axial Flow Turbines - Fluid Mechanics and Thermodynamics*. Robert E. Krieger Publishing Company, 1973.

[55] M. C. Huppert. Compressor surge. Technical report, Chapter XII of NASA SP-36, 1965.

[56] M. C. Huppert and W. A. Benser. Some stall and surge phenomena in axial flow compressors. *Journal of Aeronautical Science*, 1953.

[57] F. P. Incropera and D. P. DeWitt. *Fundamentals of Heat and Mass Transfer*. John Wiley & Sons Inc, 1985.

[58] H. Ishii and Y. Kashiwabara. A numerical study of surge and rotating stall in axial compressors. *AIAA-91-1896*, 1991.

[59] E. Iturriaga. Through flow analysis of transonic compressors: stall / surge inception. Master's thesis, School of Engineering (Cranfield University), 2011.

[60] N. John. A shock loss model for transonic compressors. Master's thesis, School of Engineering (Cranfield University), 2012.

[61] S. G. Koff. Stall flow characteristics for axial compressors. Master's thesis, Massachusetts Institute of Technology, 1983.

[62] S. G. Koff, R. E. Davis, and E. M. Greitzer. A control volume model of rotating stall in multistage axial compressors. *AIAA-87-2090*, 1987.

[63] L. D. Landau and E. M. Lifschitz. *Fluid Mechanics - Course of Theoretical Physics*. Pergamon Press, 1987.

[64] A. Liñan. *Mecánica de Fluidos*. Publicaciones de la E.T.S.I. Aeronáuticos, 2005.

[65] J. W. Lindau and A. K. Owen. Nonlinear quasi-three-dimensional modeling of rotating stall and surge. *AIAA-97-2772*, 1997.

[66] M. C. Llorens. Secondary air system dynamics modelling during shaft failure. Master's thesis, School of Engineering (Cranfield University), 2010.

[67] J. P. Longley. Calculating the flowfield behaviour of high-speed multi-stage compressors. In *Proceedings of the 1997 International Gas Turbine & Aeroengine Congress & Exhibition*, 1997.

[68] J. P. Longley. Calculating stall and surge transients. In *Proceedings of ASME Turbo Expo 2007: Power for Land, Sea and Air - GT2007-27378*, 2007.

[69] T. Markert and M. McLaren. Analysis of the EFE IP shaft failure. Technical report, Rolls-Royce Deutschland E-TR0683/10-ISS01, 2010.

[70] N. Markopoulos, Y. Neumeier, J. V. R. Prassad, and B. T. Zinn. An extended analytical model for compressor rotating stall and surge. *AIAA-99-2124*, 1999.

[71] A. B. McKenzie. *Axial Flow Fans and Compressors: Aerodynamic Design and Performance*. Ashgate Publishing, 1997.

[72] J. L. Montañés. *Motores de Reacción y Turbinas de Gas*. Publicaciones de la E.T.S.I. Aeronáuticos, 2007.

[73] F. K. Moore and E. M. Greitzer. A theory of post-stall transient in axial compression system: Part I - Development of equations. *Journal of Enginnering for Gas Turbines and Power*, 1986.

[74] H. L. Moses and S. B. Thomason. Axisymmetrically stall flow performance for multistage axial compressors. *Journal of Turbomachinery*, 1986.

[75] A. Muñoz. Compressor stability limit prediction. Master's thesis, School of Engineering (Cranfield University), 2012.

[76] W. F. O'Brien. Dynamic simulation of compressor and gas turbine performance. *AGARD -LS-183*, 1992.

[77] E. W. Otto and B. L. Taylor. Dynamics of a turbojet engine considered as a quasi-static system. *NACA Technical Note 2091*, 1950.

[78] J. M. Owen and H. S. Onur. Convective heat transfer in a rotating cylindrical cavity. *Journal of Engineering for Power*, 1983.

[79] J. M. Owen and R. H. Rogers. *Flow and Heat Transfer in Rotating Disc Systems, Volume 1 - Rotor-Stator Systems*. Research Studies Press ltd., 1989.

[80] V. Peña. Compressor performance modelling at reverse flow conditions. Master's thesis, School of Engineering (Cranfield University), 2012.

[81] C. E. Pearson. Surge behaviour in a three-stage compressor. *Journal of Aeronautical Science*, 1955.

[82] S. Poncet and R. Schiestel. Numerical modelling of heat transfer and fluid flow in rotor-stator cavities with throughflow. *International Journal of Heat and Mass Transfer*, 2007.

[83] A. Psarra. *Gas Turbine Shaft Failure Modelling / Friction and Wear Modelling of Turbines in Contact.* PhD thesis, School of Engineering (Cranfield University), 2010.

[84] D. Rivas and C. Vázquez. *Cálculo Numérico I.* Publicaciones de la E.T.S.I. Aeronáuticos, 2004.

[85] P. J. Roache. Quantification of uncertanty in computational fluid dynamics. *Annual Review Fluid Mechanics*, 1997.

[86] A. L. Rowe. Private conversation.

[87] A. L. Rowe. Shaft failure review - large fan engines. Technical report, Rolls-Royce PTR90865, 2003.

[88] A. L. Rowe. HP shaft failure - estamation of terminal speeds. Technical report, Rolls-Royce PRT91297, 2013.

[89] A. L. Rowe. IP shaft failure - the effects of inertia split and variable geometry schedule. Technical report, Rolls-Royce PTR91301, 2013.

[90] P. Rubini. Turbine blade cooling lecture notes. Cranfield University Notes.

[91] A. Sancho. Performance improvement assessment of a new technology for VIGVs. Master's thesis, School of Engineering (Cranfield University), 2013.

[92] C. Soria. Compressor VIGV and VSV schedule optimisation. Master's thesis, School of Engineering (Cranfield University), 2010.

[93] C. Soria, P. Sanchis, L. Gallo, and F. Andreu. Secondary air system dynamics model. Technical report, Perf Eng UTC TR 2013-1, 2013.

[94] D. J. Taylor. Development of Trent 500 model for increased accuracy in fuel spiking predictions. Technical report, Rolls-Royce PTR 90911, 2004.

[95] G. I. Taylor. Stability of a viscous liquid contained between two rotating cylinders. *Proceedings of the Royal Society A*, 1923.

[96] M. Torralba. Through flow analysis of transonic compressors. Master's thesis, School of Engineering (Cranfield University), 2011.

[97] G. Torres. 3-D CFD analysis of turbine NGV at high negative incidence. Master's thesis, School of Engineering (Cranfield University), 2008.

[98] J. Tu, G. H. Yeoh, and C. Liu. *Computational Fluid Dynamics: A Practical Approach*. Elsevier Butterworth, 2008.

[99] S. Zoppellari. *Analytical Modelling of Rotating Stall and Surge*. PhD thesis, School of Engineering (Cranfield University), 2014.